



TECHNISCHE UNIVERSITÄT MÜNCHEN

TUM School of Natural Sciences

**Development and Validation Studies on Cell Hardware
and Advanced Diagnostic Methods for Material and
Electrode Characterization in All-Solid-State Lithium-Ion
Batteries**

Christian Michael Sedlmeier

Vollständiger Abdruck der von der TUM School of Natural Sciences der
Technischen Universität München
zur Erlangung des akademischen Grades eines

Doktors der Naturwissenschaften (Dr. rer. nat.)

genehmigten Dissertation.

Vorsitzender: Prof. Dr. Sebastian Günther

Prüfer der Dissertation: 1. Prof. Dr. Hubert A. Gasteiger

2. Prof. Dr. Thomas F. Fässler

Diese Dissertation wurde am 20.06.2023 bei der Technischen Universität
München eingereicht und durch die TUM School of Natural Sciences am
18.07.2023 angenommen.

Abstract

The discipline of lithium-ion all-solid-state batteries (ASSBs) is an important and emerging research field. It covers a large variety of aspects, from the synthesis of solid lithium-ion conductors to electrode preparation and cell testing. Thereby, researchers profit from the experience and knowledge gained with liquid electrolyte-based lithium-ion batteries (LIBs) due to many similarities in the cell chemistry between solid and liquid electrolyte systems. However, a few practical aspects still constrain ASSB, research such as the laborious preparation of pelletized samples or the absence of standardized and widely available cell hardware for battery testing, like e.g. Swagelok® T-cells for conventional LIBs. As a consequence, essential analytics such as reference electrodes are rarely applied, even though they would permit valuable insights into the fundamental understanding of ASSBs.

The first part of this PhD thesis focuses on the preparation and characterization of slurry-processed $\text{Li}_6\text{PS}_5\text{Cl}/\text{HNBR}$ composite separator-sheets. We use these thin and flexible sheets to develop ASSB pouch cells featuring a micro-reference electrode (μ -RE). The μ -RE consists of a thin, polyimide insulated gold wire, which is electrochemically lithiated, providing a stable potential and allowing for electrode-resolved electrochemical impedance spectroscopy (EIS). With the μ -RE at hand, we investigate In-Li-anodes and demonstrate that the electrochemical accessibility of the lithium strongly depends on the preparation method, which has important implications for SSB cell testing.

In the second part, we investigate the ionic conductivity of lithium phosphides – a novel class of solid lithium-ion conductors – and evaluate their chemical reactivity against selected ambient atmosphere components.

For each study, we developed a tailor-made cell hardware, considering the specific requirements for the respective system. In total, we present three cell generations: (i) a high-pressure cell for conductivity determination; (ii) a spring-loaded cell for lab-scale battery testing; and (iii) an ASSB pouch cell setup in a three-electrode configuration. We provide the design, the specifications, and the validation procedures for each cell to illustrate their functionality.

Kurzfassung

Lithiumionen Festkörperbatterien (ASSB) sind ein wichtiger und dynamischer Forschungsbereich, welcher Arbeiten von der Synthese von Festkörperelektrolyten, hin über die Elektrodenherstellung bis hin zur Zelltestung umspannt. Dabei profitieren Forscher von den gesammelten Erfahrungen und dem Wissen aus Lithiumionenbatterien (LIBs) mit flüssigem Elektrolyten, da die Zellchemie flüssiger und fester Systeme in vielen Aspekten ähnlich ist. Nichtsdestotrotz gibt es einige Aspekte, die die Forschung an Festkörperbatterien erschweren. Das aufwändige Herstellen von pelletisierten Proben oder die Tatsache, dass es keine weitverbreiteten Testzellen wie Swagelok[®] T-Zellen gibt, sind nur zwei Beispiele. Eine Folge daraus ist, dass essentielle Analytik, wie der standardmäßige Einsatz einer Referenzelektrode, kaum realisiert werden, obwohl so wichtige Informationen gewonnen werden könnten.

Der erste Teil dieser Arbeit beschäftigt sich mit der Herstellung und Untersuchung von nassprozessierten $\text{Li}_6\text{PS}_5\text{Cl}/\text{HNBR}$ Separatoren. Diese dünnen und biegbaren Schichten werden im nächsten Schritt dazu verwendet, um ASSB-Pouchzellen mit einer Mikroreferenzelektrode (μ -RE) herzustellen. Dabei besteht die μ -RE aus einem dünnen, isolierten Golddraht, welcher elektrochemisch lithiiert wird, ein stabiles Potenzial besitzt und darüber hinaus halbzellaufgelöste Impedanzspektroskopie (EIS) ermöglicht. Mithilfe der Referenzelektrode untersuchen wir In-Li-Anoden und zeigen, dass deren elektrochemischen Eigenschaften stark davon abhängen, wie sie hergestellt wurden.

Im zweiten Teil, untersuchen wir die ionische Leitfähigkeit einer neuen Klasse von Festkörperelektrolyten – der Lithiumphosphide. Zudem bewerten wir deren chemische Stabilität gegenüber den einzelnen Bestandteilen von Luft.

Für jede Studie wurde eigens eine Testzelle konstruiert, um den Ansprüchen des jeweiligen Systems gerecht zu werden. Insgesamt entstanden so drei verschiedene Zelltypen: (i) eine Zelle zur Bestimmung der Leitfähigkeit bei hohem Druck; (ii) eine Federzelle für Zelltestungen im Labormaßstab; und (iii) eine Pouchzelle für Messungen mit drei Elektroden. Dabei wird auf jede einzelne Zelle separat eingegangen und deren wichtigsten Bestandteile und Eigenschaften erklärt.

Contents

Abstract	I	
Kurzfassung.....	II	
Contents	III	
List of Acronyms	V	
1	INTRODUCTION	1
1.1	THEORETICAL BACKGROUND ON LI-ION BATTERIES.....	3
1.2	LIQUID VERSUS SOLID ELECTROLYTE LIBS.....	8
1.2.1	<i>Solid Electrolytes</i>	8
1.2.2	<i>Composite Cathodes</i>	11
1.2.3	<i>Anodes</i>	13
1.3	PROMISES OF ALL-SOLID-STATE BATTERIES.....	14
1.4	STRUCTURE OF THE THESIS	16
2	EXPERIMENTAL METHODS.....	17
2.1	DEVELOPMENT OF ASSB CELL SETUPS FOR MATERIAL AND CELL CHARACTERIZATION	17
2.1.1	<i>Cell Generations</i>	18
2.1.2	<i>Sealing Concepts</i>	21
2.1.3	<i>Pressure Application via Screws and Springs</i>	26
2.1.4	<i>Geometric Considerations for Dies</i>	30
2.1.5	<i>Stray Capacitance</i>	32
2.2	ELECTROCHEMICAL IMPEDANCE SPECTROSCOPY (EIS) ON SOLID ELECTROLYTES	36
2.3	<i>IN SITU</i> DIFFUSE REFLECTANCE INFRARED FOURIER-TRANSFORM SPECTROSCOPY (DRIFTS).....	43
2.4	FURTHER TECHNIQUES FOR MATERIAL CHARACTERIZATION.....	46
2.4.1	<i>X-Ray Powder Diffraction Analysis (XRPD)</i>	46
2.4.2	<i>X-Ray Photoelectron Spectroscopy (XPS)</i>	46
2.4.3	<i>Scanning Electron Microscopy (SEM) and Energy- Dispersive X-Ray Spectroscopy (EDX)</i> ..	48
2.4.4	<i>Brunauer-Emmett-Teller (BET) Physisorption Measurements</i>	49
2.4.5	<i>Direct Current (DC) Measurements for Determination of Electrical Conductivity</i>	50
3	RESULTS.....	51
3.1	DEVELOPMENT OF SHEET-TYPE COMPONENTS FOR ALL-SOLID-STATE BATTERY POUCH CELLS	52
3.1.1	<i>Preparation of Sulfidic Solid Electrolyte/Polymer Separator-Sheets</i>	52

Contents

3.1.2	<i>Development of a μ-Reference Electrode for Advanced Diagnostics in All-Solid-State Battery Pouch Cells.....</i>	<i>69</i>
3.2	CHARACTERIZATION OF LITHIUM PHOSPHIDES – A NOVEL CLASS OF SOLID LITHIUM-ION CONDUCTORS....	83
3.2.1	<i>Conductivity Determination of Lithium Phosphidosilicates with a High-Pressure Cell Setup</i>	<i>83</i>
3.2.2	<i>Reactivity of Lithium Phosphides with Ambient Atmosphere.....</i>	<i>120</i>
4	CONCLUSIONS.....	127
	References.....	131
	List of Figures	148
	Acknowledgements	152
	Scientific Contributions	154

List of Acronyms

Abbreviation	Description
AAM	anode active material
ASSB	all-solid-state battery
ATR	attenuated total reflection
BET	Brunauer-Emmett-Teller
BEV	battery electric vehicle
CAM	cathode active material
CPE	constant phase element
DC	direct current
DEC	diethyl carbonate
DFT	density functional theory
DRIFTS	diffuse reflectance infrared fourier transform spectroscopy
EC	ethylene carbonate
EDX	energy-dispersive X-ray analysis
EIS	electrochemical impedance spectroscopy
EMC	ethyl methyl carbonate
GWRE	gold-wire micro-reference electrode
HNBR	hydrogenated nitrile butadiene rubber
LATP	lithium aluminum titanium phosphate ($\text{Li}_{1.3}\text{Al}_{0.3}\text{Ti}_{1.7}(\text{PO}_4)_3$)
LCO	lithium cobalt oxide (LiCoO_2)
LFP	lithium iron phosphate (LiFePO_4)
LGPS	lithium germanium phosphorus sulfide ($\text{Li}_{10}\text{GeP}_2\text{S}_{12}$)
LIB	lithium-ion battery
LISICON	lithium-ion superionic conductor
LiTFSI	lithium bis(trifluoromethanesulfonyl)imide ($\text{LiN}(\text{SO}_2\text{CF}_3)_2$)
LLZO	lithium lanthanum zirconium oxide ($\text{Li}_7\text{La}_3\text{Zr}_2\text{O}_{12}$)
LPS-711	lithium phosphorus sulfide ($\text{Li}_7\text{P}_3\text{S}_{11}$)
LPSBr	lithium phosphorus sulfur bromide ($\text{Li}_6\text{PS}_5\text{Br}$)

List of Acronyms

LPSCl	lithium phosphorus sulfur chloride ($\text{Li}_6\text{PS}_5\text{Cl}$)
LSiPS	lithium silicon phosphorus sulfide ($\text{Li}_{10}\text{SiP}_2\text{S}_{12}$)
LSPS	lithium tin phosphorus sulfide ($\text{Li}_{10}\text{SnP}_2\text{S}_{12}$)
LTO	lithium titanate ($\text{Li}_4\text{Ti}_5\text{O}_{12}$)
MAS NMR	magic-angle-spinning NMR
NASICON	sodium superionic conductor
NCA	lithium nickel cobalt aluminum oxide ($\text{Li}[\text{Ni}_{1-x-y}\text{Co}_x\text{Al}_y]\text{O}_2$)
NCMabc	lithium nickel cobalt manganese oxide ($\text{Li}[\text{Ni}_a\text{Co}_b\text{Mn}_c]\text{O}_2$, ($a + b + c = 1$))
NMR	nuclear magnetic resonance
OCV	open-circuit voltage
PAN	polyacrylonitrile
PEEK	polyether ether ketone
PEIS	potentiostatic electrochemical impedance spectroscopy
PEO	polyethylene oxide
PND	powder neutron diffraction
PTFE	polytetrafluoroethylene
RE	reference electrode
SE	solid electrolyte
SEI	solid electrolyte interphase
SEM	scanning electron microscopy
SN	succinonitrile
XR(P)D	X-ray (powder) diffraction
XPS	X-ray photoelectron spectroscopy

1 Introduction

Today's lithium ion batteries (LIBs) for consumer electronics have become a key technology for the dynamic and fast-paced everyday modern life. For portable applications such as smart phones or laptops, LIBs are an indispensable power supply. In other applications, rechargeable batteries add a lot of comfort to our daily lives, such as there are for vacuum cleaners, drilling machines, or lawn mowers, since no power cord is required anymore or in case of e-bikes and e-scooters, travelling certain distances becomes physically less exhausting. The LIB technology as we know it today was commercialized in 1991 by Sony and has become a success story in itself ever since.¹

The foundation for today's rechargeable LIB technology was laid by *M. Stanley Whittingham* in 1976 by discovering the reversible inter- and deintercalation of lithium ions into TiS_2 .^{2,3} The reversible capacity of TiS_2 is with 210 mAh/g actually higher than of modern cathode active materials (CAMs), however, the material suffered from two major drawbacks. A very low average voltage of 1.9 V vs. Li^+/Li resulted in a comparably low energy density. Furthermore, the material could not be produced in its lithiated form (LiTiS_2), which meant that a lithium metal anode had to be used, but this turned out to be problematic for the long-term cell performance. A few years later in 1981, *John B. Goodenough* reported LiCoO_2 (LCO) as CAM for batteries, describing the reversible deintercalation and reintercalation of lithium ions.⁴ Compared to TiS_2 , LCO offered a lower reversible capacity of ~150 mAh/g but a higher average voltage of 3.8 V vs. Li^+/Li . Most importantly, LCO could be produced in the lithiated state and metallic lithium was not required anymore as anode material.⁵ Eventually, this was realized by *Akira Yoshino* and co-workers in 1985 by the implementation of a carbon-based anode.⁶⁻⁸ For these achievements, Whittingham, Goodenough and Yoshino received the Nobel Prize in 2019.⁹

The first generation of LIBs by Sony offered a gravimetric energy density of 80 Wh/kg on the cell level.¹⁰ Over the years, constant optimization of the cell chemistry and design has led to energy densities of 260 Wh/kg of state-of-the-art LIBs. This progress was mainly driven by the automotive industry to build battery electric vehicles (BEVs) with a few hundreds of km driving range. It is estimated that an energy density of 350 Wh/kg at cell level, which corresponds to roughly 800 Wh/kg at material level, is required to make BEVs fully compatible with cars based on an internal combustion engine.¹¹ To reach these goals, current research is directed towards both optimization of the current cell chemistry but also towards exploring new cell chemistries such as all-solid-state batteries (ASSBs). This thesis focuses on the development of cell components and cell hardware for solid-state lithium-ion batteries. The following chapters will provide more insights into the cell chemistry of ASSBs, the similarities and differences to liquid electrolyte-based LIBs as well as electrode preparation and testing in sulfide-based ASSBs.

1.1 Theoretical Background on Li-Ion Batteries

Operating principle

The main working principle of today's rechargeable Li-ion batteries is the so-called rocking chair principle.^{12,13} This concept describes the reversible shuttling of Li-ions between both electrodes, as schematically depicted in Figure 1.1. The three main components of an LIB are cathode, anode, and electrolyte (in combination with the separator, not displayed in the illustration). The electrode with the higher electrochemical potential is the positive electrode and by convention referred to as cathode, regardless whether the battery is in the charge or discharge process. The most commonly used cathode active materials (CAMs) are layered transition metal oxides of the general formula LiMO_2 ($M = \text{Ni, Mn, Co}$) and are discussed more in detail further on. Accordingly, the negative electrode is referred to as anode and possesses the lower electrochemical potential. The typical anode active material (AAM) is graphite (C_6), which can host lithium between its graphene layers. However, there are more anode materials that host lithium by different mechanisms, as will be shown later on. The electrodes are physically separated by a porous membrane, the so-called separator, typically made from a polymer, which serves to avoid direct contact of the electrodes with each other. The pores of the separator as well as of the porous electrodes are filled with the electrolyte. The electrolyte allows for ionic transport inside the cell, while the electrons have to travel via an external electrical circuit due to the dielectric property of the electrolyte. The separation of ionic and electronic transport is the fundamental principle, that enables to obtain electrical energy from the battery.

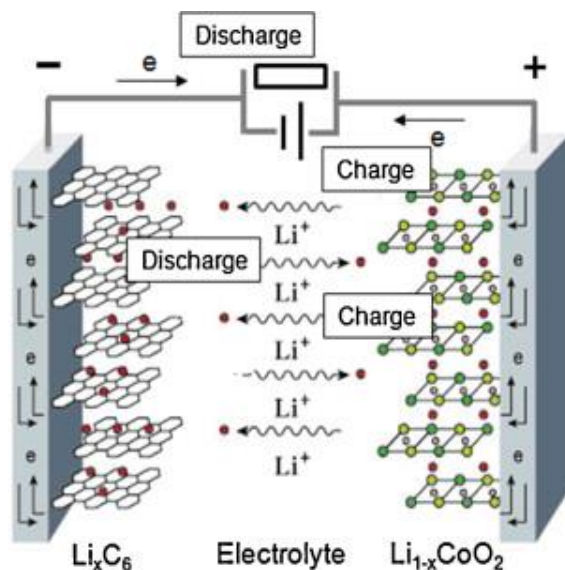
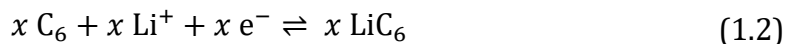
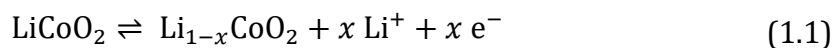


Figure 1.1: Schematic illustration of the main components and operation principle of a Li-ion battery (LIB). The cathode (positive electrode, right) consists in this case of LiCoO_2 (LCO) as cathode active material containing the Li-ions (red), which migrate through the electrolyte towards the anode (negative electrode, left), at which they intercalate into the graphite. The electrons travel via an external circuit, which a load is connected to, from cathode to anode and recombine with the lithium ions. Upon discharge, all processes are reversed. The figure is reprinted from Hausbrand *et al.*¹³ under a Creative Common BY-NC-ND 3.0 license.

During charge, the lithium is extracted from the initially fully lithiated cathode active material (LiCoO_2 (LCO) in the case of Figure 1.1) to a certain degree x , see Equation (1.1). At the same time, lithium ions are intercalated into graphite and recombine with the electrons transported via the external circuit, as shown in Equation (1.2).¹⁴



Upon discharge, the processes are reversed and Li^+ -ions are shuttled back and reintercalate into the LCO cathode. Note that during charge, energy has to be put into the system, or can be stored in the battery, respectively, whereas the discharge provides energy.

Typically, a material has a defined electrochemical potential as a function of its degree of lithiation and therefore is a characteristic of the material (neglecting completely lithiated or delithiated materials and hysteresis effects). The potentials are commonly

referenced to the potential of the Li^+/Li redox couple, set to 0 V by definition. The cell voltage V_{cell} is determined by the difference of cathode and anode potentials:

$$V_{\text{cell}} = V_{\text{cathode}} - V_{\text{anode}} \quad (1.3)$$

If no current is drawn, the cell voltage is usually referred to as open circuit voltage (OCV). In contrast, the cell voltage during operation can significantly differ from the OCV due to the presence of various overpotentials η that occur during current flow. These overpotentials arise from resistive effects in the cell (ionic, interfacial, and/or electric resistances) and their magnitude scales with the applied current.

The capacity of a charge or discharge cycle $Q_{\text{ch/dis}}$ can be assessed by integrating the applied current I over the time t , over which that current was applied:

$$Q_{\text{ch/dis}} = \int_0^t I dt \quad (1.4)$$

Typically, the capacity is normalized to the mass of CAM yielding the so-called specific capacity $q_{\text{ch/dis}}$ in units of $[\text{Ah} \cdot \text{g}_{\text{CAM}}^{-1}]$.

The specific energy E_{cell} of a battery cell can be calculated from the cell voltage V_{cell} and the specific capacity of the cell q_{cell} and given in units of $[\text{Wh} \cdot \text{g}_{\text{cell}}^{-1}]$:

$$E_{\text{cell}} = \int_0^{Q_{\text{cell}}} V_{\text{cell}}(q_{\text{cell}}) dq_{\text{cell}} \quad (1.5)$$

Since the occurrence of overpotentials strongly affects the measured capacity, in battery research the term of the so-called C-rate has been established. The C-rate is a characteristic for battery testing, which relates the applied current I to the cell capacity Q_{cell} and is given in units of $[\text{h}^{-1}]$ according to:

$$\text{C-rate} = \frac{I}{Q_{\text{cell}}} \quad (1.6)$$

Accordingly, a C-rate of 0.5 h^{-1} means that with the applied current a full charge of the cell needs two hours.

Cathode active materials (CAMs)

The cathode active material is the material that determines the capacity of the cell, since it contains the cyclable lithium atoms. As already mentioned, layered transition metal oxides with the formula LiMO_2 are commonly used as CAMs. In these structures, the lithium ions are located between layers of interconnected $[\text{MO}_6]$ octahedra. Upon delithiation, the lithium ions are removed from the layers, which is called deintercalation. For each lithium that is deintercalated, one transition metal atom has to change its oxidation state from +III to +IV, upon which one electron is released and travels to the anode. During reintercalation (discharge) this process is reversed. The first industrially relevant CAM of this type was LCO with a specific capacity of 150 mAh/g and an average voltage of 3.8 V vs. Li^+/Li . Later, mixed layered oxides have been developed such as $\text{LiNi}_{1/3}\text{Co}_{1/3}\text{Mn}_{1/3}\text{O}_2$ (NCM111; 160 mAh/g, 3.9 V). Replacing Co by Ni and Mn allows to extract more Li from the layers without compromising the structural stability of the material. In the strive for higher energy density, gradually more Co and also Mn have been replaced by Ni, leading to Ni-rich NCMs such as NCM622 (180 mAh/g, 3.9 V) or NCM811 (210 mAh/g, 3.8 V).^{10,15,16}

An alternative CAMs is the lithium iron phosphate LiFePO_4 (LFP), which can be structurally attributed to the olivines. In contrast to NCMs, LFP features a lower specific capacity (160 mAh/g) and average voltage (3.4 V vs. Li^+/Li), yet has some specific advantages such as its low-cost raw materials, eco friendliness, and an increased thermal stability, which justifies its use in applications.^{17,18}

Anode active materials (AAMs)

The anode primarily serves to host the lithium from the cathode in the charged state of the battery. There are different types of AAMs, i.e. intercalation materials such as graphite¹⁹ and lithium titanate $\text{Li}_4\text{Ti}_5\text{O}_{12}$ (LTO)²⁰, or alloying materials such as silicon^{21,22}. Each material has its benefits and drawbacks. Graphite is currently the most prevalent AAM and features a reversible capacity of ~360 mAh/g. The low potential of ~0.1 V vs. Li^+/Li in the lithiated stage offers a high cell potential, which is beneficial for the energy density.¹⁹ The downside of such a low potential is the decomposition of the electrolyte at the AAM/electrolyte interface, forming solid decomposition products, the so-called solid electrolyte interphase (SEI). The SEI is ionically conductive as well as kinetically stable and prevents further electrolyte decomposition once it has been

established.^{14,23,24} The composition of the SEI can be affected by the electrolyte composition and the choice of certain additives or the temperature at which the first charge/discharge cycles are conducted. The first (few) charge/discharge cycles are commonly referred to as “formation” cycles during which the SEI is being formed. The aim of the formation is to minimize the contribution of the SEI to the cell resistance. In comparison to graphite, LTO features with 175 mAh/g a lower specific capacity. Together with a significantly higher operating voltage of ~ 1.55 V vs. Li^+/Li , the achievable energy density using LTO is much less compared to graphite. Moreover, no SEI is formed on LTO due to the high operating voltage. Additionally, LTO allows for fast charging-applications since high overpotentials (~ 1.5 V) during fast-charging can be tolerated before running into the danger of lithium plating.^{20,25,26}

The continuous strive for higher energy densities led to the use of silicon as anode material. Silicon forms alloys with lithium and can accommodate up to 3.75 atoms of Li per Si, forming the crystalline phase $\text{Li}_{15}\text{Si}_4$. Thereby, a high specific capacity of ~ 3580 mAh/g and a comparably low average potential of ~ 0.2 V vs. Li^+/Li are very promising for maximizing the energy density. However, a large volume expansion of nearly 300% upon lithiation leads to a mechanical disintegration of the Si particles. The repetitive expansion and contraction of the particles upon cycling continuously ruptures the formed SEI. Consequently, a severe capacity fading is observed and the cycling stability tremendously compromised.^{21,22,27,28}

Pure lithium metal would offer the highest energy density due to its high specific capacity ~ 3860 mAh/g and its low operating voltage. However, the formation of lithium dendrites upon cycling poses a safety risk, as the dendrites eventually lead to short circuiting of the cell.^{14,29}

Electrolytes & separator

The electrolyte in a conventional LIB consists of an organic, aprotic solvent (mixture), in which a lithium salt (e.g. LiPF_6) is dissolved, typically in a concentration of 1 M. Usually a mixture of cyclic carbonates such as ethylene carbonate (EC) and linear carbonates like ethyl methyl carbonate (EMC) or diethyl carbonate (DEC) is used to optimize electrolyte properties such as viscosity, usable temperature range, the formation of a stable SEI, and the solubility of the Li-salts. For the separator, typically a thin (~ 15 - 30 μm), porous polyolefin membrane is used.¹⁴

1.2 Liquid versus Solid Electrolyte LIBs

Knowing the working principle and the main components of a liquid electrolyte-based LIB, we now focus on Li-ion all-solid-state batteries (ASSBs). The basic operating principle, i.e. the reversible shuttling of Li-ions, is the same and even many of the cathode and anode active materials, such as NCM, silicon, or lithium, are used as well. However, replacing the liquid electrolyte and the separator by a solid electrolyte (ionically conductive, electronically insulating) substantially changes the cell chemistry and the mechanics inside the cell. While the liquid electrolyte in conventional LIBs can penetrate into the porous electrodes and thereby ensures a good ionic contact between active material and electrolyte, the situation in ASSBs is more complex. Here, the physical contact of two, more or less rigid, solids determines the ionic conduction. Increasing the cell pressure to several hundreds of bars ensures a good contact in lab-scale cells, but is not an option that can be considered on an industrial level. Therefore, a clever interfacial design is one main criterium for well-performing ASSBs.

In the following, we further elucidate the materials and the different cell chemistries of ASSBs and elaborate the main differences in the electrode design to conventional LIBs. Lastly, we critically evaluate the promises and possible chances of ASSBs and if these still hold true.

1.2.1 Solid Electrolytes

An ASSB is defined by the class of solid electrolyte (SE) of which it is composed. There exist three main classes of solid lithium ion conductors: polymers, oxides and sulfides. Recently, there is also the evolving class of halides to consider.^{30,31} Within each class, different types of SEs can be distinguished, as shown further on.

Polymeric systems consist of an organic polymer (e.g. polyethylene oxide (PEO)), in which a lithium salt (e.g. LiPF₆ or LiTFSI) is dissolved.³² The advantage of polymeric systems is their mechanical flexibility and the comparatively easy preparation from low-cost materials. The downside however is that PEO-based systems feature a very low ionic conductivity ($10^{-8} - 10^{-7}$ S cm⁻¹) at room temperature due to limited chain motion and thus require high operation temperatures of >50°C for a sufficiently high ionic conductivity of the polymer. Attempts have been made to increase the chain flexibility at low temperatures by the addition of plasticizers such as succinonitrile (SN) or by blending with other polymers such as polyacrylonitrile (PAN), which can indeed increase

the ionic conductivity by a few orders magnitude at room temperature. However, its absolute value is still too low at room temperature, so that this still remains a challenge for polymeric systems.^{33–36}

Oxide-based solid ion conductors mainly consist of three structure families: garnets^{37–40} (e.g. $\text{Li}_7\text{La}_3\text{Zr}_2\text{O}_{12}$ (LLZO)), NASICON-like materials^{41,42} (e.g. $\text{Li}_{1.3}\text{Al}_{0.3}\text{Ti}_{1.7}(\text{PO}_4)_3$ (LATP)), and perovskites^{43–45} (e.g. $\text{La}_{0.5}\text{Li}_{0.5}\text{TiO}_3$). The latter class is of high academic interest, since it facilitates the mechanistic understanding of ion conduction in solids by structural modifications such as the deliberate introduction of vacancies by aliovalent doping.^{30,43} Optimized garnets and NASICON-like materials offer moderate values for the ionic conductivity ($10^{-3} - 10^{-4} \text{ S cm}^{-1}$) at room temperatures and promising properties regarding atmospheric and (electro-)chemical stability.³⁷ Still, major drawbacks of oxide-based systems with regards to their application in ASSBs are their brittleness and high interfacial resistances. The latter can be reduced by high-temperature annealing, which however is an additional laborious and costly processing step.^{30,37} Their brittleness however, remains an issue, which often causes mechanical failure of the cell by cracking.

Sulfide-based systems can be divided into thio-LISICON materials and argyrodites. The thio-LISICON class has been established by Kanno et al. in the early 2000s by reporting several compounds with a high lithium ion conductivity within the lithium-germanium-sulfide system. One of the early representatives of this material family is the compound $\text{Li}_{3.25}\text{Ge}_{0.25}\text{P}_{0.75}\text{S}_4$ featuring an ionic conductivity of $\sim 2 \cdot 10^{-3} \text{ S cm}^{-1}$ at room temperature.^{46–48} Later on, the ionic conductivity could be even further increased to $12 \cdot 10^{-3} \text{ S cm}^{-1}$ at room temperature with the compound $\text{Li}_{10}\text{GeP}_2\text{S}_{12}$ (LGPS), which is similar to the conductivity of liquid electrolytes.⁴⁹ Attempts were made to substitute the expensive Ge in LGPS by Sn and Si resulting in the more affordable compounds $\text{Li}_{10}\text{SnP}_2\text{S}_{12}$ (LSPS) and $\text{Li}_{10}\text{SiP}_2\text{S}_{12}$ (LSiPS) as well as solid solutions thereof with slightly lower but still substantial conductivities of $\sim 6 \cdot 10^{-3} \text{ S cm}^{-1}$ (LSPS) and $\sim 2 \cdot 10^{-3} \text{ S cm}^{-1}$ (LSiPS) at room temperature, respectively.^{50–52}

At the same time, progressively more attention was drawn to the family of lithium argyrodites of the general formula $\text{Li}_6\text{PS}_5\text{X}$ ($\text{X} = \text{Cl}, \text{Br}, \text{I}$).^{53–57} The two most prominent compounds of this family are $\text{Li}_6\text{PS}_5\text{Cl}$ (LPSCl) and $\text{Li}_6\text{PS}_5\text{Br}$ (LPSBr), each of them

offering a high ionic conductivity of $> 10^{-3} \text{ S cm}^{-1}$. Therefore, argyrodites are currently the most commonly used electrolyte material in the ASSB research field.

Compared to the other SE systems, sulfides offer in general the highest ionic conductivity. Structurally, this observation can be explained by a larger radius and a higher polarizability of sulfur anions compared to oxygen anions, which is beneficial for the ionic transport through the structure.⁵⁸ In analogy to the structure motif in LISICONs such as $\gamma\text{-Li}_3\text{PO}_4$, the main building unit in thio-LISICONs and argyrodites are isolated and/or interconnected $[\text{PS}_4]$ -units and $[\text{ES}_4]$ -units ($E = \text{Si, Ge, Sn}$), respectively, which is why sulfide-based materials are also referred to as thiophosphates.^{30,59,60}

Sulfides attract great interest in research not only due to their high ionic conductivity but also due to their favorable mechanical properties. Their ductility allows for a straightforward preparation of dense samples by cold-pressing of the powder, resulting in pelletized cell components. On the other hand, one main issue of sulfidic SEs is their limited electrochemical stability. On both interfaces towards anode and cathode, severe decomposition reactions are expected to occur, contributing significantly to the overall cell resistance.^{61,62} Hence, additional protective interfaces are generally mandatory for the use of sulfide-based SEs. Additionally, the poor chemical stability against ambient atmosphere is a major obstacle for thiophosphates. The P-S bonds are susceptible to hydrolysis by water vapor in ambient atmosphere, which significantly decreases the ionic conductivity due to decomposition of the material.^{63–67} Furthermore, toxic H_2S is released, which poses a risk to health and hence an obstacle to the commercialization of sulfides. However, modifications to the material by surface coatings or O-substitution allow handling of the material under dry-room conditions without major losses in the ionic conductivity.^{68–70}

In addition to pelletized samples that are obtained by cold-pressing of the pure powder, sulfidic SEs also allow for thin, sheet-type composites by slurry processing of the SE with a polymer. In doing so, many research groups focus on the selection of appropriate solvent and binder systems.^{71–76} Applying this method, 50 – 100 μm thin separator-sheets with several tens of centimeters in lateral dimension can be easily produced on the lab-scale, while separators of these dimensions with oxides cannot be produced by as easily. Hence, the superior processability of sulfides might be the key property enabling the transition from lab- to pilot-scale production and eventually to an industrial level.^{77,78}

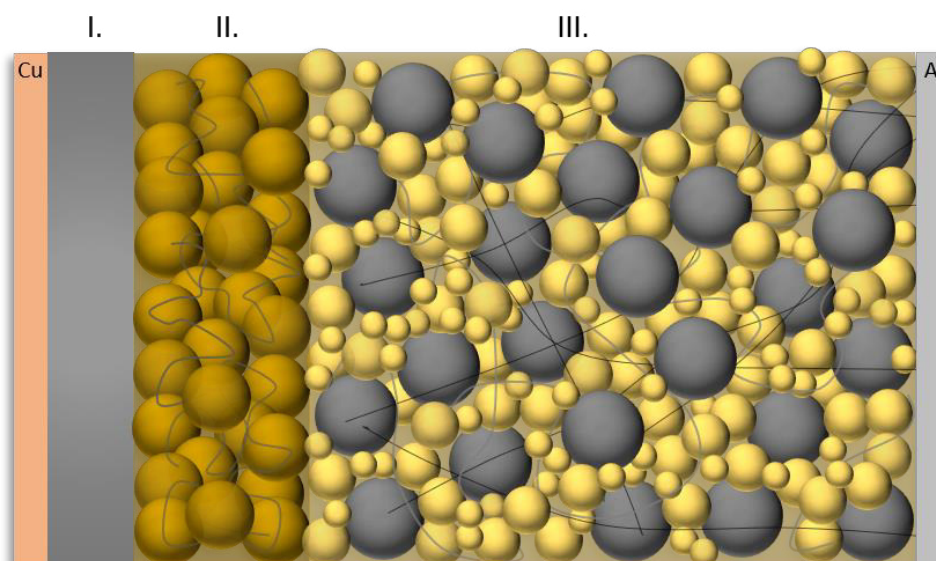


Figure 1.2: Schematic illustration of a sheet-type, sulfide ASSB and its components: **I.** Metal anode on a copper current collector. **II.** Separator-sheet consisting of a sulfide solid electrolyte (dark yellow particles) and a polymeric binder (gray lines). **III.** Composite cathode coated on an aluminum current collector consisting of a CAM (gray particles), sulfidic catholyte (yellow particles), polymeric binder (gray lines) and conductive additive (black lines). Note that in this illustration a bimodal particle size distribution for the catholyte is used. Sulfidic electrolytes in separator and cathode are displayed in differently shaded colors since the used SEs in separator and composite cathode must not necessarily be the same. Dimensions of the electrodes are not drawn to scale. Compression effects such as particle rearrangement or deformation are neglected for simplicity.

1.2.2 Composite Cathodes

In this subsection, the design of composite cathodes and the material requirements will be elucidated. Note that the presented concepts apply only to sulfide-based ASSBs and may be different in certain aspects for oxide- and polymer-based systems.

Similar to the separator, one has to distinguish pellet-type and sheet-type cathodes. In the simplest case, pellet-type cathodes, consist of SE and CAM only, which are cold-pressed into a pellet, usually with several mm in diameter and 0.2 – 1 mm in thickness.^{79,80} Sheet-type cathodes are typically slurry-processed in a solvent and tape-casted on an aluminum foil.^{72,81,82} Thereby, mechanical stability is obtained by the addition of a binder. Recently, first studies have also reported dry-processed electrodes.^{83–87} Additionally, conductive carbon additives are required to ensure good electric conductivity throughout the electrode, which becomes important especially at high rates. Here, the choice of a suitable carbon type appears to be crucial, since decomposition reactions of the SE can be facilitated by the conductive additive.^{88,89}

Compared to cathodes for conventional LIBs, there are two main differences of composite cathodes for ASSBs. First, a protective surface coating of the CAM is generally required to prevent oxidative decomposition of the solid electrolyte and the formation of a resistive interphase between SE and CAM. Thereby, the coating layer serves to bridge the potential gap between the limited electrochemical stability window of the SE and the CAM.⁹⁰ Widely applied coatings are based on layers of SiO₂,^{91–93} LiNbO₃,⁹⁴ LiNb_{0.5}Ta_{0.5}O₃,⁹⁵ or ZrO₂⁹⁶ on the CAM, with thicknesses in the range from 1 – 200 nm.

The second major difference is of mechanical nature and concerns the physical contact of electrolyte and CAM. For a good ionic connection of the CAM particles, a seamless contact with the SE is required, and voids within the electrode should be minimized. Usually this is realized by high compressive forces during electrode preparation so that the CAM particles are firmly embedded into the softer SE, which deforms upon compression. However, the CAM particles often mechanically crack before a perfect contact of all particles can be established, so that the material parameters have to be matched. One of these essential parameters is the mass ratio of CAM:SE. In doing so, a SE fraction of at least 30 wt.% is required to ensure a good cycling stability. Further increasing the SE contents reduces the energy density of the composite cathode but has no beneficial effect on CAM accessibility.⁹⁵ Furthermore, the particle size ratio of CAM and SE has proven to be another essential parameter for well performing cathodes.^{97,98} Shi and co-workers defined for this purpose the parameter λ , which relates the diameter of the CAM particle to the size of the used SE, and show that the SE particle size has to be at least three times smaller in diameter to ensure an ionic connection of all CAM particles for high CAM fractions.⁹⁸ Since the spherical CAM particles cannot pack fully dense, it is beneficial to use smaller SE particles to fill the void between CAM particles. A bimodal particle size distribution of the SE may additionally help to effectively fill the voids with the electrolyte, as indicated in Figure 1.2.^{98,99}

1.2.3 Anodes

In terms of anode materials, different concepts can be found in the research field of ASSBs. For lab-scale testing and studies on separator and cathode, indium has proven to be a very reliable material. Indium forms defined alloys with lithium. The $\text{In}/\text{In}_1\text{Li}_1$ redox couple has a defined potential of 0.62 V vs. Li^+/Li , which the cell potential can be referenced to.^{100–102} Additionally, the higher potential compared to lithium metal mitigates decomposition reactions at the interface to the separator. Typically, a metallic indium foil is attached to the separator. Recent studies however indicate kinetic limitations of pure indium metal foil anodes, so that composites of indium-lithium and SE are preferred.^{103,104}

Silicon is a very promising anode material for ASSBs and is used either as pure silicon powder or as composite, blended with SE. Different groups reported the observation of columnar Si-structures after the first lithiation and subsequent delithiation. The origin of the formed columns is not fully understood yet. Upon further lithiation, the material can expand into the formed voids, so that the volume variation of the material appears to be less problematic compared to liquid electrolyte-based LIBs. Consequently, the full capacity of the material can be utilized making silicon an attractive option to increase the energy density.^{105–107}

Lithium metal offers the highest specific capacity amongst the available AAMs, as already discussed. However, in combination with sulfidic SEs as separator various problems arise. One is the chemical incompatibility of thiophosphates with metallic lithium, leading to a resistive interphase.^{62,108,109} Similar to the CAM/SE-interface, a protective coating is required, yet only a few materials are chemically stable against metallic lithium. Second, the high cell pressure of several tens of MPa that is required for operating sulfide-based ASSBs leads to a compressive force induced creep of the metallic lithium that can result in short circuits.^{104,110,111} Consequently, the cell pressure has to be reduced to a few MPa in case lithium metal is used, which compromises the performance of the cathode. Lastly, lithium dendrite formation limits the cell lifetime and poses a significant risk to cell safety for bigger cells. Recent studies show that voids are formed at the lithium/separator interface upon stripping of lithium from the anode, resulting in local contact loss. Those voids lead to high local current densities during plating and facilitate dendrite growth.^{112,113}

In summary, this section provided an overview of the materials used for ASSBs and described the main differences to conventional LIBs, based on a liquid electrolyte. It can be clearly seen that ASSBs have some intrinsic chemical and mechanical drawbacks that are related to the cell chemistry and the use of solids only. On the other hand, there are also certain potential advantages of the ASSB technology, which will be discussed in the next section.

1.3 Promises of All-Solid-State Batteries

Throughout the literature there are three central claims why ASSBs could be superior to conventional LIBs: (i) SEs might enable the use of a lithium metal anode, since their rigid nature prevents the growth of dendrites, thereby enabling batteries with a higher energy density. (ii) The absence of lithium-ion concentration gradients due to a transference number of 1 for the lithium ion transport should allow for fast rates and hence an increased power density. (iii) Battery safety might be enhanced due to the use of noninflammable materials only.^{114,115}

These potential advantages are mostly based on the inherent material properties rather than on actual measurements, so that it still remains to be proven by full-cell tests that they indeed can be realized

The chemical stability of sulfides against lithium metal has already been discussed above, concluding that sulfidic SEs become chemically reduced when in contact with Li metal, leading to the formation of resistive interphases. A similar behavior has been observed for most oxide-based SE systems.^{116,117} Solely LLZO is considered to be chemically compatible with lithium metal; although it was found that zirconium in LLZO is reduced (reduction potential ~ 0.05 V vs. Li^+/Li) and that an oxygen depleted interlayer is established, this interlayer appears to be kinetically stable which prevents further reduction.¹¹⁸ Doping LLZO with either Al or Ta is reported to provide an even better LLZO/Li interface.¹¹⁹ Even though it is chemically and/or kinetically stable, there is still the issue of Li dendrites that propagate along the grain boundaries or through mechanical defects in the LLZO-based separator. Most likely the dendrites result from high local current densities due to pit formation upon Li stripping, as the rigid LLZO cannot compensate for local contact losses.^{120,121} To mitigate this problem, several research groups implemented a flexible polymer layer between lithium metal and LLZO showing dendrite-free cycling of the cell.^{122,123} Although PEO is not stable at such low potentials,

a stable SEI is formed.¹²⁴ Lastly it is worth mentioning that even though the use of Li metal anodes might be feasible for an all-solid-state battery (ASSB) and would thus boost the energy density on a cell level, another important metric, particularly for BEV applications is the energy density on a module level. Due to the higher necessary stack pressure for ASSBs, compared to conventional LIBs, a more massive housing is required, which might cancel out the gain in energy density by the use of a Li metal anode.

Secondly, high power densities should be possible due to a transference number for the lithium ions of 1. In this case, high charge and discharge rates should be possible without the occurrence of overpotentials due to concentration gradients in the electrolyte phase. In principle, this holds true for inorganic SEs such as sulfides and oxides, as the anions are fixed in the crystal lattice. Note that is not true for polymeric systems that are based on a mixture of a polymer and a lithium salt, in which a concentration gradient can be build up, since the anions are mobile similar to a liquid electrolyte. For polymer SE/hybrid electrolyte, however, high charge/discharge currents could be demonstrated under special conditions for a sulfide-based system.^{114,115} For the sake of completeness, it has to be mentioned that currently poor contacting between the electrode materials dominates the internal cell resistance and thus the entire overpotential of the cell. Accordingly, the electrolyte inherent advantage of the high transference number can only be exploited if the contacting between the electrode materials is optimized. Nevertheless, the statement is true for oxygen- and sulfur-based systems.

Lastly, the inherent safety of ASSBs may be increased compared to conventional LIBs. As already discussed above, it has been claimed short circuiting by Li dendrites can be excluded by the use of polymer layer on the lithium metal. Yet, short circuits are not the only safety risk for a battery, as a thermal runaway can represent a tremendous safety hazard. Similar to organic liquid electrolytes, organic polymer electrolytes are flammable. While oxide-based SEs are not expected to be flammable, recent studies show that sulfides can exothermally react with oxygen that is released by NCM-based CAMs at high states-of-charge (i.e., at a high degree of delithiation).¹²⁵ Furthermore, the release of toxic H₂S upon contact of the ASSB with water (e.g. when the battery module would be severely damaged in a car accident) has to be considered. Hence, only oxide-based systems can be declared as inherently safe.

In conclusion, none of the currently used SEs have so far been confirmed to fulfill all of the three above mentioned promises. Therefore, the general statement that ASSBs are inherently superior in terms of energy density, power density and/or safety compared to conventional LIBs, cannot yet be claimed. However, a clever combination of the beneficial properties of the various materials might eventually fulfill at least partially these promises.

1.4 Structure of the Thesis

This section is supposed to explain the structure and main topics of the thesis and thus serves the reader for a better orientation within this thesis.

Chapter 1 provides an overview about the lithium ion battery (LIB) technology, the underlying working principles and the used materials. The concept of an all-solid-state battery (ASSB) is introduced, describing its different components. Finally, the promises of ASSBs are critically discussed.

Chapter 2 focuses on the used experimental methods. Thereby section 2.1 explains in detail the design and the validation measurements for the three different cell generations that have been developed during this PhD thesis. The presented concepts of this section are not published; however, a substantial amount of time and effort has been invested into the development of the cell hardware, which has become the standard cell hardware for anyone in the group working on ASSBs. Sections 2.2 - 2.4 explain the used analytics and how they are applied in the context of ASSB research.

Chapter 3 summarizes the conducted scientific work. First, a study on the development and characterization of composite separator-sheets, made from a sulfide solid electrolyte and a polymer binder, is presented (subsection 3.1.1), followed by their implementation in ASSB pouch cells with a micro-reference electrode (subsection 3.1.2). The second section focuses on the characterization of lithium phosphides, a novel class of solid electrolytes, discovered by the group of Prof. Thomas Fässler (a cooperation partner at TUM). We thoroughly investigated selected compounds of this material class with respect to their ionic conductivity and activation energy (subsection 3.2.1) as well as their reactivity with ambient atmosphere (subsection 3.2.2).

Lastly, **Chapter 4** concludes the findings and learnings of this PhD thesis.

2 Experimental Methods

The purpose of this chapter is to provide an overview about the most important experimental methods that were applied in the frame of this PhD thesis. First, we present different types of cell hardware and measurements to validate their performance. Afterwards, the focus is on further characterization methods we used. For each technique, a short but concise description of the theoretical principle is provided with references to textbook literature for a more detailed account. The main focus is to describe the specific benefits of each method, the reason why we chose to use them, and why we considered them as appropriate for our purposes. Essential mathematical calculations as well as assumptions we made are provided for a better understanding of how we obtained the measured and determined parameters.

2.1 Development of ASSB Cell Setups for Material and Cell Characterization

During this PhD, three different types of cells have been developed, each with its own and very specific field of application. Since there is no publicly available literature on “*how to build an ASSB test cell*”, we want to share our thoughts and the experiences we made on our journey to develop ASSB cell hardware. In the following, all three cell setups are presented. Subsequently, we discuss the major learnings we experienced upon designing, building, validating, and refining the cells, namely with regard to: (i) the sealing concept, (ii) the pressure application and control, (iii) the geometric requirements and choice of materials for specific cell components, and (iv) the stray capacitance of the cell and its influence on EIS measurements.

2.1.1 Cell Generations

The chronologically first cell generation, also referred to as “screw cell”, is shown in Figure 2.1. This cell was mainly used in order to determine the ionic conductivity of solid electrolytes from the class of the lithium phosphides (cf. subsection 3.2.1). One main characteristic of these materials is their brittle nature, so that effectively no pellet preparation in a hydraulic press was possible, since the pellets crumbled upon removal from the pressing tool. Hence, the approach was to load an appropriate test cell with the powdered material and to densify the sample *in situ*. For the here designed test cell (see Figure 2.1), the pressure is applied by fastening the six screws at a defined torque, which provides a sufficiently high force that in combination with a small sample area (8.0 mm diameter corresponding to $\sim 0.50 \text{ cm}^2$) yielded the desired high cell pressures (100 – 600 MPa). Since the sample could not be extracted from the cell without breaking into pieces, the sample thickness was determined by measuring the distance between lower and upper current collector at selected points and subtracting the respective values from a blank measurement without sample. For this purpose, we drilled six holes in a symmetric configuration into the outer face of the current collectors, to which the tips of a caliper would fit (holes not shown in the drawing). Sealing the cell is realized by two O-rings.

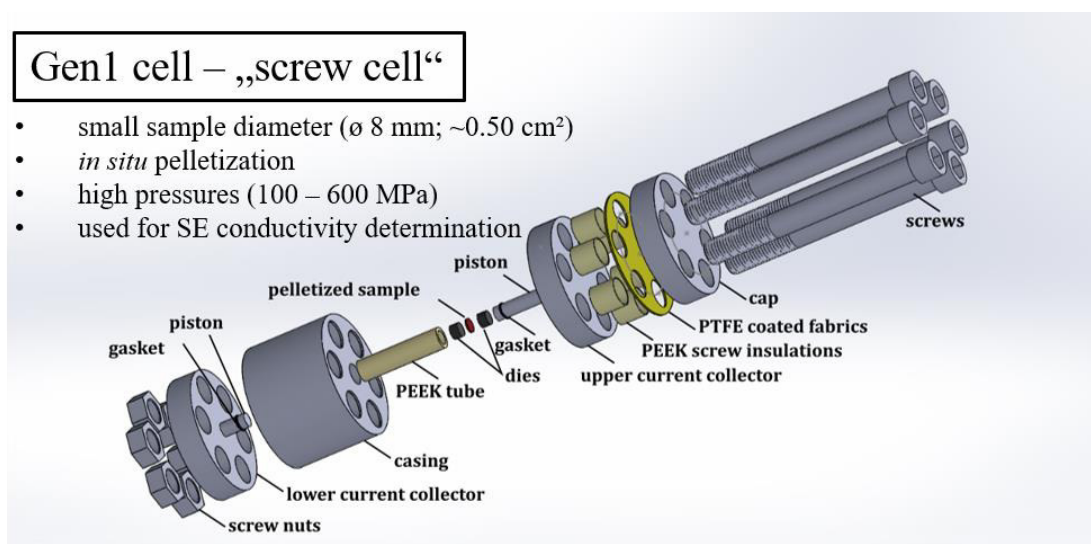


Figure 2.1: Exploded-view drawing of the first cell generation, showing and labelling all components and describing the main characteristics of the cell. Adapted with permission from Strangmüller et al.¹²⁶. Copyright 2019 American Chemical Society.

The second cell generation is the so-called “spring cell” displayed in Figure 2.2. This cell was mainly used for two purposes. First, for the conductivity determination of separator-sheets made from sulfidic SEs and a polymer binder (cf. subsection 3.1.1), which are either compressed inside the spring cell, or pre-compressed at higher pressures using a hydraulic press and then inserted into the spring. Second, the cell can be used for electrochemical testing using electrodes and separator sheets with 8.0 mm. Compared to the screw cell, the spring cell has a lower pressure range (10 – 100 MPa), which, however, is sufficient for charge/discharge cycling experiments. For the spring cell, the pressure is adjusted by the defined compression of a spring (see Figure 2.2a). Furthermore, we implemented a refined sealing concept by the use of a Cu-gasket and a PTFE flat seal (see Figure 2.2b), since we observed insufficient sealing by the use of O-rings, as discussed later on.

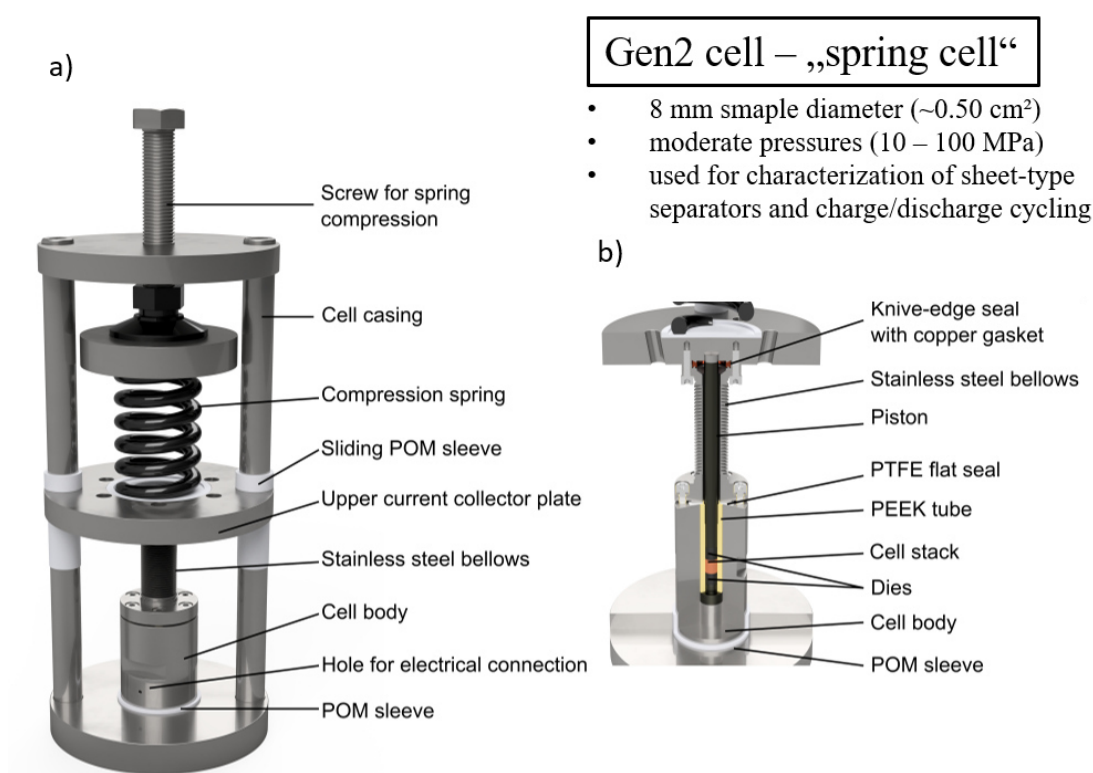
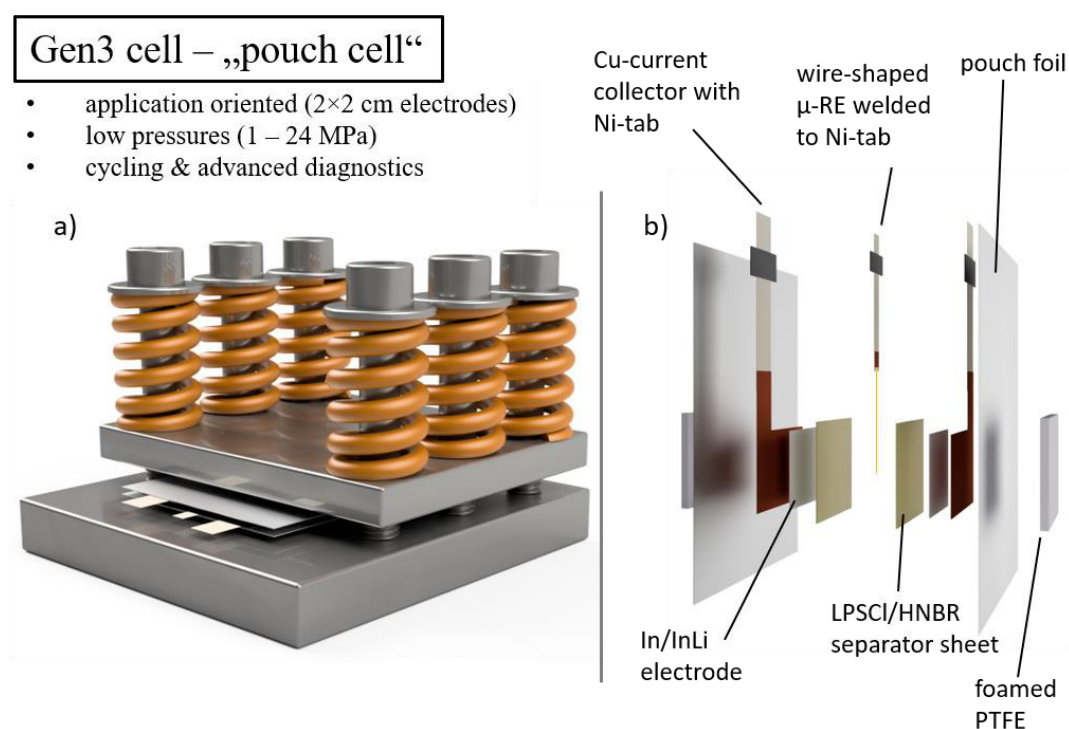


Figure 2.2: Drawing and main characteristics of the second cell generation in side (a) and sectional view (b) with, showing and labelling all components. Reproduced from *Sedlmeier et al.*¹²⁷ with permission from J. Electrochem. Soc. under the terms of the Creative Commons Attribution 4.0 License.

The third cell generation is a pouch cell configuration for charge/discharge cell cycling and is displayed in Figure 2.3. By progressively increasing the electrode area (2×2 cm) and decreasing the cell pressure (1 – 24 MPa), we aimed to make the transition from purely lab-scale cells to a more application-oriented test cell hardware. Furthermore, the open geometry of a pouch cell enables the integration of a reference electrode, as described in subsection 3.1.2. The here implemented μ -reference electrode (μ -RE) allows for advanced diagnostic methods, such as electrode-resolved impedance spectroscopy or the exact determination of the half-cell potentials via the μ -RE.



2.1.2 Sealing Concepts

A reliable long-term sealing is an indispensable key-requirement for any ASSB test cell, since both sulfidic and phosphidic SEs are air-sensitive compounds and degrade upon contact with water vapor. Occasionally cells can be measured inside the glovebox, but practically this is not really desired, as the integration of a battery cycler or a temperature chamber into the glovebox is impractical. Hence, a proper sealing is strongly desired.

Screw cell sealing design

For generation 1 cell, we chose O-rings made from fluoro-rubber, which are commonly used gaskets, and equipped both pistons with one O-ring each, referred to as “gaskets” in Figure 2.1. A groove in the piston guarantees the correct position of the gasket. Upon insertion of the pistons into the PEEK tube, the gasket is compressed, since it is slightly bigger in diameter (8.1 mm) than the PEEK tube (8.0 mm). In order to validate the tightness, we loaded the cell with air-sensitive Li_8SiP_4 SE and conducted electrochemical impedance spectroscopy (EIS) measurements outside the glovebox in a temperature chamber at 25°C, monitoring the impedance evolution over a course of 16 hours, with one spectrum being recorded every two hours, as displayed in Figure 2.4a. From the impedance spectra it can be clearly seen that the impedance increases over time, which indicates a gradual decomposition of the SE material, presumably by intrusion of moisture into the cell. Over the course of 16 hours, the solid electrolyte resistance R_{SE} increases by ~33% (see Figure 2.4c). Remarkably, most of the increase occurs during the first two hours (~22%), after which the increase in impedance becomes progressively less over time, indicating a passivation of the SE material. Once grease is applied to the section of both pistons that is between the gasket and the current collector, the cell is air-tight, indicated by a constant impedance over time (see Figure 2.4b and d). However, when applying grease to the pistons it is important to take care that no grease gets in contact with the sample or the dies, as this might affect the measurement due to the electrically insulating properties of the silicone grease.

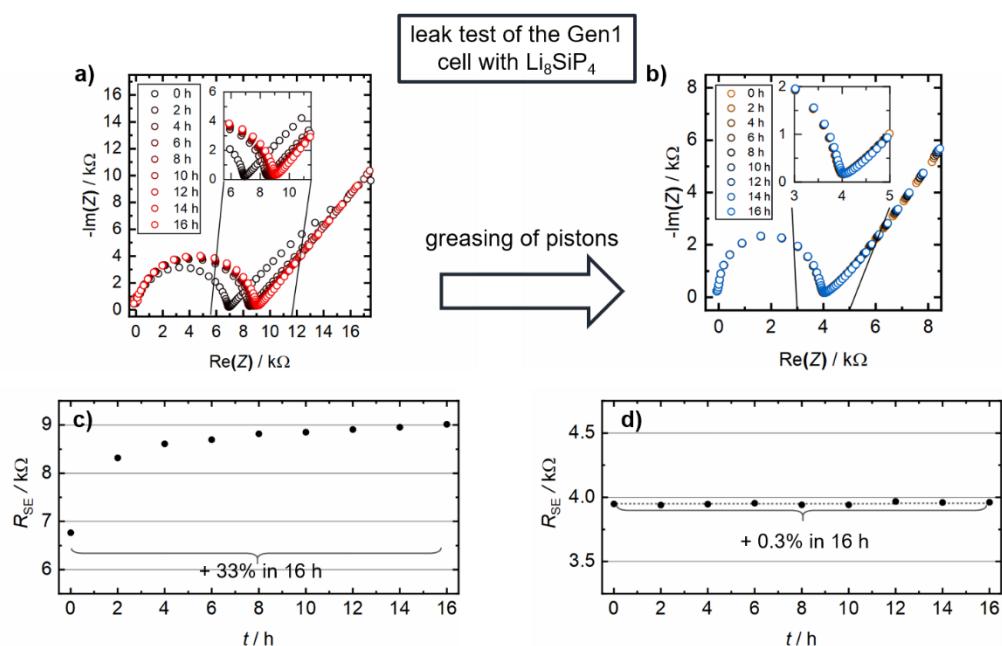


Figure 2.4: Leak test of the generation 1 cell with water vapor sensitive Li_8SiP_4 , conducted by monitoring the impedance evolution over the course of 16 hours. One spectrum (7 MHz – 1 Hz, 10 mV perturbation voltage) is recorded every 2 hours. Cells were assembled inside an argon filled glovebox at 25°C and measured under ambient atmosphere in a temperature chamber at 25°C. Screws were fastened with 30 Nm torque each. The cell, which is tightened by two O-rings applied to the ungreased pistons (a) leaks over time, indicated by the continuous increase in impedance, whereas additional greasing of both pistons (b) ensures a firm sealing over the course of 16 hours. The electrolyte resistance R_{SE} , obtained by an $R/Q+Q$ fit of the spectrum, is displayed versus time in (c) and (d) using non-greased and greased pistons, respectively. Note that the amount of sample is different for both cells and hence also the total resistance. The dashed line in (d) is a guide-to-the-eye.

Although O-rings are commonly used for sealing purposes, our approach did not result in an air-tight sealing without additional greasing of the pistons. We believe, that inserting the piston with the gasket into the PEEK tube and pushing the pistons several centimeters further down to the middle of the PEEK cylinder is the reason for the observed leaks. Although the gasket is larger than the inner diameter of the PEEK tube, the gasket might be damaged upon pushing the piston further into the tube. Additionally, it has to be considered that the inner side of the PEEK tubes was mechanically cleaned with a brush each time after usage, which might cause small grooves that cannot be sufficiently sealed by the gasket in the way we used it.

In the literature however, gaskets are used to seal cell for ASSB research. For example, the test cell built by the company rhd instruments (Darmstadt, Germany)¹²⁸ and the lab-cell used at the university of Gießen^{95,129} feature O-rings. However, in both cell designs, the O-rings are actively compressed between two metal plates or with a screw, which appears to provide a more reliable sealing.

Spring cell sealing design

Having made this experience, we refined the sealing concept for the second cell generation. Here, the sealing is realized via a flexible, custom-made steel bellows (Metallic Flex GmbH, Germany). This kind of component is used for ultra-high vacuum applications and hence absolutely air-tight. Additionally, steel bellows are flexible, so that the pressure onto the sample can be varied during the experiment, which is not possible for O-rings. The upper end of the steel bellows is connected to the upper current collector via a copper gasket and a knife edge seal (DN 16 CF). At the lower end of the steel bellows, the use of a copper gasket is not possible, since the cell body and the upper current collector have to be electrically insulated from each other. Hence, we chose to use a PTFE flat-seal. For this purpose, the steel bellows is equipped with a metal socket to press the PTFE flat-seal against the cell body (cf. Figure 2.2). Upon compression, realized by fastening six M4 screws, the PTFE expands and adapts to the surface roughness, thereby sealing the gap between the bellows and the cell body. In order to design the dimensions of the PTFE flat seal appropriately, some essential considerations have to be made:

- I. The expansion of the PTFE must be large enough to compensate for the surface roughness.
- II. PTFE is quite permeable for water vapor; hence the seal has to be as thin as possible to minimize water permeation along the radial direction of the flat-seal.
- III. Permeability scales inversely to the radial width of the seal; however, the force that can be applied is limited by the dimension of the steel bellows and the tear strength of the M4 screws (A4 steel).

The cell body and the metal socket are made by using a lathe and a milling machine, which allow for an average surface quality of $R_a = 3.2$ (according to DIN EN ISO 1302) and $R_a = 0.8$ for a fine finish, which describe the mean surface roughness in micrometer. Accordingly, the PTFE flat seal has to compensate for up to $6.4 \mu\text{m}$ of surface roughness in the most extreme case (two opposing $3.2 \mu\text{m}$ pits in cell body and socket). Compressing the PTFE to a yield point of 10% implies the PTFE foil should be at least $64 \mu\text{m}$ thick. Practically, it is recommended to account for some tolerance and use a thicker PTFE seal.

Initially, we started with a 340 μm thick PTFE foil and validated the quality of the sealing by means of a vacuum leak test. The setup is displayed in Figure 2.5. We assembled a system with a vacuum pump, a pressure gauge and several valves, to which the cell body and the steel bellows could be connected. All valves, stainless-steel lines and fittings are Swagelok® products. First, a blank measurement is performed (blue curve). In doing so, the connection of the line with the steel bellows is closed with a blind plug. Subsequently, the setup is evacuated for 5 min, before valves 2 and 3 were closed. Note that valve 1 (for venting the system) was always kept closed and valve 4 open during the experiments. The blank measurement shows an initial increase in the pressure during the first 24 hours, which completely levels out afterwards. We attributed this to desorption of physisorbed water on the steel surface and do not consider the setup to leak. Performing the same experiment with the cell body and steel bellows connected via a 340 μm thick PTFE seal, we observed similar results and concluded that the PTFE flat-seal is sufficiently tight.

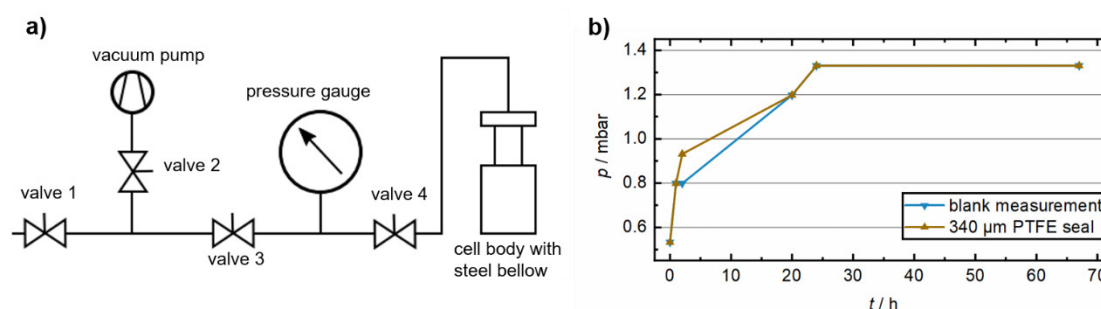


Figure 2.5: Setup for the vacuum leak test of the PTFE flat-seal in the generation 2 cell. The steel bellows is attached to the empty cell body with a 340 μm thick PTFE flat-seal (compressed to 10% yield point). The bellows is attached to the steel line by a copper knife-edge gasket. All connections and valves in the experimental setup are connected via Swagelok® line fittings (a). Recording of the pressure in the experimental setup over the course of 70 hours after evacuation to ~ 0.5 mbar (b). For the blank measurement (blue line), the connection of the line with the steel bellows was closed with a blind plug. The measurement to evaluate the sealing properties of the PTFE flat-seal is displayed in orange. Note that no data points were taken in the interval between 24-70 hours.

In a second step, we gradually reduced the thickness of the PTFE flat-seal, since PTFE is quite permeable to water vapor and since minimizing water intrusion into the cell is crucial for long-term measurements. Reducing the thickness of the seal reduces the effective cross-sectional area for permeation. Eventually, we found that a thickness of 100 μm is sufficient to provide a good tightness of the cell, which is confirmed by the observation that the impedance of an LSPS sample stays constant over the course of at

least 100 hours (data not shown). Interestingly, we also found a 50 μm thick PTFE foil to seal sufficiently well. This means, that the surface roughness of the cell body and the metal socket is even less than the initially specified surface quality (see above). In this context it is worth to mention that we could not determine the surface roughness experimentally but made our initial calculations based on the maximum tolerance values.

The permeation of water scales inversely to the length on which the seal is compressed, hence a larger diameter of the seal appears to be more effective. On the other hand, the size of the seal is limited by the size of the components and the force that can be applied by the six M4 screws, with which the steel bellows is fixed to the cell body. For the used PTFE foil, a yield point of 10% can be achieved with a pressure of 18 N mm^{-2} (provided by the supplier, Angst+Pfister, Switzerland). The final dimensions of the metal socket are 23 mm for the outer and 10 mm for the inner diameter. Hence the compression area is $\sim 337 \text{ mm}^2$, which results in a required force of $\approx 6.1 \text{ kN}$. This can be achieved with a torque of $\sim 2.4 \text{ Nm}$ per screw (see Equation 2.1 and Table 2.1). Accordingly, we designed the PTFE flat-seal with an outer diameter of 25 mm and an inner diameter of 8 mm so that there is an overhang of 2 mm of the PTFE flat-seal at both the outer and inner rim of the metal socket. Note that the effective compression area is unaffected by the overhang of the PTFE foil and is merely due to a better handling.

In this context it is important to mention that for tightness evaluations via EIS it has to be assured that all cell parts are sufficiently dried, especially plastic components that can take up a substantial amount of water. We experienced that a drying procedure of 70°C under dynamic vacuum for 16 hours is not sufficient to completely dry the PTFE seal and the PEEK tube. This was shown by EIS measurements inside a glove box, where an impedance increase over time was observed for 70°C drying temperature, while drying at 120°C yielded a stable impedance over time.

2.1.3 Pressure Application via Screws and Springs

Along with the sealing concept, the mode of pressure application is an important feature of a test cell for ASSB research. In general, there are many different concepts to apply force on a sample, such as the use of springs, the fastening of screws, or the compression of the cell within a press (either via hydraulics or a servo motor). Each of the mentioned options, has its benefits and drawbacks. Springs for example allow for a very precise and reproducible adjustment of the cell pressure and can compensate for expansion/contraction of the materials when measurements are conducted at varying temperatures. However, the overall applicable force is rather low compared to the other options. The fastening of screws allows to establish a high cell pressure, yet the exact adjustment is rather imprecise without the use of a load cell, as shown later on. By the use of a press, high cell pressures can be reached and precisely adjusted. However, since one press per cell is required, this approach is the most cost and laboratory space intensive one and is limited to probably only a couple of cells per lab.

For the generation 1 cell, a high cell pressure for *in situ* compaction and pelletization of the sample was required, as described above. Hence, we chose to apply the force via fastening six M14 screws, knowing the possible drawbacks to this system. Since it was not possible to integrate a load cell into the system, we tried validating the pressure by other means. First, we determined the ionic conductivity of LSPS by EIS measurements as a function of the applied torque per screw. As shown in Figure 2.6, we found the ionic conductivity to increase with progressively higher applied torques before it levels out at torques of 25 Nm and beyond. At this torque, we determined an ionic conductivity of $\sim 4 \text{ mS cm}^{-1}$ at 26°C , which is in good agreement with the bulk conductivity of LSPS reported in the literature.⁵⁰ At this torque, the LSPS sample was found to have a residual porosity of $\approx 17\%$, calculated by assuming a crystal density of 2.254 g cm^{-3} (data from spec sheet of supplier, NEI Corporation, USA). From the literature it is known that several hundred MPa are required to compress sulfide-based SEs to such little porosities.^{50,130,131} Hence, we calculated the theoretical pressure, that should result by fastening the screws with a torque of 30 Nm and compared the thus obtained value to the values from the literature. The calculation and material parameters in the following are based on a textbook in mechanical engineering.¹³²

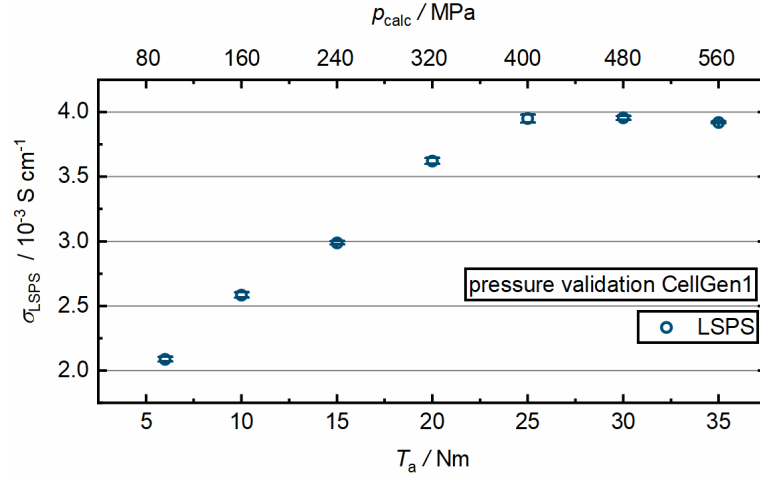


Figure 2.6: Lithium ion conductivity for an LSPS sample determined from EIS measurements conducted in a generation 1 cell inside a glovebox at 26°C. The conductivity is plotted against the torque T_a , which each of the six screws was fastened with. The corresponding calculated pressure (p_{calc}) for each torque is displayed on the upper x-axis and was calculated according to equation (2.1). Error bars correspond to the min/max values of two measurements with the same cell.

The applied torque T_a in units of [Nmm] is calculated via the following formula:

$$T_a = F \cdot \left(\frac{d_2}{2} \cdot \tan(\varphi + \rho') + \mu_k \cdot \frac{d_k}{2} \right) \quad (2.1)$$

The meaning and the numerical values of the parameters are explained in the context of Table 2.1 (see end of this subsection), which additionally provides the values for metric M4 screws (compression of the PTFE flat-seal in the spring cell) and for metric M14 screws (pressure application in the screw cell). F is the resulting force given in Newton. If not given, the lead angle φ can be calculated knowing the thread pitch (p) and the effective diameter of the thread (d_2) according to:

$$\tan(\varphi) = \frac{p}{\pi \cdot d_2} \quad (2.2)$$

The friction angle ρ' depends on the thread, the material, and the lubrication via the relationship given in Equation (2.3). We used a metric normal thread with a pitch angle of $\beta = 60^\circ$ and applied a standard PTFE lubricant to the screws made from A2 steel. Hence, we assumed the thread friction coefficient between $\mu_g = 0.26 - 0.45$. We performed the calculation for the minimal and maximum friction values, since we could not determine μ_g and found that the resulting force deviates by $\sim 20\%$. For our system,

we assumed the higher friction coefficient of $\mu_g = 0.45$, since the lower values are reported for special lubricants only.

$$\rho' = \arctan\left(\frac{\mu_g}{\cos\left(\frac{\beta}{2}\right)}\right) \approx \arctan(1.155 \cdot \mu_g) \quad (2.3)$$

Thus, for one M14 screw fastened with 30 Nm torque follows according to Equation (2.1):

$$30 \text{ Nm} = F \cdot \left(\frac{12.701 \text{ mm}}{2} \cdot \tan(2.87^\circ + 27.46^\circ) + 0.35 \cdot \frac{21 \text{ mm}}{2} \right)$$

Solving for the force F applied by each screw yields:

$$F = \frac{30 \cdot 10^3 \text{ Nmm}}{7.3904 \text{ mm}} = 4059 \text{ N}$$

Tightening the six screws to a torque of 30 Nm and considering the sample area of $A = 0.5026 \text{ cm}^2$ yields a pressure of:

$$p_{\text{cell}} = \frac{6 \cdot 4059 \text{ N}}{50.26 \text{ mm}^2} \approx 485 \text{ MPa}$$

This value is in fairly good agreement with the expectation stated above. Furthermore, we compared the obtained porosity of an LSPS pellet compressed in the cell at a torque of 30 Nm (17% residual porosity, see Figure 2.6) with the porosity of a pellet that was compressed using a hydraulic press and a pressing tool. In the latter case, we found a residual porosity of $22 \pm 1\%$ for an LSPS sample, which was compressed at $\sim 490 \pm 20 \text{ MPa}$ (accuracy based on the readability of pressure gauge of hydraulic press). Hence, we conclude our approach to calculate the pressure for the screw cell works sufficiently well for its main purpose, i.e. to determination of the ionic conductivity for various SE materials. Note that ex-situ pelleting is possible for ductile lithium sulfides like LSPS but not for the brittle lithium phosphides, for which this cell was actually designed; this is why we performed the above described validation measurements with LSPS. We might have underestimated the applied pressure in the screw cell due to the assumed friction coefficients. In total however, we believe to know the pressure

sufficiently well based on the calculated force; however, in addition, a pressure validation should be performed for each type of solid electrolyte that is investigated with this cell.

For the generations 2 and 3 cells, springs are used to adjust the pressure. Knowing the spring constant allows to precisely adjust the applied force by a defined compression of the springs. For both cell generations, block springs were used and operated in a range of 10 – 90% of the possible compression length in order to exclude changes of the spring constant at very low and very high spring compression. Setting the cell pressure this way is more precise and more reliable compared to screws in our opinion. The pressure was validation by compression tests using a pressure sensitive film (Prescale, Fujifilm, US) in the respective pressure range and found to be in good agreement with the set pressure (data not shown). However, the achievable pressure by springs is less compared to screws for the same cell and sample dimensions. This is due to the limited spring constants and compression lengths of the springs in those dimensions, which are still practical to handle in a lab-scale environment. For example, in the spring cell, a heavy-duty spring with a spring constant of 254 N mm^{-1} and compression length of 23.1 mm is implemented. With that, the pressure on the samples of the same size as in the screw cell (8.0 mm diameter) is limited to $\sim 100 \text{ MPa}$. However, for the charge/discharge cycling of sulfidic ASSBs this is more than sufficient, since sulfidic SEs can be pre-compressed in a hydraulic press at higher pressures, so that operating pressures in the range from 20 – 70 are sufficient (even lower pressures are typically used with Li metal anodes).^{79,95,104,107,133}

Table 2.1: Parameters used for the torque-to-force calculation using screws with metric M4 and M14 regular threads. Values are based on “*Handbuch Maschinenbau – Grundlagen und Anwendungen der Maschinenbau-Technik*”¹³².

parameter	meaning	M4	M14
d_2 [mm]	effective diameter	3.545	12.701
φ [°]	lead angle	3.60	2.87
ρ' [°] for $\mu_g=0.26$	friction angle	16.71	16.71
ρ' [°] for $\mu_g=0.45$		27.46	27.46
μ_k [-]	headrest friction coefficient	0.35	0.35
d_k [mm]	headrest diameter	7	21
p [mm]	thread pitch	0.70	2.0
β [°]	pitch angle	60	60
μ_g [-]	thread friction with lubrication	0.26 - 0.45	0.26 - 0.45

2.1.4 Geometric Considerations for Dies

The geometry of the die that is in contact with the SE sample is an essential property, since its surface quality, such as angularity and roughness determine the contact area with the sample. However, this phenomenon is barely discussed in literature.^{127,134} For samples that can be compressed upon applying pressure in the cell, the following might not necessarily be problematic, however, once the sample was externally pre-compressed at higher pressure compared to the operating pressure, the sample becomes rigid and cannot compensate anymore for the minor geometric deviations that are discussed in the following.

The purpose of this subsection is not to quantitatively evaluate the effect of angularity and surface roughness based on tolerance values of the respective preparation method but we rather want to raise awareness of two specific geometric considerations that we experienced to be very important: (i) angularity α and (ii) surface roughness R_a . Figure 2.7 depicts two examples of poor contacting phenomena we have observed during the development and validation of the spring cell. It shall be mentioned that the examples are depicted in an exaggerated way for a better illustration of the problem. Figure 2.7a

describes poor plane-parallelism of the die and the sample due to angularity of the die (here referred to as the deviation of the angle between the face of a cylindrical die and the central axis of the cylinder from 90° and marked by the angle α in Figure 2.7). To a certain extent, this can be induced by the tolerance of the facing step during manufacture (either via lathe turning or milling). However, we also observed angularity if dies are improperly polished by hand during the cleaning procedure. Especially any manual operation is very prone to introduce a slope into the surface of the die. The angularity (α), which can be tolerated for the respective sample, can be estimated by the change in thickness a , which the sample can compensate for upon its compression in the measurement cell and the diameter d of the die:

$$\alpha = \tan\left(\frac{a}{d}\right) \quad (2.4)$$

A rough surface introduces in principal the same problem of an irregular and inhomogeneous contacting between die and sample (see Figure 2.7b), which results in an increased apparent ionic resistance of an SE sample, which in fact is a measurement artifact. Hence, the use of mechanically polished dies is recommended.

These two considerations (i.e., the angularity and surface roughness) are predominantly important for cells that are designed like the screw and the spring cell, with all cell parts are rigid and cannot move or tilt in order to compensate for any irregularities. In contrast, in the pouch cell setup we introduced a buffer layer between the outer surface of the pouch cell (viz., foamed PTFE, see Figure 2.3b) and the steel plate through which the pressure is applied, so certain geometric inhomogeneities and irregularities can be compensated for. However, the applicable pressure range of the buffer layer has to be considered (typically 0.1 – 15 MPa). Furthermore, the surface roughness of the current collector in pouch cells is also less of a problem, since the current collector typically is a metal foil that is prepared by roller pressing instead of machine turning.

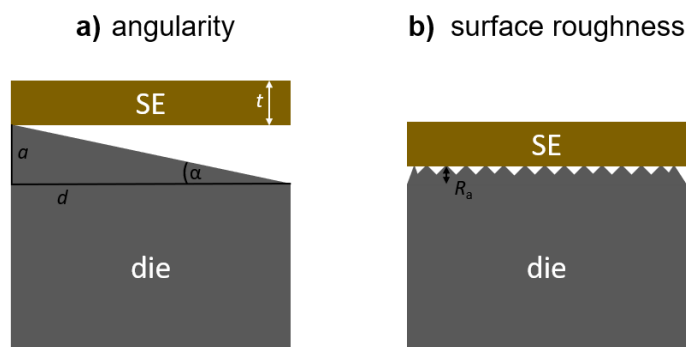


Figure 2.7: Illustration of the geometric effects that we faced during designing and validation the spring cell. Both phenomena have a negative impact on the contacting between the die (gray) and a rigid solid electrolyte (SE) sample (ocher). Important parameters to consider are the diameter of the die d , the deviation upon manufacture a , the angularity α , and the sample thickness t , as well as the surface roughness R_a .

2.1.5 Stray Capacitance

Lastly, we want to discuss the stray capacitance of a cell and its influence on impedance measurements. In fact, a valuable comment of an unknown reviewer to a publication¹³⁵ made us aware of this problem in our screw cell design, which however, can be mitigated by certain modifications of the cell design. First, we discuss the observed stray capacitance, its origin, as well as its influence on the impedance measurements and the thereof determined ionic conductivity. Second, we compare the stray capacitances of the screw cell, the spring, and the pouch cell setups.

The stray capacitance C_{cell} is observed if both electrodes are capacitively coupled via certain cell components.¹³⁶ C_{cell} can be described by an additional capacitor in the equivalent circuit that is connected in parallel to the sample, which itself is described by an R/C element (R_{sample} and C_{sample}). Hence, the stray capacitance adds up with C_{sample} , and the via EIS probed capacitance is thus $C_{\text{total}} = C_{\text{sample}} + C_{\text{cell}}$. Depending on the magnitude of C_{cell} , the probed sample capacitance might be significantly affected or, in extreme cases, entirely dominated by C_{cell} .

In order to assess C_{cells} , we identified its origin inside the cell. Figure 2.8 displays a sectional view of the screw cell. Metallic components, which are in physical contact and thus electrically connected, are displayed in the same shade of gray. The colored boxes mark areas, where metallic components that are not in electrical contact are separated by

an insulating layer, forming a capacitor. Hence, these features determine the stray capacitance of the cell. In total, there are three individual capacitors:

- I. Plate capacitor C_1 between upper current collector and cap, separated by a 155 μm thick PTFE coated fabric (blue).
- II. Cylindrical capacitor C_2 between upper current collector and screws, separated by a 1.0 mm thick PEEK insulation (orange, six times in total).
- III. Cylindrical capacitor C_3 between piston/die and casing, separated by a 2.0 mm thick PEEK insulation (red).

The individual contributions can be calculated knowing the respective dimensions.

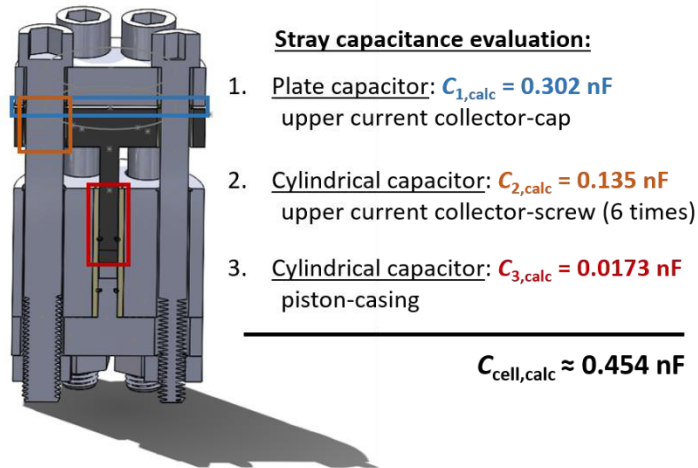


Figure 2.8: Contributions to the calculated stray capacitance of the screw cell. Positions where the capacitors are located in the cell are marked by colored boxes and assigned to the respective cell parts. The capacitor indicated by the orange box is found for all six screws in the cell. For better visibility, cell components which are electrically connected are displayed in the same shade of gray. An exploded-view drawing of the cell is shown in Figure 2.1.

The capacitance of a plate capacitor is calculated by

$$C_{\text{plate}} = \varepsilon_0 \varepsilon_r \cdot \frac{A}{t} \quad (2.5)$$

with A being the area, t the thickness of the insulating media, ε_r its relative permittivity and ε_0 the vacuum permittivity ($8.854 \times 10^{-12} \text{ AsV}^{-1}\text{m}^{-1}$).

For C_1 (blue box) follows

$$C_1 = \varepsilon_0 \cdot 2 \cdot \frac{26.42 \text{ cm}^2}{0.0155 \text{ cm}} = 3.02 \times 10^{-10} \text{ F.}$$

For the PTFE coated glass fiber fabric, we here assumed the permittivity of pure PTFE with $\epsilon_r(\text{PTFE}) = 2.0$, since no information about the composite could be obtained. The area is calculated with a diameter of 70 mm of the circular piece of fabric, from which the area of six holes with a diameter of 16 mm (pass holes for screws) was subtracted.

The capacitances C_2 and C_3 are calculated using the equation for a cylindrical capacitor

$$C_{\text{cylindrical}} = 2\pi \cdot \epsilon_0 \epsilon_r \cdot \frac{l}{\ln\left(\frac{R_2}{R_1}\right)} \quad (2.6)$$

with l as the length of the cylinder, R_2 the outer and R_1 the inner radius of the dielectric from the center of the cylinder. C_2 (orange box) is built from an M14 screw (14 mm diameter) that is passed through a 16 mm pass hole and isolated by a 1.0 mm thick PEEK insulation at a length of 15 mm. Hence follows for $\epsilon_r(\text{PEEK}) = 3.6$:

$$C_{2,\text{per screw}} = 2\pi \cdot \epsilon_0 \cdot 3.6 \cdot \frac{15 \text{ mm}}{\ln\left(\frac{8 \text{ mm}}{7 \text{ mm}}\right)} = 2.25 \times 10^{-11} \text{ F}$$

Since there are six screw, the contribution is calculated to $C_2 = 1.35 \times 10^{-10} \text{ F}$.

The last contribution is a cylindrical capacitor made from the piston and die, which are inserted over a length of 35 mm into the PEEK tube (12 mm outer diameter, 8 mm inner diameter) in the casing (red box).

$$C_3 = 2\pi \cdot \epsilon_0 \cdot 3.6 \cdot \frac{35 \text{ mm}}{\ln\left(\frac{6 \text{ mm}}{4 \text{ mm}}\right)} = 1.73 \times 10^{-11} \text{ F}$$

The thus estimated overall stray capacitance of the screw cell id:

$$C_{\text{cell,calc}} = C_1 + C_2 + C_3 = (3.02 + 1.35 + 0.173) \times 10^{-10} \text{ F} = 4.54 \times 10^{-10} \text{ F}$$

Experimentally, the stray capacitance was determined by coworkers to be $1.83 \times 10^{-10} \text{ F}$ by performing an EIS measurement of the empty cell, i.e., without any sample inside and thereby adjusting a distance of 1 mm between the dies.¹³⁵ To obtain the true stray capacitance, the plate capacitor of the pistons would have to be subtracted, however, due to the large distance of 1 mm between the pistons, its contribution ($\sim 4 \times 10^{-13} \text{ F}$) can be neglected. While the here calculated and

experimentally determined differ by a factor of ~ 3 , the order of magnitude is captured correctly, so that we believe that the main contributions to the observed stray capacitance are captured correctly.

If we compare the stray capacitance of the cell to capacitances we measured for solid electrolyte samples (e.g. 4.2×10^{-10} F for $\text{Li}_{14}\text{SiP}_6$)¹²⁶, we believe there is indeed a strong influence of the stray capacitance on the measurement. This might also explain the almost perfect semi-circles at high frequencies in the impedance spectra using the screw cell. However, we also believe that the determined conductivity is not influenced by the stray capacitance, since the R/Q fit of the semi-circle should still yield the correct value of R_{SE} , as no resistances are added to the system. This is confirmed by the observation that the R/Q fit of the semi-circle and the linear fit of the low-frequency tail (see Figure 2.9) result in similar values for R_{SE} . Nevertheless, we are very grateful for the unknown reviewer's comment, since it pointed out this issue, so that we can consider the stray capacitance for future cell designs.

In the meanwhile, modifications to the screw cell setup were made by the coworkers from the group of Thomas Fässler, inspired by the cell setup from Shirley Meng's group.¹³⁴ In doing so, the stray capacitance was significantly reduced. This can easily be done by (i) significantly increasing the thickness of the insulation between the upper current collector and the cap to several mm (see blue marked region in Figure 2.8), thereby decreasing C_1 by a few orders of magnitude; (ii) making the upper current collector smaller in diameter so that the screws are not passed through the current collector (see blue orange region in Figure 2.8), in which case C_2 disappears; (iii) replacing the steel casing by a significantly thicker PEEK tube, so that C_3 disappears (see red marked region in Figure 2.8).

In contrast to the screw cell, the spring cell has a much lower stray capacitance, since the only capacitors are (i) the steel bellows | cell body, separated by the PTFE flat-seal, (ii) the piston | cell body, separated by the peek tube, and (iii) the M4 screws | steel bellows, separated by PEEK sleeves, as shown in Figure 2.2. In analogy to the above-mentioned calculations, the stray capacitance was estimated to 8.1×10^{-11} F and experimentally determined to be 1.6×10^{-11} F. Since in the spring cell mainly sulfidic SE composite sheets with a capacitance in the order of $\sim 10^{-8} - 10^{-7}$ F had been

investigated,¹²⁷ we do not expect a significant influence of the stray capacitance on the measurements.

For the pouch cells, no geometric stray capacitances are expected, based on the cell components.

2.2 Electrochemical Impedance Spectroscopy (EIS) on Solid Electrolytes

Throughout this thesis, electrochemical impedance spectroscopy (EIS) was mainly used to determine the ionic conductivity of separator-sheets (subsection 3.1.1) and novel solid electrolytes (subsection 3.2.1), the activation energy for lithium ion conduction (subsection 3.2.1), and to characterize the electrochemical state of electrodes (subsection 3.1.2). This section provides a short but concise insight into the working principle of EIS and its main characteristics. For a more detailed explanation of the basics and fundamentals of impedance spectroscopy, the reader may refer to textbooks, on which the following insights are based on.^{137,138} Instead, the main focus shall be directed towards the application of EIS to inorganic solid electrolytes and solid-state batteries and discussing their impedance response.

Impedance spectroscopy is a non-destructive method and in the context of LIB research widely applied to study interfacial processes, such as redox reactions at electrodes, kinetics of reactions, as well as transport properties and diffusion processes. In a potentiostatic EIS (PEIS) experiment, a sinusoidal excitation potential with a small amplitude is applied to the sample and at the same time the current response is recorded. The input signal is varied over a wide frequency range, typically from several MHz to the mHz region. In doing so, the impedance characteristics of the sample is probed, since the complex impedance Z is the ratio of the complex voltage to complex current. The results are typically presented in a *Nyquist* ($-\text{Im}(Z)$ vs. $\text{Re}(Z)$) or *Bode* phase plot (phase shift and voltage over current amplitude ratio vs. frequency). To evaluate the measurement, the data are fitted with an electrical equivalent circuit model, which describes the respective cell components and processes in the cell by a combination of simplified circuit elements, typically resistors, capacitors, the combination of both, a so-called R/C element, and Warburg elements reflecting diffusion processes.

The impedance of a resistor R is independent from the frequency, hence has no phase-shift and can be expressed as $Z_R(\omega) = R$. In contrast, the impedance of a capacitor C is dependent on the frequency and experiences a phase-shift by $-\pi/2$ of the current signal with respect to the voltage signal. Mathematically, the impedance of an ideal capacitor can be written in complex notation as $Z_C(\omega) = \frac{1}{i\omega C}$ (here: $i \equiv \sqrt{-1}$). The parallel connection of a resistor and a capacitor, a so-called R/C element, is commonly used to describe electrochemical interfaces, since electrode/electrolyte interfaces often experience a charge-transfer reaction and double-layer charging/discharging at the same time. In the *Nyquist* diagram, an R/C element is represented by a semi-circle with the radius R . The highest point of the semi-circle appears at a certain frequency, f_{apex} , which is well-defined for a true R/C element by:

$$f_{\text{apex}} = \frac{1}{2\pi \cdot RC} \quad (2.7)$$

Since impedance measurements are conducted over a wide frequency range, different processes can be probed and appear at different locations (i.e., frequencies) in the *Nyquist* plot, depending on the time constant τ of a given process; for R/C elements and for a resistor and capacitor in series, the time constant of the process is described by:

$$\tau = RC \quad (2.8)$$

With this in mind, we take a closer look at the impedance response of a solid electrolyte that is placed between two blocking metal electrodes. The “ideal” solid electrolyte would consist of one large single crystal with no grain boundaries within the sample. In this case, lithium ion conduction takes place through the entire bulk of the material and can be described by an R/C element, yielding a single semi-circle in the *Nyquist* representation. In this, R represents the resistance for lithium ion transport and C accounts for the dielectric properties, such as bulk polarization of the lattice, induced by localized opposite charges such as defects or vacancies and lithium ions.^{139,140} However, most solid electrolytes are polycrystalline materials, whose impedance response can be described in a simplified way by the brick-layer-model.¹⁴¹ This model describes a polycrystalline solid-state ion conductor as a material composed of many uniform and cubic crystallites (“bricks”). Thereby, the contact areas of the “bricks”

represent thin but resistive grain boundaries of the material. Therefore, grain boundaries are described by an R/C element, with R being the inter grain resistance R_{gb} and C as the double-layer capacitance C_{gb} for the grain boundaries.^{139,142} In theory, grain and grain boundary contributions should be distinguishable, since their capacitances are expected to be different, so that the respective semi-circles would appear at different frequencies according to Equation (2.7). The grains are thought to have rather low capacitances ($\sim 10^{-12}$ F), since they can be assigned to rather thick layers, representing the bulk material. In contrast, grain boundaries are comparably thin layers. Thus, according to Equation (2.5), grain boundary capacitances are generally much higher ($\sim 10^{-11} - 10^{-7}$ F), depending on the specific grain boundary properties. Well-sintered materials possess a larger grain boundary capacitance than samples with resistive layers between the boundaries or poor contacting of the grain.^{139,143}

In fact, the brick-layer model is not valid in many real scenarios and merely serves as a model picture to imagine a polycrystalline material, since it does not account for: (i) a broad grain size distribution, inducing a tortuous path of the ions due to different values for the grain (R_{grain}) and the grain boundary resistance (R_{gb}); (ii) an inhomogeneous grain size distribution, inducing preferential pathways for the ions to travel in regions with a low grain boundary density; (iii) inhomogeneous grain shapes.^{141,144,145} Additionally, the brick-layer model neglects poor contacting of the crystallites, which often is accounted for in the more recent literature.^{50,146} This leads to the fact that often grain and grain boundary contributions to the lithium ion transport cannot be separated and only the superposition of the bulk (intra grain) and grain boundary (inter grain) lithium ion transport can be determined. Consequently, the *Nyquist* representation shows only one semi-circle. A separation of grain and grain boundary contributions can be achieved for material systems, in which the activation energy (E_A) to grain and grain boundary ion conduction are different, by the use of EIS measurements at very low temperatures, since the lithium ion conduction are subject to *Arrhenius*-type behavior.^{50,51}

Furthermore, solid electrolytes are not ideally polarizable materials, since the double-layer capacitance is not purely capacitive and often displays a certain frequency dispersion. Hence, instead of an ideal capacitor C , a non-ideal capacitor Q , also referred to as constant phase element (CPE), is used to describe solid electrolytes. The impedance

of a CPE in complex notation is given by $Z_Q(\omega) = \frac{1}{(i\omega)^\alpha Q}$ and accounts for a non-ideal behavior by the exponent α . Note that Q is given in units of $[\text{F s}^{(\alpha-1)}]$.

In most practical applications, as presented in subsections 3.1.1 and 3.2.1, the overall conductivity of the used solid electrolyte is the desired parameter and calculated from the solid electrolyte resistance R_{SE} . For this purpose, it is not necessarily required to resolve the grain and grain boundary contributions to the lithium ion transport, as it is the case for fundamental studies.^{50,130} This simplifies the impedance analysis for the conductivity determination to a certain extent. Figure 2.9 presents an example of an LSPS/HNBR separator-sheet that was analyzed via EIS in the spring cell. The impedance spectrum shows one high-frequency semi-circle and a low-frequency tail. The latter feature can be assigned to the electrode polarization (gray CPE (Q_{pol}) in the inset of Figure 2.9), while the semi-circle is attributed to the grain boundary contribution (blue R/Q element). For the grain contribution another semi-circle is expected, which however, cannot be resolved at the given frequency range and temperature. Hence, its contribution is mimicked by an additional resistor R_{HFR} (green) in the equivalent circuit. We call this the high-frequency resistance (HFR), which consist of the internal cell resistance R_{cell} and the grain resistance R_{grain} . In the most cases however, R_{cell} is negligibly small and the HFR is basically equal to R_{grain} ; nevertheless, we recommend to determine this cell parameter, e.g. by an impedance measurement of the empty cell without any sample. Hence, the separator resistance R_{SE} is obtained from the sum of grain and grain boundary contributions. Note that the shape of the impedance spectrum and to which degree the features can be resolved strongly depends on the material, the sample preparation, and the measurement conditions, such as cell, temperature, pressure, frequency range, etc.^{50,130,147}

A complementary and/or alternative way to assess R_{SE} when neither grain nor grain boundary contributions can be resolved, is via a linear fit of the low-frequency tail. Its intercept with the x -axis corresponds to the solid electrode resistance, since the impedance of a resistor (here: electrolyte resistance) is only a point on the real axis in the *Nyquist* representation. Both methods are shown in Figure 2.9 and lead to the same values within the range of the fitting errors (~ 1 -5%). The determined resistance can be used in Equation (2.9), to calculate the lithium ion conductivity when knowing the sample thickness (t) and sample area (A). Note that this equation is only valid for very dense

samples (residual porosity $\varepsilon < 10\%$), since geometric factors such as sample porosity and tortuosity are neglected.

$$\sigma_{Li} = \frac{t}{R_{SE} \cdot A} \quad (2.9)$$

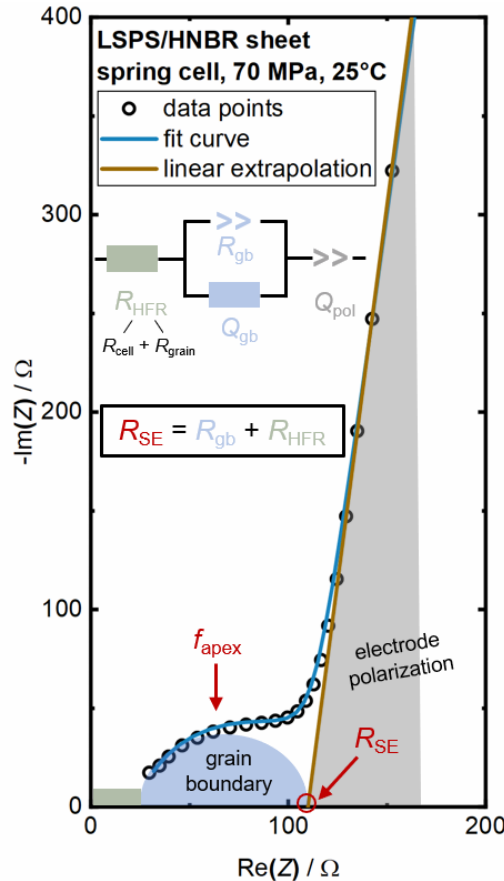


Figure 2.9: Illustration of an EIS spectrum for the conductivity determination of three stacked LSPS/HNBR (5.8 vol.-% HNBR) separator-sheets, measured in the spring cell at 70 MPa and 25°C in a frequency range from 7 MHz – 100 Hz. Data points (black circles) are displayed in a frequency range from 7 MHz – 10 kHz. The fit (blue line) was obtained by fitting the data with an R_1+R_2/Q_2+Q_3 equivalent circuit, as displayed. The other line results from a linear fit of the low-frequency tail between 30 – 4 kHz, which was extrapolated to the x-axis. The high-frequency resistance R_{HFR} (green) represents a superposition of the cell resistance and the grain bulk resistance R_{grain} . For the latter we expect an R/Q element, which however cannot be resolved at the used frequency and temperature. The blue semi-circle illustrates the grain boundary resistance R_{gb} . Note that the green and blue features are manually added but their magnitude is in scale to the values obtained by the fit. The values for the solid electrolyte resistance R_{SE} determined via the equivalent circuit fit and the one obtained by the extrapolation of the linearly fitted low-frequency tail deviate by ~1%. Sample thickness is 0.026 cm and sample area 0.50 cm².

Additionally, PEIS measurements at different temperatures allow to determine the activation energy for the lithium ion conduction. The conductivity of charged species in a material can be expressed via its charge q , the concentration of charge carriers N and its mobility μ according to:

$$\sigma = q \cdot N \cdot \mu \quad (2.10)$$

In doing so, the mobility can be related to the diffusion coefficient D via the *Einstein-Smoluchowski* equation¹⁴⁸

$$\mu = \frac{q \cdot D}{k_B \cdot T} \quad (2.11)$$

with T being the temperature and k_B the *Boltzmann* constant. Inserting Equation (2.11) into Equation (2.10) yields the following expression for the conductivity:

$$\sigma = \frac{q^2 \cdot N \cdot D}{k_B \cdot T} \quad (2.12)$$

The diffusion coefficient is related to the hopping frequency ω and the hopping distance x . Furthermore, we have to correct for the 6 spatial directions (x -, y - and z -direction, all of which back and forth) since we only look at the motion in one direction:

$$D = \frac{x^2 \cdot \omega}{6} \quad (2.13)$$

In doing so, the hopping frequency is the property that is thermally activated and thus subjected to *Arrhenius* behavior:

$$\omega = \omega_0 \cdot e^{\frac{-E_A}{k_B T}} \quad (2.14)$$

Hence follows for the conductivity:

$$\sigma = \frac{q^2 \cdot N \cdot x^2 \cdot \omega_0}{6 k_B \cdot T} \cdot e^{\frac{-E_A}{k_B T}} \quad (2.15)$$

This equation can now be transformed to the general *Arrhenius*-type equation by defining the preexponential factor σ_0 as

$$\sigma_0 = \frac{q^2 \cdot N \cdot x^2 \cdot \omega_0}{6 k_B} \quad (2.16)$$

Note that σ_0 is defined as a constant and hence T cannot be included to σ_0 for EIS measurements performed at different temperatures. The activation energy can then be assessed via the linear equation:

$$\log(\sigma \cdot T) = \frac{-E_A}{k_B} \cdot \frac{1}{T} + \log(\sigma_0) \quad (2.17)$$

Replacing k_B by the gas constant R , the activation energy E_A in units of $[\text{kJ} \cdot \text{mol}^{-1}]$ can be extracted from the slope by plotting $\log(\sigma \cdot T)$ over $1000/T$ as exemplarily shown in Figure 2.10.

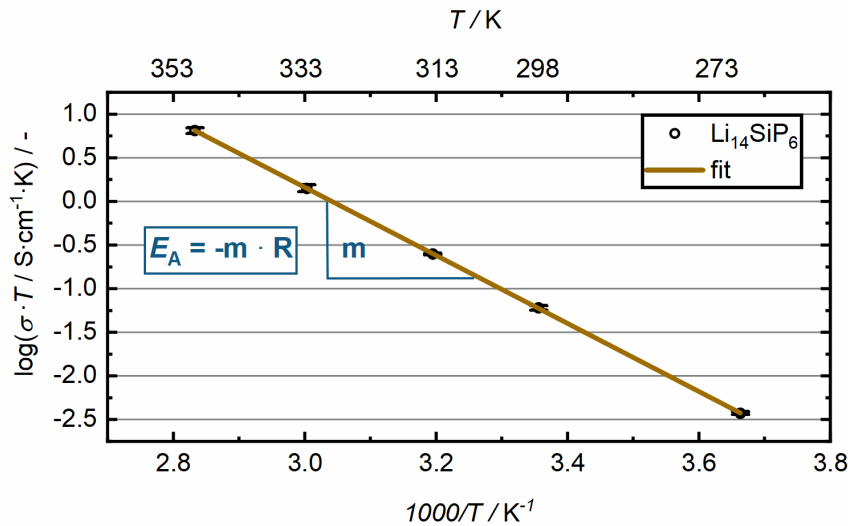


Figure 2.10: Illustration of an exemplary *Arrhenius* plot of the product of conductivity and temperature ($\sigma \cdot T$) versus $1000/T$ and linear fit of the data points for $\text{Li}_{14}\text{SiP}_6$. Error bars are based on the standard deviation from three independent measurements. The activation energy E_A for lithium ion conduction in units of $[\text{kJ} \cdot \text{mol}^{-1}]$ is obtained from the slope m of the linear fit and the universal gas constant R .

2.3 *In Situ* Diffuse Reflectance Infrared Fourier-Transform Spectroscopy (DRIFTS)

In order to probe the reactivity of different solid electrolytes with ambient atmosphere, we used our setup for diffuse reflectance infrared Fourier-transform spectroscopy (DRIFTS). DRIFTS is a very surface sensitive type of infrared spectroscopy, in which the diffusely reflected radiation on rough surfaces is collected by a special, ellipsoidal mirror optics. This technique was already used in our group to investigate surface contaminants and surface passivation strategies on CAMs.^{149–151} In this context, we developed a setup for *in situ* DRIFTS, with which it is possible to expose the sample to various gas mixtures while recording IR spectra, as displayed in Figure 2.11.¹⁵² We can adjust the gas stream composition using different gas supplies, i.e., CO₂ (1000 ppm in Ar), O₂, and Ar. Additionally, the setup allows for a humidification thereby introducing water vapor into the system by saturating the gas stream with H₂O. Thereby we can simulate the composition of ambient atmosphere, using argon instead of nitrogen, and can selectively evaluate the reactivity of SEs against either of the three main components of ambient air (O₂, H₂O, CO₂, neglecting N₂ for which no reactivity is expected) or defined combinations of them.

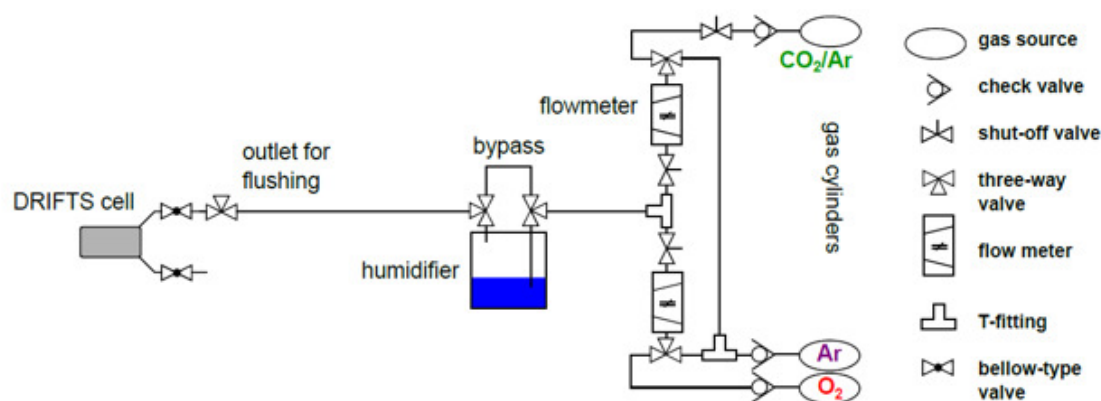


Figure 2.11: Setup for *in situ* DRIFTS measurements exposing powdered solid electrolyte samples to of various gas atmospheres containing different components of ambient atmosphere. The gas mixture can be adjusted by mixing gases from different sources using Ar as carrier gas: 1000 ppm CO₂ in Ar (green), Ar (violet) and O₂ (red); via the humidifier, it is possible to introduce water vapor into the system. The gas tight DRIFTS cell, which contains the sample, is placed in the IR spectrometer. Symbols of the components are explained on the right. Reprinted from *Christian Sedlmeier's* Master's thesis.¹⁵²

The *in situ* DRIFTS setup consisted of three different gas supplies featuring 1000 ppm CO₂ in Ar (99.9% CO₂ in 99.999% Ar, Westfalen, Germany), Ar (99.999%, Westfalen, Germany) and O₂ (99.999%, Westfalen, Germany), which feed into a gas line system (all parts are made from stainless steel and purchased from Swagelok, USA). A self-made humidifier, consisting of a modified and tightly sealed glass vial (Schott, Germany) allowed to introduce water vapor into the cell. In case experiments were performed in the absence of water vapor, the “bypass” route allowed for experiments with dry gases. Via an additional outlet in direct vicinity to the DRIFTS cell, the entire system could be preconditioned to ensure a defined atmosphere before connecting the DRIFTS cell to the gas stream. The overall gas flow was adjusted via two flow meters to 10 ml/min.

Measurements were conducted on a Cary 670 FTIR spectrometer (Agilent Technologies, USA) using parabolic Praying Mantis™ mirror optics (Harrick Scientific Products Inc, USA). Spectra were taken between 6000 – 400 cm⁻¹ with a resolution of 1 cm⁻¹, using a liquid nitrogen cooled mercury cadmium telluride (MCT) detector. The sampling chamber was constantly flushed with dried air (DPS-2 air purifier, FST GmbH, Germany). The sample was prepared in an argon filled glovebox (MBraun, Germany), placing the SE powder (~60 mg) into the DRIFTS cell (Praying Mantis™ high temperature reaction chambers, Harrick Scientific Products Inc, USA) and then sealing the cell. Subsequently, the cell was transferred to the IR spectrometer and mounted into the sampling chamber as well as connected to the gas line. Prior to the first measurement, it was waited for 15 min to purge the sampling chamber with dry air. In doing so, water vapor inside the sampling chamber is removed that would otherwise lead to experimental artifacts.

The measurements were performed following a defined procedure:

- I. Initial spectrum without gas flow, with the sample in the cell under “glovebox atmosphere”.
- II. Gas exposure for 2 hours; spectra (1 spectrum per 5 min) taken under dynamic gas flow (20 ml/min) with defined gas atmosphere.
- III. Ar purge for 1 hour to remove the atmosphere from step II taking one spectrum every 10 min.

Possible gas mixtures in step II were: Ar, O₂, 1000 ppm CO₂/Ar, Ar-H₂O (humidified Argon with an estimated dew point of $T_{dp} \sim 13$ °C corresponding to ~ 14700 ppm H₂O in Ar) and 1000 ppm CO₂/ Ar-H₂O (humidified CO₂/Argon with an estimated dew point of $T_{dp} \sim 13$ °C corresponding to ~ 14700 ppm H₂O in Ar). For each gas mixture, an individual measurement was performed, so that in total five experiments had to be performed for one complete set. Prior to introducing the gas stream into the cell, the gas line system was preconditioned for 1 hour to ensure a constant atmosphere. The volume of the cell was 34 ml, hence roughly once every two minutes the atmosphere in the cell was exchanged. It is worth to mention that we did not mix the sample with any dilution media such as KBr, CaF₂, SiC etc., since we observed a quite significant interaction of all of the examined dilution media with the water vapor, resulting in artifacts.

Spectra are displayed (see subsection 3.2.2) in reflectance units R_{sample} , which are defined as the ratio of the sample intensity (I_{sample}) divided by the intensity of a background measurement (I_{Au}) using a self-made, gold sputtered sand paper (400 grit).

$$R_{sample} = \frac{I_{sample}}{I_{Au}} \quad (2.18)$$

2.4 Further Techniques for Material Characterization

2.4.1 X-Ray Powder Diffraction Analysis (XRPD)

X-Ray Diffraction (XRD) analysis is a bulk-sensitive technique that can be used to determine both the qualitative and quantitative phase composition of a crystalline material. The main working principle of XRD is based on the diffraction of incoming X-rays at the electron shell of the atoms in the sample. The lattice parameters of the crystal system can be determined from the diffraction angles in XRD and the wavelength of the used X-rays (typically 1-10 nm). With the help of databases or reference measurements, it is often possible to identify the respective substances.¹⁵³ In the field of ASSB research, XRD has been used to study the composition, phase purity and synthesis conditions of SEs^{51,71,154} or the chemical compatibility of SEs with solvents and binders for slurry-processed separator-sheets.^{71-73,75} In the frame of this thesis, we used XRD in order to characterize pristine materials in the as-received state from the supplier in order to first assess the phase purity of the material and hence its quality. Second XRD was used to probe for decomposition products upon exposure towards ambient atmosphere during production and/or shipping of the material and lastly to evaluate possible decomposition during wet processing in toluene for the binder-sheet fabrication (see subsection 3.1.1). All diffractograms were collected at room temperature on a STOE STADI P diffractometer (STEO, Germany) in transmission mode in the 2θ range of 10° - 90° , using Mo- $K_{\alpha 1}$ radiation (0.7093 Å, 50 kV, 40 mV) a Ge(111)-monochromator and a Dectris Mythen 1 K detector (step size 0.015, integration time/step 150 s). Raw data were processed with WinXPOW software (version 3.0.2.1). Powdered samples were measured in airtight sealed 0.5 mm borosilicate capillaries.

2.4.2 X-Ray Photoelectron Spectroscopy (XPS)

X-ray photoelectron spectroscopy (XPS) is a widely used technique to probe surfaces. In simplified terms, a sample is illuminated with an X-ray beam of a defined energy, whereupon the sample, in turn, emits photo electrons with a specific energy. The main characteristics of XPS analysis are: (i) its superior surface sensitivity due to the limited free path for electrons in solids (several nm); (ii) the ability to probe chemical

state information, such as the atomic species and local bonding environment; and, (iii) the possibility of a (semi-)quantitative analysis.^{155,156}

In the context of sulfide-based ASSBs, XPS analysis has been used to extensively study the oxidative^{80,88} decomposition of the SE in the composite cathode or the reductive SE decomposition^{109,157} at the interface of the separator towards the Li metal anode, as well as, or the interphase formation with PEO-based¹⁵⁸ protective coatings. Furthermore, XPS analysis is a suitable tool to investigate the chemical compatibility of SEs with different solvents and polymers for slurry-processed separator-sheets^{71–73,75} and to evaluate the material degradation under dry room conditions.¹⁵⁹

In this thesis, XPS was used in order to identify the surface species of the used SEs that could indicate material decomposition. In doing so, the analysis was particularly performed for two purposes: (i) to characterize the pristine material in the as-received state in order to probe for exposure towards ambient atmosphere during production and/or shipping of the material; (ii) to evaluate possible decomposition during wet-processing in toluene for the binder-sheet fabrication (see section 3.1.1).

Measurements were carried out on an Axis Supra Spectrometer from Kratos (UK). Samples were prepared inside an argon-filled glovebox by pressing the SE powder or binder sheet to pellets (3 mm diameter) and mounting them on a stainless-steel sample holder. The transfer to the XPS was realized by an inert transfer shuttle by Kratos under Ar atmosphere, avoiding any air or moisture exposure of the samples. The samples were kept in the flexi-lock antechamber of the XPS system until a stable pressure of $\approx 10^{-8}$ torr was reached, and afterwards transferred to the surface analysis chamber, in which the pressure was always kept at $\approx 10^{-9}$ torr during an experiment. Measurements were conducted using a monochromatic Al K_{α} source (1486.6 eV) and an emission current of 15 mA. Survey spectra were recorded for all samples with a stepsize of 0.5 eV and at a pass energy 160 eV. Spectra with focus on the S 2p and P 3p region were recorded with a step size of 0.2 eV, and an emission current of 15 mA and a pass energy of 20 eV. For all measurements, a charge neutralizer was used and the spectra were calibrated to the adventitious carbon peak with a binding energy of 284.8 eV. In order to ensure high data quality, several spectra were recorded and averaged by the Escape software from Kratos. Fitting was done with a mixture of Lorentzian and Gaussian shape function after a Shirley background subtraction.

2.4.3 Scanning Electron Microscopy (SEM) and Energy-Dispersive X-Ray Spectroscopy (EDX)

Scanning electron microscopy (SEM) is used to image surfaces by scanning the sample with a focused electron beam in a certain raster scan pattern. Upon irradiation of the sample with the electron beam, secondary electrons are generated by the atoms of the sample. The position of the beam is combined with the intensity of the detected signal to produce the final picture. Due to their low energy ($\sim 0 - 30$ eV), secondary electrons are very surface sensitive and the obtained picture is representative for the surface of the sample. In case back scattered electrons (~ 50 eV – 20 keV) are analyzed, progressively more depth information (up to several μm) is obtained with rising energy of the back scattered electrons. In EDX analysis, the chemical information of the electrons, emitted by the sample, can be used to determine which elements are present in the sample.¹⁶⁰

In ASSB research, SEM is mainly used to investigate the morphology of the used materials, such as the SE and CAM particles, or of prepared electrodes. Additionally, EDX analysis allows to assess the distribution of the components in composite electrodes.^{97,161}

In this work, we use SEM to assess the morphology of the used SEs in term of particle size, particle size distribution, and agglomerate size as well as to evaluate the homogeneity of coated separator-sheets. Especially the slurry-processing procedure might affect the morphology of the SEs, as agglomerates can be broken up during mixing, as shown in Figures 2c and f of the study on the separator-sheet development¹²⁷ presented in subsection 3.1.1. Furthermore, the binder distribution inside a composite can be assessed. SEM analysis is performed both in top-view and also in cross-section mode to gain further information about the structure of the composites.

SEM images were acquired using a JSM-IT2000 InTouchScope™ (JEOL, Japan) field emission microscop at 15 kV with a multi segmental secondary electron detector. EDX-mappings were performed at an incident electron beam energy of 12 kV. Cross-sections were prepared by Ar-ion beam polishing, using a cross-section polisher of the type IB-19530CP (JEOL, Japan).

2.4.4 Brunauer-Emmett-Teller (BET) Physisorption Measurements

BET physisorption measurements were performed in order to determine the specific surface area of the SE particles. Measurements were conducted using an Autosorb-iQ (Quantachrome, USA) at 77 K with krypton as adsorbate. Prior to the experiment, samples were outgassed at 120 °C for 12 h under dynamic vacuum. The specific surface area was calculated according to the BET-theory, whereby the ideal linear range is selected by the Micropore BET Assistant of the ASiQwin software.

Knowing the exact surface area of the used material is important to adjust the binder content in the separator-sheets. Assuming a uniform distribution of the binder all over surfaces, the binder film thickness can be approximated knowing the volume content of the binder and the surface area of all the other components according the following “rule of thumb”:¹⁶²

$$t_{\text{binder layer}} = \frac{V_{\text{binder}}}{\sum_i m_i \cdot A_{\text{BET},i}} = \frac{\frac{m_{\text{binder}}}{\rho_{\text{binder}}}}{\sum_i m_i \cdot A_{\text{BET},i}} \quad (2.19)$$

Flexible LSPS/HNBR separator-sheets with very good mechanical properties could be obtained for a binder content of $\chi = 5.0$ wt.% (cf. subsection 3.1.1). According to Equation (2.19), this corresponds to a nominal binder film thickness of

$$t_{\text{binder layer}} = \frac{5 \text{ g}}{\frac{0.96 \text{ g cm}^{-3}}{95 \text{ g} \cdot 3.25 \text{ m}^2 \text{ g}^{-1}}} \approx 17 \text{ nm}. \quad (2.20)$$

Usually, a thickness of ~5 nm is required for mechanically stable components¹⁶², hence this value is high but still quite reasonable. However, in the study on the separator-sheets¹²⁷, mechanically stable sheets with less binder could also be prepared.

Note that during the slurry-processing the BET surface area of the LSPS material (~1.38 m² g⁻¹ in the as-received state) changes significantly, since agglomerates are broken up, resulting in a BET surface area of ~3.25 m² g⁻¹ after slurry-processing. This

underlines the importance of the precise determination of the surface area in order to adjust the properties of the prepared composites accordingly.

2.4.5 Direct Current (DC) Measurements for Determination of Electrical Conductivity

As a complementary analysis to the determination of the ionic conductivity σ_{ion} , also the residual electrical conductivity σ_{el} is an important parameter. Experimentally, this was realized by applying voltages of $U = 50, 100$ and 150 mV for 15 h each to a SE pellet or SE separator-sheet sample and recording the resulting current I . With the use of *Ohm's* law, the electrical resistance R_{el} is obtained:

$$R_{\text{el}} = \frac{U}{I} \quad (2.21)$$

Hence, σ_{el} is obtained knowing the geometric sample area A and the sample thickness t according to:

$$\sigma_{\text{el}} = \frac{t}{R_{\text{el}} \cdot A} \quad (2.22)$$

3 Results

This chapter presents the published work as well as unpublished data of this PhD thesis. The articles are thematically grouped into two sections.

Section 3.1 focuses on the transition from powdered, pellet-based electrodes and SE separators towards cells with sheet-type components, which are closer to real application. In doing so, a slurry-based process was developed (**subsection 3.1.1**) in order to prepare composite separator-sheets made from a sulfidic SE powder and an HNBR binder. Moreover, the process can be adapted to also prepare sheet-type cathodes. Furthermore, a new cell setup was developed in order to determine the ionic conductivity of separator-sheets as a function of the volumetric binder content and the used SE. Being capable of producing such sheet-type separators and electrodes opens up the possibility to build pouch cells. Additionally, this allows for advanced diagnostics, such as the integration of a micro-reference (μ -RE) electrode into the cell (**subsection 3.1.2**). Using this three-electrode design, we thoroughly investigated the electrochemical state of the commonly used indium-lithium anodes, depending on their preparation method.

In **section 3.2**, the focus lies on the characterization of lithium phosphides, a novel class of solid, inorganic lithium ion conductors. This is a cooperation project with the Chair for Inorganic Chemistry with Focus on Novel Materials of Prof. Thomas. F. Fässler, at which the development and synthesis of the materials were performed. Our contribution to this cooperation was the development of a measurement cell in order to determine the ionic conductivity and the activation energy for the lithium ion conduction. The first of several articles that were published in the frame of this cooperation is presented in **subsection 3.2.1**, introducing the measurement cell and the measurement protocols. The study was realized using the compound $\text{Li}_{14}\text{SiP}_6$. Other articles on related but different materials are listed under “scientific contributions” in the Appendix. In addition, we probed the reactivity of lithium phosphides, in this case using Li_9AlP_4 , against ambient atmosphere by means of *in situ* DRIFTS analysis (**subsection 3.2.2**).

3.1 Development of Sheet-Type Components for All-Solid-State Battery Pouch Cells

3.1.1 Preparation of Sulfidic Solid Electrolyte/Polymer Separator-Sheets

The article “*From Powder to Sheets: A Comparative Electrolyte Study for Slurry-Based Processed Solid Electrolyte/Binder-Sheets as Separators in All-Solid-State Batteries*” was submitted in April 2022 and published in July 2022 in the peer-reviewed Journal of the Electrochemical Society.¹²⁷ It is available as an “open access” article under the terms of the Creative Commons Attribution 4.0 License (CC BY). The permanent web link can be found under: <https://iopscience.iop.org/article/10.1149/1945-7111/ac7e76>. Tobias Kutsch presented the article at the 241st Meeting of the Electrochemical Society in Vancouver, Canada in May 2022 (Meeting Abstract MA2022-01 161).

Most reports in the field of ASSB research featuring sulfidic SEs are based on pellet-type separators with thicknesses of several hundreds of microns to millimeters. These cells are extensively used for purposes of fundamental research, namely the benchmarking of new electrolytes, the analysis of degradation phenomena upon cycling, or the evaluation of interfacial properties. However, pellet-type cells are limited to small-scale laboratory cells, as pellets cannot be produced in larger dimensions by cold pressing without mechanical defects, which is why in recent years more and more research focused on wet-processed SE/binder composites, investigating appropriate binder and solvent combinations.^{71,72,74,163}

We present a wet-chemical process in toluene to prepare composite separator-sheets made from a sulfidic SE and an HNBR binder. Since toluene was reported to have a negative impact on sulfidic SEs, we performed Raman, XRD, and XPS analysis to screen for possible decomposition reactions and their influence on the ionic conductivity.⁷³ Upon exposing LPSCl to toluene for 20 min, which is the duration of the mixing step, we could not detect any changes of the used SE, so that the solvent processing is not expected to have a negative impact. Merely upon a long-term exposure of 48 hours partial

decomposition as well as a decrease in ionic conductivity of ~35% could be observed, which we attributed to residual water in the dried solvent.

Furthermore, we introduced an in-home cell design to determine the ionic conductivity of the samples. In doing so, we compared different sheets made from three SEs (LPSCl, LPS-711, and LSPS) and determined the ionic conductivity as a function of the volumetric binder content. Normalizing the sheet conductivity to the conductivity of the pure powder, i.e., without any binder, we found that the decay in ionic conductivity is purely dependent on the binder content and independent from the used SE.

Lastly, we elucidated the importance of compaction and the extent of residual porosity on the ionic conductivity and could confirm that a pre-pressing step at a higher fabrication pressure is beneficial for the apparent sheet conductivity.¹³⁴

Author contributions

C.S. designed and validated the measurement cell and furthermore developed the slurry-based mixing process. C.S., T.K., R.B., M.T., and M.B. prepared separator-sheets with the different SEs and with different volumetric HNBR contents, and determined the ionic conductivity and porosity values thereof. The data was analyzed by C.S and T.K. Raman and XRD measurements were conducted and the obtained data treated by T.K. L.H. conducted the XPS measurements and evaluated the XPS data. C.S., T.K., M.T., and M.B. conducted the experiments for evaluating the influence of the solvent on the ionic conductivity of the used SEs. T.K. and M.T. performed SEM and EDX experiments. All data were discussed by C.S., T.K., and R.S. All authors commented on the results. C.S. and T.K. wrote the manuscript, which was edited by H.A.G. C.S. and T.K. contributed equally as co-shared first authors.



From Powder to Sheets: A Comparative Electrolyte Study for Slurry-Based Processed Solid Electrolyte/Binder-Sheets as Separators in All-Solid-State Batteries

Christian Sedlmeier,^{1,2,*} Tobias Kutsch,^{1,2,*} Robin Schuster,^{1,2} Louis Hartmann,^{1,*} Raphaela Bublitz,¹ Mia Tominac,² Moritz Bohn,¹ and Hubert A. Gasteiger^{1,**}

¹Chair for Technical Electrochemistry, Department of Chemistry and Catalysis Research Center, Technische Universität München, Lichtenbergstraße 4, D-85748 Garching, Germany

²TUMint-Energy Research GmbH, Lichtenbergstraße 4, D-85748 Garching, Germany

A key for the market penetration of large-scale and high energy All-Solid-State Batteries (ASSBs) are sheet-type cell components. Herein, we report a slurry-based process to obtain free-standing solid electrolyte (SE)/binder composite sheets as ASSB separators. We investigate three different sulfidic solid electrolyte systems ($\text{Li}_6\text{PS}_5\text{Cl}$, $\text{Li}_7\text{P}_3\text{S}_{11}$ and $\text{Li}_{10}\text{SnP}_2\text{S}_{12}$) in combination with a hydrogenated nitrile butadiene rubber (HNBR). By means of electrochemical impedance spectroscopy (EIS), the influence of separator composition and processing on the ionic sheet conductivity is evaluated. Independent of the solid electrolyte material, a reduction by a factor of three compared to the pristine powder conductivity at 70 MPa operation pressure and by a factor of eight compared to the maximum powder conductivity is observed. This can be attributed to the addition of the ionically isolating binder, which however is necessary for the production of freestanding sheets. We show the beneficial effect of pre-compressing the sheets to little porosity values on the apparent sheet conductivity. Lastly, we investigate and decouple the influence of fabrication and operating cell pressure on the produced separator sheets.

© 2022 The Author(s). Published on behalf of The Electrochemical Society by IOP Publishing Limited. This is an open access article distributed under the terms of the Creative Commons Attribution 4.0 License (CC BY, <http://creativecommons.org/licenses/by/4.0/>), which permits unrestricted reuse of the work in any medium, provided the original work is properly cited. [DOI: 10.1149/1945-7111/ac7e76]



Manuscript submitted April 14, 2022; revised manuscript received June 14, 2022. Published July 13, 2022.

All-solid-state batteries (ASSBs) are considered as up-and-coming candidates for the next generation of energy storage systems, e.g., for electric vehicles and mobile devices. Replacing the inflammable organic electrolyte in conventional Li-ion batteries (LIBs) by a non-flammable solid electrolyte (SE) promises to increase battery safety, allow for higher gravimetric and volumetric energy densities as well as higher fast-charging capability.^{1,2}

In general, three different types of ASSB cells can be distinguished, namely thin-film, pellet-type, or sheet-type cells.^{3–5} Thin-film batteries are mainly used for consumer electronics that require little overall energy or as model systems to study the storage mechanisms and the kinetics of ASSB materials.⁵ The applicability of thin-film batteries to high-energy batteries for battery electric vehicles (BEVs) is limited due to their low energy storage capacity and their laborious production processes.⁶ ASSB cells featuring pellet-type separators with thicknesses of several hundreds of microns are intensively studied in terms of fundamental research, benchmarking new electrolyte materials, analyzing degradation phenomena upon cycling, or evaluating interfacial properties. Despite of being widely used in ASSB research, pellet-type cells and separators are generally limited to small-scale laboratory cells, as large-format pellets cannot be produced in a continuous process. Furthermore, in order to be competitive or superior to state-of-the-art LIBs, the thickness of the solid electrolyte separator in ASSBs should be substantially less than 100 μm .⁷ Thin and large-format solid electrolyte based separators can in principle be produced by slurry-based processes, that would also allow for straightforward production scale-up. In recent years, more and more focus has been placed on the preparation of sheet-type separators, investigating appropriate solvents and binders for wet-processed SE/binder composites.^{4,7–14}

Among the various classes of inorganic solid electrolytes, sulfidic electrolytes are promising candidates for the integration into sheet-type large-format ASSBs. Compared to other SE materials, sulfidic electrolytes offer higher room temperature Li-ion conductivity and a relatively low interfacial resistance, due to their softness and ductility.^{6,15–19} Their favorable mechanical properties allow for the

preparation of free-standing SE/binder separator sheets and a straightforward densification by calendaring, which can be integrated into a continuous roll-to-roll process. Low residual porosities are desired to increase energy densities and to maximize lithium ion conductivity.²⁰ Furthermore, at least for oxide based solid-electrolytes, low residual porosities are reported to allow for higher current densities prior to separator shorting by lithium dendrites.^{21,22}

In this work, we present a comparative solid electrolyte study for wet-processed SE/binder separator sheets using the sulfidic electrolytes $\text{Li}_6\text{PS}_5\text{Cl}$ (also referred to as LPSCl), $\text{Li}_7\text{P}_3\text{S}_{11}$ (also referred to as LPS711), or $\text{Li}_{10}\text{SnP}_2\text{S}_{12}$ (also referred to as LSPS) in combination with a hydrogenated nitrile butadiene rubber (HNBR) binder. We first perform a through morphological analysis of the resulting separator sheets and then evaluate the influence of the binder content on the ionic conductivity of the separator sheets. Lastly, we show the importance and the impact of the fabrication as well as operation pressure on the ionic conductivity of the SE/HNBR separator sheets.

Experimental

Materials.—The handling of all materials and all processing steps were conducted inside an Ar filled glovebox ($\text{O}_2 < 0.1$ ppm, $\text{H}_2\text{O} < 1$ ppm, MBraun, Germany), unless described differently. The solid electrolytes $\text{Li}_6\text{PS}_5\text{Cl}$ (LPSCl) and $\text{Li}_7\text{P}_3\text{S}_{11}$ (LPS711) were purchased from All Solids (China), while $\text{Li}_{10}\text{SnP}_2\text{S}_{12}$ (LSPS) was purchased from NEI Corporation (USA); all SEs were used without further purification. Hydrogenated nitrile butadiene rubber (HNBR, $5.5 \times 10^5 \text{ g} \cdot \text{mol}^{-1}$, 17 wt% acetonitrile, < 1% residual double bonds) was provided by Arlanxeo (Netherlands). The HNBR binder was dried at 70 °C under dynamic vacuum for 72 h in a drying oven (Büchi B-585, Büchi, Switzerland). For all experiments, a 5 wt% HNBR stock solution in toluene was used, which was kept under continuous stirring. Toluene (anhydrous) was purchased from Merck Millipore (Germany) and dried over a molecular sieve (pore size 3 Å, Merck Millipore, Germany) for at least 24 h. The water content of the toluene was determined by Karl-Fischer-Titration (Titro Line KF trace, Schott Instruments GmbH, Germany) to be < 1 ppm.

Processing of solid electrolyte/binder-sheets.—The SE/HNBR-sheets were prepared by a slurry-based process using a dissolver (Dispermat LC30, VMA-Getzmann, Germany). For this, all

[†]Equal Contribution.

*Electrochemical Society Student Member.

**Electrochemical Society Member.

[‡]E-mail: tobias.kutsch@tum.de

components, i.e., the SE powder, the 5 wt% stock solution of HNBR in toluene, and a defined additional amount of toluene were put together in an HDPE beaker (12 ml Thinky beaker, C3 Prozess- und Analysetechnik GmbH, Germany) in the respective weight ratios, depending on the desired binder content according to Table I. All batches were prepared with a total amount of 2 g of solids, which is defined as the sum of the mass of SE and HNBR. The solid content in the slurry was adjusted to 35%–50% depending on the binder content in order to obtain a suitable slurry viscosity.

In the lid of the HDPE beaker, a centered 16 mm hole was punched in order to pass through the rotating shaft of the dissolver. The mixture was then stirred using a 20 mm dissolver disk (stainless steel, VMA-Getzmann) according to the following sequential mixing procedure (adapted to that reported by Riphaut et al.⁷): 500 rpm for 1 min, 1000 rpm for 1 min, 2000 rpm for 2 min, 5000 rpm for 5 min, and 10,000 rpm for 11 min. The long-duration final step at 10000 rpm serves to break up agglomerates and thoroughly disperse the particles, resulting in a homogeneous slurry. The slurry was coated onto a siliconized polyester foil (PPI Adhesive Products GmbH, Germany) by means of the doctor blade technique, using a 400 μm gap-bar (ERICHSEN, Germany). The deposited films were dried at room temperature for at least 12 h. Prior to further experiments, the sheets or punched samples were dried at 70 °C under dynamic vacuum for at least 16 h. The final free-standing separator sheets had a dry-film thickness of roughly 120 μm , as measured by a thickness gauge (see below).

Initially, LPSCI/HNBR coatings with different gravimetric HNBR binder contents (x_{HNBR}) were prepared (see left-most column in Table I). In order to provide a more rigorous comparison of the compression-dependent porosity and conductivity of separators made with different solid electrolytes, separator sheets with identical binder volume fractions (ϕ_{HNBR}) rather than binder mass fractions were prepared. Therefore, the mass fractions used for the LPSCI/HNBR separator sheets were first converted into binder volume fractions (ϕ_{HNBR}) via Eq. 1:

$$\phi_{\text{HNBR}} = (x_{\text{HNBR}}/\rho_{\text{HNBR}})/(x_{\text{HNBR}}/\rho_{\text{HNBR}} + (1 - x_{\text{HNBR}})/\rho_{\text{SE}}) \quad [1]$$

with ρ representing the bulk densities of the different materials, which were taken from the product specification sheets (HNBR: 0.96 g cm⁻³; LPSCI: 1.64 g cm⁻³; LPS11: 1.98 g cm⁻³; LSPS: 2.25 g cm⁻³). Subsequently, coatings with the same volumetric binder contents using LPS711 and LSPS were prepared (see Table I; note that the LSPS/HNBR coating with a binder content of 1.7 vol% could not be prepared, as no suitable slurry viscosity for a good coating could be obtained).

Porosity determination.—Free-standing samples of the separators were punched with an 8 mm punch (Rennsteig, Germany) and their weight (Entris II Sartorius, Germany) and thickness (micrometer screw gauge, Mitutoyo, Japan, with an error of $\pm 2 \mu\text{m}$) were measured, either in its uncompressed or compressed state. From the

measured areal weight of the separator coating (L_{sep}) and from the measured thickness (t_{sep}), the void volume fraction of the separator sheet (ε) was determined, using the above given bulk densities of the HNBR binder and the respective solid electrolytes:

$$\varepsilon = 1 - (L_{\text{sep}}/t_{\text{sep}}) \times (x_{\text{HNBR}}/\rho_{\text{HNBR}} + x_{\text{SE}}/\rho_{\text{SE}}) \quad [2]$$

The thus determined porosity of the uncompressed separator sheets varies between 50%–60%.

For separator densification at pressures between 100–980 MPa, an 8 mm pressing tool (Lab Club, Germany) and a manual hydraulic press (Atlas 15 T, Specac, UK) were used, pressing several (typically 3) stacked-up separator sheets for 5 min, unless described differently. For densification at pressures between 20–70 MPa, the spring cell setup, which is later described in detail, was used. The compressed thickness of the separator sheets for use in Eq. 2 was determined by a micrometer crew gauge (Mitutoyo, Japan), with an approximate error of $\pm 2 \mu\text{m}$. The measured compressed thicknesses ranged between roughly 210–290 μm .

Scanning electron microscopy (SEM) and (EDX).—The scanning electron microscopy (SEM) images were acquired using a JSM-IT200 InTouchScope™ (JEOL) field emission SEM at 15 kV with a multi segmental secondary electron detector. To avoid reactions of the sulfidic electrolyte with ambient air, the samples were prepared in an argon-filled glovebox, transferred under inert atmosphere into a dry-room using a Büchi oven tube (B-585, Büchi Labortechnik AG, Switzerland), and from there were transferred into the SEM that was located in the dry-room (the sample exposure time to the dry-room atmosphere (dew point $< -25^\circ$) was < 1 min). To determine the binder distribution, EDX-mappings were performed at an incident electron beam of 12 kV.

Cross-section polishing.—Cross-sections were prepared by argon ion beam polishing, using a cross-section polisher of the type IB-19530CP (JEOL, Japan). An 8 mm disc was punched from the dried SE/HNBR-sheet, fixed with copper tape (PPI Adhesive Products, Ireland) in the sample holder, and then inertly transferred into the device using an inert transfer shuttle (LB-11620TVCA, JEOL Japan) under argon atmosphere. It was polished at 25 °C first for 1 h at 6 kV and then 1 h with 4 kV acceleration voltage.

Effect of toluene exposure on the SE.—To investigate the influence of the exposure of the solid electrolyte to the toluene solvent on its (surface) composition and ionic conductivity, toluene was added to the pristine Li₆PS₅Cl (LPSCI) powder, preparing dispersions with a solid content of 40%. For short term treatments, the LPSCI powder was dispersed in an HDPE beaker using a dissolver, analogous to the procedure used for preparing SE/HNBR separator sheets. For long-term treatments, the obtained dispersions were stirred for 48 h in the glovebox using a glass vial and magnetic

Table I. Overview and composition of the prepared SE/HNBR sheets for the different SEs (SE = Li₆PS₅Cl; Li₇P₃S₁₁; Li₁₀SnP₂S₁₂) with varying HNBR binder content, whereby the HNBR weight content (x_{HNBR} , in [wt%]) for the different SEs was adjusted to obtain equal volume percentages of HNBR (ϕ_{HNBR} , in [vol%]). A binder content of 0 wt% corresponds to the pure SE powder, which was used as a pellet and therefore was not wet-processed. The LSPS coating with a volumetric binder content of 1.7% is marked with an *, as this coating could not be prepared.

Li ₆ PS ₅ Cl (LPSCI)		Li ₇ P ₃ S ₁₁ (LPS711)		Li ₁₀ SnP ₂ S ₁₂ (LSPS)	
x_{HNBR} [wt%]	ϕ_{HNBR} [vol%]	x_{HNBR} [wt%]	ϕ_{HNBR} [vol%]	x_{HNBR} [wt%]	ϕ_{HNBR} [vol%]
0.0	0.0	0.0	0.0	0.0	0.0
1.0	1.7	0.8	1.7	0.7*	1.7*
2.0	3.4	1.7	3.4	1.5	3.4
3.5	5.8	2.9	5.8	2.6	5.8
5.0	8.2	4.2	8.2	3.7	8.2
7.0	11.4	5.9	11.4	5.2	11.4
10.0	16.0	8.4	16.0	7.5	16.0

stirring bar. Afterwards, the solvent was evaporated under dynamic vacuum at room temperature for 3 h using a small vacuum pump, which was connected to a sealed SCHOTT®-glas in the glovebox. For the complete removal of the solvent, the materials were dried under dynamic vacuum at 70 °C using a Büchi oven (B-585, Büchi Labortechnik AG, Switzerland) for at least 12 h to obtain the toluene-treated LPSCI powders.

Raman spectroscopy.—For Raman spectroscopy analysis, the pristine and the toluene exposed LPSCI powder as well as a final LPSCI/HNBR separator sheet were placed onto a microscopy glass slide and sealed with adhesive-coated Kapton® tape in an argon-filled glovebox to prevent reactions with ambient air and humidity. The measurements were performed at room temperature by focusing the incoming laser beam through the glass slide, using a Renishaw inVia Reflex Raman System (Germany) equipped with a 532 nm excitation laser (Renishaw RL532C, Class 3B) set to a laser power of 2 mW. An integration time of 10 s and an averaging of five subsequently recorded spectra was used. Raman spectra in the range of 47–1548 cm^{-1} were recorded with a spectral resolution of 3–5 cm^{-1} . The obtained data were processed using the software Renishaw WiRE™.

X-ray powder diffraction (XRD).—Diffractograms were collected at room temperature on a STOE STADI P diffractometer (STOE, Germany) in transmission mode in the 2θ range of 10°–90°, using Mo- $K_{\alpha 1}$ radiation (0.7093 Å, 50 kV, 40 mA), a Ge(111)-monochromator, and a Dectris Mythen 1 K detector (step size 0.015, integration time/step 150 s). The pristine and the toluene exposed LPSCI powder were measured in airtight sealed 0.5 mm borosilicate capillaries, while a final LPSCI/HNBR separator sheet was measured in a rotating flat-bed sample holder sealed with Kapton® foil. Raw data were processed with WinXPOW, version 3.0.2.1 software.

X-ray photoelectron spectroscopy (XPS).—The surface analysis of the as-received LPSCI powder, long- and short-term toluene-treated LPSCI powder, and the final LPSCI/HNBR separator sheet was carried out by X-ray photoelectron spectroscopy (Axis, Supra, Kratos, UK). The powders and the LPSCI/HNBR separator sheet were pressed to pellets and mounted on a stainless steel sample holder. All prepared samples were transferred into the XPS antechamber using an inert transfer shuttle under Ar atmosphere. The samples were kept in the antechamber until a pressure of $\approx 10^{-8}$ Torr was reached, and afterwards transferred to the sample analysis chamber, where the pressure was always kept at $\approx 10^{-9}$ Torr during the entire measurement. Sample irradiation was carried out with monochromatic Al K_{α} radiation (1486.6 eV), using an emission current of 15 mA. Survey spectra were recorded for all samples with a stepsize of 0.5 eV and a pass energy (PE) of 160 eV. For high-resolution spectra, a stepsize of 0.05 eV and a pass energy of 15 eV were chosen. All recorded spectra were calibrated to the adventitious carbon peak with a binding energy (BE) of 284.8 eV. For data analysis, the CasaXPS software (version 2.3.23, Casa Software Ltd.) was used. After subtraction of a Shirley background, the spectra were fitted using a mixture of a Lorentzian (30%) and Gaussian (70%) shape function, considering the binding energy and full-width-at-half-maximum (FWHM) constraints listed in Table II.

Newly developed ASSB test cell design and cell assembly.—In order to investigate solid-state electrolytes and all-solid-state batteries, a special cell setup is required that is hermetically sealed and that allows the defined and, ideally, variable application of different compressions on the cell stack. Unfortunately, to the best of our knowledge, there is no commonly and widely used cell format commercially available at the moment. Only some specialized cell hardware is available (e.g. by rhd instruments and sphere energy), but owing to its cost, it has not yet been established as a standardized cell format, such e.g. coin cells or Swagelok® T-cells have been for

conventional lithium-ion battery research. For this reason, various research groups have come up with individual solutions for their ASSB research.^{2,20}

In our group, we have developed a new in-house designed spring-cell setup that is hermetically sealed and that allows for the application of a well-defined variable compression of the cell stack in the range of 20–100 MPa. This cell design is depicted in Fig. 1, consisting of two main parts: the cell body (Fig. 1b), which contains the cell stack, and the cell casing (Fig. 1a), which serves to apply the desired compression on the cell stack via a compression spring. At first, the sample is placed inside a PEEK (polyetheretherketone) tube with an inner diameter of 8.0 mm (yellow colored in Fig. 1b) that is located in the stainless steel cell body, and contacted by hardened stainless steel dies with a diameter of 8.0 mm gray colored) and a hardened stainless steel piston that transfers the compression spring force onto the cell stack. Then, the cell body is inserted into the cell casing and sealed to the stainless steel bellows (10 mm inner diameter; Metallic Flex GmbH, Germany) with a 50 μm PTFE (polytetrafluoroethylene) flat-seal (white colored; Angst+Pfister AG, Switzerland), which at the same time electrically insulates the stainless steel bellows from the cell body. The PTFE flat-seal is compressed by a special-made stub at the lower end of the bellows, which is fixed to the cell body by six screws. At the upper end, the bellows is mounted to the cell casing via a knife-edge seal with a copper gasket, ensuring a completely gas-tight connection.

As illustrated in Fig. 1a, the operating cell pressure is applied by the defined compression of the compression spring (47 mm outer diameter, 23 mm uncompressed height, and compression rating of 254 N mm^{-1} ; LHL 200 C 02, Lee Spring GmbH, Germany) with a screw that allows to adjust the length and thus the force of the spring, using appropriately sized spacers. Thereby, the applicable cell stack compression can be controlled between 20–100 MPa. A potentiostat can be connected to the cell by inserting the cable plugs into small holes drilled into the lower part of the cell body and the upper current collector plate. At several points, the cell casing is electrically insulated from the cell body by POM (polyoxymethylene) insulations, which are displayed in Fig. 1a by a white color. The stray capacitance of this cell was estimated to be $\approx 8.1 \cdot 10^{-11}$ F (based on the dimension of the various metal/insulator/metal interfaces) and is in reasonably good agreement with the experimentally determined capacitance of $\approx 1.6 \cdot 10^{-11}$ F. The latter value is at least three orders of magnitude lower than the values measured for the samples investigated here, so that the stray capacitance of the setup does not affect the results of our impedance analysis of the separator sheets. The internal resistance of the cell was determined to $< 1\Omega$.

In addition to the cell displayed in Fig. 1, a slightly modified setup thereof was used for impedance measurements with an operation pressure $p_{\text{oper}} > 70$ MPa. For this, only the cell body together with the cell interior (PEEK tube and dies) was used without the cell casing and equipped with a special piston, shown in Fig. A-1 of the Appendix. Inside an Ar-filled glove box, this cell configuration was put into a hydraulic press (Atlas 15 T, Specac, UK), and electrically insulated from the press by putting a thin polyimide foil between the cell body and the press and between the piston and the press. The applied pressure on cell stack is calculated from the compressed area (0.503 cm^2) and the manually adjusted press tonnage in units of tons. Thereby, the pressure could be set within a range of 100–590 MPa (0.5–3 tons) with an accuracy of ± 20 MPa, which results from the accuracy of the pressure gauge of the device. Higher pressures could not be applied to the cell shown in Fig. 1, as deformation of some cell parts at pressures > 590 MPa was observed (note that pressures up to 1000 MPa could be used for the setup shown in Fig. A-1). During the impedance measurements, the pressure is held constant within the described accuracy. In order to validate this cell setup, the conductivity of LPSCI/HNBR-sheets were determined at an operation pressure of $p_{\text{oper}} = 100$ MPa with both cell setups (i.e., at the upper limit of the spring-cell and the lower limit of the cell in the hydraulic press),

Table II. XPS peak fitting parameters used for the identification and quantification of the different surface species of the pristine and the toluene-exposed LPSCI powders as well as of the final LPSCI/HNBR separator sheet. The ratio between $S_{2p_{3/2}}$ and $S_{2p_{1/2}}$ was fixed at 2:1.

element/region	assigned species	binding energy [eV] (constrained range)	FWHM [eV] (constrained range)
carbon C 1 s	“adventitious carbon”	284.8 (fixed)	1.0–1.3
sulfur S 2p	“PS ₄ ”	S 2p _{3/2} : 161.3 (±0.1)	1.0–1.3
		S 2p _{1/2} : S2p _{3/2} + 1.2	1.0–1.3
	“Sulfide S ²⁻ ”	S 2p _{3/2} : 160.0 (±0.1)	1.0–1.3
		S 2p _{1/2} : S2p _{3/2} + 1.2	1.0–1.3

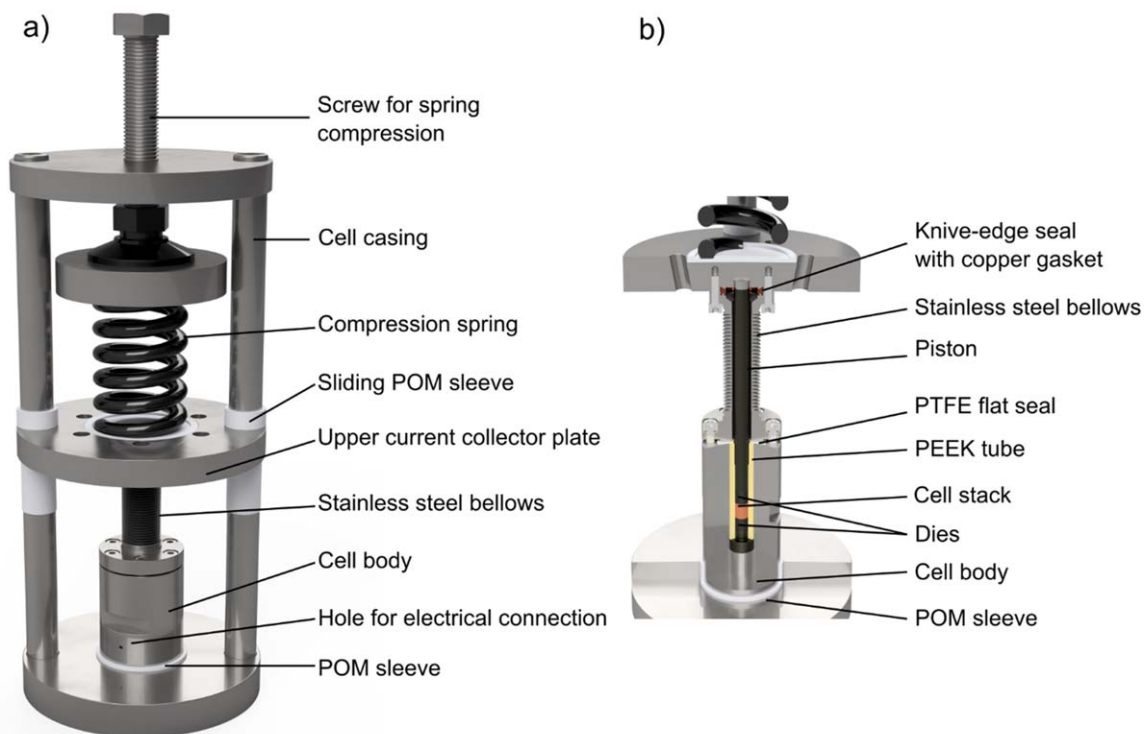


Figure 1. Hermetically sealed spring-cell setup for ASSB performance and impedance measurements under defined and variable compression of the cell stack between 20–100 MPa. (a) Cell casing (outer frame) to apply the desired cell stack compression by adjusting the height of a compression spring. The stainless steel bellows are sealed at their upper end by a knife-edge flange to the upper current collector plate and at their lower end to the stainless steel cell body, using an electrically insulating PTFE flat-seal. Electrical connection to the cell stack is made by the small holes placed in the lower part of the cell body (see figure) and in the upper current collector plate (not shown). The cell body is electrically isolated from the cell casing by a POM sleeve (shown in white); it is also electrically insulated from the casing by two sliding POM sleeves. The cell stack is contacted via hardened stainless steel dies and a piston placed inside the PEEK tube. (b) The cross-sectional illustration of the cell body and the stainless steel bellows shows the location of the cell stack (orange colored), the 8.0 mm diameter hardened stainless steel dies (gray colored), the 8.0 mm inner diameter PEEK tube (yellow colored), the PTFE flat-seal (white colored) against the bellows, and the stainless steel piston that transfers the force from the compression spring onto the cell stack (note that the view is rotated by 90° in comparison to Fig. 1a). The cell has an overall dimension of a height of ≈ 31 cm and an outer diameter of ≈ 12 cm.

yielding the same values within roughly $\pm 6\%$. This proves that the modified cell setup is a valid option for impedance measurements under high operation pressures, whereby it is however restricted to measurements at room temperature (i.e., the temperature inside the glovebox).

To conduct impedance measurements, separator sheet samples with a diameter of 8 mm were punched out, and three sheets were stacked for one measurement inside the cell body. After assembly of the cell, the compression on the cell stack was set to the desired value (between 20 and 70 MPa) by compressing a spring. Afterwards the cell was taken out of the glovebox and placed in a temperature chamber (KB53, BINDER, Germany) that was set to 25 °C. Impedance measurements at pressures higher than 70 MPa were conducted in the glovebox at a temperature of 25 °C \pm 1 °C. For this, the above described different measurement setup with the hydraulic press was used. Note that for the pre-compression of sheet compressions up to 1000 MPa in course of the porosity

determination was possible by using a different pressing tool, described in the section of porosity determination, which however did not allow for impedance measurements.

Potentiostatic electrochemical impedance spectroscopy (PEIS).— Measurements outside the glovebox were performed using a VSP-300 potentiostat (BioLogic, France), whereas a SP-300 device (BioLogic, France) was used for measurements inside the glovebox. Prior to impedance measurements, the cell was left to rest for 1 h in order to allow for thermal and mechanical equilibration. Impedance spectra were recorded in a frequency range from 7 MHz to 100 mHz and a potential amplitude of ± 10 mV. Data were treated using the software EC-Lab (V 11.36). For acquiring impedance measurements, the following procedure was followed: First, the fabrication pressure was applied in the cell body using the setup displayed in Fig. A-1 in combination with a hydraulic press. During this step at the fabrication pressure, the sample can adapt for small irregularities of the dies.

Then, after the initial compression, the entire cell body was transferred into the cell casing of the cell setup displayed in Fig. 1, and the operating pressure was set by compression of the spring. Here it must be noted that during the transfer of the cell body from the press into the cell casing, the dies which are in direct contact with the sample remained in the exact same position and that only the piston is changed from the setup in Fig. A-1 to that in Fig. 1. In this way, resistances due to poor contacting of the sample and the dies are minimized.

Results and Discussion

The following sections will present the morphological characteristics of the SE materials and of the resulting SE/HNBR separators, the interaction of the toluene solvent with sulfidic SEs (exemplarily for LPSCI), the achievable porosities of SE/HNBR separators, and the effect of the composition and the compression of SE/HNBR separators on their ionic conductivity. The three SEs represent the three commonly used types of sulfidic SEs: LPSCI with argyrodite structure, LPS711 as a glass-ceramic and LSPS as an LGPS-derivative from the class of thio-LISICONs. The values for their electrochemical properties such as lithium ionic conductivity and the electrochemical stability window are reasonably similar.^{23,24}

Morphology and binder distribution.—To assess the morphology of the SE/HNBR separators prepared by the slurry-processing route, the solid electrolytes and the corresponding SE/HNBR separator sheets were characterized by means of SEM and EDX. Figure 2 shows the top-view SEM images of the different SE powders. First examining the LPSCI powder and separator, Fig. 2a shows that the pristine LPSCI particles are somewhat rounded, with an approximate average particle size on the order of $\approx 5 \mu\text{m}$. After the slurry processing with toluene to prepare the LPSCI/HNBR separator sheet, the SE particle size in the separator sheet seems unchanged and has a similar morphology as the pristine SE powder (see Fig. 2d). The visually open structure of the separator sheet reflects its high porosity of $\approx 50\%$ (determined by Eq. 2). Figure 2g displays the mapping of the carbon EDX signal that exclusively originates from the HNBR binder (8.2 vol%). Thus, the distribution of the HNBR in the composite sheet is reflected by the carbon distribution map, which gives a qualitative indication that the HNBR binder distribution within the LPSCI/HNBR sheet is reasonably homogeneous, suggesting that the slurry mixing procedure is effective.

For the composite system LPS711/HNBR (Figs. 2b, 2e, and 2h), similar observations can be made. The size of pristine LPS711 particles is also on the order of $\approx 5 \mu\text{m}$, without any bigger agglomerates, and the LPS711 particle morphology is not affected by the mixing procedure. This is different for the pristine LSPS powder (Fig. 2c), which next to small particles of also $\approx 5 \mu\text{m}$ shows a large fraction of bigger agglomerates with $20 \mu\text{m}$ and more in size. However, the slurry processing appears to break up these large LSPS agglomerates, resulting in a similar LSPS/HNBR separator sheet morphology (Fig. 2f) that was observed for the LPSCI/HNBR and the LPS711/HNBR separator sheets. Reasons for size reduction of the LSPS particles could be due to the HNBR binder acting as a surfactant or the high stirring step in the mixing procedure. However, as the reference experiment without HNBR present, meaning with only LSPS and solvent, also leads to a break-up of the agglomerates, we believe this is entirely due to mixing at high revolutions.

Figure 3 displays the SEM cross-section images of the uncompressed LPSCI/HNBR separator sheets with 1.7, 8.2, and, 16.0 vol% HNBR in combination with the corresponding carbon EDX-mapping. For the lowest binder content, a homogenous distribution without any binder accumulation can be observed from the EDX-mapping (Fig. 3b). With increasing volume fractions of HNBR, more and more binder accumulations can be found in the voids between the LPSCI particles, indicated by intense red signals in the

EDX-mappings (Figs. 3d and 3f). Note, that in the corresponding SEM pictures, the binder cannot be distinguished from the LPSCI particles. For all three separator samples, a red stripe at the top of the EDX-maps can be observed, which is located at the surface near-region of the separator that was opposite of the PP support film, i.e., the surface from which the evaporation of the toluene solvent took place. This seems to indicate a significant binder migration to the free surface, caused by the evaporation of the toluene solvent during the drying process, analogous to the binder migration observed for battery electrodes.²⁵ However, the possible effects of binder migration on the conductivity of the separator sheets and how it can be influenced by the drying process have not been investigated in this study.

Interaction of the toluene solvent with the solid electrolyte.—

For slurry-based processes, the solvent needs to be chosen carefully to prevent the degradation of the sulfidic electrolyte. The two main requirements for a suitable solvent are the ability to sufficiently dissolve or disperse all the components and to not react with the components, as that might negatively affect the ionic conductivity. Yamamoto et al.¹² have investigated the compatibility of Li_3PS_4 with different solvents, which is chemically similar to LPSCI.^{9,12} The results show that the biggest decrease in ionic conductivity is observed for solvents with a donor number higher than 14, on account of their reaction with Li_3PS_4 . A protic solvent like ethanol with a high donor number of 19²⁶ reacts by a nucleophilic attack, leading to the decomposition of sulfidic electrolytes and the evolution of H_2S . Therefore, the most suitable candidates are toluene, p-xylene, heptane, anisole, or dichloroethane. The first four, for example, have already been successfully used for the preparation of SE/binder separator sheets, and the results showed no significant decrease in Li-ion conductivity.^{7,9,13} However, recently Ruhl et al. showed a decrease in ionic conductivity and a change in morphology of $\text{Li}_3\text{PS}_6\text{Cl}$ powder treated with toluene for very long contact times of 48 h.²⁷ These findings appear contradictory to the already established slurry preparation method from Riphaut et al.,⁷ where toluene was used as a solvent and where no detrimental effects of the exposure of the LSPS solid electrolyte to toluene was observed. Therefore, XRD, Raman spectroscopy, and XPS were used to assess whether any reaction between toluene with a sulfidic SE (exemplarily done for LPSCI) would occur.

Figure 4a shows the influence of the slurry-based processing (20 min dispersion in toluene) on the LPSCI structure investigated by XRD. The pristine LPSCI powder is displayed in brown, the slurry-processed LPSCI/HNBR separator sheet (8.2 vol% HNBR) in beige, and the slurry-processed and compressed (at 590 MPa) LPSCI/HNBR separator sheet in yellow. The diffraction patterns of the LPSCI/HNBR separator sheets provide no evidence for a degradation of the LPSCI material, even though the slurries had been mixed with toluene for 20 min. Furthermore, no changes are observed for the compressed separator sheet, proving that the steps to prepare the compressed separator sheets do not introduce any artefacts. The overall features of the diffractograms are consistent with the experimentally observed patterns of the pristine LPSCI powder, showing the argyrodite structure with $F\bar{4}3m$ symmetry (CIF No. 418490).^{28–30} In neither case, typical decomposition products like Li_2S (gray shaded area) or LiCl (blue shaded area) that are found in the case of alcohol solvents²⁷ could be detected.

The samples were also examined by Raman spectroscopy (Fig. 4b), following the same color coding as was used for the XRD data. The pronounced Raman signal in each spectrum at a wavenumber of $426\text{--}427 \text{ cm}^{-1}$ can be assigned to the PS_4^{3-} tetrahedra of the argyrodites;^{27,31} the typical decomposition products such as polysulfides (broad range between $476\text{--}506 \text{ cm}^{-1}$ ^{27,31}) cannot be found in the spectra of the slurry-processed separator sheets. Hence, the Raman data are in good agreement with the results obtained by XRD and provide no evidence for any reaction between of the LPSCI solid electrolyte during our slurry-processing method with toluene.

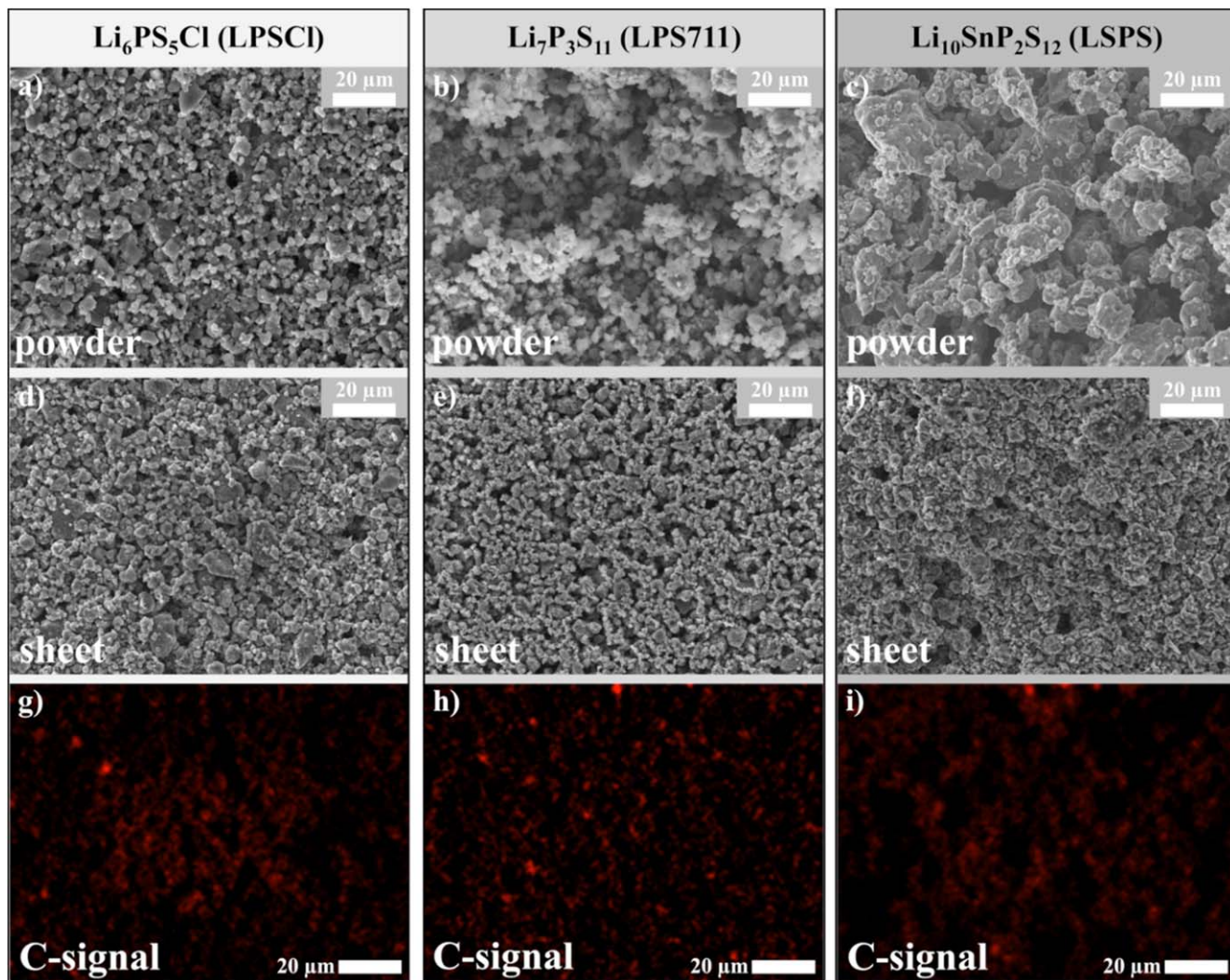


Figure 2. Top-view SEM images of the pristine SE powders (a) $\text{Li}_6\text{PS}_5\text{Cl}$ (LPSCI), (b) $\text{Li}_7\text{P}_3\text{S}_{11}$ (LPS711), (c) $\text{Li}_{10}\text{SnP}_2\text{S}_{12}$ (LSPS) and, (d)–(f), of the thereof prepared separator sheets with 8.2 vol% HNBR. (g)–(i) Corresponding EDX-maps of the C-signal as marker for the binder distribution within the prepared separator sheets.

Since the detrimental effect of toluene on the ion conductivity of LPSCI powder observed by Ruhl et al.²⁷ was after an exposure of 48 h, much longer than the exposure time during our slurry-processing procedure of only 20 min, and thus significantly less than in the experiments by Ruhl et al., we also conducted further experiments where the LPSCI powder was exposed to toluene for 48 h and analyzed by PEIS and XPS. The conductivity of the three LPSCI powder samples was measured in the spring-cell at an operating cell pressure of 70 MPa (without any pre-compression of the powders). The thereby obtained conductivity for the pristine LPSCI powder of ($1.43 \pm 0.04 \text{ mS cm}^{-1}$) is essentially identical to that of the LPSCI powder that was dispersed with the dissolver in an HDPE beaker with toluene for 20 min, analogous to the process used for preparing the slurry-processed LPSCI/HNBR separator sheets ($1.35 \pm 0.02 \text{ mS cm}^{-1}$; the error bars represent the standard deviation of three repeat measurements), consistent with the absence of any changes in their Raman and XRD spectra (Fig. 4). On the other hand, the conductivity of the LPSCI powder that was obtained after stirring it with toluene in a glass beaker for 48 h dropped slightly by a factor of roughly 1.5 ($0.98 \pm 0.06 \text{ mS cm}^{-1}$). However the detrimental impact of long-term toluene treatment on LPSCI powders, which was described by Ruhl et al.,²⁷ could not be observed. We cannot clearly identify the reason for the discrepancy of the results. There is no chemical reactivity to expect between the

sulfidic SE and toluene, therefore one hypothesis for the described detrimental impact observed by Ruhl et al.²⁷ is the presence of traces of water in the system either due to insufficient drying of the solvent or a leakage during the solvent treatment.

Furthermore, we used XPS analysis in order to have a higher sensitivity on changes in the near-surface region of the LPSCI material, analyzing the S 2p region. Comparing the high-resolution S 2p spectrum of the pristine LPSCI powder that only shows the S 2p feature of the PS_4^{3-} units of LPSCI³² (Fig. 5a) with that of the LPSCI powder that was mixed with toluene in an HDPE beaker using the dissolver for 20 min (Fig. 5b; analogous to the process used for preparing the slurry-processed LPSCI/HNBR separator sheets), indeed no changes in the S 2p feature can be observed. Similarly, the same is true when comparing the pristine LPSCI powder and the as-prepared $\text{Li}_6\text{PS}_5\text{Cl}$ /HNBR separator sheet (Fig. 5d), indicating also no features that could be ascribed to potential decomposition products, such as lithium sulfide (Li_2S) and polysulfides (S_x^{2-}). On the other hand, for the LPSCI powder that was stirred in a glass vial with toluene for 48 h (as was done by Ruhl et al.²⁷), small signals in the S 2p region characteristic of lithium sulfide and polysulfides³² can be observed (Fig. 5c), which may explain the slightly drop in ionic conductivity.

In summary, we can conclude that the short-term exposure of LPSCI to toluene, mimicking the exposure that occurs during our

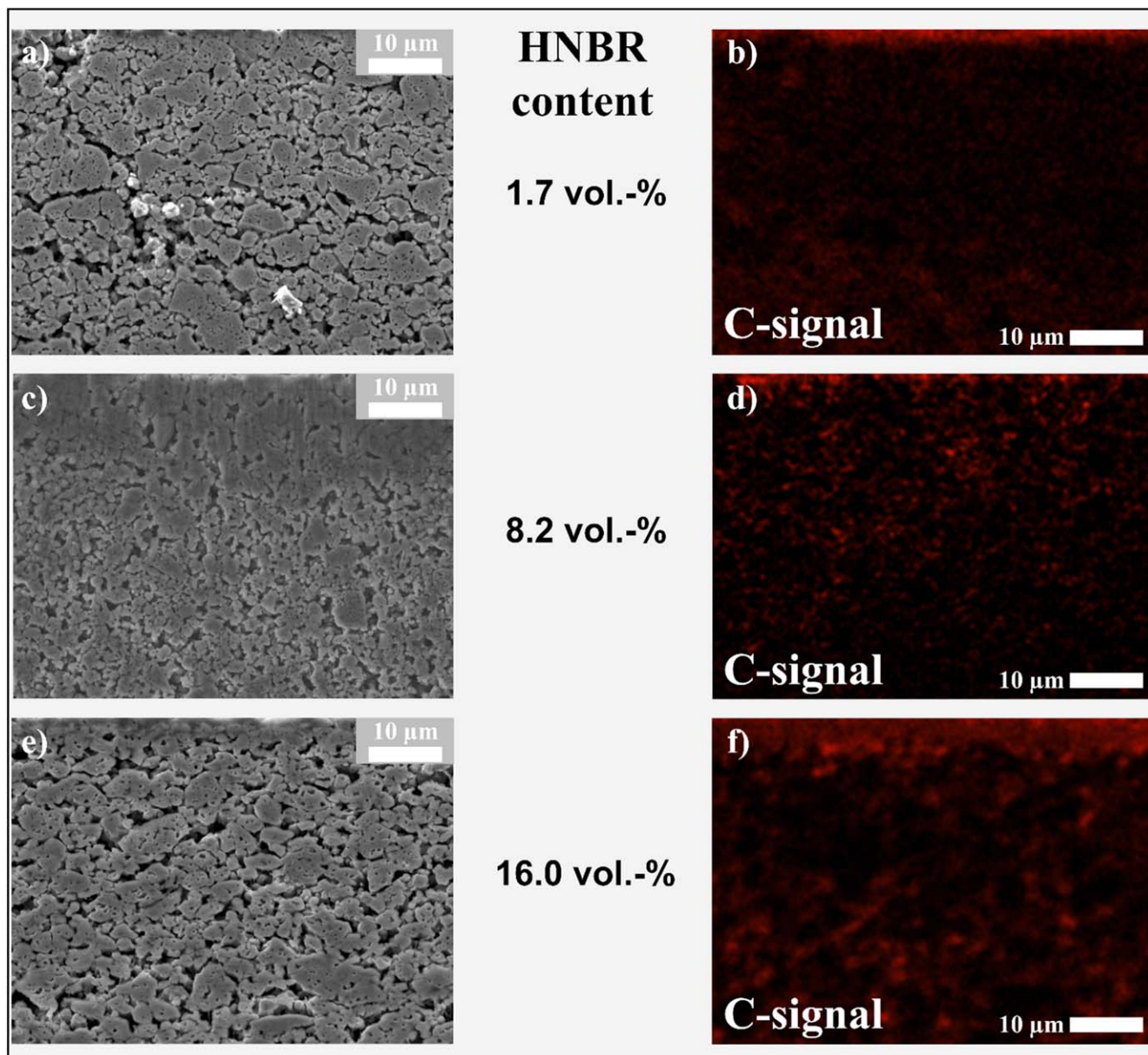


Figure 3. Cross-section SEM images for LPSCI/HNBR separator sheets with different amounts of HNBR binder: (a) 1.7 vol%; (c) 8.2 vol%; and, (e) 16.0 vol%. The right panels show the corresponding EDX carbon-mapping of the SEM cross-sections: (b) 1.7 vol%; (d) 8.2 vol%; and, (f) 16.0 vol%.

slurry-processing with toluene, does not lead to any detectable changes in structure and composition by XRD, Raman, and XPS, and does not affect the conductivity of the LPSCI powder.

Dependence of the separator sheet porosity on the fabrication pressure.—Throughout the literature, a beneficial effect of a low porosity on the ionic conductivity of pellet-type solid electrolyte separators is reported,^{16,20} so that a high degree of densification is desirable. For the mechanically ductile sulfidic solid electrolytes, this can be easily achieved by compression at room temperature. Figure 6a presents the influence of the fabrication pressure (p_{fabr}) on the SE/HNBR separator sheet porosity for the three different solid electrolytes. The porosity for the as-prepared uncompressed SE/HNBR separator sheets with an HNBR content of 8.2 vol% ranges from roughly 50% for LPSCI (red) and LSPS (green) to almost 60% for LPS711 (blue). Upon applying a fabrication pressure of up to 980 MPa for 5 min, the separator sheet porosity can be reduced to below 5% for the LPSCI/HNBR and the LPS711/HNBR separator sheets and to $\approx 8\%$ for the LSPS/HNBR separator sheets. Note that

based on the measurement accuracy of the thickness of the compressed separator sheets, the estimated absolute error of the porosity values is on the order of $\pm 1\%$. In order to compare the porosity values of sheet-type and pellet-type separators, we determined the porosity of the powder pellet-type samples at 70 MPa to $\varepsilon = 28\%$ (LPSCI), 32% (LPS711) and 33% (LSPS) and at 590 MPa to $\varepsilon = 11\%$ (LPSCI), 13% (LPS711) and 20% (LSPS). This compares with $\varepsilon = 24\%$ (LPSCI) and 33% (LPS711 and LSPS) at 70 MPa and $\varepsilon = 3\%$ (LPSCI), 6% (LPS711) and 12% (LSPS) at 590 MPa for separator sheets of the different SEs with a binder content of 8.2 vol%. While at 70 MPa values are quite similar, the porosity values of the sheet-type separators are significantly smaller compared to powder pellet-type samples. This suggests that the binder can effectively fill the voids and therefore sheet-type separators feature lower porosities at the same fabrication pressure.

The largest changes in the porosity of the separator sheets occur up to a fabrication pressure of 590 MPa, after which only minor changes occur. Over the entire fabrication pressure range, the porosity of the LPSCI/HNBR separator sheets is lowest and that of

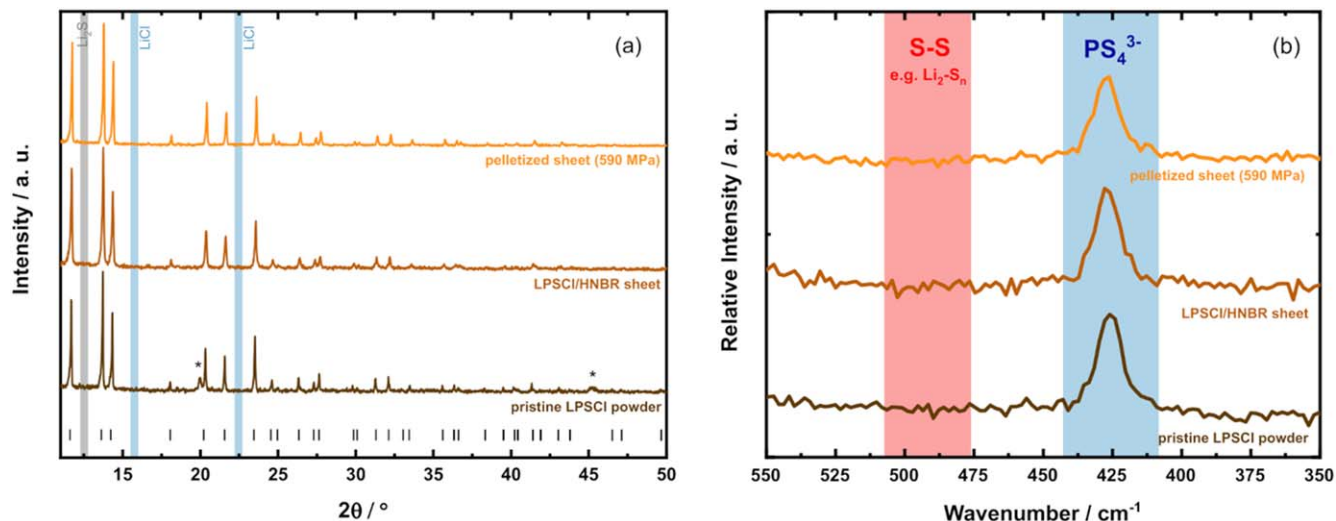


Figure 4. Influence of the slurry-processing with toluene on the chemical structure of LPSCI, comparing the pristine LPSCI powder (brown lines) and the slurry-processes LPSCI/HNBR separator sheets (8.2 vol% HNBR) both uncompressed (beige lines) or compressed at a fabrication pressure of 590 MPa for 5 min (yellow lines). (a) XRD diffraction pattern (recorded with Mo- $K_{\alpha 1}$ radiation), with the black ticks marking the reflex positions of LPSCI (from CIF no. 418490) and the asterisks marking reflexes from the glass capillary. The gray and blue shaded areas mark the main reflexes for Li_2S and LiCl , respectively; the diffractograms are arbitrarily offset in the y-direction. (b) Raman spectra with indicated regions of characteristic PS_4^{3-} -units with a maximum of the signal at $426\text{--}427\text{ cm}^{-1}$ (blue) and of polysulfides ($476\text{--}506\text{ cm}^{-1}$) (red).²⁷ The spectra are arbitrarily offset in the y-direction.

the LSPS/HNBR separator sheets is highest, which may be due to the slightly lower plastic deformability of LSPS.^{33–38} In the literature, the plastic deformability is described by the so-called Pugh's ratio G/B , which relates the shear modulus G to the bulk modulus B . Sulfidic SEs generally feature a low G/B ratio of < 0.5 , reflecting their ductile nature, whereas for most oxides the G/B ratio lies between 0.5–0.6. The G/B ratio of LPSCI (0.28) and LPS711 (0.34) are clearly lower than for LSPS (0.48), consistent with the trends observed in Fig. 6a and thus the most likely explanation why at a given fabrication pressure the LPSCI/HNBR and the LPS711/HNBR separator sheets can be densified to substantially lower porosities than the LSPS/HNBR separator sheets.

Besides the fabrication pressure, we also investigated the influence of the compression time on the separator sheet porosity. This is shown in Fig. 6b for LPSCI/HNBR separator sheets with a binder content of 8.2 vol% for fabrication pressures of either 100 MPa or 590 MPa, indicating that there is no change in porosity when applying these fabrication pressures between 5–120 min. While for the sake of clarity only data for LPSCI/HNBR separator sheets at these two fabrication pressures are shown, it should be noted that the same behavior was found for the separator sheets based on the other two SEs and for all other fabrication pressures.

Figure 7 displays top-view (left panels) and cross-section (right panels) SEM images of LPSCI/HNBR separator sheets with 8.2 vol% HNBR either uncompressed or compressed uniaxially at room temperature for 5 min at 100 MPa or 590 MPa. Both the top-view and the cross-section SEM pictures show a loose distribution of LPSCI particles for the uncompressed separator sheet (Figs. 7a and 7b), with large and numerous voids in between the LPSCI particles. For the separator sheet prepared at a fabrication pressure of 100 MPa (Figs. 7c and 7d), the packing of the LPSCI particles appears to be much denser, which is consistent with the ≈ 2 -fold lower porosity determined in this case (see Fig. 6a). The cross-section image of that sample reveals that the drop in porosity not only results from smaller and fewer voids, but from the plastic deformation of the LPSCI particles. Still, quite large voids can be seen, indicating a not yet complete densification of the LPSCI/HNBR composite. Upon compressing at 590 MPa (Figs. 7e and 7f), single LPSCI particles cannot anymore be identified clearly, and LPSCI particles appear to have aggregated into bigger domains without visible boundaries in between. Voids can only be observed in very few instances and are

randomly distributed, giving evidence for an almost complete densification of the LPSCI/HNBR composite. This is consistent with the very low porosity of $\approx 3\%$ that was determined in Fig. 6a for this material when compressed at 590 MPa.

Lithium ion conductivity of the SE/HNBR separators.—Besides morphology and porosity, the lithium ion conductivity is the most important property of the produced separator sheets. In order to investigate the lithium ion conductivity, electrochemical impedance spectroscopy was performed. All measurements in this section were conducted at an operating cell pressure of $p_{\text{oper}} = 70\text{ MPa}$ and a fabrication pressure of $p_{\text{fabr}} = 0\text{ MPa}$. Herein, the operating cell pressure refers to the pressure, which is applied on the sample during the measurement by the compression of the spring (see Fig. 1). Hence, p_{oper} is independent from the fabrication pressure p_{fabr} , which refers to the prior, cell-external compression of the separator sheet by the hydraulic press (as was done similarly by Doux et al.²⁰).

Figure 8 displays the Nyquist plots for LPSCI/HNBR separator sheets with different binder contents, recorded at $p_{\text{oper}} = 70\text{ MPa}$ and normalized to the separator sheet thickness that was determined after the measurement; for comparison, the data for pure LPSCI powder (black symbols) are also shown. Spectra for the other SEs are shown in Fig. A-2. The Nyquist plots exhibit a semi-circle at high frequencies and a low-frequency tail that can be attributed to the blocking electrodes. The semi-circle at high frequencies can be described by a parallel circuit element of a resistor and a constant phase element (R/Q), with R representing both intragrain and grain boundary contributions to the lithium ion transport, which could not be resolved at the investigated temperature.^{39–41} Comparing the impedance spectra for different binder contents, it can be seen that the semi-circle increases for higher binder contents. We attribute this effect on the ionically insulating nature of the binder, which is located in between the LPSCI particles and impedes the ionic transport across the grain boundaries.

The lithium ion conductivity was determined from the total separator resistance R that is obtained from the fit of the R/Q element, as exemplarily shown in Fig. 8 for the 16.0 vol% sample (gray line). Based on the fitted separator resistance, the lithium ion conductivity (σ_{sheet}) was determined from the thickness of the separator, which was taken after the measurement and outside the cell (t_{sep}), i.e., with no applied pressure, according to:

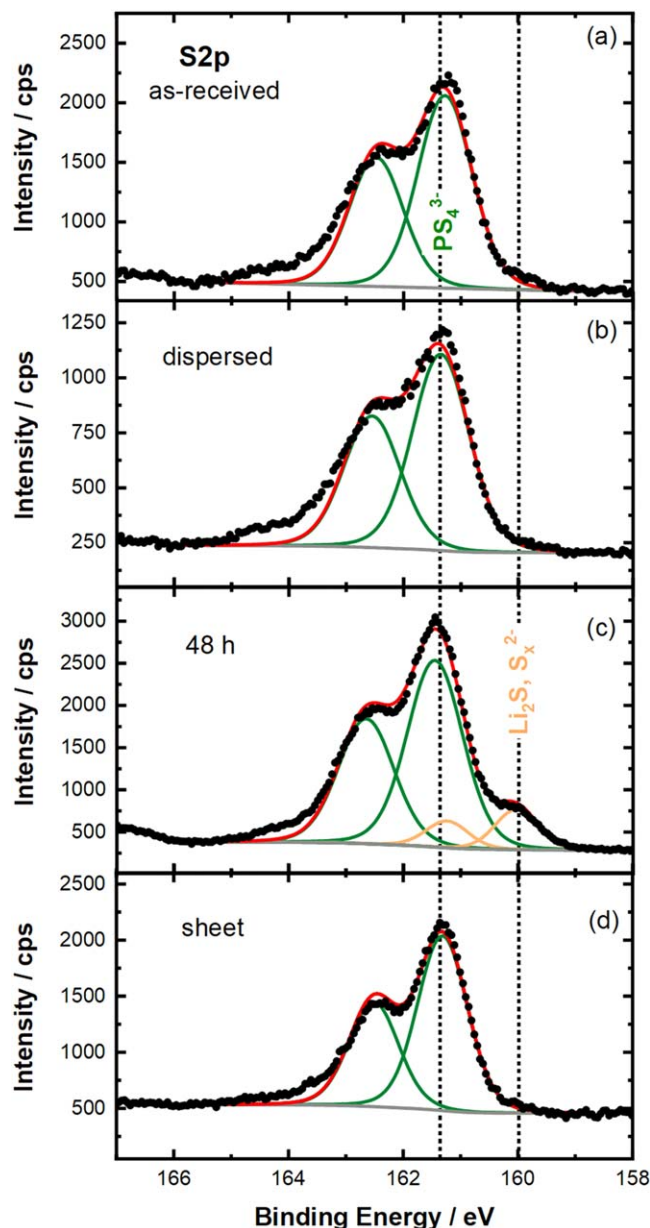


Figure 5. Investigation of the influence of the exposure of LPSCI to toluene, examining the high-resolution XPS signals in the S 2p region: (a) of the pristine LPSCI powder; (b) of the LPSCI powder after mixing it with the dissolver in an HDPE beaker with toluene for 20 min (mimicking the slurry-processing method); (c) of the LPSCI powder after stirring it in a glass beaker with toluene for 48 h; and, (d) of the slurry-processed LPSCI/HNBR separator sheet containing 8.2 vol% HNBR. The powder samples were dried at room temperature, followed by a subsequent drying under dynamic vacuum at 70 °C. The green peaks can be attributed to the PS_4^{3-} units of LPSCI, while the orange peaks in case of the LPSCI powder stirred with toluene in a glass vial for 48 h can be ascribed to lithium sulfide (Li_2S) or polysulfides (S_x^{2-}), indicating a partial decomposition of the LPSCI upon long-term exposure to toluene.

$$\sigma_{sheet} = t_{sep}/(A \cdot R) \quad [3]$$

where A is the cross-sectional area of the 8.0 mm diameter separator (0.50 cm^2). Note that the DC resistance (i.e., the electron conduction resistance) is at least four orders of magnitude larger than the AC resistance and is thus negligible. Figure 9a shows the obtained conductivities (σ_{sheet}) for separator sheets made from different SEs without compression (i.e., $p_{fabr} = 0 \text{ MPa}$) as a function of the

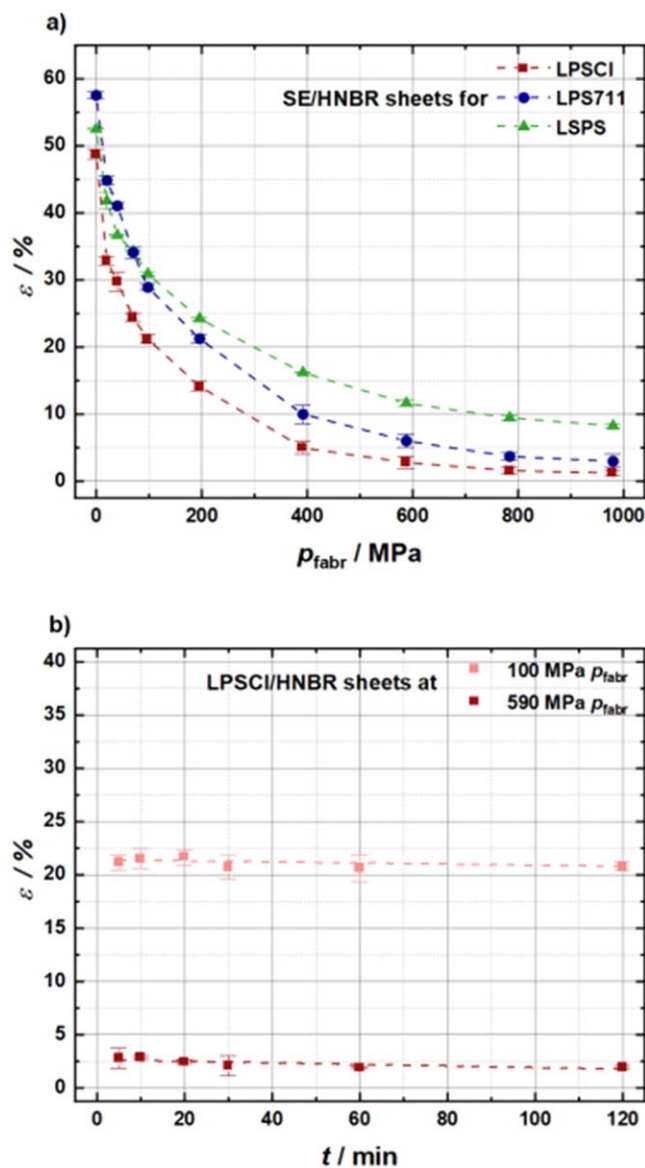


Figure 6. (a) Influence of different fabrication pressures (uniaxially pressed at room temperature for 5 min) on the porosity of SE/HNBR separator sheets made with 8.2 vol% HNBR binder and different solid electrolytes; LPSCI (red), LPS711 (blue), and LSPS (green). (b) Influence of the pressing time on the porosity of LPSCI/HNBR separator sheets (8.2 vol% HNBR) for low and high fabrication pressures of 100 and 590 MPa, respectively. In each case, samples were prepared by stacking three 8 mm diameter separator sheets in the cell setup shown in Fig. A-2. For each data point, three independent measurements were conducted, and error bars represent the standard deviation. Dashed lines are a guide to the eye.

volumetric binder content (ϕ_{HNBR}) at an operating cell pressure of $p_{oper} = 70 \text{ MPa}$. A binder content of 0 vol% corresponds to the pure SE powders and serves as a reference in order to investigate the change in conductivity by the addition of the HNBR binder. For all SEs, the determined powder conductivity is roughly 1.5 mS cm^{-1} at $p_{oper} = 70 \text{ MPa}$ and the measured porosity ranges from $\varepsilon = 28\%–33\%$. The addition of only 1.7 vol% of HNBR binder results in a significant, ≈ 2 -fold decrease in conductivity for the LPSCI/HNBR and the LPS711/HNBR separator sheets (unfortunately, no mechanically stable separator sheets could be obtained with 1.7 vol% of HNBR for the LSPS/HNBR composites). Further increasing the binder content has a progressively smaller impact on the conductivity, whereby the here examined SE/HNBR composites follow the same trend and show essentially identical conductivities

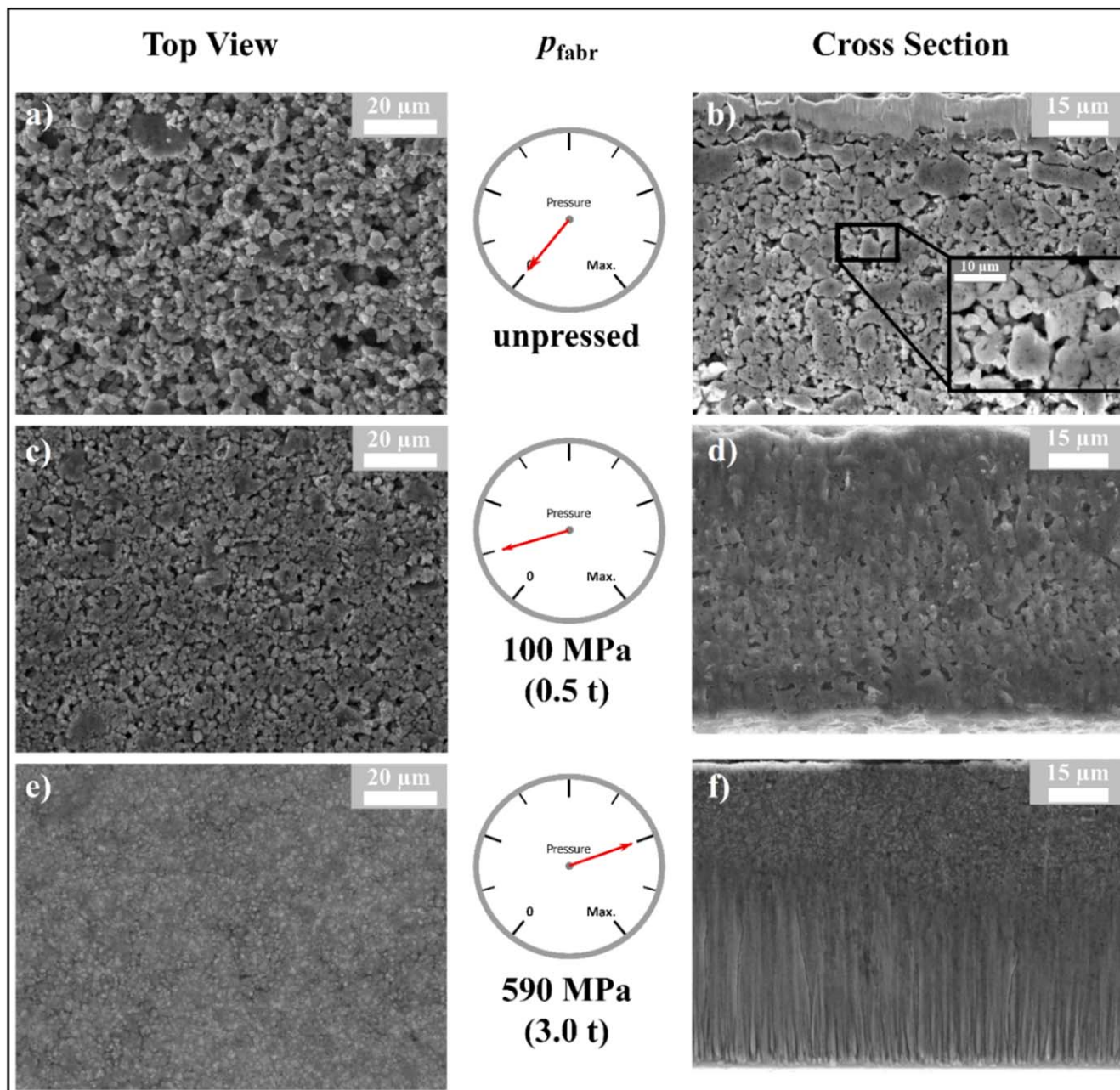


Figure 7. (a) Influence of the fabrication pressure (applied uniaxially at room temperature for 5 min) on an 8 mm sample on the morphology of LPSCI/HNBR separator sheets with 8.2 vol% HNBR, as observed in top-view (left panels) and cross-section (right panels) SEM images. (a) & (b) uncompressed; (c) & (d) compressed at 100 MPa; (e) & (f) compressed at 590 MPa.

within the measurement error, with values of $\approx 0.5 \text{ mS cm}^{-1}$ for 8.2 vol% HNBR and of $\approx 0.3 \text{ mS cm}^{-1}$ for 16.0 vol%. These values refer to $p_{\text{oper}} = 70 \text{ MPa}$, which is a typical pressure used when testing small-scale ASSB laboratory cells.^{2,20}

In addition, measurements at $p_{\text{oper}} = 590 \text{ MPa}$ were conducted in order to investigate the maximum achievable conductivity. For this purpose a slightly modified cell setup was used, which is shown in Fig. A-1. Contrary to the fairly similar conductivities of the different SE/HNBR separator sheets obtained at $p_{\text{oper}} = 70 \text{ MPa}$, the conductivities of the samples with different solid electrolytes differ somewhat when determined at the higher operating cell pressure of $p_{\text{oper}} = 590 \text{ MPa}$, as illustrated in Fig. 9b. The pure SE powder conductivities range from $2.8 \pm 0.18 \text{ mS cm}^{-1}$ for LPS711 (blue, $\varepsilon = 13\%$) to $3.2 \pm 0.23 \text{ mS cm}^{-1}$ for LSPS (green, $\varepsilon = 20\%$) and $3.4 \pm 0.13 \text{ mS cm}^{-1}$ for LPSCI (red, $\varepsilon = 11\%$), and are in reasonably

good agreement with the literature ($\approx 4 \text{ mS cm}^{-1}$ for LSPS reported by Bron et al.⁴² and $\approx 1.3 \text{ mS cm}^{-1}$ for LPSCI reported by Boulineau et al.⁴³). For a more quantitative comparison, the fabrication pressure and the operating cell pressure need to be considered, as outlined by Doux et al.²⁰ and by Ohno et al.⁴¹ For example, for $p_{\text{fabr}} = 370 \text{ MPa}$ and $p_{\text{oper}} = 70 \text{ MPa}$, Doux et al.²⁰ report $\approx 3 \text{ mS cm}^{-1}$ for LPSCI when using their optimized carbon powder coated current collector, which is in good agreement with the data in Fig. 9b, where the maximum pressure seen by the sample was 590 MPa. As observed for the above data at $p_{\text{oper}} = 70 \text{ MPa}$, the overall trend of the conductivity decrease with increasing binder content is also very similar for all three SE/HNBR composites at $p_{\text{oper}} = 590 \text{ MPa}$, with the difference that the LPSCI- and LSPS-based separator sheets outperform those based on LPS711. At a binder content of 8.2 vol% (i.e., at a binder content of 3.7–5.0 wt%, see Table II), the ionic

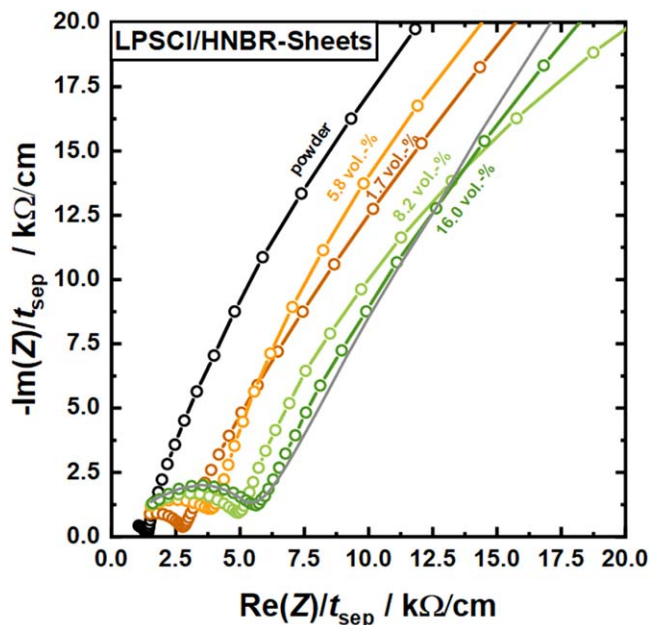


Figure 8. Nyquist plots of the impedance spectra of LPSCI/HNBR separator sheets, obtained at 25°C and at an operating cell pressure (p_{oper}) of 70 MPa; the spectra are normalized to the separator sheet thickness that was determined ex-situ after the measurements. The separator sheets were prepared without compression (i.e., $p_{\text{fabr}} = 0$ MPa) and with different amounts of HNBR binder: 0 vol% (black), 1.7 vol% (brown), 5.8 vol% (orange), 8.2 vol% (light green), and 16.0 vol% (dark green); note that 0 vol% corresponds to the pure LPSCI powder without any solvent exposure. For the measurements, three 8 mm diameter separator sheets were stacked up in the cell; for the binder-free sample, 60 mg of LPSCI powder were used. The apex frequency of the R/Q -element for the separator sheets lies between 2.9–1.2 MHz (both decreasing with increasing HNBR content) and the shown data were acquired between 3 MHz and 1 kHz. The lines in the plot serve as a guide to the eye. For the sake of clarity, spectra of separator sheets with an HNBR content of 3.4 and 11.4 vol% are not displayed. An exemplary fit with an $R_1/Q_1 + Q_2$ equivalent circuit of the impedance data from a LPSCI/HNBR sheet with a binder content of 16.0 vol% is displayed in gray.

conductivities are rather similar, with 0.93 ± 0.04 mS cm⁻¹, 0.84 ± 0.05 , and 0.70 ± 0.03 mS cm⁻¹ for the LPSCI/HNBR, the LSPS/HNBR, and the LPS711/HNBR separator sheets, respectively.

In order to more rigorously compare the decrease of the ionic conductivity with increasing volumetric HNBR binder fraction for the different SE/HNBR separator sheets, the measured σ_{sheet} values were normalized by the respective SE powder conductivity values (σ_{powder}), thereby decoupling the absolute conductivity differences of the different SEs from that of the corresponding SE/HNBR composites. Thus, the lower panels in Fig. 9 show the values of $\sigma_{\text{sheet}}/\sigma_{\text{powder}}$ vs ϕ_{HNBR} for $p_{\text{oper}} = 70$ MPa (Fig. 9c) and 590 MPa (Fig. 9d). Up to a volumetric HNBR binder fraction of 11.4 vol%, the decrease in conductivity is largely independent of the sulfidic SE type (we ascribe the differences at 1.7 vol% to small errors in weight measurements, which become important at this steep part of the curve). This is somewhat surprising, as at both operating cell pressures the porosity of the SE/HNBR separator sheets measured for 8.2 vol% HNBR (see Fig. 6a) differ quite significantly (ε ranging from $\approx 23\%$ – 34% at $p_{\text{oper}} = 70$ MPa and from $\approx 3\%$ – 12% at $p_{\text{oper}} = 590$ MPa). This suggests that small differences in porosity do not significantly affect the conductivity of the SE/HNBR separator sheets. Only at the highest volumetric binder fraction of 16.0 vol%, significant differences can be observed, with a ≈ 2 -fold higher normalized conductivity for the LPSCI/HNBR separator sheet compared to the LPS711/HNBR and LSPS/HNBR separator sheets. When plotting the $\sigma_{\text{sheet}}/\sigma_{\text{powder}}$ vs ϕ_{HNBR} data acquired at low (70 MPa) and high (590 MPa) operating cell pressure for the

separators based on a given SE, as shown in Fig. A-3, it can be seen that the operating cell pressure has no significant impact on the binder-induced conductivity decrease.

Although the mechanical properties of the here discussed SE/HNBR separator sheets were not investigated in detail, some conclusions can be drawn from handling the separator sheets: an HNBR binder content of < 5 vol% results in rather brittle separator sheets that are challenging to work with, whereas an HNBR binder content of > 11 vol% yields very flexible sheets with almost rubbery properties. At the same time, as discussed above, the higher the HNBR binder content, the lower is the ionic conductivity of the separator sheets. Thus, for the here described SE/HNBR separator sheets, the qualitatively best trade-off between ionic conductivity and mechanical properties is found for separator sheets with an HNBR binder content of 8.2 vol%, where $\approx 25\%$ – 30% of the conductivity of the equally compressed SE powder can be obtained (see Figs. 9c and 9d). Therefore, the following experiments were only conducted with this binder content.

Effect of the fabrication pressure on SE/HNBR separator conductivities.—Both the literature and the afore described experiments show higher ionic conductivities at higher operating cell pressures, due to a lower sample porosity.²⁰ In the case of the here examined separator sheets, it should be noted that for the separators based on different SEs, differences in porosity of roughly 10 percentage points were found to not yield significant differences in their $\sigma_{\text{sheet}}/\sigma_{\text{powder}}$ values (see above). At the same time, low porosities might be beneficial for suppressing the formation of Li dendrites and thus enable cell operation at higher current densities.^{21,22} However, for actual applications it is not feasible to apply several hundred MPa on a battery, as this would add an excessively large weight to the battery and thus reduce its overall energy density. Therefore, the effect of pre-pressing (or pre-calendering) of separator sheets on their conductivity (i.e., using a high fabrication pressure) will be examined next. In doing so, we compare the conductivity of uncompressed ($p_{\text{fabr}} = 0$ MPa) separator sheets at $p_{\text{oper}} = 20, 40, 70,$ and 590 MPa with that of separator sheets that had been pre-pressed at $p_{\text{fabr}} = 590$ MPa and afterwards measured at operating pressures of 20, 40, and 70 MPa. In each case, the separator thickness was determined after the experiments, i.e., without any pressure applied.

Figures 10a–10c shows the results for the three different SE/HNBR separators with 8.2 vol% HNBR, with exemplary separator thickness-normalized Nyquist plots shown in Figs. 10d–10f. In case of uncompressed LPSCI/HNBR-sheets ($p_{\text{fabr}} = 0$ MPa, other markers in Fig. 10a), the conductivity values range from 0.17 ± 0.04 mS cm⁻¹ (33% porosity) at 20 MPa cell operating pressure to 0.43 ± 0.02 mS cm⁻¹ (24% sample porosity) at $p_{\text{oper}} = 70$ MPa, reaching a maximum value of 0.94 ± 0.05 mS cm⁻¹ (3% sample porosity) at $p_{\text{oper}} = 590$ MPa. When the separator sheets are pre-pressed at $p_{\text{fabr}} = 590$ MPa before the conductivity is determined, higher values are observed for all operation pressures, e.g., 0.57 ± 0.05 mS cm⁻¹ (3% sample porosity) at $p_{\text{oper}} = 70$ MPa (olive green marker). It is striking that the conductivity of this sample pre-pressed at $p_{\text{fabr}} = 590$ MPa and measured at $p_{\text{oper}} = 70$ MPa is almost 2-fold lower than the uncompressed sample that was measured at $p_{\text{oper}} = 590$ MPa, even though both samples have the same porosity of $\approx 3\%$. Doux et al.²⁰ observed a similar increase of the conductivity with increasing operating cell pressure for LPSCI powder samples pre-compressed at $p_{\text{fabr}} = 370$ MPa (≈ 2 -fold when increasing p_{oper} from 20 to 70 MPa), which they attributed to poor contacting of their SE powder samples by metal current collectors at low cell operating pressures. This is based on their observation that the conductivity increase with p_{oper} could be reduced substantially by placing layers of conductive carbon between their metal current collectors and their SE powder sample (≈ 1.4 -fold when increasing p_{oper} from 20 to 70 MPa). Considering that the increase in conductivity with the operating cell pressure is similar in the experiments shown in Fig. 10a, it is also likely due to the effect of contact resistances

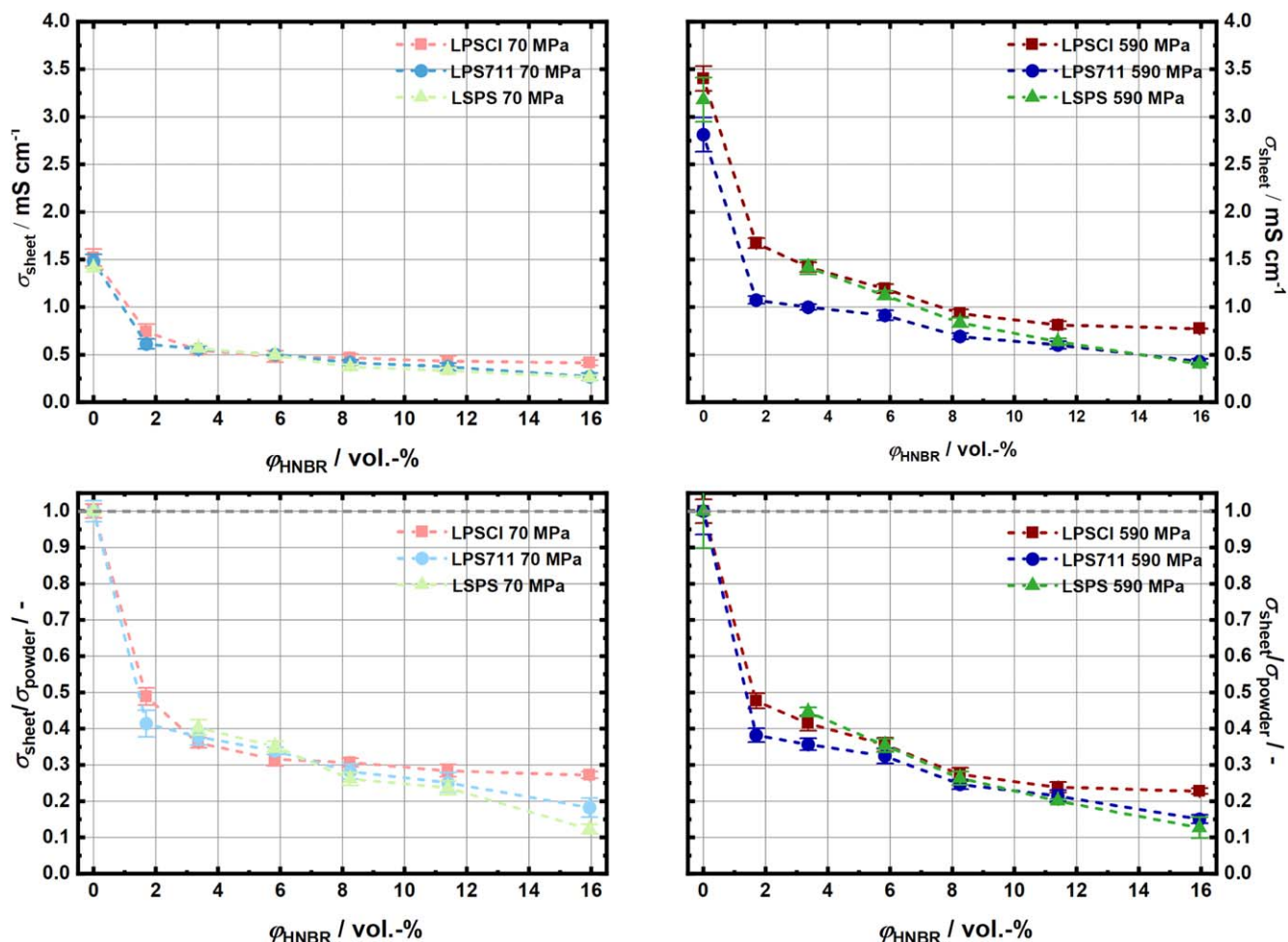


Figure 9. Separator sheet conductivity (σ_{sheet}) at 25 °C of different SE/HNBR separators (red: LPSCI; blue: LPS711; green: LSPS) that were prepared without compression (i.e., $p_{\text{fabr}} = 0$ MPa) as a function of volumetric binder content (ϕ_{HNBR}) at two different operating cell pressures: (a) $p_{\text{oper}} = 70$ MPa; (b) $p_{\text{oper}} = 590$ MPa. Note that the point at 0 vol% corresponds to the pure SE powder without any solvent exposure and that σ_{sheet} is determined from Eq. 2. Note that the sample thickness is determined after the measurement and outside the cell, i.e. with no pressure applied. The lower panels show the σ_{sheet} values normalized to the pure SE powder conductivity (σ_{powder} , depicted at 0 vol% HNBR) at the respective operating cell pressures: (c) $p_{\text{oper}} = 70$ MPa; (d) $p_{\text{oper}} = 590$ MPa. The dotted, grey line at $\sigma_{\text{sheet}}/\sigma_{\text{powder}} = 1$ corresponds to the powder conductivity at the respective operating pressure. For each data point, three samples were taken and error bars were obtained by the standard deviation of the three independently measured samples. Dashed lines are a guide to the eye.

between the metal current collectors of the cell and the separator sheets, as reported by Doux et al.²⁰ Nevertheless, it is clear that higher fabrication pressures result not only in much reduced porosities of the LPSCI/HNBR separator sheets, but also in ≈ 1.5 -fold higher conductivities at any given operating cell pressure.

Figure 10d compares the impedance data of the LPSCI/HNBR separator prepared without compression and measured at $p_{\text{oper}} = 70$ MPa (ocher; porosity of 24%) with the uncompressed sample measured at $p_{\text{oper}} = 590$ MPa (ocher, porosity of 3%), the decrease of the semi-circle can be correlated with an enhanced grain boundary conduction due to a better contacting of the particles upon densification, i.e., at lower porosity. On the other hand, when the LPSCI/HNBR separator is pre-compressed at 590 MPa (again resulting in a low porosity of 3%) and measured at $p_{\text{oper}} = 70$ MPa (olive green), the semi-circle increases and the apparent conductivity decreases. This can be interpreted either as the effect of a higher contact resistance at lower operating cell pressure (see above) or as an internal relaxation of the binder and SE particles due to a spring back leading to a microscopic contact loss of the SE particles without a macroscopic change in the sample thickness.

Similar dependencies of the conductivity on fabrication and operating cell pressure can be observed for the LPS711/HNBR separators (8.2 vol%). The only significant difference between the LPSCI/HNBR and the LPS711/HNBR separators is that the latter

have slightly higher porosity values, as already observed in Fig. 6. Exemplary thickness-normalized Nyquist plots of uncompressed and pre-pressed LPS711/HNBR separators are shown in Fig. 10e.

Surprisingly, for the LSPS/HNBR separators (8.2 vol%), no change of the conductivity after pre-compression when measured at a given operating pressure can be observed (see Fig. 10c). For example, the sheets measured at an operating cell pressure of 70 MPa give a conductivity of $0.32 \pm 0.01 \text{ mS cm}^{-1}$ when prepared with $p_{\text{fabr}} = 0$ MPa and $0.34 \pm 0.01 \text{ mS cm}^{-1}$ when prepared with $p_{\text{fabr}} = 590$ MPa. One apparent difference between the pre-compressed separators based on LSPS vs those based on LPSCI or LPS711, is the substantially higher porosity of the latter (3% and 6% for the former, 12% for the latter). In order to investigate whether this difference in porosity could explain why the LSPS/HNBR separator sheets yield the same conductivity at $p_{\text{oper}} = 70$ MPa for uncompressed and pre-compressed samples, we will next examine the effect of porosity on conductivity. Unfortunately, it was not possible for the LSPS/HNBR separator sheets to achieve a final porosity value of 3% that can be reached for LPSCI/HNBR separator sheets. Hence, we conducted the following evaluation on the effect of porosity using LPSCI/HNBR separator sheets with 8.2 vol% HNBR, which were subjected to different fabrication pressures ranging between 0 and 590 MPa, after which their conductivity was determined at an operating cell pressure of 70 MPa (see Fig. 11). For a fabrication pressure of 215 MPa, resulting in a porosity of 11%, the

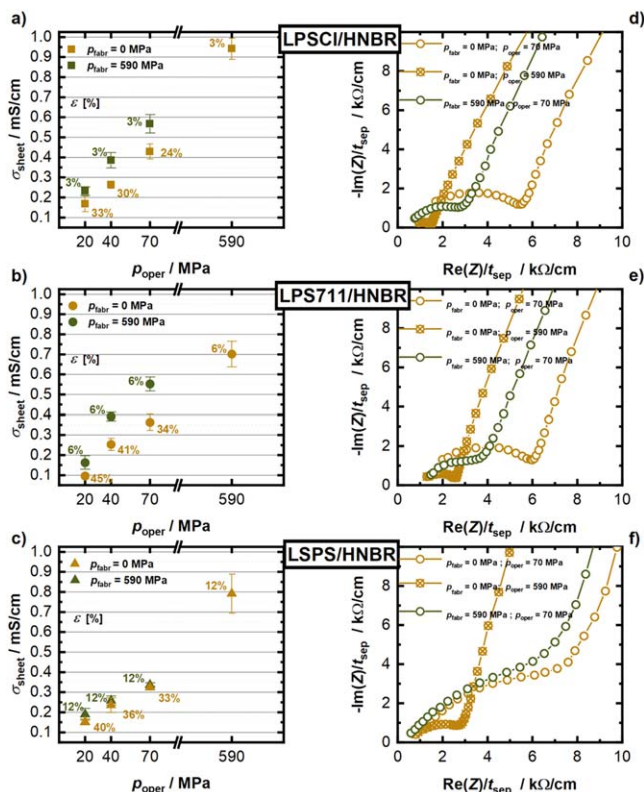


Figure 10. (a)–(c) Conductivity of different SE/HNBR separator sheets with 8.2 vol% HNBR (red: LPSCI; blue: LPS711; green: LSPS) that were prepared either without pre-compression ($p_{\text{fabr}} = 0$ MPa, ocher) or with a high fabrication pressure of $p_{\text{fabr}} = 590$ MPa (olive green), determined at operating cell pressures of $p_{\text{oper}} = 20$ MPa, 40 MPa and 70 MPa, as well at 590 MPa. Values are given as the average of three measurements and error bars represent the standard deviation thereof. Porosity values of the samples are given in percent and written next to corresponding data points. (d)–(f) Corresponding Nyquist plots, normalized to sample thickness for measurements at $p_{\text{oper}} = 70$ MPa (circles in ocher and olive green) and 590 MPa (circle cross in ocher).

LPSCI/HNBR separator conductivity of 0.46 ± 0.004 mS cm^{-1} is only marginally larger than that of the uncompressed sample with a porosity of 24% (0.43 ± 0.02 mS cm^{-1}), a difference which is within the error range of the measurements. Only upon pre-compression at $p_{\text{fabr}} = 295$ MPa, resulting in a porosity of 9%, the conductivity increases by $\approx 20\%$ compared to the uncompressed sample (i.e., to 0.52 ± 0.01 mS cm^{-1}). Finally, at $p_{\text{fabr}} = 590$ MPa and 3% porosity, a conductivity gain of $\approx 31\%$ compared to the uncompressed sample is observed (with a value of 0.57 ± 0.04 mS cm^{-1} at $p_{\text{fabr}} = 590$ MPa). For the LPSCI/HNBR separator sheets, this shows that substantial conductivity gains for pre-compressed separators can only be observed once the porosity decreases below 11%. Thus, if one were to assume a similar conductivity vs porosity dependence for the LSPS/HNBR separator sheets, one could explain why there was no improvement of their conductivity between uncompressed samples and samples pre-compressed to 590 MPa (see Fig. 10c), where the porosity was still 12%. In summary, the data in Fig. 11 suggest that a pre-compression of the SE/HNBR separator sheets only significantly improves their conductivity when very low porosities (on the order of lower than 10%) can be obtained, which for materials like LSPS would require fabrication pressures of more than 800 MPa (see Fig. 6).

Conclusions

In this work, we report the preparation of thin separator sheets composed of solid electrolyte (SE) and HNBR binder for potential use in all-solid-state batteries (ASSBs) by a slurry-based process,

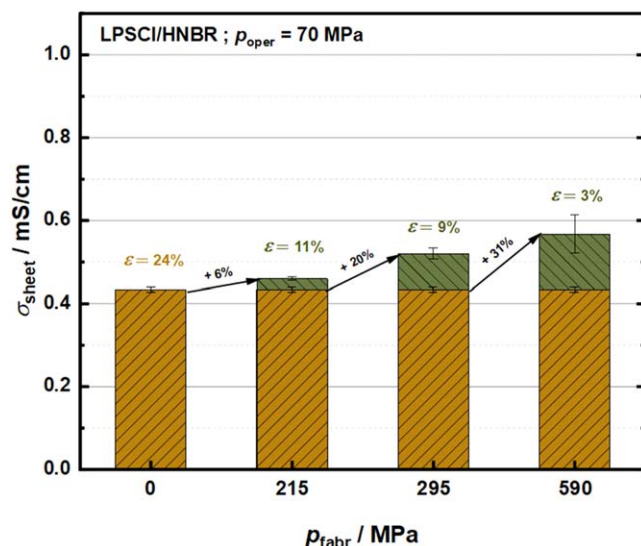


Figure 11. Influence of the fabrication pressure and the porosity on the ionic conductivity of LPSCI/HNBR (8.2 vol%) separator sheets, recorded at an operation cell pressure of 70 MPa. Yellow bars represent the separator sheet conductivity of uncompressed samples and green bars indicate the gain in conductivity after pre-compression at the given fabrication pressure. Corresponding porosity values after the pre-compression step are given in green numbers and in yellow numbers for the uncompressed samples. The numbers on the black arrows mark the percentage increase in conductivity compared to the uncompressed samples.

investigating three different solid electrolytes, viz., $\text{Li}_6\text{PS}_5\text{Cl}$ (LPSCI), $\text{Li}_7\text{P}_3\text{S}_{11}$ (LPS711), and $\text{Li}_{10}\text{SnP}_2\text{S}_{12}$ (LSPS). Using these separator sheets, we investigate the influence of time and fabrication pressure on the porosity of the sheets. Additionally, we investigate their ionic conductivity as a function of the volumetric binder content, the fabrication pressure of the separator sheets, and the operation cell pressure during the conductivity measurements using an in-house developed cell design.

The prepared separator sheets have a dry-film thickness of ≈ 100 μm and a porosity around 50% in their uncompressed, as-prepared state. Substantial densification of the separator sheets is easily achieved by compression at room temperature, reaching porosities at pressures of 590 MPa that are as low as 3%–12% (corresponding to thicknesses as low as ≈ 48 – 76 μm), depending on the solid electrolyte. Thereby, the applied compression has a significant influence on the final separator sheet porosity, whereas the compression time has none.

Even small amounts of binder lead to a significant decrease in ionic conductivity, which further decreases for further increasing binder contents. The separator sheets feature 25%–30% of the conductivity of the pure SE powder when compared at the same fabrication pressure. The observed decrease in conductivity is mainly a function of the volumetric binder content rather than of the used solid electrolyte. In this study, a binder content of 8.2 vol% proved to be the best compromise between achieving adequate mechanical properties for a good handling of the sheets and obtaining a reasonably high ionic conductivity with respect to the pure SE powder. For this binder content, room temperature conductivities of roughly 0.5 mS cm^{-1} could be obtained. Owing to the fact that the SE/HNBR separators are comparably thin, the separator sheets have approximately the same areal resistance as the typically much thicker pellet-type separators, but enable for a simpler preparation of large-format cells.

Lastly, we evaluate on the influence of fabrication and operation cell pressure on the ionic conductivity of the separator sheets. We show that a densification of the separator sheets at high fabrication pressures to low porosities can be used to increase their conductivity at lower operating cell pressures. Additionally, we show, that the

porosity cannot directly be correlated to the conductivity, as the operating cell pressure has a significant influence on the sheet conductivity, even for low residual porosities.

Acknowledgments

We gratefully thank Erik Faber, Marc Schönberger and Patrick Gieb from the mechanical workshop at the TUM Chemistry Department for their support in building our solid-state cell hardware. Furthermore, we thank Philip Rapp and Hasan Camci for their assistance with the cell illustrations as well as Hans-Christoph Töpfer and Raimund Koerver for valuable discussions. This work is part of the project “Industrialisierbarkeit Festkörperelektrolyte” funded by the Bavarian Ministry of Economic Affairs, Regional Development and Energy.

Appendix

Cell setup for high cell stack compression.—The following figure shows the details of the cell setup used in combination with a hydraulic press located in the glovebox in order to reach cell stack compressions of 100–590 MPa, with an accuracy of ± 20 MPa. The theoretically determined capacitance of this cell is $\approx 1.3 \cdot 10^{-11}$ F, which is in good agreement with the experimentally determined value of $\approx 1.0 \cdot 10^{-11}$ F. The stray capacitances of the setup are at least three order of magnitude lower than the capacitances of the cell and thus do not influence the results of the PEIS measurements. The internal resistance of the cell was determined to $< 0.2 \Omega$.

Impedance spectra of the LPS711/HNBR and LSPS/HNBR separator sheets.—The following figure shows the impedance

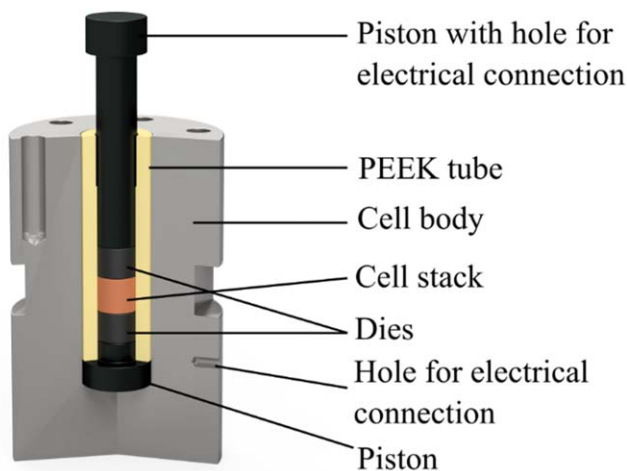


Figure A-1. Cross-sectional illustration of the cell design used for measurements at $p_{\text{oper}} > 100$ MPa. In order to apply the pressure, the cell was put into a hydraulic press. The bottom of the cell body and the top of the piston were electrically insulated from the press by a polyimide foil. The cell body is made from stainless steel; pistons and dies from hardened stainless steel.

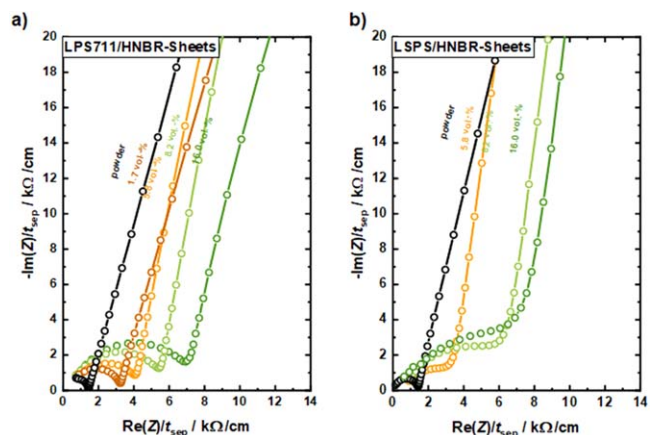


Figure A-2. Thickness-normalized Nyquist plots of the impedance spectra obtained at 25 °C and at an operating cell pressure of $p_{\text{oper}} = 70$ MPa for LPS711/HNBR (left) and LSPS/HNBR separator (right) that were prepared without compression (i.e., $p_{\text{fabr}} = 0$ MPa) and with different binder contents: 0 vol% (black), 1.7 vol% (brown), 5.8 vol% (orange), 8.2 vol% (light green), and 16.0 vol% (dark green); note that 0 vol% corresponds to the pure SE powder without any solvent exposure. Samples were prepared by stacking three 8 mm separator sheets or using an amount of 60 mg SE powder for the binder-free samples. For the sake of clarity, spectra of separator sheets with an HNBR content of 3.4 and 11.4 vol% are not displayed. In case of the LSPS/HNBR system, the 1.7 vol% HNBR separator sheet could not be prepared. The apex frequency of the R/Q -element for the LPS711-based composites ranges between 2.9–0.9 MHz and for the LSPS-based composites ranges between 2.9–1.2 MHz (both decreasing with increasing HNBR content). The shown data points span the frequency range of 3 MHz–1 kHz, and the lines serve as guide to the eye.

measurements for uncompressed ($p_{\text{fabr}} = 0$ MPa) separator sheets obtained at a cell operating pressure of $p_{\text{oper}} = 70$ MPa. In accordance to the observations described for LPSCI/HNBR sheets (cf. Fig. 8 in the main text), the spectra exhibit a semi-circle at high frequencies, representing grain and grain boundary contributions to the lithium ion transport, and a low-frequency tail due to the blocking electrode configuration. With increasing binder content, the magnitude of the semi-circle increases, leading to a decreasing ionic conductivity.

Dependence of the separator conductivity on the operating cell pressure.—Figures 9, 10c and 10d in the main part show the normalized separator sheet conductivities ($\sigma_{\text{sheet}}/\sigma_{\text{powder}}$) vs ϕ_{HNBR} , comparing the three different SE systems at an operating cell pressure of 70 and 590 MPa each. Here we additionally compare $\sigma_{\text{sheet}}/\sigma_{\text{powder}}$ vs ϕ_{HNBR} for the same SE systems at low (70 MPa, data points in lighter colors) and high (590 MPa, data points in darker colors) operating cell pressure in order to investigate its impact on the separator sheet conductivity. Figure A.3 shows that, within the range of the experimental error, the normalized separator conductivity is essentially independent of the operating cell pressure and only a function of the volumetric binder content.

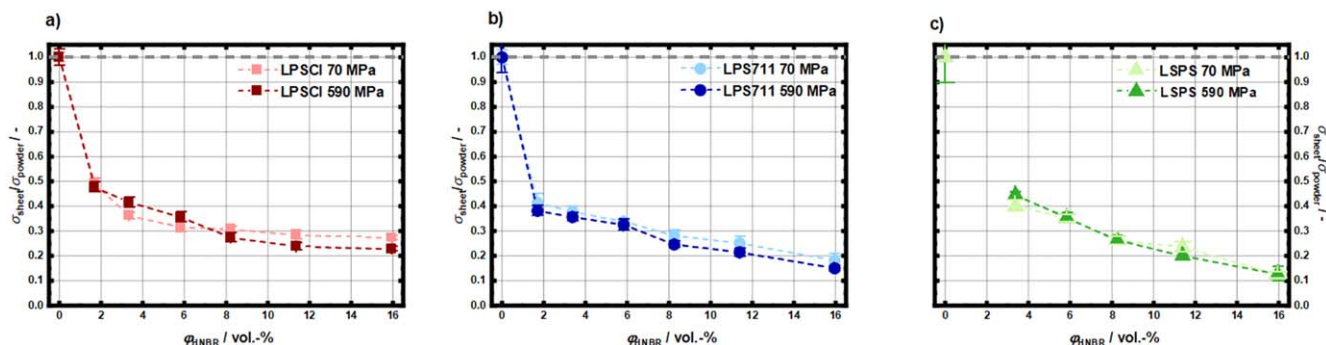


Figure A-3. Separator sheet conductivity (σ_{sheet}), normalized to the pure SE powder conductivity (σ_{powder}) at $p_{\text{oper}} = 70$ MPa (lighter color) and at $p_{\text{oper}} = 590$ MPa (darker color) as function of the volumetric HNBR binder content (ϕ_{HNBR}) for the different SE/HNBR separator sheets prepared with $p_{\text{fabr}} = 0$ MPa: (a) SE = LPS/CI (red); (b) SE = LPS/711 (blue); (c) SE = LPS/S (green). For each data point, three samples were taken and error bars were obtained by the standard deviation of the three independently measured samples. Dashed lines are a guide to the eye. Note that the LPS/HNBR-sheet with $\phi_{\text{HNBR}} = 1.7$ vol% could not be prepared.

ORCID

Tobias Kutsch <https://orcid.org/0000-0002-7529-3376>
 Louis Hartmann <https://orcid.org/0000-0002-3964-1935>
 Hubert A. Gasteiger <https://orcid.org/0000-0001-8199-8703>

References

- J. Janek and W. G. Zeier, *Nat. Energy*, **1**, 1 (2016).
- W. Zhang et al., *ACS Appl. Mater. Interfaces*, **9**, 17835 (2017).
- S. Randau et al., *Nat. Energy*, **5**, 259 (2020).
- T. Ates, M. Keller, J. Kulisch, T. Adermann, and S. Passerini, *Energy Storage Mater.*, **17**, 204 (2019).
- P. Schichtel, M. Geiß, T. Leichtweiß, J. Sann, D. A. Weber, and J. Janek, *J. Power Sources*, **360**, 593 (2017).
- M. R. Busche et al., *Chem. Mater.*, **28**, 6152 (2016).
- N. Riphaut, P. Strobl, B. Stiaszny, T. Zinkevich, M. Yavuz, J. Schnell, S. Indris, H. A. Gasteiger, and S. J. Sedlmaier, *J. Electrochem. Soc.*, **165**, A3993 (2018).
- K. Lee, S. Kim, J. Park, S. H. Park, A. Coskun, D. S. Jung, W. Cho, and J. W. Choi, *J. Electrochem. Soc.*, **164**, A2075 (2017).
- A. Sakuda, K. Kuratani, M. Yamamoto, M. Takahashi, T. Takeuchi, and H. Kobayashi, *J. Electrochem. Soc.*, **164**, A2474 (2017).
- F. Shen, M. B. Dixit, W. Zaman, N. Hortance, B. Rogers, and K. B. Hatzell, *J. Electrochem. Soc.*, **166**, A3182 (2019).
- S. Wang et al., *Journal of Materiomics*, **6**, 70 (2020).
- M. Yamamoto, Y. Terauchi, A. Sakuda, and M. Takahashi, *Sci Rep.*, **8**, 1212 (2018).
- Y.-G. Lee et al., *Nat. Energy*, **5**, 299 (2020).
- J. Zhang, C. Zheng, J. Lou, Y. Xia, C. Liang, H. Huang, Y. Gan, X. Tao, and W. Zhang, *J. Power Sources*, **412**, 78 (2019).
- Z. Deng, Z. Wang, I.-H. Chu, J. Luo, and S. P. Ong, *J. Electrochem. Soc.*, **163**, A67 (2015).
- A. Sakuda, A. Hayashi, and M. Tatsumisago, *Sci Rep.*, **3**, 2261 (2013).
- H. Tsukasaki, S. Mori, H. Morimoto, A. Hayashi, and M. Tatsumisago, *Sci Rep.*, **7**, 4142 (2017).
- S. Teragawa, K. Aso, K. Tadanaga, A. Hayashi, and M. Tatsumisago, *J. Power Sources*, **248**, 939 (2014).
- L. Zhou, K.-H. Park, X. Sun, F. Lalère, T. Adermann, P. Hartmann, and L. F. Nazar, *ACS Energy Lett.*, **4**, 265 (2018).
- J.-M. Doux, Y. Yang, D. H. S. Tan, H. Nguyen, E. A. Wu, X. Wang, A. Banerjee, and Y. S. Meng, *J. Mater. Chem. A*, **8**, 5049 (2020).
- M. B. Dixit, M. Regala, F. Shen, X. Xiao, and K. B. Hatzell, *ACS Appl. Mater. Interfaces*, **11**, 2022 (2019).
- F. Shen, M. B. Dixit, X. Xiao, and K. B. Hatzell, *ACS Energy Lett.*, **3**, 1056 (2018).
- J. C. Bachman et al., *Chem. Rev.*, **116**, 140 (2016).
- Y. Zhu, X. He, and Y. Mo, *ACS Appl. Mater. Interfaces*, **7**, 23685 (2015).
- R. Morasch, J. Landesfeind, B. Suthar, and H. A. Gasteiger, *J. Electrochem. Soc.*, **165**, A3459 (2018).
- M. Ansari Fard, G. H. Rounaghi, M. Chamsaz, and K. Taheri, *J. Inclusion Phenom. Macroscopic Chem.*, **64**, 49 (2009).
- J. Ruhl, L. M. Riegger, M. Ghidui, and W. G. Zeier, *Advanced Energy and Sustainability Research*, **2**, 2000077 (2021).
- M. Xuan, W. Xiao, H. Xu, Y. Shen, Z. Li, S. Zhang, Z. Wang, and G. Shao, *J. Mater. Chem. A*, **6**, 19231 (2018).
- H. J. Deiseroth, S. T. Kong, H. Eckert, J. Vannahme, C. Reiner, T. Zaiss, and M. Schlosser, *Angew. Chem. Int. Ed. Engl.*, **47**, 755 (2008).
- R. P. Rao, N. Sharma, V. K. Peterson, and S. Adams, *Solid State Ionics*, **230**, 72 (2013).
- C. Dietrich, D. A. Weber, S. J. Sedlmaier, S. Indris, S. P. Culver, D. Walter, J. Janek, and W. G. Zeier, *J. Mater. Chem. A*, **5**, 18111 (2017).
- F. Walther, R. Koerver, T. Fuchs, S. Ohno, J. Sann, M. Rohnke, W. G. Zeier, and J. Janek, *Chem. Mater.*, **31**, 3745 (2019).
- A. Hwang et al., *Int. J. Electrochem. Sci.*, **12**, 7795 (2017).
- S. Choi, J. Ann, J. Do, S. Lim, C. Park, and D. Shin, *J. Electrochem. Soc.*, **166**, A5193 (2018).
- J. Zhang, H. Zhong, C. Zheng, Y. Xia, C. Liang, H. Huang, Y. Gan, X. Tao, and W. Zhang, *J. Power Sources*, **391**, 73 (2018).
- D. Pérez-Coll, E. Sánchez-López, and G. C. Mather, *Solid State Ionics*, **181**, 1033 (2010).
- J.-M. Doux, L. Leguay, A. Le Gal La Salle, O. Joubert, and E. Quarez, *Solid State Ionics*, **324**, 260 (2018).
- A. Banerjee et al., *ACS Appl. Mater. Interfaces*, **11**, 43138 (2019).
- P. Bron, S. Dehnen, and B. Roling, *J. Power Sources*, **329**, 530 (2016).
- M. A. Kraft, S. P. Culver, M. Calderon, F. Bocher, T. Krauskopf, A. Senyshyn, C. Dietrich, A. Zevalkink, J. Janek, and W. G. Zeier, *J. Am. Chem. Soc.*, **139**, 10909 (2017).
- S. Ohno et al., *ACS Energy Lett.*, **5**, 910 (2020).
- P. Bron, S. Johansson, K. Zick, J. Schmedt auf der Gunne, S. Dehnen, and B. Roling, *J. Am. Chem. Soc.*, **135**, 15694 (2013).
- S. Boulineau, M. Courty, J.-M. Tarascon, and V. Viallet, *Solid State Ionics*, **221**, 1 (2012).

3.1.2 Development of a μ -Reference Electrode for Advanced Diagnostics in All-Solid-State Battery Pouch Cells

This section presents the article “*A Micro-Reference Electrode for Electrode-Resolved Impedance and Potential Measurements in All-Solid-State-Battery Pouch Cells and Its Application to Indium-Lithium Anodes*”, which was submitted in January 2023 and published in March 2023 in the peer-reviewed Journal of the Electrochemical Society.¹⁶⁴ It is available as an “open access” article under the terms of the Creative Commons Attribution 4.0 License (CC BY). The permanent web link is available under: <https://iopscience.iop.org/article/10.1149/1945-7111/acc699/pdf>. Christian Sedlmeier presented the article at the 241st Meeting of the Electrochemical Society in Vancouver, Canada in May 2022 (Meeting Abstract MA2022-01 207).

A three-electrode setup featuring a micro-reference electrode (μ -RE) for electrode-resolved EIS measurements is a powerful and widespread tool in liquid electrolyte-based LIB research.^{165–169} However, this technique has yet not really found its way into ASSB research, which is reflected by the fact that up to now most of the reported impedance measurements are conducted in a full-cell configuration.^{107,108,170–174} Due to similar time constants for anode and cathode impedance contributions, no reliable quantitative interpretation of the impedance spectra is possible. Only a handful of studies report electrode-cell resolved impedance spectra in sulfide-based ASSB, all of which use pellet-type cells, which are contained in a rigid cylinder.^{103,104,175–177} We believe that the mechanical and geometrical very demanding integration of the RE into pellet-type cells is a major factor hindering the implementation of a μ -RE from becoming a standard method. For exactly that reason we developed sheet-type separators (see subsection 3.1.1), which allow a straight-forward integration of a wire-shaped reference electrode. Using a pouch cell configuration that is spatially not confined towards the edges of the separator, like it is the case for cells contained in a cylinder, it is quite simple to ensure a good electrical contact of the RE.

In this study, we report the implementation of a micro-reference electrode into an ASSB pouch cell, which is inspired by an approach for liquid electrolyte LIBs from our group.¹⁶⁷ The reference electrode was made from a thin gold wire (50 μm core diameter) with an insulating polyimide coating (7 μm thickness) that was sandwiched between two

equally thick LPSCI/HNBR separator-sheets. This preparation method guaranteed a central position inside the cell and the identical distance from both electrodes, both of which are essential requirements for obtaining artifact-free half-cell impedance spectra.^{165,178,179} Subsequently, the gold wire was *in situ* electrochemically lithiated from one of the electrodes, forming a lithium-gold-alloy with a stable potential of 0.31 V vs. Li^+/Li .¹⁸⁰ Using a Li|Li cell equipped with a gold wire micro-reference electrode (GWRE), we successfully showed that the GWRE can be used in ASSB research.




With the aid of the GWRE, we investigate indium-lithium anodes that were prepared by stacking and subsequent compression of indium and lithium foils with an atomic ratio of In:Li = 76:24. Here we could show that the lithium reservoir of the electrode is electrochemically accessible only if the Li-enriched side faces the separator. In the case where the side of pure indium, of which an excess is used, is attached to the separator, the lithium is electrochemically not accessible, since the lithium transport through the pure indium is slow. Since indium and indium-lithium electrodes are commonly used as counter/reference electrodes in ASSB lab-cells for cathodes investigations, we evaluate the practical relevance of our results: (i) no homogeneous lithium distribution within the InLi electrode (nominal composition $\text{In}_{0.76}\text{Li}_{0.24}$) could be detected after 34 days of OCV; instead our measurements indicate two distinct phases, i.e., an InLi phase with a 1:1 stoichiometry (In_1Li_1) and a solid solution phase of ~ 1 at% Li dissolved in indium ($\text{In}(\delta\text{Li})$); (ii) attaching a piece of lithium on the backside of an indium foil provides a stable reference electrode potential of 0.62 V vs. Li^+/Li , however, the large lithium reservoir contained in the indium-lithium electrode configuration is not electrochemically accessible at practically relevant current densities; and (iii) for experiments that require a reservoir of cyclable lithium, it is mandatory to use the In_1Li_1 phase at the electrochemically active interface towards the separator; experimentally, this configuration is best achieved by an *ex situ* preparation of the indium-lithium electrode prior to cell assembly.

Author contributions

C.S. and C.F.S. developed the three-electrode design in order to implement the gold wire into the cell. C.S. performed all the experiments and entirely analyzed the data. The data were discussed by C.S., R.S., and H.A.G. The manuscript was written by C.S. and edited by H.A.G.



A Micro-Reference Electrode for Electrode-Resolved Impedance and Potential Measurements in All-Solid-State Battery Pouch Cells and Its Application to the Study of Indium-Lithium Anodes

Christian Sedlmeier,^{1,2,z}  Robin Schuster,^{1,2} Carina Schramm,^{1,*}  and Hubert A. Gasteiger^{1,**} 

¹Chair for Technical Electrochemistry, Department of Chemistry and Catalysis Research Center, Technische Universität München, Lichtenbergstraße 4, D-85748 Garching, Germany

²TUMint-Energy Research GmbH, Lichtenbergstraße 4, D-85748 Garching, Germany

Impedance measurements are a powerful tool to investigate interfaces in lithium-ion batteries (LIBs). In order to deconvolute the anode and cathode contributions to the cell impedance, a reference electrode (RE) is required. However, there are only very few reports on the use of a three-electrode setup with an RE for all-solid-state batteries (ASSBs), which is due to the complexity of integrating an RE with a suitable geometry into the typical ASSB test cells that are based on a compressed electrolyte pellet. In this study, we present a straightforward approach to implement a micro-reference electrode (μ -RE) for electrode-resolved impedance and potential measurements into ASSB pouch cells. The μ -RE consists of an insulated $\sim 64 \mu\text{m}$ diameter gold wire that is sandwiched between two $\text{Li}_6\text{PS}_5\text{Cl}$ /polymer separator sheets and activated by in situ electrochemical lithiation. Using this μ -RE, we investigate the electrode potential and the accessibility of cyclable lithium at the separator interface of indium-lithium anodes, which are prepared by stacking lithium and indium foils with a molar excess of indium. We compare two different cell assembly configurations, with the separator faced by either (i) the formerly In-side or (ii) the formerly Li-side, showing that only the latter case provides a reservoir of cyclable lithium.

© 2023 The Author(s). Published on behalf of The Electrochemical Society by IOP Publishing Limited. This is an open access article distributed under the terms of the Creative Commons Attribution 4.0 License (CC BY, <http://creativecommons.org/licenses/by/4.0/>), which permits unrestricted reuse of the work in any medium, provided the original work is properly cited. [DOI: 10.1149/1945-7111/acc699]



Manuscript submitted January 31, 2023; revised manuscript received March 20, 2023. Published March 30, 2023.

The properties of lithium-ion battery (LIB) electrodes and the mechanisms that lead to their long-term degradation are often studied by means of electrochemical impedance spectroscopy (EIS),^{1–4} as it allows for the deconvolution of kinetic and transport resistances.^{5,6} However, the analysis of the impedance spectra obtained in a conventional two-electrode configuration can often be ambiguous, as they give only the sum of both electrode impedances, so that the properties and/or the degradation of either cathode or anode cannot be deconvoluted. For this reason, research efforts in the field of LIBs based on liquid electrolytes aimed at developing methods to acquire the impedance spectra of individual electrodes, e.g., by the use of symmetric cells or of micro-reference electrodes (μ -REs).^{7–11} In contrast to LIB cells with liquid electrolyte, for which cycled cells can easily be disassembled to harvest the electrodes and to reassemble them as symmetric cells (with only anodes or cathodes), this method is practically not feasible for all-solid-state batteries (ASSBs), as the high compression required during cell assembly and cell testing does generally not permit a subsequent retrieval of the individual electrodes. Hence, a three-electrode setup with a reference electrode (RE) has to be used whenever the impedance of either one of the individual electrodes in a cell is to be investigated.

In the research field of sulfidic ASSBs, only very few reports have been published with cells featuring a three-electrode configuration, most of which use the RE primarily to control the electrode potentials.^{12–15} Only a few studies report EIS spectra that make use of RE in a three-electrode configuration, e.g., by using a circular indium-lithium RE that is located around the outer perimeter of a solid electrolyte (SE) separator pellet,¹⁶ a gold-plated tungsten wire embedded in an SE pellet (representing a pseudo-RE for EIS measurements),¹⁷ or an LTO-coated Ni mesh embedded into an SE pellet.¹⁸ The small number of reports that demonstrate EIS spectra of individual electrodes in three-electrode ASSB cells likely reflects the experimental difficulties of integrating a RE into a pellet-type cell that is typically contained within a rigid cylinder. At the same time,

it is crucial to fulfill certain requirements regarding the position and shape of the RE to obtain artifact-free impedance spectra.^{19–24}

Herein, we report on a μ -RE design for an ASSB pouch cell, which is based on our previous approach developed for liquid electrolyte LIBs.¹¹ The μ -RE is made from a $\sim 64 \mu\text{m}$ diameter insulated gold wire ($\sim 7 \mu\text{m}$ thick insulation around a $\sim 50 \mu\text{m}$ diameter gold wire) from whose tip the insulation is removed and that is placed between two SE/polymer composite based separator sheets; subsequently, the de-insulated part of the gold wire is electrochemically lithiated from one of the two electrodes, forming a lithium-gold alloy with a defined potential. Based on our previous work, we will refer to this kind of μ -RE as gold wire reference electrode (GWRE). Its mechanical integration into the here used pouch cell configuration is straightforward, as the gold wire is placed between two equally thick SE/polymer separator sheets, which guarantees a centered position midway between working (WE) and counter electrode (CE). Moreover, the unconstrained geometry of a pouch cell at the edges of the separator allows for a simple electrical contacting of the μ -RE, which is much more straightforward than for a SE pellet-type cell configuration that is typically constrained within a closed cylinder.

To demonstrate the here developed μ -RE concept, we use the GWRE to study the characteristics and the impedance of indium-lithium (InLi) electrodes assembled in ASSB battery cells in two different configurations. Indium-lithium alloy electrodes are commonly used as CE in ASSB laboratory test cells, as less degradation at the interface between a sulfidic SE separator and an InLi CE compared to a metallic lithium CE is expected due to the higher potential of indium-lithium compared to pure lithium.²⁵ Furthermore, the indium-lithium alloy has a constant potential plateau of $\sim 0.62 \text{ V vs Li}^+/\text{Li}$ over a wide compositional range, namely from a very low lithium content (near $\sim 1 \text{ at}\%$) up to close to $\sim 50 \text{ mol}\%$ Li (i.e., In_1Li_1), indicating the formation of a two-phase region (In and In_1Li_1) and providing a well-defined reference potential.^{26–28} Throughout the literature, there are different ways to prepare indium-lithium CE and to implement them into an ASSB cell. The most simple way is to use a pure indium foil with a capacity high enough to accommodate the entire lithium from a cathode electrode (e.g., based on NCM or LFP cathode active materials),^{29,30} whereby an indium-lithium alloy is formed in situ by

*Electrochemical Society Student Member.

**Electrochemical Society Fellow.

^zE-mail: c.sedlmeier@tum.de

electrochemical lithiation upon the initial charging of the cell (i.e., upon the initial delithiation of the cathode active material). In this case, the indium CE very quickly develops a stable open circuit voltage (OCV) of ~ 0.62 V vs Li^+/Li (for x between ~ 0.01 and ~ 1.0 in In_1Li_x ²⁸), but does not provide any extra lithium reservoir that could compensate for any lithium inventory losses during cycling (e.g., caused by the formation of a solid electrolyte interphase (SEI) at the CE). An option to attain an indium-based CE with an additional lithium reservoir is to chemically prelithiate the indium to form an indium-lithium alloy prior to cell assembly. For pellet-type ASSB cells, this is typically realized by first pressing an indium foil onto the pre-pressed SE pellet-type separator and then attaching a small piece of lithium onto the back-side of the indium.^{18,28,31}

Thereby, the molar fraction of lithium must not exceed ~ 47 at% to stay in the two-phase region that extends between ~ 1 and ~ 50 at% Li and that has a stable OCV of 0.62 V vs Li^+/Li .^{26–28,32} An alternative to stacking indium and lithium foils to prepare an indium-lithium CE is the milling of indium and lithium powders³³ or the melting of indium and lithium metal chunks at 700 °C,³⁴ both leading to the formation of an indium-lithium alloy. Recently, also composite electrodes composed of a mixture of indium-lithium particles with a nominal In:Li molar ratio of 1:2 (we will refer to this based on its nominal composition as $\text{In}_1\text{Li}_{0.5}$, even though it does not necessarily form a single phase) and of solid electrolyte particles ($\text{In}_1\text{Li}_{0.5}/\text{SE}$) have been reported,^{13,16} whereby lithium was enfolded inside an indium foil to form a brittle $\text{In}_1\text{Li}_{0.5}$ mixture, which in a second step was ground to fine particles and mixed with a sulfidic solid electrolyte. The increased electrochemically active surface area is supposed to prevent lithium diffusion limitations compared to pure indium-lithium anodes without additional SE.¹³

Considering the above options for preparing an indium-lithium alloy CE for use in ASSB pouch cells with SE/polymer composite based separator sheets, the approach of stacking indium and lithium foils has proven to be practically most feasible. The alloy composition that is best suited to obtain a well-defined OCV that is stable over a wide range of lithium content should be within the two-phase region up to 50 at% Li, as was used in several previous studies (22 at%,³¹ 33 at%,¹³ 44 at%²⁸). In this case, the indium-lithium electrode should consist of a (nearly) pure indium phase and an indium-lithium phase with a stoichiometry of close to “ In_1Li_1 ,” as the average molar fraction of indium is >50 at%. Since in the typical assembly procedure the lithium foil is attached to the backside of the indium foil that in turn is in direct contact with the solid electrolyte separator, the lithium is initially not present at the indium/separator interface; however, one might expect that lithium will diffuse towards the indium/separator interface due to its mobility in the alloy. On the other hand, if below 50 at% lithium a true two-phase solution of pure indium and In_1Li_1 phase were to be formed, one would not expect that a homogenous lithium distribution would be obtained, as in this case pure indium would coexist with a In_1Li_1 phase, so that even in equilibrium a pure indium phase would persist near the indium/separator interphase. For the actual case where a solid solution of small amounts of lithium in indium (~ 1.0 – 1.5 at%^{32,35}) is in equilibrium with an In_1Li_1 phase, a small concentration of lithium (viz., ~ 1.0 – 1.5 at%) would be expected at the interface to the separator at equilibrium. While this would still yield an OCV of ~ 0.62 V vs Li^+/Li , it would not provide a significant lithium inventory that is accessible during cell cycling studies.

In order to investigate the lithium distribution in indium-lithium electrodes more in detail, we prepared ASSB pouch cells with indium-lithium electrodes, prepared by stacking and subsequent compressing indium and lithium metal foils. In one case, we have used the conventional configuration with the lithium attached to the back-side of the indium foil that in turn is in contact with the SE separator, so that the lithium at least initially is not in contact with the SE separator. In the other case, we have flipped the indium-lithium electrode so that the side where the lithium was pressed onto the indium foil faces the SE separator. Implementing a GWRE into

the cells, we perform electrode-resolved electrochemical impedance spectroscopy and galvanostatic pulsing to investigate the availability of lithium of at the separator interface, i.e., whether the available lithium inventory can be accessed electrochemically. As already suggested by the above discussion, we will show that the two different indium-lithium configurations in the cell assembly yield the same OCV but differ in the lithium inventory that they can provide, i.e., only one of the two configurations can be used to mitigate lithium inventory loss (analogous to a lithium metal CE in a liquid electrolyte-based LIB cell).

Experimental

Materials.—The handling of all materials and all processing steps were conducted inside an Ar filled glovebox ($\text{O}_2 < 0.1$ ppm, $\text{H}_2\text{O} < 1$ ppm, MBraun, Germany). Non-moisture sensitive materials and cell parts, stored at ambient atmosphere, were dried at 70 °C under dynamic vacuum in a glass oven (Büchi B-585, Büchi, Switzerland) for at least 16 h prior to transfer into the glovebox and subsequent usage. The solid electrolyte $\text{Li}_6\text{PS}_5\text{Cl}$ (LPSCI) was purchased from Solid Ionics (China) and used without further purification. Hydrogenated nitrile butadiene rubber (HNBR, 5.5×10^5 g · mol⁻¹, 17 wt% acetonitrile, $< 1\%$ residual double bonds) was provided by Arlanxeo (Netherlands). Lithium foil (battery grade, 0.075 mm thickness) was purchased from Chemical Foote Corp. (USA) and indium foil (99.99% purity, 0.28 mm thickness) from ChemPur (Germany). The insulated gold wire (50 μm diameter with a 7 μm thick polyimide insulation) was purchased from Goodfellow Cambridge Ltd (UK).

Separator and electrode and preparation.—LPSCI/HNBR-composite separator sheets with 5 wt-% HNBR were prepared by a slurry-based process in toluene, as described in our previous work.³⁶ Pure indium and lithium electrodes were punched using a square punch (Spahn GmbH & Co. KG, Germany) with a side length of 20 mm.

Electrodes made from indium-lithium alloy were prepared by stacking an indium foil (cut to 22×22 mm, 0.28 mm thickness) and lithium foil (cut to 19×19 mm, 0.075 mm thickness) on top of each other and compressing the stack between two polypropylene sheets (0.09 mm thickness, Leitz, Germany) in a homemade compression tool, using a manual hydraulic press (Atlas 15 T, Specac, UK) at a tonnage of three metric tons (~ 60 MPa) for 5 min. Upon compression, both metal foils would merge with each other and expand ~ 1 mm in each direction. Subsequently 20×20 mm electrodes (4.0 cm²) were punched out, yielding indium-lithium electrodes with an average Li content of ~ 24 at% (corresponding to a nominal composition roughly $\text{In}_1\text{Li}_{0.32}$), calculated from the respective density ρ and molecular mass M of indium ($\rho(\text{In}) = 7.31$ g cm⁻³; $M(\text{In}) = 114.82$ g mol⁻¹) and lithium ($\rho(\text{Li}) = 0.534$ g cm⁻³; $M(\text{Li}) = 6.94$ g mol⁻¹) and assuming a homogenous areal distribution of indium and lithium upon compression. In this case, considering that the final area of the electrode made from the merged and punched foils is 4.0 cm² (i.e., 20×20 mm), the indium-lithium delithiation capacity would be ~ 14 mAh cm⁻² (slightly higher for a not perfectly homogeneous areal distribution); its lithiation capacity until the complete conversion of the roughly $\text{In}_1\text{Li}_{0.32}$ phase to the In_1Li_1 average composition would be roughly ~ 30 mAh cm⁻² (slightly lower for a not perfectly homogeneous areal distribution). Note that the thus prepared indium-lithium electrodes in principle feature two different faces as depicted in Figs. 1a–1c: an optical image of the side where the lithium foil was pressed onto the indium foil is shown in Fig. 1b and will further on referred to as “InLi-(Li),” whereas Fig. 1c depicts the optical image of the opposite side of the electrode, which further on is referred to as “InLi-(In).” The difference in their optical appearance after preparation already indicates that they are not identical, i.e., that they do not have the same composition; as will be shown later, they also do not have the same electrochemical properties.

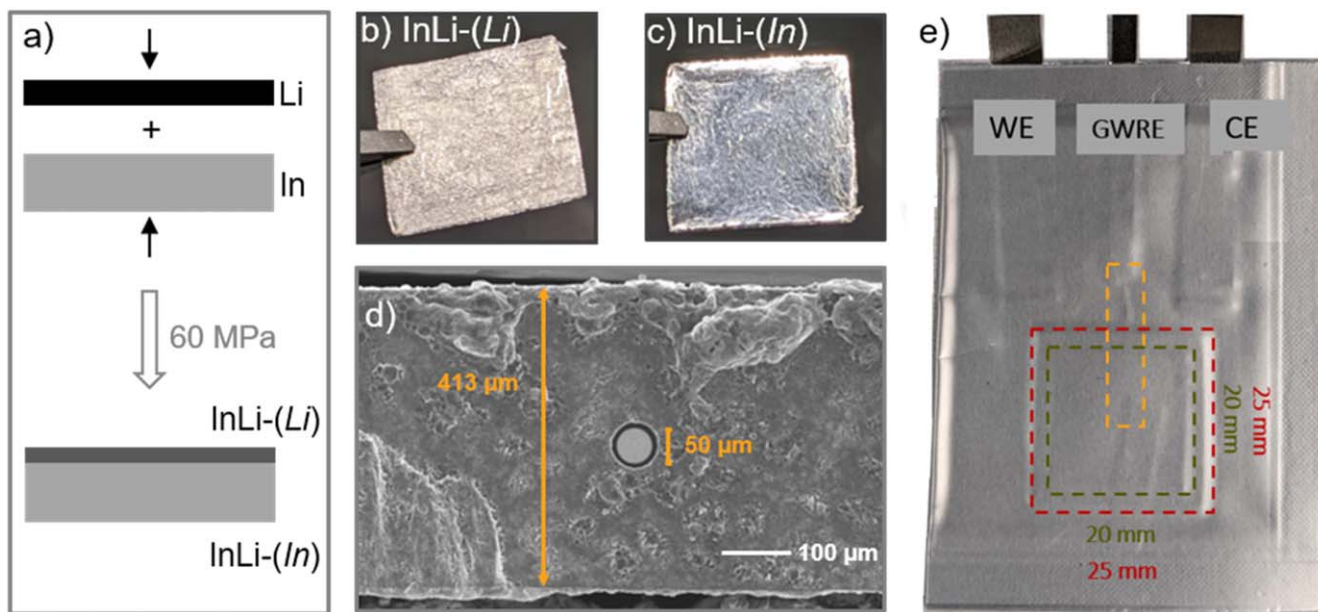


Figure 1. (a) Schematic illustration for the preparation of an InLi alloy by stacking and subsequent compression of Li and In foils, resulting in an average composition of $\text{In}_{1.1}\text{Li}_{0.32}$. The resulting electrode has two optically different faces: (b) the side, where the lithium foil was pressed onto the indium foil, further on referred to as “InLi-(Li)”; (c) the opposite side, further on referred to as “InLi-(In).” (d) SEM image of an ion-milled cross-section of the $50\ \mu\text{m}$ diameter gold wire with a $7\ \mu\text{m}$ polyimide insulation, embedded in an LPSCI/HNBR separator. The Au wire was sandwiched between two porous LPSCI/HNBR sheets (initial thickness $\sim 380\ \mu\text{m}$ each, initial porosity $\sim 51\%$) and the entire stack was then compressed at $\sim 70\ \text{MPa}$, resulting in an overall separator thickness of $413\ \mu\text{m}$ and a residual porosity of $\sim 15\%$. (e) Picture of an ASSB pouch cell in a three-electrode configuration, featuring a working electrode (WE), a gold wire reference electrode (GWRE) and a counter electrode (CE). The dimension of the separator (red; $25 \times 25\ \text{mm}$) and CE (green; $20 \times 20\ \text{mm}$) are marked by dashed lines (the WE electrode has the same dimensions and the same in-plane position as the CE). The position of the gold wire is indicated by the golden dashed line.

For the micro-reference electrode, a roughly 3 cm long piece of Au wire ($50\ \mu\text{m}$ core diameter) with a $7\ \mu\text{m}$ thick polyimide insulation was used, of which the insulation at one end was removed by hand with a scalpel at a length of $\sim 0.5\ \text{mm}$. The other end of the wire was attached to a nickel tab (PI-KEM, UK) using an ultrasonic welder (type Omega from Ultrasonic-weldsolution, Germany). During the welding process, the insulating polyimide cover is broken up, ensuring a good electrical connection between the Au wire and the nickel tab. Next, the gold wire was sandwiched between two LPSCI/HNBR-composite separator sheets ($25 \times 25\ \text{mm}$, $\sim 370\ \mu\text{m}$ initial thickness each, $\sim 51\%$ initial porosity) in such a way that the de-insulated part of the gold wire is in the center of the separator. Subsequently, the sandwich was compressed in the hydraulic press inside the glove box at a tonnage of 4.5 metric tons (corresponding to $\sim 70\ \text{MPa}$), firmly embedding the Au wire inside the separator. The final LPSCI/HNBR separator sheets with the embedded GWRE had a thickness of $\sim 413\ \mu\text{m}$ and a porosity of $\sim 15\%$ and Fig. 1d shows a representative SEM image of an ion-milled cross-section. In this context it is important to mention that for the LiLi cell, four separator sheets were used instead of two as it is the case for all the other cells. This was done in order to exclude Li creep upon cell compression.

Cell design and assembly.—Pouch cells were assembled in a three-electrode setup, featuring a working electrode (WE), a RE and a CE. The compressed separator containing the RE was placed in a pouch bag (DNP, Japan). To each side of the separator, the WE (Li, In, or InLi-(In)) and the CE (Li or InLi-(Li)) were attached. Onto each electrode, a copper foil ($11\ \mu\text{m}$ thick; GELON, China) serving as current collector was placed, to which a nickel tab with an adhesive polymer tap (PI-KEM, UK) was connected. The pouch bag was sealed at a pressure of 25 mbar using a vacuum sealing device (MULTIVAC, Germany). Figure 1e shows a photograph of a pouch cell with the indicated dimensions and position of the separator, the electrodes and the gold wire RE. For electrochemical testing, the

pouch cell was taken out of the glovebox and placed between two stainless steel plates (upper plate: 10 mm thickness, bottom plate: 15 mm thickness), which are pressed together by several springs ($224\ \text{N mm}^{-1}$; LHL 1000D 01, Lee Spring, Germany). The springs are oriented in a symmetric configuration, such that the electrode stack is located in the center of force. Additionally, one piece of 2 mm thick, foamed polytetrafluoroethylene (PTFE) (Garlock®, ENPRO Industries Inc., USA) on each side of the pouch cell was used to ensure a homogeneous pressure distribution. The compression of the springs can be adjusted via a compression screw and a spacer. In case of LiLi cells, two springs were used, setting a cell pressure of 3 MPa, whereas six springs were used for InLi-(In)/InLi-(Li) and InLi-(In)/InLi-(Li) cells, setting the overall cell pressure to 20 MPa. Cells with the two latter electrode configurations are schematically depicted in Figs. 3a & 3b for better visualization of the electrode configurations. The lower cell pressure of 3 MPa in case of the LiLi cell is used to avoid lithium creep.

Galvanostatic pulsing and impedance experiments.—Electrochemical testing was performed inside a temperature chamber (KB53, BINDER, Germany) at $25\ ^\circ\text{C}$. The gold wire RE was lithiated by applying a current of 500 nA for 6 h between the CE (Li or InLi-(Li)) using a multi-channel potentiostat (VMP-3, BioLogic, France); this corresponds to a total charge of $3\ \mu\text{Ah}$, which is negligible compared to the capacity of typical anode or cathode electrodes (on the order of several mAh). Cell cycling was performed at a current density of $0.2\ \text{mA cm}^{-2}$ unless described differently. Potentiostatic electrochemical impedance spectroscopy (PEIS) in half-cell configuration (i.e., in a three-electrode configuration) controlled by the lithiated GWRE was performed on a VMP-3 in a frequency range from 100 kHz–50 mHz recording 8 data points per decade using a potential amplitude of $\pm 10\ \text{mV}$. Full-cell impedance spectra (i.e., in a two-electrode configuration) in a frequency range from 7 MHz–50 mHz were recorded on a VSP-300 or VMP-300 multi-channel potentiostat (BioLogic, France).

During OCV rest phases for one or four weeks, one data point every 20 min was taken. Data were treated using the software EC-Lab (V. 11.43).

Cross-section polishing.—Cross-sections were prepared by argon ion beam polishing, using a cross-section polisher of the type IB-19530CP (JEOL, Japan). A $\sim 5 \times 5$ mm piece of the separator sheet/Au wire/separator sheet sandwich was cut out, fixed with adhesive copper tape (PPI Adhesive Products, Ireland) in the sample holder, and then inertly transferred into the device using an inert transfer shuttle (LB-11620TVCA, JEOL Japan) under argon atmosphere. The sample was polished at -80 °C first for 4 h at 6 kV acceleration voltage, followed by a second step for 2 h at 4 kV.

Scanning Electron Microscopy (SEM).—The scanning electron microscopy (SEM) images were acquired using a JSM-IT200 InTouchScope™ (JEOL) field emission SEM at 15 kV with a multi-segment secondary electron detector. The samples were prepared inside an argon-filled glovebox and transferred under inert atmosphere to the SEM device. While the mounting of the sample in the SEM chamber was done under ambient atmosphere, the exposure time of the LPSCI/HNBR separator to ambient lab atmosphere was < 30 s, so that the degradation of the sulfidic solid electrolyte was minimal. The cross-sectional SEM image of the ion-milled separator is shown in Fig. 1d.

Results and Discussion

GWRE potential stability & validation of its suitability for impedance measurements.—As a first step, the lithiation of the gold wire and its potential after lithiation were investigated using a symmetric LiLi cell, where one electrode will further on be denoted as WE and the other electrode as CE. The gold wire was lithiated using a current of 500 nA for 6 h between the Li CE and the GWRE. This adapted lithiation procedure based on Solchenbach et al. accounts for the ~ 40 fold higher surface area of the gold wire in contact with the electrolyte when used for ASSB cells, where the insulation is removed over a wire length of ~ 0.5 mm.¹¹ For liquid electrolyte-based LIBs, the wire is cut exposing a very small surface area of $\sim 2 \times 10^{-3}$ mm² as only the cross-section of the gold wire is in contact with the electrolyte. Trying this in our configuration did not provide good contact, therefore we cylindrically deisolated the wire at a length of ~ 0.5 mm, which offers a much higher contactable area of ~ 0.08 mm². Therefore, we adapted the lithiation procedure accordingly. However, most of the wire is still insulated. The light blue curve in Fig. 2a displays the potential of the GWRE versus the Li CE during the lithiation step (between 0 – 6 h). Initially, the potential drops to -0.8 V and then stays constant at roughly -5 mV during the lithiation step. The initial potential drop can be associated to the reduction of surface oxides and/or the nucleation of the lithium-gold-phase.^{37,38} During the OCV step after the 6 h lithiation, the potential first stays constant at ~ 0.25 V for roughly 30 min (hour 6.0-6.5 in Fig. 2a), followed by a gradual relaxation to ~ 0.31 V vs Li⁺/Li. The first plateau at lower potentials can be attributed to a higher lithiated Li_xAu₁ phase with $x \sim 1.3$, which is formed due to the relatively fast lithiation of the Au wire. With the gradual radial diffusion of the lithium into the core of the gold wire, a homogeneous lithium-gold alloy phase is established, with an OCV of ~ 0.31 V vs Li⁺/Li that is characteristic for Li_xAu alloys with $0 < x < 1.2$ and that is also in agreement with the reported lithiated GWRE potential in liquid electrolyte cells.^{11,38} Figure 2b shows the potentials of the lithium working and CE recorded via the lithiated GWRE. Note that the values are displayed as measured, meaning via the lithiated GWRE, which has a potential of 0.31 V vs Li⁺/Li. Both lithium electrodes show the expected potential of -0.31 V vs the lithiated GWRE, which is stable over the course of 2 h and thus proves that the lithiated GWRE is suitable for half-cell potential measurement; its longer-term stability will be examined more in detail later.

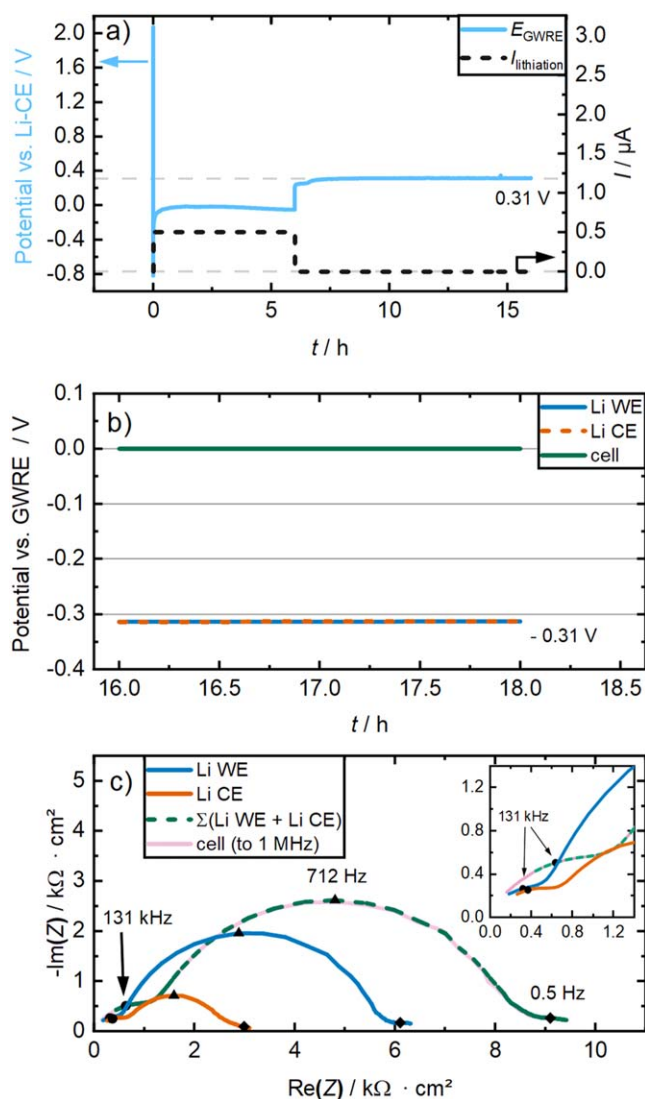


Figure 2. (a) Potential of the gold wire vs the Li counter electrode (CE) in a LiLi cell (3 MPa cell pressure) during lithiation for 6 h at a current of 500 nA via the Li CE, followed by a 10 h OCV period (light blue line) as well as the corresponding current profile (dashed black line). The gray dashed lines are a guide-to-the-eye. (b) Potentials of the Li CE (orange) and the Li WE (blue) recorded via the lithiated GWRE; the corresponding LiLi cell potential is drawn in green. (c) Nyquist plot of the individual electrode impedances of the Li WE (blue) and the Li CE (orange) recorded at OCV using the GWRE (lithiated via the Li CE), in a frequency range from 200 kHz–50 mHz with a 10 mV AC perturbation; the green dashed line represents the resulting sum of WE and CE impedances. The cell impedance (pink line) recorded between the Li WE and the Li CE from 1 MHz to 50 mHz at 10 mV AC perturbation. The apex frequencies of the three semi-circles in the electrode and cell impedances are indicated by the circles at 131 kHz, the triangles at 712 Hz, and the diamonds at 0.5 Hz.

In order to evaluate whether the GWRE is a suitable tool to investigate the individual electrode impedances in a sulfidic ASSB cell, we measured the individual electrode and the cell impedances at OCV for a symmetric LiLi cell with a lithiated GWRE. As displayed in Fig. 2c, the Nyquist plots of the impedances of both the Li WE (blue) and the Li CE (orange) recorded via the lithiated GWRE feature three semi-circles, two smaller ones at high and low frequency and a dominant one in a mid-frequency range; the same can be observed for the cell impedance (purple; recorded without the using the GWRE, which can be acquired to frequencies up to 1 MHz without artifacts¹¹). The semi-circles at high frequencies ($f_{\text{apex}} = 131$ kHz, marked by black dots) can be ascribed to the separator

resistance.³⁶ The latter can be more clearly seen in the cell impedance (purple line; see inset), indicating a separator resistance of $\sim 960 \Omega \text{ cm}^2$; considering the separator thickness of $\sim 760 \mu\text{m}$ (note that a ~ 2 -fold thicker separator was used for the LiLi cell compared to that shown in Fig. 1d), leads to a separator conductivity of $\sim 0.08 \text{ mS cm}^{-1}$, which is in good agreement with our previous data for a separator porosity of $\sim 15\%$ and a stack pressure of 3 MPa.³⁶ The resistance contributions of the separator to the Li WE and the Li CE are $464 \Omega \text{ cm}^2$ and $492 \Omega \text{ cm}^2$, respectively, indicating that the GWRE is located midway between the two electrodes, which is an important prerequisite for artifact-free impedance measurements using a $\mu\mu\text{-RE}$.^{22,39}

For the individual electrode impedances, the large semi-circle at mid-frequencies (23 kHz–4 Hz; $f_{\text{apex}} = 712 \text{ Hz}$, marked by the black triangles) can be assigned to the interface resistance of the separator and the Li metal electrodes, which includes the SEI formed on the lithium metal and the physical contact between lithium and the separator, whereas the low-frequency semi-circles (4 Hz–50 mHz; $f_{\text{apex}} = 0.5 \text{ Hz}$, marked by black diamonds) represent the charge-transfer resistance.^{4,16,40–43} Note that the mid-frequency semi-circle of the Li CE, which was used to lithiate the GWRE, is significantly smaller than that of the Li WE. A similar behavior was observed for the use of the GWRE in liquid-electrolyte cells, where it was hypothesized that the stripping of lithium from the lithium electrode used for lithiation of the GWRE would cause a roughening of the Li surface, meaning a higher surface area and hence a smaller impedance.¹¹ Additionally, a slight unintentional misalignment of WE and CE during assembly is reported to cause a relative shift in the quantitative scaling factors of the individual electrode impedance responses, which cannot be excluded with certainty, as the cell was assembled by hand without the use of a template.^{24,39} However, since the separator contributions are more or less equal, the roughening is expected to be the dominant reason for the difference. Comparing the sum of the Li WE and the Li CE impedances (green dashed line) with the cell impedance recorded without the use of the GWRE up to 1 MHz, no significant difference can be discerned. Thus, we believe that the GWRE is a suitable tool for impedance measurements of individual electrodes.

Experimental design to evaluate the properties of InLi-(In) vs InLi-(Li) electrodes.—The focus of the following section is to systematically elaborate the differences between the InLi-(In) and the InLi-(Li) configuration for the here prepared indium-lithium electrodes (Figs. 1a–1c). By means of potential measurements, PEIS, and galvanostatic pulsing experiments, both electrode configurations are examined in order to determine whether their Li reservoir is electrochemically accessible and can be used to lithiate another electrode or to provide an additional lithium inventory, as one would expect for a proper indium-lithium CE. For comparison, the same tests are performed with a pure indium electrode in combination with an InLi-(Li) electrode. Therefore, we designed a sequence of consecutive experiments (listed in Fig. 3c) and conducted them with InLi-(In)|InLi-(Li) (WE|CE; see Fig. 3a) and In|InLi-(Li) (WE|CE; see Fig. 3b) cells, each featuring a GWRE. The experiments were performed with three cells of each type; as each cell type yielded identical results, only one representative data set is shown for each cell type.

Directly after cell assembly, the cells were held at OCV for 6 days (step 1 in Fig. 3c), monitoring the OCV of the cell in order to understand whether the potential of the as-assembled electrodes changes over time under the compressive force in the cell ($\sim 20 \text{ MPa}$). The duration of step 1 was chosen to be several days, as it takes at least 8 h before potentials can be recorded via the GWRE (based on the 6 h lithiation procedure and the $\sim 2 \text{ h}$ required to reach a stable potential, see Fig. 2a); note that the time from cell assembly and mounting into the cell holder to starting the OCV monitoring did not exceed 1 h. Subsequently, the GWRE was lithiated via the CE (step 2) as described above. Afterwards, PEIS measurements were performed to acquire the impedance of the WE

and of the CE using the GWRE as well as the cell impedance (step 3). This was followed by holding the cells at OCV for 4 weeks (step 4), monitoring the WE and CE potentials via the lithiated GWRE, followed by another PEIS measurement (step 5). Steps 3–5 serve to track any changes of the indium-lithium electrodes, which could be caused by lithium diffusion within the indium-lithium electrodes.

Following these initial experiments where the WE and CE electrode were always at OCV (except for the small currents applied to the InLi-(Li) CE to lithiate the GWRE), a series of lithiation and delithiation steps of the WE (either InLi-(In) or In, see Figs. 3a or 3b, respectively) were conducted. First, a delithiation current of 0.2 mA cm^{-2} was applied to the WE for 15 min or until its potential would rise to 2.0–2.2 V vs Li^+/Li (step 6): in case of the InLi-(In) WE (see Fig. 3a), this is meant to determine whether the lithium applied at the backside of the InLi-(In) WE during fabrication (see Figs. 1a and 1c) can diffuse through the electrode towards the interface to the separator; in case of an indium WE (see Fig. 3b), no current is expected. Subsequently, the current was reversed (step 7) and the WE was lithiated at 0.2 mA cm^{-2} via the InLi-(Li) CE for 15 min. This was followed by another delithiation of the WE at 0.2 mA cm^{-2} , but this time for a twice as long delithiation time of 30 min or until the WE potential would rise to 2.0–2.2 V vs Li^+/Li (step 9): in case of the InLi-(In) WE, the twice as long delithiation time compared to the lithiation time in step 7 was chosen to investigate whether only the charge that was put into the InLi-(In) WE during step 7 can be removed or whether more charge can be retrieved, namely from the nominally very large Li reservoir of the indium-lithium electrode ($\sim 14 \text{ mAh cm}^{-2}$, see experimental section); in case of the In WE, the delithiation time before the potential cut-off is reached is expected to be $\leq 15 \text{ min}$ (depending on the coulombic efficiency).

Several PEIS measurements (steps 8 and 10) were performed between the lithiation and delithiation steps, as changes in the low-frequency region of the impedance response of the electrodes upon lithiation and delithiation are expected.¹⁶ Lastly, the WE was lithiated at 0.2 mA cm^{-2} for 15 h from the InLi-(Li) CE (step 11), demonstrating that an InLi-(Li) electrode is capable to provide a lithiation charge of at least 3.0 mAh cm^{-2} , which is a typical capacity for an NCM-based cathode; this shows that an InLi-(Li) electrode has a sufficiently large and accessible lithium inventory to serve as a CE in a true half-cell configuration, i.e., that it can compensate cyclable lithium losses of cathode or anode electrodes that are being investigated (analogous to a lithium CE in half-cells with liquid electrolyte).

OCV and accessible lithium inventory of InLi-(In) vs InLi-(Li) electrodes.—The initial OCV monitoring in the beginning of the test sequence (step 1) shows a cell voltage of $E_{\text{cell}} \sim 0.35 \text{ V}$ for the InLi-(In)|InLi-(Li) cell (see Fig. 4a, light green), which relaxes to $\sim 20 \text{ mV}$ after one day and levels out at $\sim 8 \text{ mV}$ after 3 days. This indicates that both electrodes basically have the same potential after several days, which might reflect the time required for lithium diffusion across the indium segment of the InLi-(In) WE or the time to build a stable SEI on both electrodes. A similarly long OCV transient can be observed for the In|InLi-(Li) cell (see Fig. 4b, light green), with an initial cell potential of $E_{\text{cell}} \sim 1.20 \text{ V}$ that rises within one day to $\sim 1.40 \text{ V}$ and after six days features a value of 1.45 V. Assuming no chemical change in the indium WE, the change in cell voltage would have to be attributed to the InLi-(In) CE, which then would suggest that it takes roughly one day to fully establish its equilibrium potential.

For the lithiation of the RE (step 2) and the impedance measurements (step 3), the potential monitoring had to be interrupted for roughly 10 h, indicated by the gray box. Potential curves for the lithiation of the RE (step 2) are not discussed in further detail, as they are similar to that in Fig. 2a, (for the interested reader they are shown in Figure A-1 in the Appendix). The impedance spectra in step 3 will be discussed later in the context of Fig. 5. After the GWRE lithiation, the potential monitoring was continued via the

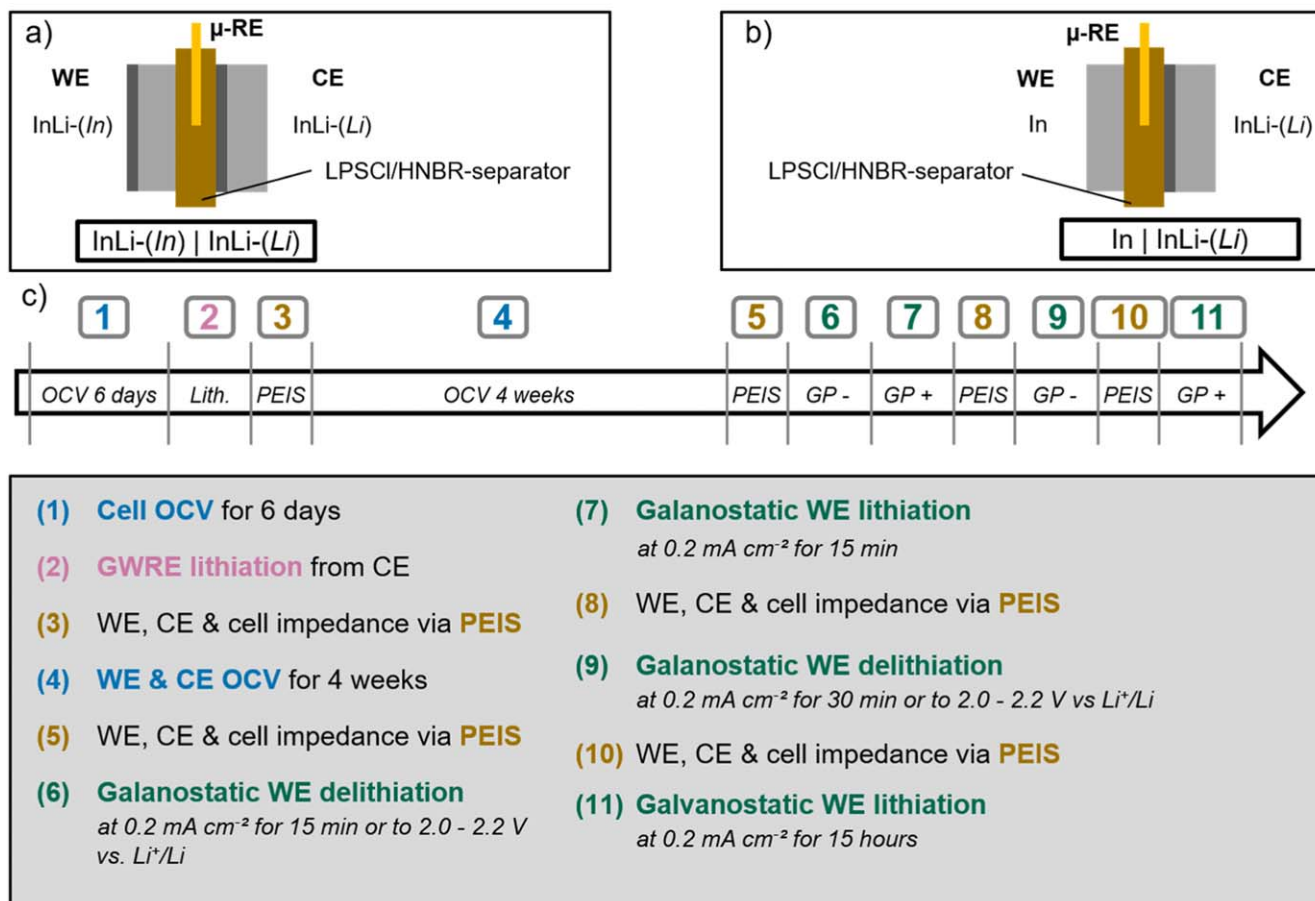


Figure 3. Schematic illustration of the two cell setups used for evaluating InLi electrodes: (a) InLi-(In) WE (see Fig. 1c) paired with an InLi-(Li) CE (see Fig. 1b); (b) In WE paired with an InLi-(Li) CE. Both cell setups use an LPSCI/HNBR-separator and a GWRE. The electrodes are 20×20 mm and the separators are 25×25 mm (thickness $\sim 400 \mu\text{m}$). (c) Experimental design to evaluate the properties of In, InLi-(In) and InLi-(Li) electrodes in the InLi-(In)|InLi-(Li) and In|InLi-(Li) cell configurations shown in a) and b): (1) 6 days of cell OCV monitoring; (2) GWRE lithiation via the InLi-(Li) CE at 500 nA for 6 h; (3) PEIS measurements of the cell impedance (7 MHz–50 mHz, 10 mV AC perturbation) and of the WE and CE impedance using the GWRE (100 kHz–50 mHz, 10 mV AC perturbation); (4) WE and CE OCV monitoring via the lithiated GWRE over 4 weeks; (5) repeated PEIS measurements of cell as well as of WE and CE impedances; (6) galvanostatic delithiation (GP-) of the WE (InLi-(In) or In) at 0.2 mA cm^{-2} for 15 min or until a WE cut-off potential of 2.0-2.2 V vs Li^+/Li is reached; (7) galvanostatic lithiation (GP+) of the WE at 0.2 mA cm^{-2} from the InLi-(Li) CE for 15 min; (8) repeated PEIS measurements of WE and CE impedances; (9) galvanostatic delithiation (GP-) of the WE at 0.2 mA cm^{-2} for 30 min or until a WE cut-off potential of 2.0-2.2 V; (10) repeated PEIS measurements of WE and CE impedances; (11) galvanostatic lithiation (GP+) of the WE at 0.2 mA cm^{-2} from the InLi-(Li) CE for 15 h. Tests were performed with three cells of each type, of which only one data set per cell type is exemplarily shown. For the ease of following the experiments, the numbering and color-coding of the individual steps will be kept throughout the following figures; also, the icons for each cell type will be used in each figure to better illustrate to which cell type the data refer to.

lithiated RE over 4 weeks (step 4), showing that both the InLi-(In) WE (blue) and the InLi-(Li) CE (orange) potentials in the InLi-(In)|InLi-(Li) cell (Fig. 4a) are at 0.62 V vs Li^+/Li (calculated based on a GWRE potential of $+0.31 \text{ V}$ vs Li^+/Li), as reported for an indium-lithium electrode with $<50 \text{ at-}\%$ Li.^{27,28} In the In|InLi-(Li) cell (see Fig. 4b), the potential of the InLi-(Li) CE also is at 0.62 V vs Li^+/Li (orange), whereas the potential of the pure In WE is at $\sim 2.1 \text{ V}$ vs Li^+/Li (blue). Over the course of 28 days, all potentials shift less than 3 mV, demonstrating that the lithiated GWRE is a suitable tool for potential monitoring, even for long-term cycling experiments. In summary, both configurations of the indium-lithium electrode yield a stable and well-defined reference potential of 0.62 V vs Li^+/Li .

The cell impedance of the InLi-(In)|InLi-(Li) cell in Fig. 5a (pink line), which is recorded up to 7 MHz without the use of the RE, has three distinct features, namely a large semi-circle at high frequencies, followed by a smaller semi-circle at mid frequencies and a low-frequency tail, which partially overlaps with the mid-frequency region. The impedance to 7 MHz is performed in order to fully resolve the high-frequency feature, which represents the separator resistance^{29,36} and amounts to $\sim 490 \Omega \text{ cm}^2$ (this is consistent with the $\sim 960 \Omega \text{ cm}^2$ observed in Fig. 2c for the cell with the ~ 2 -fold

thicker separator). The individual electrode impedances obtained with the lithiated GWRE are only possible up to $\sim 100 \text{ kHz}$ (the practical upper frequency limit when using the GWRE¹¹) and are shown for the InLi-(In) WE (blue) and the InLi-(Li) CE (orange); their vector sum is depicted by the dashed green line and overlaps nicely with the cell impedance (pink line), showing that the high-frequency semi-circle can be sufficiently well resolved even up to only 100 kHz, so that changes in the separator resistance or possible overlapping with the mid-frequency feature can be accounted for. Therefore, in the further analysis we have not included the cell impedance up to 7 MHz in each step.

By evaluating the cell impedance of the InLi-(In)|InLi-(Li), our first assumption was that both electrodes would have qualitatively similar impedances, since their potentials are equal at the end of step 1 (see Fig. 4a). At first glance, the mid- and low-frequency features could be easily interpreted as a small charge-transfer resistance (InLi alloy at the separator interface) followed by diffusion tail (lithium diffusion in the InLi alloy), as this shape is typical for lithium ion battery materials.⁴⁴ However, this interpretation of the cell impedance is incorrect, as the electrode-resolved impedances (via the GWRE) reveal that indeed the InLi-(In) WE and the InLi-(Li) CE do

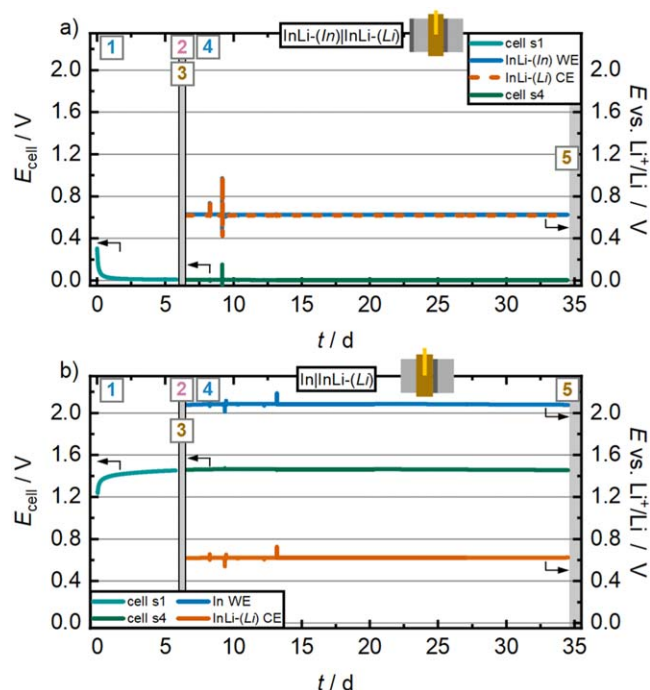


Figure 4. Potential monitoring following the steps outlined in Fig. 3c (marked here in the squares) for the cells with GWRE shown in Figs. 3a and 3b: (a) InLi-(In)InLi-(Li) (WE|CE); b) InInLi-(Li) (WE|CE). *Step 1 (s1):* cell OCV for 6 days prior to lithiation of the GWRE (light green). *Steps 2&3:* lithiation of the WEs via the InLi-(Li) CEs and PEIS measurements (indicated by the gray boxes). *Step 4 (s4):* WE (blue) and CE (orange) potentials measured via the lithiated GWRE over 4 weeks and plotted vs Li^+/Li (right-hand axes, calculated based on a GWRE potential of $+0.31\text{ V}$ vs Li^+/Li); the cell potential, i.e., the sum of WE and CE potentials is plotted in green. The spikes in the WE and CE potentials resulted from an accidental touching of the cables. Note that the time between cell assembly and start of the potential monitoring in step 1 is $<1\text{ h}$. *Step 5:* PEIS measurements (indicated by the gray box on the right) at the end of these potential monitoring experiments.

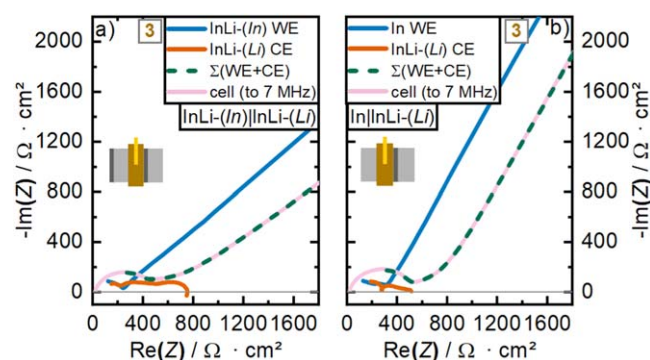


Figure 5. Nyquist plots of the initial PEIS measurements (step 3 in Fig. 3c) for the cells with GWRE shown in Figs. 3a and 3b: (a) InLi-(In)InLi-(Li) (WE|CE); (b) InInLi-(Li) (WE|CE). The impedances of the WEs and of the InLi-(Li) CEs were recorded via the lithiated GWRE (100 kHz–50 mHz with 10 mV AC potential perturbation), and the green dashed line represents their vector sum. The cell impedance spectra (pink) were recorded without the use of the GWRE (7 MHz–50 mHz, 10 mV AC perturbation). The cell and the WE impedances are depicted until 5 Hz.

not have the same impedance response, underlining the importance of electrode-resolved impedance spectroscopy. Looking at the impedance of the InLi-(In) WE (blue), it can be clearly seen that this electrode determines the shape and the magnitude of the cell impedance at low frequencies, whereas, the InLi-(Li) electrode

(orange) features an additional semi-circle at low frequencies and has a substantially lower impedance. The individual contributions to the impedance response of the InLi-(In) and the InLi-(Li) electrodes will be discussed in more detail in the context of Fig. 7. For now, it should only be mentioned that the low-frequency semi-circle of the InLi-(Li) CE electrode (orange) represents the charge-transfer reaction, indicating an electrochemically accessible Li reservoir at the interface of the InLi-(Li) electrode and the separator, while the Warburg-like behavior of the InLi-(In) WE electrode (blue) suggests that there is no charge-transfer reaction taking place, as will be confirmed in the following galvanostatic pulse experiments. In fact, the InLi-(In) impedance is very similar to that of an indium electrode, as shown in Fig. 5b (blue). Note that the half-cell spectra of the InLi-(Li) CE electrodes have low-frequency artifacts (i.e., an inductive loop), which are caused by the fact that the difference of WE and CE impedance becomes very large at low-frequency, as described in the literature.^{39,45} Another possibility for the inductive contribution might be ongoing side reactions which cannot be excluded. However, the qualitative comparison of WE and CE impedances is not affected by this.

To quantify the ability of the InLi-(In) WE to provide lithium to the cell, a first galvanostatic delithiation current of 0.2 mA cm^{-2} was applied for 15 min (step 6, see Fig. 6a), which would amount to a delithiation charge of $50\text{ }\mu\text{Ah cm}^{-2}$ (rather negligible compared to its theoretical delithiation capacity of $\sim 14\text{ mAh cm}^{-2}$). However, the potential of the InLi-(In) reached the set cut-off potential of 2.0 V vs Li^+/Li already after only 9 s (blue line, Fig. 6a) concomitant with the passage of only $0.39 \pm 0.21\text{ }\mu\text{Ah cm}^{-2}$ (mean and standard deviation of all three InLi-(In)InLi-(Li) cells). Thus, the Warburg-like behavior of the InLi-(In) electrode in Fig. 5a indeed reflects the inability of this electrode to provide a significant delithiation current. For the pure indium electrode, shown in Fig. 6b, the cut-off potential of 2.2 V vs Li^+/Li is reached after 3 s (blue line) and the passed charge is also only $0.32 \pm 0.23\text{ }\mu\text{Ah cm}^{-2}$. The tiny amount of passed charge can result from small lithium impurities on the respective WE electrode introduced during cell assembly or from simple capacitive currents (i.e., double-layer charging); in the case of the InLi-(In) electrode, it could also come from the prior formation of an indium-lithium solid solution with a very low lithium content (suggested to be $\sim 1.0\text{--}1.5\text{ at-}\%$ ^{32,35}). Note that for the In electrode, a cut-off potential of 2.2 V vs Li^+/Li was chosen, as the OCP of the indium WE already exceeds 2.0 V vs Li^+/Li ; due to the steep increase of the WE potential during experiment, the difference between the two cut-off criteria of 2.0 or 2.2 V is negligible. Finally, for the InLi-(Li) CEs (orange), the maximum deviation of their potential during the 0.2 mA cm^{-2} step is $\sim 0.1\text{ V}$, which corresponds to the overpotential for lithium alloying into the InLi-(Li) CE.

In the subsequent OCV phase, the electrode potentials relax to their previous values of 0.62 V and 2.1 V vs Li^+/Li for InLi-(In) and In, respectively. In step 7, the current was reversed and the WEs were lithiated from the InLi-(Li) CEs for 15 min at 0.2 mA cm^{-2} . The InLi-(Li) CE is easily capable to provide this current, as can be seen by a constant delithiation overpotential of the CEs of $\sim 0.16\text{ V}$ (orange lines) for each cell type. In total, a lithiation charge of $50.0\text{ }\mu\text{Ah cm}^{-2}$ was applied to the WEs. Upon lithiation, the potentials of both the InLi-(In) WE (blue, Fig. 6a) and the In WE (blue, Fig. 6b) exhibit an initial peak-like drop, which can be interpreted as a nucleation potential, and then plateau at an overpotential of $\sim 0.08\text{ V}$. In the subsequent OCV phase, the potentials of all electrodes relax to the equilibrium potential of the In/In₂Li₃ two-phase region of 0.62 V vs Li^+/Li (indicated by the gray line). The PEIS measurements in step 8 that will be discussed in the context of Fig. 7 show that the impedances of the InLi-(In) and the In WEs are now qualitatively similar to that of the InLi-(Li) CE, indicating the presence of an indium-lithium alloy phase with a low charge-transfer resistance at the interface to the separator.

In step 9, the current pulse was reversed, i.e., a delithiation current of 0.2 mA cm^{-2} was applied to the WEs in order to extract the previously added lithiation charge from the WEs and, moreover,

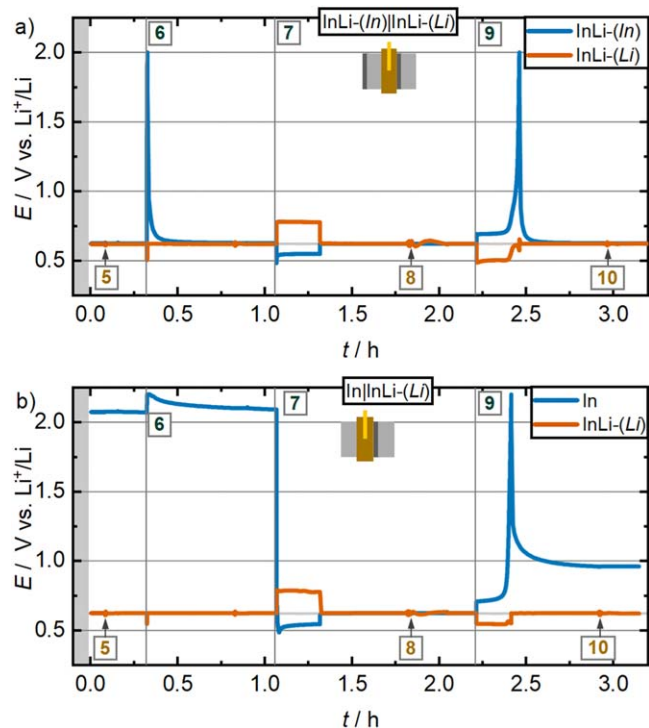


Figure 6. WE (blue) and CE (orange) potentials during galvanostatic (de) lithiation pulses (steps 6, 7, and 9 in Fig. 3c, marked in the squares) for the cells with GWRE shown in Figs. 3a and 3b: (a) InLi-(In)InLi-(Li) (WE|CE); (b) InInLi-(Li) (WE|CE). *Step 6:* applying a delithiation current of 0.2 mA cm^{-2} to the WE for 15 min or until a WE cut-off potential of $2.0 \text{ V vs Li}^+/\text{Li}$ for (a) or $2.2 \text{ V vs Li}^+/\text{Li}$ for (b). *Step 7:* applying a lithiation current of 0.2 mA cm^{-2} to the WE for 15 min. *Step 8:* PEIS measurements (shown in Fig. 7), with a 30 min. OCV before and a 10 min. OCV afterwards. *Step 9:* repeated application of a delithiation current of 0.2 mA cm^{-2} to the WE, but this time for 30 min, with the same WE cut-off potentials as in step 6. *Step 10:* PEIS measurements (shown in Fig. 7), with the same OCV periods as in step 8. The gray lines at $0.62 \text{ V vs Li}^+/\text{Li}$ mark the OCV of the In/In₁Li₁ two-phase region and serve as a guide-to-the-eye. Note that at the time of 0 h in this figure, the cell had been assembled for ~ 35 days (i.e., 0 h here corresponds to ~ 35 days in Fig. 4).

to probe if additional charge can be extracted from the nominally large lithium reservoir of the InLi-(In) WE, since the delithiation time is pulse is applied for 30 min. In fact, as shown in Fig. 6a, the cut-off potential of the InLi-(In) WE was reached after $14.7 \pm 0.25 \text{ min}$ (based on three cells), resulting in an extracted charge of $49 \pm 0.8 \mu\text{Ah cm}^{-2}$. This equates to a coulombic efficiency of $98 \pm 1.6\%$ for the initial lithiation and delithiation of the InLi-(In) electrode. Since no additional charge can be extracted from the InLi-(In), we have to conclude that its nominally very large lithium reservoir is electrochemically not accessible at the separator interface, i.e., that the lithium concentration at this interface must have remained very low (or zero). However, the OCP of the InLi-(In) WE relaxed to the OCV that is characteristic of the In/In₁Li₁ two-phase region. In case of the InInLi-(Li) cells (Fig. 6b), the delithiation of the indium WE in step 9 reached the cut-off potential after $11.5 \pm 3.0 \text{ min}$ (based on three cells), with an extracted charge of $38 \pm 0.8 \mu\text{Ah cm}^{-2}$, equating to a coulombic efficiency of only $76 \pm 20\%$. An explanation for the higher coulombic efficiency of the InLi-(In) compared to the In WE might be an already established SEI for the InLi-(In) WE that had been at a potential of $0.62 \text{ V vs Li}^+/\text{Li}$ for over 30 days where the LPSCl electrolyte is not stable.⁴⁶ In contrast, at the potential of the indium electrode ($\sim 2.1 \text{ V vs Li}^+/\text{Li}$, see Fig. 4b), LPSCl is stable⁴⁷ and thus, only upon its first lithiation in step 7 the LPSCl electrolyte decomposition can take place, leading to the here observed lower coulombic efficiency of the indium WE.

Interestingly, the initial nucleation overpotential peak observed for each of the WEs in step 7 (blue) was not observed for the InLi-(Li) CEs (orange) during their lithiation in step 9, which we ascribe to the fact that an InLi alloy that does not show any nucleation overpotential is already present at the CE/LPSCl interface. Furthermore, it is striking that the OCP of the In WE at the end of step 9 remains at $\sim 1 \text{ V vs Li}^+/\text{Li}$. Since it is known from the indium-lithium phase diagram that at most $\sim 1 \text{ at}\%$ Li is required to establish the In/In₁Li₁ potential of $0.62 \text{ V vs Li}^+/\text{Li}$,^{27,28} this suggests that the indium can be delithiated essentially completely. In turn, this implies that in an NCMIn cell, the potential of the indium CE cannot be assumed to stay invariant at $0.62 \text{ V vs Li}^+/\text{Li}$ towards the end of discharge (i.e., upon relithiation of the NCM), as this would depend on the overall loss of cyclable lithium (depending on the balance of lithium loss to SEI formation and the first-cycle irreversible capacity loss of the NCM).

PEIS measurements recorded in steps 5, 8, and 10 (see Fig. 3c) are displayed in Fig. 7. Starting with the PEIS data taken in step 5, a comparison of the upper panels of Fig. 7 with Fig. 5 shows that the shape of the WE, CE, and cell impedance spectra does not change significantly over the course of the OCV hold period of 28 days. Whereas the InLi-(Li) impedance response (orange) has two distinct semi-circles (neglecting the separator contribution at high frequencies), InLi-(In) has a prominent low-frequency Warburg-like tail and one mid-frequency semi-circle (blue), which however cannot be clearly seen, due to a partial overlap with the low-frequency tail (Fig. 7a). In case of an indium WE (blue, Fig. 7d), the low-frequency tail has a steeper angle, so that the mid-frequency semi-circle can be better resolved.

Upon lithiation of the WEs in step 7 (middle panels in Fig. 7), the low-frequency tail of InLi-(In) WE disappears and instead a semi-circle can be observed (blue, Fig. 7b). At the same time, the low-frequency artifacts in the InLi-(Li) CE spectrum (orange) vanish, as the magnitude of WE and CE impedances are similar, which now permits a detailed description of the InLi-(Li) impedance: the mid-frequency region ($23 \text{ kHz} - 30 \text{ Hz}$; $f_{\text{apex}} = 720 \text{ Hz}$, triangle) can be ascribed to the interface resistance of electrode and separator, i.e., to a combination of the physical contact resistance and the SEI resistance; the low-frequency semi-circle ($30 \text{ Hz} - 50 \text{ mHz}$; $f_{\text{apex}} = 1 \text{ Hz}$, diamond) is thought to represent the charge-transfer resistance.^{16,44} It is striking that both interface and charge-transfer resistance for the InLi-(Li) CE are significantly higher compared to that of the InLi-(In) WE. Similar to the case in Fig. 2c, an unintentional misalignment of the electrodes leading to different scaling factors cannot be excluded.^{24,39} Another possible reason might be a difference in the SEI contribution to the interface resistance, as in case of the InLi-(Li) electrode more chemical degradation of the solid electrolyte is expected, as the InLi alloy indeed is in contact with the SE, which is not the case for the InLi-(In) electrode except for short times during which it was galvanostatically lithiated (i.e., in step 7). The lithiation overpotential in step 7 for the InLi-(In) WE is $\sim 75 \text{ mV}$ at 0.2 mA cm^{-2} (see Fig. 6a), which corresponds to an electrode resistance of $\sim 375 \Omega \text{ cm}^2$ and is in good agreement with the low-frequency resistance found by the impedance measurement ($\sim 365 \Omega \text{ cm}^2$, Fig. 7b). The same is true for the InLi-(Li) CE, featuring a delithiation overpotential of $\sim 150 \text{ mV}$ at 0.2 mA cm^{-2} (see Figs. 6a or 6b), i.e., $\sim 750 \Omega \text{ cm}^2$ in comparison to the impedance based low-frequency resistance of $\sim 800 \Omega \text{ cm}^2$ (Figs. 7b or 7e). This suggests that the SEI resistance of both electrodes indeed is different and that the impedance measurements yield reliable values. The higher charge-transfer resistance of the InLi-(Li) CE compared to the InLi-(In) WE ($\sim 320 \Omega \text{ cm}^2$ vs $\sim 90 \Omega \text{ cm}^2$) might be explained by a depleted lithium concentration at the separator interface of the InLi-(Li) CE after a partial delithiation, which in turn would imply that the 30 min. OCV hold prior to the PEIS measurement was not long enough for the bulk InLi to compensate for the depleted lithium at the interface. Such a depletion of lithium at the interface of an indium-lithium electrode

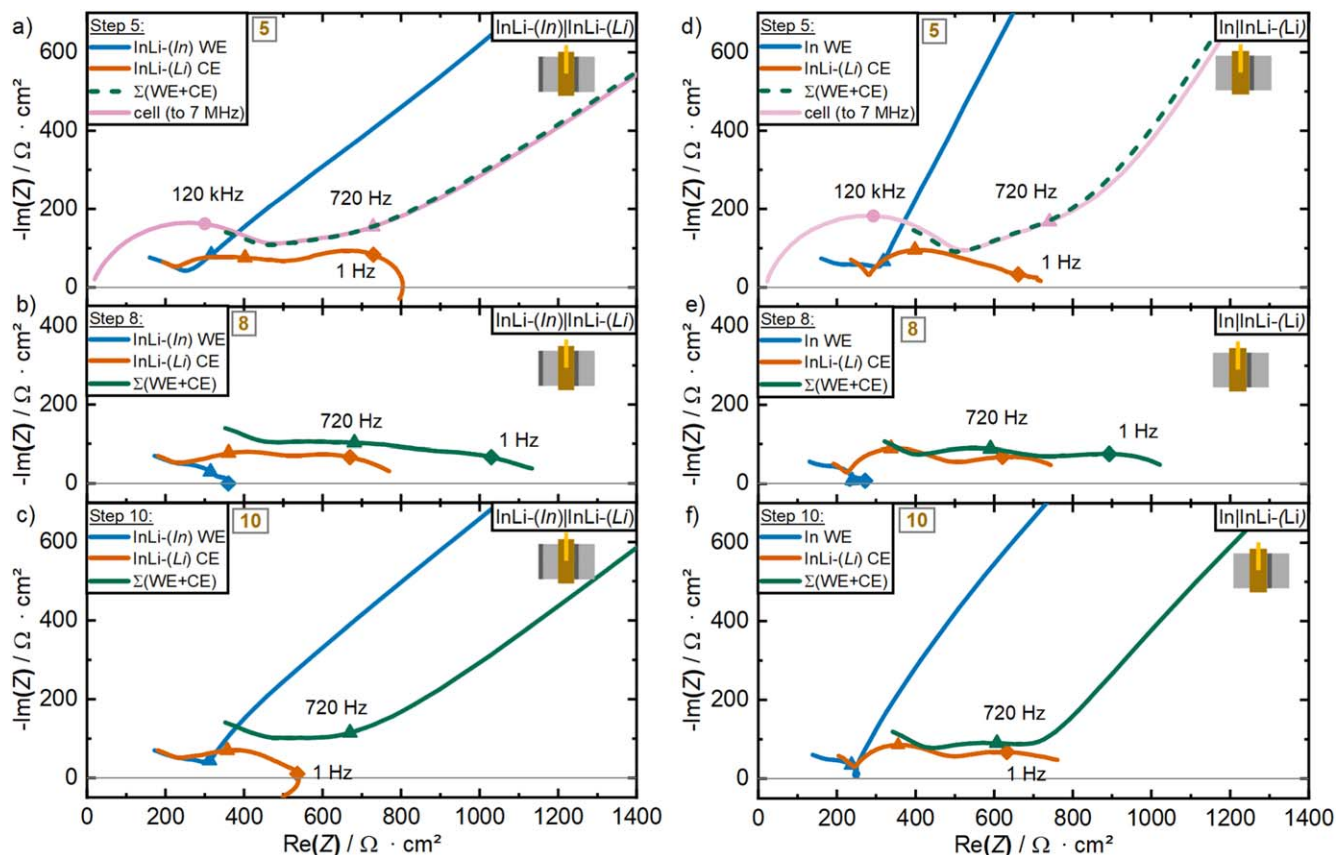


Figure 7. Nyquist plots of an InLi-(In)InLi-(Li) (a), (b), (c) and of an InInLi-(Li) (d), (e), (f) cell recorded at steps 5, 8, and 10 of the experimental procedure (see Fig. 3c, marked in the squares). The WE (blue) and CE (orange) impedance spectra were recorded via the lithiated GWRE (100 kHz–50 mHz with a 10 mV AC perturbation), whereby their vector sum is plotted in green. In step 5, the cell impedance was also measured directly without using the GWRE (pink; 7 MHz–50 mHz with a 10 mV AC perturbation). Points at specific frequencies are marked: circles at 120 kHz (only for cell impedances), triangles at 720 Hz, and diamonds at 1 Hz. *Step 5, upper panels:* impedance spectra (shown until 20 Hz) after 4 weeks of OCP monitoring (step 4) for the InLi-(In)InLi-(Li) (a) and the InInLi-(Li) (d) cell. *Step 8, middle panels:* impedance spectra after lithiation of the WEs (step 7) for the InLi-(In)InLi-(Li) (b) and the InInLi-(Li) (e) cell. *Step 10, bottom panels:* impedance spectra (shown until 20 Hz) of the InLi-(In)InLi-(Li) (c) and the InInLi-(Li) (f) cell after delithiation of the WEs (step 9).

to the separator after electrochemical delithiation was experimentally observed by Nam et al.¹³

After delithiation of the InLi-(In) WE in step 9, the semi-circle for the charge-transfer reaction has evolved to the low-frequency tail (Fig. 7c), which indicates the lack of electrochemically accessible Li at the separator interface, as already suggested by the galvanostatic pulsing tests. In case of the In WE, the same observations are made (blue lines in Figs. 7d–7e), showing that the impedances of the InLi-(In) and the In WEs are very similar under all conditions and clearly distinct from that of the InLi-(Li) CE.

In summary, the impedance experiments are consistent with the galvanostatic delithiation experiments (Fig. 6a) that showed that no cyclable lithium is present at the interface between InLi-(In) and the separator to sustain a current of 0.2 mA cm^{-2} , even after one month of OCV hold that should be long enough to allow for Li diffusion. This reflects the behavior of the In electrode, which cannot provide cyclable lithium and has the same impedance features. Only when the InLi-(In) and the In electrodes are being lithiated, their general impedance features are similar to those of the InLi-(Li) electrodes.

Finally, in step 11, the InLi-(Li) CEs of the InLi-(In)InLi-(Li) and the InInLi-(Li) cell are delithiated for 15 h at 0.2 mA cm^{-2} (Fig. 8), providing a total charge of 3.0 mAh cm^{-2} . This corresponds to the full capacity of a typical cathode electrode that would be used in studies with laboratory-scale cells. Thus, the InLi-(Li) configuration is a suitable CE for experiments, in which the CE is meant to compensate for cyclable lithium losses of cathode or anode electrodes under investigation (analogous to a lithium CE in half-cells with liquid electrolyte). The lithiation overpotentials of InLi-(In) (Fig. 8a) and In (Fig. 8b) are very similar. After lithiation, the In WE has an OCP of 0.62 V vs Li^+/Li , as

expected for the In/In₁Li₁ two-phase region. It should be noted that the here observed lithiation and delithiation overpotentials at 0.2 mA cm^{-2} are relatively high. For example, the delithiation overpotential of the InLi-(Li) CE is $\sim 150 \text{ mV}$, which equates to an areal resistance of $\sim 750 \Omega \text{ cm}^2$, which is in good agreement with the impedance based low-frequency resistance in step 8 (see Fig. 7b). We believe that such high resistances are due to the low fabrication ($\sim 70 \text{ MPa}$) and the low applied stack pressure ($\sim 20 \text{ MPa}$). Increasing both fabrication and stack pressure is reported to decrease the lithiation and delithiation overpotentials, consistent with the study by Ikezawa et al., who for a 3-fold higher fabrication pressure report a delithiation overpotential at 0.37 mA cm^{-2} (corresponding to their C/2 cycle) of only $\sim 40 \text{ mV}$, which equates to a much lower areal resistance of $\sim 110 \Omega \text{ cm}^2$.¹⁸

Discussion of the results and their practical relevance.—The here investigated indium-lithium electrodes, prepared by compressing an indium and a lithium foil at $\sim 70 \text{ MPa}$, showed different electrochemical properties depending on which face of the electrode was attached to the separator (see Figs. 1a–1c). The results of the impedance and of the galvanostatic pulse experiments unambiguously show that only the InLi-(Li) configuration of the electrode provides a cyclable Li reservoir, while no lithium could be extracted from the InLi-(In) configuration, despite its nominally high capacity ($\sim 14 \text{ mAh cm}^{-2}$). At the same time, the InLi-(In) electrode nevertheless shows an OCV that corresponds to the reported redox potential of the In/In₁Li₁ two-phase region (Fig. 4a).²⁸ In view of the indium-lithium phase diagram,^{32,35} this would be consistent with the formation of a solid solution of ~ 1 at% lithium in indium (further on referred to as In(δ Li)) that is in equilibrium with a In₁Li₁ phase: the

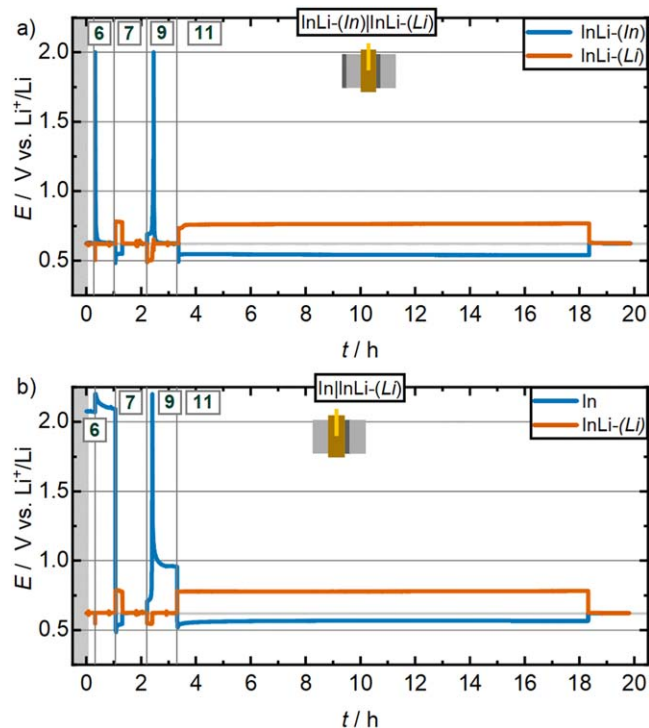


Figure 8. WE (blue) and CE (orange) potentials during galvanostatic (de) lithiation pulses (steps 6, 7, 9, and 10 in Fig. 3c, marked in the squares) for the cells with GWRE shown in Figs. 3a and 3b: (a) InLi-(In)/InLi-(Li) (WE|CE); (b) In/InLi-(Li) (WE|CE). Steps 6, 7, and 9: these are explained in Fig. 6. Step 11: applying a delithiation current of 0.2 mA cm^{-2} to the InLi-(Li) CE for 15 h, followed by monitoring the WE and CE potentials in OCV for 1.5 h (measured vs the GWRE and converted to the Li^+/Li scale based on a GWRE potential of $0.31 \text{ V vs Li}^+/\text{Li}$). The gray lines at Li^+/Li mark the OCV of the In/InLi₁ two-phase region and serve as a guide-to-the-eye. Note that at the time of 0 h in this figure, the cell had been assembled for ~ 35 days.

In(δLi) phase sandwiched between the In₁Li₁ phase and the separator of the InLi-(In) electrode would provide a stable OCV of $0.62 \text{ V vs Li}^+/\text{Li}$, but the rate at which the In(δLi) phase can provide lithium would be very low owing to its ~ 50 -fold lower lithium concentration compared to the In₁Li₁ phase that is in contact with the separator for the InLi-(Li) electrode.

Based on the average indium/lithium molar ratio of 76/24, the above observations and consideration would imply that $\sim 32\%$ of the indium would be consumed to form an In₁Li₁ phase exposed that would be in equilibrium with a solid solution of $\sim 1\%$ of lithium in the remaining 68% of the indium (constituting the In(δLi) phase). The In₁Li₁ phase would be exposed at the face of the electrode that we referred to as InLi-(Li), while the In(δLi) phase would be exposed at the face of the electrode that we referred to as InLi-(In). Based on the OCV transients upon cell assembly (Fig. 4a), the formation of the two-phase In(δLi)/In₁Li₁ composition would have to be completed after $t \approx 5 \text{ h}$ ($\sim 18000 \text{ s}$), from which one can estimate the required diffusion coefficient (D_{Li}) of lithium through the $\sim 280 \mu\text{m}$ thick indium foil (ignoring its slight thinning upon compression) via $D_{\text{Li}} \approx x^2/t$, equating to a minimum required diffusion coefficient of $\sim 4.4 \times 10^{-8} \text{ cm}^2 \text{ s}^{-1}$. To the best of our knowledge, we are not aware of any values for the diffusion coefficient of Li in In and/or In₁Li₁ at room temperature, so that the here estimated minimum value of the lithium diffusion coefficient cannot be compared to literature data.

In summary, on the basis of our observations and phase diagram based arguments, we believe that the indium-lithium electrodes prepared by the compression of lithium and indium foils, whose thicknesses are chosen to yield an average lithium content of $< 50\%$, does not lead to a homogeneous indium-lithium phase, but will rather result in the formation of an In₁Li₁ phase in equilibrium with a

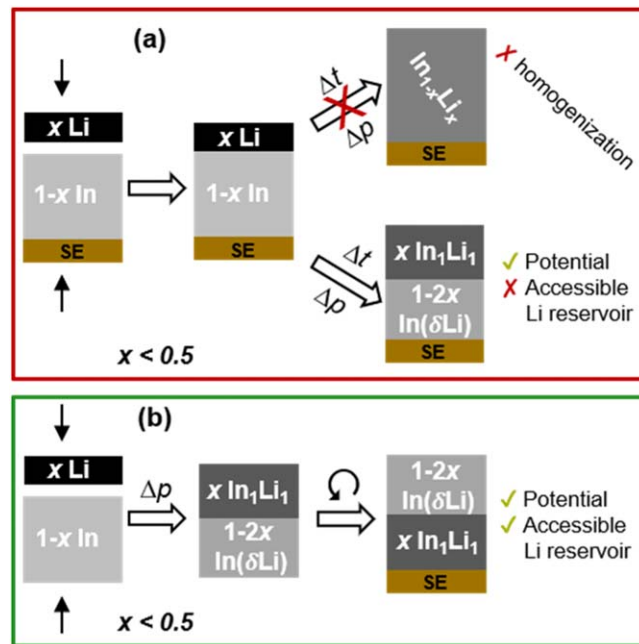


Figure 9. (a) Commonly used in situ preparation of an indium-lithium electrode of the nominal composition In_{1-x}Li_x ($x < 0.5$; for our study: $x = 0.24$) by attaching a piece of lithium onto an indium foil that is already firmly attached to the solid electrolyte (SE) separator in an ASSB test cell. Our study suggests that the lithium will not distribute homogeneously within the indium-lithium electrode (upper arrow) even after months under compression; instead, a defined In₁Li₁ phase is formed at the backside of the separator that is in equilibrium with a solid solution phase with $\sim 1\%$ at% Li dissolved in indium (In(δLi)) located at the interface towards the separator. The indium-lithium electrode features the stable In/In₁Li₁ potential of $0.62 \text{ V vs Li}^+/\text{Li}$, but the Li reservoir is electrochemically not accessible (bottom arrow). (b) Ex-situ preparation of an indium-lithium electrode by stacking and compressing indium and lithium foils; a subsequent cell assembly with the In₁Li₁ phase facing the separator provides both a stable reference electrode potential and an electrochemically accessible Li reservoir.

very dilute solid solution phase of lithium in indium ($\sim 1\%$ Li). This is illustrated in Fig. 9a. While it would in principle be possible to adjust the thickness of the metal foils such that the average lithium content is 50 at%, this type of material would not only be too brittle for preparing large electrodes, but would also not have a stable reference potential upon lithiation.²⁸

However, stacking indium and lithium foils in the InLi-(In) configuration is a commonly used way to prepare an indium-lithium anode (see Fig. 9a).^{18,28,31,48} In some instances, this type of electrode is even reported in the literature to be able to deliver a delithiation current,^{28,31} which is at variance with our measurements. While we do not know the origin of this discrepancy, it might be that stacking indium and lithium foils inside a cylinder to prepare a powder-type cell, where no radial expansion under the applied compressive force is possible, might lead to a Li creep between the edge of the indium foil and the wall of the cylinder towards the separator.⁴⁹ In this case, cyclable lithium would be available at the interface with the solid electrolyte. Therefore, we believe that it is better to prepare the indium-lithium electrode ex situ prior to cell assembly in order to avoid Li creep, using the method proposed here or other approaches reported in the literature.^{13,16,33,34} In doing so, the lithiated side of the electrode can be attached to the separator, which is the only reliable way to ensure an electrochemically accessible reservoir of cyclable Li (see Fig. 9b).

Conclusions

Herein, we report a micro-reference electrode (μ -RE) for electrode-resolved impedance and potential measurements for use in ASSB pouch cells. The μ -RE consists of a $50 \mu\text{m}$ diameter gold

wire with a 7 μm thick polyimide insulation, which is sandwiched between two SE/binder-composite separator sheets (LPSCI/HNBR) and activated by in-situ electrochemical lithiation.

Using the $\mu\text{-RE}$ in combination with galvanostatic pulse experiments and electrochemical impedance spectroscopy (EIS), we investigate the electrochemical properties of an indium-lithium electrode which is prepared by stacking and compressing In and Li foils, whose thicknesses are such that the average molar ratio of In:Li is roughly 76:24. The main objective is to probe the availability of electrochemically accessible and thus cyclable Li at the interface towards the separator as a function of the electrode orientation: either in the so-called InLi-(Li) geometry, in which the originally Li-foil-side of the electrode faces the separator, or in the so-called InLi-(In) configuration, in which the originally In-foil-side of the electrode faces the separator (see Figs. 1a–1c). Based on these experiments and phase-diagram based considerations, the following conclusions can be drawn:

- No homogenous lithium distribution within the InLi electrode of the nominal composition $\text{In}_{0.76}\text{Li}_{0.24}$ could be detected after 34 days in OCV; instead, our measurements indicate two distinct phases, i.e., an InLi phase with a 1:1 stoichiometry (In_1Li_1) and a solid solution phase of ~ 1 at% Li dissolved in indium ($\text{In}(\delta\text{Li})$). Thus, the more correct description of the electrode is $(\text{In}(\delta\text{Li}))_{0.52}/(\text{In}_1\text{Li}_1)_{0.24}$, considering the two-phase character of the electrode and that the In_1Li_1 phase is in equilibrium with an indium-rich rather than a pure indium phase.

- The InLi-(In) configuration, i.e., attaching a piece of lithium on the backside of an indium foil (see Fig. 1c), provides a stable reference electrode potential of 0.62 V vs Li^+/Li (from the $(\text{In}(\delta\text{Li}))_{0.52}/(\text{In}_1\text{Li}_1)_{0.24}$ couple), however, the large lithium reservoir contained in the indium-lithium electrode in the InLi-(In) configuration is not electrochemically accessible at practically relevant current densities (e.g., at $>0.1 \text{ mA cm}^{-2}$).

- For experiments that require a reservoir of cyclable lithium, it is mandatory to use the InLi-(Li) configuration, with the In_1Li_1 phase at the electrochemically active interface towards the separator (see Fig. 1b); experimentally, this configuration is best achieved by an ex situ preparation of the indium-lithium electrode prior to cell assembly.

Acknowledgments

We gratefully thank Lennart Reuter and Gioele Conforto from TUM as well as Prof. Bharatkumar Suthar from IITB Mumbai for valuable discussions. This work is part of the project “Industrialisierbarkeit Festkörperelektrolyte” funded by the Bavarian Ministry of Economic Affairs, Regional Development and Energy.

Appendix

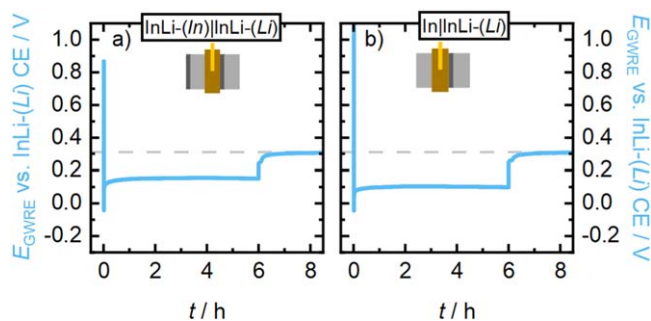


Figure A-1. Potential of the GWRE versus the InLi-(Li) CE during the lithiation of the GWREs in the two different cell types shown in Figs. 3a and 3b: (a) InLi-(In)InLi-(Li) (WE|CE); b) InLi-(Li) (WE|CE). The GWRE lithiation (step 2 in Fig. 3c) was done via the InLi-(Li) CE at a current of 500 nA over 6 h, followed by 2 h OCV for potential relaxation.

ORCID

Christian Sedlmeier <https://orcid.org/0000-0002-8566-8194>

Carina Schramm <https://orcid.org/0000-0001-9520-170X>

Hubert A. Gasteiger <https://orcid.org/0000-0001-8199-8703>

References

1. P. Iurilli, C. Brivio, and V. Wood, *J. Power Sources*, **505**, 229860 (2021).
2. P. Minnmann, L. Quillman, S. Burkhardt, F. H. Richter, and J. Janek, *J. Electrochem. Soc.*, **168**, 040537 (2021).
3. J. Landesfeind, J. Hattendorff, A. Ehrl, W. A. Wall, and H. A. Gasteiger, *J. Electrochem. Soc.*, **163**, A1373 (2016).
4. J. Illig, M. Ender, T. Chrobak, J. P. Schmidt, D. Klotz, and E. Ivers-Tiffée, *J. Electrochem. Soc.*, **159**, A952 (2012).
5. V. F. Lvovich, *Applications to Electrochemical and Dielectric Phenomena* (Hoboken, Wiley) p. 1 (2012).
6. A. Lasis, *Electrochemical Impedance Spectroscopy and Its Applications* (Berlin, Springer) p. 7 (1999).
7. C. H. Chen, J. Liu, and K. Amine, *J. Power Sources*, **96**, 321 (2001).
8. R. Landesfeind, C. P. Aiken, N. N. Sinha, J. C. Burns, H. Ye, C. M. VanElzen, G. Jain, S. Trussler, and J. R. Dahn, *J. Electrochem. Soc.*, **160**, A117 (2013).
9. A. N. Jansen, D. W. Dees, D. P. Abraham, K. Amine, and G. L. Henriksen, *J. Power Sources*, **174**, 373 (2007).
10. J. Zhou and P. H. L. Notten, *J. Electrochem. Soc.*, **151**, A2173 (2004).
11. S. Solchenbach, D. Pritzl, E. J. Y. Kong, J. Landesfeind, and H. A. Gasteiger, *J. Electrochem. Soc.*, **163**, A2265 (2016).
12. G. H. Chang, H. U. Choi, S. Kang, J. Y. Park, and H. T. Lim, *Ionics (Kiel)*, **26**, 1555 (2020).
13. Y. J. Nam, K. H. Park, D. Y. Oh, W. H. An, and Y. S. Jung, *J. Mater. Chem. A*, **6**, 14867 (2018).
14. J. Kasemchainan, S. Zekoll, D. Spencer Jolly, Z. Ning, G. O. Hartley, J. Marrow, and P. G. Bruce, *Nat. Mater.*, **18**, 1105 (2019).
15. S. Wenzel, T. Leichtweiß, D. A. Weber, J. Sann, W. G. Zeier, J. Janek, and S. Randau, *Chem. Mater.*, **28**, 2400 (2016).
16. R. Dugas, Y. Dupraz, E. Quemin, T. Koç, and J.-M. Tarascon, *J. Electrochem. Soc.*, **168**, 090508 (2021).
17. R. Schlenker, D. Stępień, P. Koch, T. Hupfer, S. Indris, B. Røling, V. Miß, A. Fuchs, M. Wilhelm, and H. Ehrenberg, *ACS Appl. Mater. Interfaces*, **12**, 20012 (2020).
18. A. Ikezawa, G. Fukunishi, T. Okajima, F. Kitamura, K. Suzuki, M. Hirayama, R. Kanno, and H. Arai, *Electrochem. Commun.*, **116**, 106743 (2020).
19. C. Delacourt, P. L. Ridgway, V. Srinivasan, and V. Battaglia, *J. Electrochem. Soc.*, **161**, A1253 (2014).
20. S. B. Adler, *J. Electrochem. Soc.*, **149**, E166 (2002).
21. D. R. Baker, M. W. Verbrugge, and X. X. Hou, *J. Electrochem. Soc.*, **164**, A407 (2017).
22. M. Ender, J. Illig, and E. Ivers-Tiffée, *J. Electrochem. Soc.*, **164**, A71 (2017).
23. J. Costard, M. Ender, M. Weiss, and E. Ivers-Tiffée, *J. Electrochem. Soc.*, **164**, A80 (2017).
24. D. W. Dees, A. N. Jansen, and D. P. Abraham, *J. Power Sources*, **174**, 1001 (2007).
25. W. D. Richards, L. J. Miara, Y. Wang, J. C. Kim, and G. Ceder, *Chem. Mater.*, **28**, 266 (2016).
26. S. A. Webb, L. Baggetto, C. A. Bridges, and G. M. Veith, *J. Power Sources*, **248**, 1105 (2014).
27. Y. S. Jung, K. T. Lee, J. H. Kim, J. Y. Kwon, and S. M. Oh, *Adv. Funct. Mater.*, **18**, 3010 (2008).
28. A. L. Santhosha, L. Medenbach, J. R. Buchheim, and P. Adelhelm, *Batter. Supercaps*, **2**, 524 (2019).
29. R. Koerver, I. Aygün, T. Leichtweiß, C. Dietrich, W. Zhang, J. O. Binder, P. Hartmann, W. G. Zeier, and J. Janek, *Chem. Mater.*, **29**, 5574 (2017).
30. A. Sakuda, H. Kitaura, A. Hayashi, K. Tadanaga, and M. Tatsumisago, *J. Power Sources*, **189**, 527 (2009).
31. W. Zhang et al., *ACS Appl. Mater. Interfaces*, **9**, 17835 (2017).
32. W. A. Alexander, L. D. Calvert, R. H. Gamble, and K. Schinzel, *Can. J. Chem.*, **54**, 1052 (1976).
33. D. Y. Oh, Y. E. Choi, D. H. Kim, Y. G. Lee, B. S. Kim, J. Park, H. Sohn, and Y. S. Jung, *J. Mater. Chem. A*, **4**, 10329 (2016).
34. Y. Wang, T. Liu, and J. Kumar, *ACS Appl. Mater. Interfaces*, **12**, 34771 (2020).
35. J. Sangster and A. D. Pelton, *J. Phase Equilibria*, **12**(1), 37 (1991).
36. C. Sedlmeier, T. Kutsch, R. Schuster, L. Hartmann, R. Bublitz, M. Tominac, M. Bohn, and H. A. Gasteiger, *J. Electrochem. Soc.*, **169**, 070508 (2022).
37. A. N. Dey, *J. Electrochem. Soc.*, **118**, 1547 (1971).
38. P. Bach, M. Stratmann, I. Valencia-Jaime, A. H. Romero, and F. U. Renner, *Electrochim. Acta*, **164**, 81 (2015).
39. M. Ender, A. Weber, and E. Ivers-Tiffée, *J. Electrochem. Soc.*, **159**, A128 (2011).
40. R. Mogi, M. Inaba, S.-K. Jeong, Y. Iriyama, T. Abe, and Z. Ogumi, *J. Electrochem. Soc.*, **149**, A1578 (2002).
41. S. Wenzel, S. J. Sedlmaier, C. Dietrich, W. G. Zeier, and J. Janek, *Solid State Ionics*, **318**, 102 (2018).
42. P. Bron, B. Røling, and S. Dehnen, *J. Power Sources*, **352**, 127 (2017).
43. J. T. S. Irvine, D. C. Sinclair, and A. R. West, *Adv. Mater.*, **2**, 132 (1990).
44. J. Landesfeind, D. Pritzl, and H. A. Gasteiger, *J. Electrochem. Soc.*, **164**, A1773 (2017).

45. R. Morasch, B. Suthar, and H. A. Gasteiger, *J. Electrochem. Soc.*, **167**, 100540 (2020).
46. D. H. S. Tan, E. A. Wu, H. Nguyen, Z. Chen, M. A. T. Marple, J. M. Doux, X. Wang, H. Yang, A. Banerjee, and Y. S. Meng, *ACS Energy Lett.*, **4**, 2418 (2019).
47. G. F. Dewald, S. Ohno, M. A. Kraft, R. Koerver, P. Till, N. M. Vargas-Barbosa, J. Janek, and W. G. Zeier, *Chem. Mater.*, **31**, 8328 (2019).
48. F. Sun et al., *J. Mater. Chem. A*, **6**, 22489 (2018).
49. A. Masias, N. Felten, R. Garcia-Mendez, J. Wolfenstine, and J. Sakamoto, *J. Mater. Sci.*, **54**, 2585 (2019).

3.2 Characterization of Lithium Phosphides – A Novel Class of Solid Lithium-Ion Conductors

3.2.1 Conductivity Determination of Lithium Phosphidosilicates with a High-Pressure Cell Setup

This section presents the article “*Fast Ionic Conductivity in the Most Lithium-Rich Phosphidosilicate $\text{Li}_{14}\text{SiP}_6$* ”, which was submitted in May 2019 and published in August 2019 in the peer-reviewed Journal of the American Chemical Society.¹²⁶ The permanent web link is available under: <https://pubs.acs.org/doi/abs/10.1021/jacs.9b05301>, where also the supporting information can be found.

The strive for new lithium ion conducting materials led to a reinvestigation of the ternary Li-Si-P system, revealing the existence of various lithium phosphidosilicates, such as LiS_2P_3 ,¹⁸¹ Li_2SiP_2 ,¹⁸² $\text{Li}_3\text{Si}_3\text{P}_7$,¹⁸³ Li_8SiP_4 ,¹⁸² or $\text{Li}_{10}\text{Si}_2\text{P}_6$.¹⁸³ The basic building block of the lithium phosphidosilicates are isolated and/or interconnected SiP_4 -units, forming various three dimensional structure motifs, with mobile lithium present in tetrahedral and/or octahedral voids. Since the ionic conductivity is directly proportional to the number of charge carriers (see Equation (2.10)), i.e., in this case the mobile Li atoms, attempts were made to increase the amount of lithium by adding “ Li_3P ” units to the known lithium phosphidosilicates. Ultimately, this led to the most lithium-rich phosphidosilicate $\text{Li}_{14}\text{SiP}_6$ (see figure 1.5 in the PhD thesis of Stefan Strangmüller¹⁸⁴).

In this study, the synthesis, structural characterization and determination of the Li-ion mobility in the compound $\text{Li}_{14}\text{SiP}_6$ is described. The article results from a cooperation between different groups. Our contribution is the design and validation of the measurement cell (viz., the screw cell) for impedance experiments as well as the experimental determination of the ionic conductivity and activation energy for lithium ion conduction. Therefore, in the following, the focus will be on our contribution of the work. For more details regarding synthesis and structural characterization by means of XRD and PND (powder neutron diffraction), the reader is referred to the PhD thesis of the first author.¹⁸⁴

The measurement cell (see Figure S12 of the publication¹²⁶) consists of a PEEK cylinder to host the sample, which is contacted by a stainless steel die on each side. Due to the brittle nature of the lithium phosphides, no free-standing pellet could be obtained by cold pressing. Therefore, the cell is designed to be filled with the pure powder and to *in situ* pelletize the sample by firm compression. The pressure is applied by fastening six screws with a defined torque of 30 Nm. Since no load cell is integrated, the applied pressure is calculated based on the torque. Additionally, reference measurements with different torques were conducted, showing that the increase of the ionic conductivity for progressively higher torques levels out at 30 Nm, corresponding to ~480 MPa. Applying this torque, the samples can be compressed to ~80% of their crystal density, yielding an ionic conductivity of ~1 mS cm⁻¹ at room temperature. The activation energy for lithium ion transport is investigated by temperature-dependent EIS measurements in a range of 273 – 353 K, yielding a value of ~32 kJ mol⁻¹ (~0.33 eV). This is in good agreement with an activation energy of ~30 kJ mol⁻¹ (~0.31 eV), determined by static ⁷Li NMR experiments. Lastly, we determined the electronic conductivity by means of DC polarization measurement to ~2 × 10⁻⁷ S cm⁻¹.

Author contributions

The compound was synthesized by S.S. and H.E. Impedance measurements were performed and evaluated by C.S and D.M. The PND experiments were carried out by A.S. and V.B. at the FRM-II neutron source in Garching, Germany. The structural analysis was carried out by S.S., H.E., and W.K. The MAS NMR experiments were performed by G.R.S. and the static ⁷Li NMR spectroscopy was done by H.K. DFT calculations were conducted by V.L.D. All authors contributed to the manuscript.

Fast Ionic Conductivity in the Most Lithium-Rich Phosphidosilicate $\text{Li}_{14}\text{SiP}_6$

Stefan Strangmüller,^{†,‡} Henrik Eickhoff,^{†,‡} David Müller,[†] Wilhelm Klein,[†] Gabriele Raudaschl-Sieber,[†] Holger Kirchhain,[‡] Christian Sedlmeier,[§] Volodymyr Baran,^{||} Anatoliy Senyshyn,^{||} Volker L. Deringer,[⊥] Leo van Wüllen,[⊥] Hubert A. Gasteiger,[§] and Thomas F. Fässler^{*,†}

[†]Department of Chemistry, Technische Universität München, Lichtenbergstrasse 4, D-85747 Garching, Germany

[‡]Department of Physics, University of Augsburg, Universitätsstrasse 1, D-86159 Augsburg, Germany

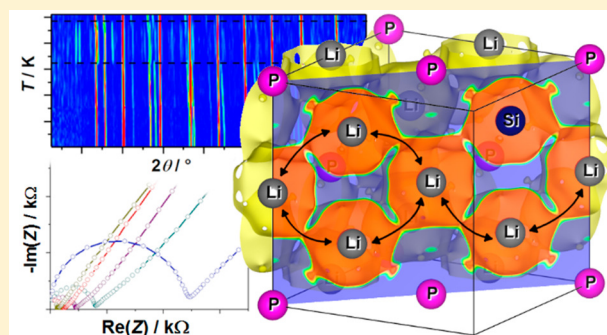
[§]Department of Chemistry, Technische Universität München, Lichtenbergstrasse 4, D-85747 Garching, Germany

^{||}Heinz Maier-Leibnitz Zentrum, Technische Universität München, Lichtenbergstrasse 1, D-85748 Garching, Germany

[⊥]Department of Engineering, University of Cambridge, Cambridge CB2 1PZ, United Kingdom

Supporting Information

ABSTRACT: Solid electrolytes with superionic conductivity are required as a main component for all-solid-state batteries. Here we present a novel solid electrolyte with three-dimensional conducting pathways based on “lithium-rich” phosphidosilicates with ionic conductivity of $\sigma > 10^{-3} \text{ S cm}^{-1}$ at room temperature and activation energy of 30–32 kJ mol⁻¹ expanding the recently introduced family of lithium phosphidotetrelates. Aiming toward higher lithium ion conductivities, systematic investigations of lithium phosphidosilicates gave access to the so far lithium-richest compound within this class of materials. The crystalline material (space group *Fm* $\bar{3}$ *m*), which shows reversible thermal phase transitions, can be readily obtained by ball mill synthesis from the elements followed by moderate thermal treatment of the mixture. Lithium diffusion pathways via both tetrahedral and octahedral voids are analyzed by temperature-dependent powder neutron diffraction measurements in combination with maximum entropy method and DFT calculations. Moreover, the lithium ion mobility structurally indicated by a disordered Li/Si occupancy in the tetrahedral voids plus partially filled octahedral voids is studied by temperature-dependent impedance and ⁷Li NMR spectroscopy.



1. INTRODUCTION

All-solid-state battery technology is currently attracting considerable interest, as such batteries possess a number of potential advantages over liquid electrolyte systems, including energy density gains and improved safety. As a consequence, a large number of inorganic materials with both crystalline and amorphous structures as well as their composite structures have been investigated experimentally and theoretically as potential solid electrolyte candidates.^{1,2} In particular the investigation of lithium ion solid electrolytes in lithium ion batteries (LIBs) has increased rapidly in order to improve the performance of electrochemical energy storage systems.³

In order to achieve a significant ionic conductivity in a crystalline solid, at first a high charge carrier density should coincide with a large number of available lattice sites. Second, solid electrolytes require a low activation energy for lithium mobility as it is found in materials in which cation sites are arranged in face-sharing polyhedra that are formed by anions.⁴ For example, for garnet-type solid electrolytes the effect of polyhedral connectivity on the ionic conductivity has been

shown recently.⁵ A large polarizability of the anions has been suggested as another factor for lowering the activation barrier for Li⁺ mobility,⁶ and accordingly sulfides, thiophosphates, and materials containing iodine such as Li-argyrodites are investigated as superionic conductors.^{7–14} For example, Li₃PS₄ shows an ionic conductivity that is several orders of magnitude higher than that of Li₃PO₄, and the same applies for Li₆PS₅Cl versus Li₆PO₅Cl.^{15,16} The best superionic conductors are found if a combination of several of these aspects appear as observed, for example, in Li₁₀GeP₂S₁₂ (LGPS), which can formally be regarded as a variation of pristine Li₃PS₄, combined with the Li-rich Li₄GeS₄ [Li₁₀(GeS₄)(PS₄)₂ = 2 Li₃PS₄ + Li₄GeS₄], or in the argyrodites Li₆PS₅X, which formally represent a combination of Li₃PS₄, Li₂S, and LiX [Li₆(PS₄)(S)X = Li₃PS₄ + Li₂S + LiX].^{6,10}

Following these concepts we recently started to reinvestigate the ternary phase systems Li/Si/P and Li/Ge/P¹⁷ and found

Received: May 17, 2019

Published: August 12, 2019

ionic conductivities up to 10^{-4} S cm^{-1} at room temperature for pure Li_8SiP_4 and Li_8GeP_4 .^{18,19} Li_8SiP_4 , comprising discrete $[\text{SiP}_4]^{8-}$ tetrahedra, fulfills most of the criteria mentioned above: (a) It has more than twice the Li^+ concentration of Li_3PS_4 ; (b) the higher formal charge of minus two at the P atoms in the $[\text{SiP}_4]^{8-}$ units hints at a higher polarizability than the formally one-fold negatively charged sulfur atoms in PS_4^{3-} ; and (c) most intriguingly, the crystal structure of Li_8SiP_4 is closely related to the anti-structure type of CaF_2 . The atom packing of Li_8SiP_4 derives from cubic close packing (*ccp*) of the P atoms, which in consequence creates eight tetrahedral and four octahedral voids per formula unit. Out of these 12 voids only one tetrahedral site is filled by a Si atom, which can be considered as covalently bound to the four P atoms. In addition eight Li atoms per formula unit can be distributed within the remaining 11 voids, and, thus, numerous empty vacancies for a possible Li^+ hopping are present. As an additional advantage in the *ccp*, tetrahedral and octahedral voids share common faces, a fact that enlarges the window for diffusion pathways, compared to edge-sharing polyhedra.^{20,21} This concept of cation disorder in lithium phosphidotetrelates should create a promising opportunity to get access to high-performance lithium ion conductors, which has already been successfully applied to the Li/Ge/P system, as indicated by the close structural relationship between Li_8SiP_4 and α - and β - Li_8GeP_4 .¹⁹

However, the Li^+ conductivity can even be further increased by using different or disordered anions. The presence of differently charged anions may allow for a fine-tuning of the Li^+ concentration within the compound, and a disorder may reduce the activation barrier.^{22,23} A well-established example for lithium ion conductors in which all these concepts are realized is the recently discovered class of Li-argyrodites $\text{Li}_6\text{PS}_5\text{X}$ ($\text{X} = \text{Cl}, \text{Br}, \text{I}$). Their cubic crystal structure ($F\bar{4}3m$) consists of two different types of anionic building blocks, tetrahedral $[\text{PS}_4]^{3-}$ units and isolated S^{2-} or X^- ions in the ratio 1:2, separated by lithium ions.

We now apply the concept of increased disorder over a larger number of polyhedral voids on one hand and of an increased overall Li^+ mobility on the other, to lithium phosphidosilicates (LSiP). The formal addition of more Li-rich Li_3P to one equivalent of Li_8SiP_4 corresponds to a line through Li_3P and Li_8SiP_4 ¹⁸ in the ternary composition diagram Li/Si/P (Figure 1). Interestingly, at the Li-poor side along this line several compounds such as $\text{Li}_{10}\text{Si}_2\text{P}_6$,²⁴ Li_2SiP_2 ,^{18,25} and LiSi_2P_3 ²⁵ are

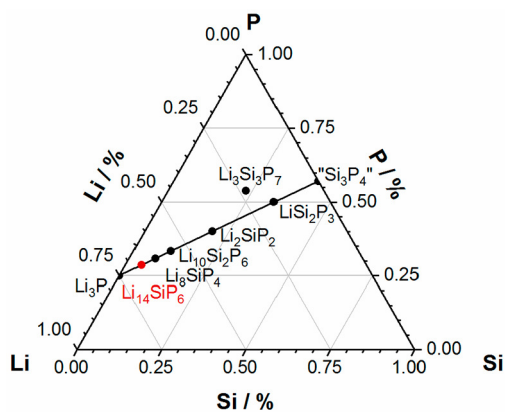


Figure 1. Composition triangle of the ternary system Li/Si/P with formulas of known compounds. The new compound $\text{Li}_{14}\text{SiP}_6$ is highlighted in red.

already known. The line hits the binary border at a nominal stoichiometry of “ Si_3P_4 ”.

Here we report on a new compound with a higher Li content than Li_8SiP_4 obtained by a formal addition of Li_3P . Based on the crystal structures of Li_8SiP_4 and Li_3P , one might expect the presence of $[\text{SiP}_4]^{8-}$ and P^{3-} as anionic building units similar to the simultaneous appearance of $[\text{PS}_4]^{3-}$ and S^{2-} in Li-argyrodites. We found a straightforward and simple synthesis route for the new phosphidosilicate $\text{Li}_{14}\text{SiP}_6$, which shows the highest Li^+ density among the more complex lithium ion conductors. This route leads to a crystalline material and comprises mechanochemical ball milling of the elements with subsequent annealing of the mixture. The crystal structure was determined by single crystal and by powder X-ray, as well as by powder neutron diffraction methods. The purity of the samples was confirmed by elemental analyses as well as by solid state ^6Li , ^{29}Si , and ^{31}P MAS NMR spectroscopy. The thermal properties of the material were studied by differential scanning calorimetry and temperature-dependent powder neutron diffraction experiments. Finally, the Li^+ migration has been investigated by electrochemical impedance spectroscopy, temperature-dependent ^7Li NMR spectroscopy, high-temperature neutron diffraction measurements (maximum entropy method), and density functional theory calculations.

2. EXPERIMENTAL METHODS

Synthesis. All syntheses were carried out under an Ar atmosphere in gloveboxes (MBraun, 200B) with moisture and oxygen levels below 0.1 ppm or in containers, which were sealed under an Ar atmosphere and vacuum ($<2 \times 10^{-2}$ mbar), respectively. Lithium phosphidosilicates are sensitive to oxygen and moisture; in particular, contact with water results in a vigorous reaction including the formation of flammable and toxic gases (e.g., phosphine). Therefore, disposal must be carried out in small amounts at a time and under proper ventilation.

Synthesis of Polycrystalline $\text{Li}_{14}\text{SiP}_6$. The synthesis route includes two steps, using stoichiometric amounts of lithium (Rockwood Lithium, 99%), silicon (Wacker, 99.9%), and red phosphorus (Sigma-Aldrich, 97%) aiming for the compositions $\text{Li}_{11}\text{SiP}_5$, $\text{Li}_{14}\text{SiP}_6$, $\text{Li}_{17}\text{SiP}_7$, and $\text{Li}_{20}\text{SiP}_8$. In the first step a reactive mixture ($m = 1.5$ – 5.0 g) is prepared by mechanochemical milling using a Retsch PM100 planetary ball mill (350 rpm, 36 h, 10 min interval, 3 min break) with a tungsten carbide milling jar ($V = 50$ mL) and three balls with a diameter of 15 mm.

In the second step, the obtained reactive mixture was pressed to pellets, sealed in batches of 0.3 to 3.0 g in carbon-coated silica glass ampules, and heated in a muffle furnace (Nabertherm, L5/11/P330) to 973 K (heating rate: 4 K min^{-1}) followed by quenching of the hot ampules in water. Annealing times between 6 and 18 h yielded products with high purity. The sample used for determination of the ionic conductivity was quenched after 9 h.

Powder X-ray Diffraction. Data were collected at room temperature on a STOE Stadi P diffractometer (Ge(111) monochromator, $\text{Cu K}\alpha_1$ radiation, $\lambda = 1.54056$ Å or $\text{Mo K}\alpha_1$ radiation, $\lambda = 0.70932$ Å) with a Dectris MYTHEN 1K detector in Debye–Scherrer geometry. Samples were sealed in glass capillaries ($\Phi = 0.3$ mm) for measurement. Raw data were processed with WinXPOW²⁶ software prior to further refinement.

Powder Neutron Diffraction. Elastic coherent neutron scattering experiments were performed on the high-resolution powder diffractometer SPODI at the research reactor FRM-II (Garching, Germany).²⁷ Monochromatic neutrons ($\lambda = 1.5482$ Å) were obtained at a 155° takeoff angle using the (551) reflection of a vertically focused composite Ge monochromator. The vertical position-sensitive multi-detector (300 mm effective height) consisting of 80 ^3He tubes of 1 in. in diameter and covering an angular range of $160^\circ 2\theta$ was used for data collection. Measurements were performed in Debye–Scherrer geometry. The powder sample (ca. 2 cm^3 in volume) was filled into a

Nb tube container (10 mm diameter, 0.5 mm wall thickness) under argon and welded using an arc-melting apparatus. The Nb container with the sample was mounted in the top-loading closed-cycle refrigerator. ^4He was used as a heat transmitter. The instantaneous temperature was measured using two Cernox thin film resistance cryogenic temperature sensors and controlled by a LakeShore340 temperature controller. Two-dimensional diffraction data were collected at fixed temperatures in the range of 4–300 K using 20 K temperature steps upon heating and then corrected for geometrical aberrations and the curvature of the Debye–Scherrer rings.

For measurements at high temperature the Nb container with the sample was mounted in the vacuum furnace equipped with Nb heating elements. Measurements and temperature control were carried out using two Type L thermocouples and a Eurotherm 2400 controller. The data were collected in the temperature range 297–1023 K using a temperature increment of 50 K. At temperatures below 573 K, ^4He was used as a thermal exchange medium, whereas at higher temperatures the furnace regulation was achieved using an isolation vacuum.

Rietveld Refinement. The data analysis was performed using the full profile Rietveld method implemented in the FullProf program package.²⁸ For the shaping of the peak profile, the pseudo-Voigt function was chosen. The background contribution was determined using a linear interpolation between selected data points in non-overlapping regions. The scale factor, zero angular shift, profile shape parameters, resolution (Caglioti) parameters, asymmetry and lattice parameters, and fractional coordinates of atoms and their displacement parameters were varied during the fitting.

In accordance with the composition gained from elemental analyses the stoichiometry was set to $\text{Li}_{14}\text{SiP}_6$ ($Z = 0.67$) or $\text{Li}_{2.33}\text{Si}_{0.17}\text{P}$ ($Z = 4$), respectively. Besides the Nb reflections only reflections consistent with cubic symmetry and face centering, according, for example, to the space group $Fm\bar{3}m$ (no. 225) of antiferroite, are present in the neutron diffraction patterns. The diffraction intensities of $\text{Li}_{14}\text{SiP}_6$ have been modeled with the P atoms located at the $4a$ site and a mixed Li/Si site occupation of the residual $4b$ and $8c$ sites. Constraining the overall Li and Si concentrations to the ones from elemental analyses, along with the assumptions of full $8c$ site occupation it can be concluded that the $8c$ site is fully occupied by Si and Li and that there is no Si located on the $4b$ site.

A joint Rietveld refinement of the powder neutron diffraction data at 300 K and of the Mo powder X-ray diffraction data at the same temperature with a single structural model was carried out, proving the accuracy of the two methods. All structures were visualized using VESTA.²⁹

Single Crystal X-ray Structure Determination. Single crystals of $\text{Li}_{14}\text{SiP}_6$ were obtained by a high-temperature reaction of the reactive mixture in a corundum crucible, which was sealed in a steel ampule under Ar. The pressed sample was annealed for 6 h at 1273 K (heating rate: 4 K min^{-1}), slowly cooled to 973 K (cooling rate: 0.05 K min^{-1}), and quenched after another 8 h in water.

A single crystal of $\text{Li}_{14}\text{SiP}_6$ was isolated and sealed in a glass capillary (0.1 mm). For diffraction data collection, the capillary was positioned in a 150 K cold N_2 gas stream. Data collection was performed with a STOE StadiVari (Mo $K\alpha_1$ radiation) diffractometer equipped with a DECTRIS PILATUS 300 K detector. The structure was solved by direct methods (SHELXS-2014) and refined by full-matrix least-squares calculations against F^2 (SHELXL-2014).³⁰

Elemental Analyses. Elemental analyses were performed by the microanalytical laboratory at the Department of Chemistry of the Technische Universität München. The amount of lithium in the samples was analyzed via atomic absorption spectroscopy using a 280FS AA spectrometer (Agilent Technologies). The amount of phosphorus was determined by photometry applying both the vanadate method and the molybdenum blue method, leading to almost identical values. The amount of silicon was also determined photometrically via silicon molybdate. To overcome disturbances of phosphorus and lithium, blank tests have been applied to calculate occurring deviations. The corresponding photometric analyses were carried out using a Cary UV–vis spectrometer (Agilent Technologies).

The analyses reveal the following composition: lithium 29.4%, silicon 8.23%, and phosphorus 57.89% (vanadate method) or 57.68% (molybdenum blue method). The observed overall loss of about 5% may be caused by abrasion of small amounts of WC during ball milling and impurities within the educts (e.g., purity of $\text{Li} \geq 99\%$ or $\text{P} \geq 97\%$) or formation of volatile decomposition products. Conversion and scaling of the determined values result in a stoichiometry of $\text{Li}_{13.64}\text{Si}_{0.94}\text{P}_6$.

Differential Scanning Calorimetry (DSC). For the investigation of the thermal behavior of the compounds a Netzsch DSC 404 Pegasus device was used. Niobium crucibles were filled with the samples and sealed by arc-welding. Empty sealed crucibles served as a reference. Measurements were performed under an Ar flow of 75 mL min^{-1} and a heating/cooling rate of 10 K min^{-1} . Data collection and handling was carried out with the Proteus Thermal Analysis program.³¹

Solid-State NMR Spectroscopy. Magic angle spinning (MAS) NMR spectra have been recorded on a Bruker Avance 300 NMR device operating at 7.04 T by the use of a 4 mm ZrO_2 rotor. The resonance frequencies of the investigated nuclei are 44.167, 59.627, and 121.495 MHz for ^6Li , ^{29}Si , and ^{31}P , respectively. The rotational frequency was set to 8 kHz (^{29}Si), 12 kHz (^{31}P), and 15 kHz (^6Li and ^{31}P). The MAS NMR spectra have been acquired at room temperature with recycle delays from 10 to 45 s and 200 to 1064 scans. All spectra regarding ^6Li were referenced to LiCl (1 M, aq) and LiCl (s), offering chemical shifts of 0.0 and -1.15 ppm, respectively. Tetrakis(trimethylsilyl)silane was used as an external standard for the ^{29}Si spectra, showing a chemical shift of -9.84 ppm referred to tetramethylsilane. The ^{31}P spectra were referred to ammonium dihydrogen phosphate (s) with a chemical shift of 1.11 ppm regarding concentrated H_3PO_4 . All spectra were recorded using single pulse excitation.

Static ^7Li single pulse acquisition NMR experiments have been performed using a Bruker Avance III spectrometer operating at a magnetic field of 7.04 T employing a 4 mm WVT MAS probe. The resonance frequency of the measured ^7Li nucleus is 116.642 MHz. The sample has been sealed in a 4 mm glass tube to avoid contact with air and moisture. The temperature calibration for the measurements has been performed using the temperature-dependent ^{207}Pb NMR shift of lead nitrate as chemical shift thermometer, which has also been measured in a sealed glass tube. The static ^7Li NMR measurements were carried out in the temperature range from room temperature to 147 K with recycle delays from 1 to 60 s and 4 scans. All spectra were referenced to LiCl (9.7 M, aq), for ^7Li .

Impedance Spectroscopy and DC Conductivity Measurements. The ionic conductivity of $\text{Li}_{14}\text{SiP}_6$ was determined by electrochemical impedance spectroscopy (EIS) in an in-house-designed cell. The setup consists of two stainless-steel current collectors, a stainless-steel casing, a PEEK tube, hardened stainless-steel dies, and pistons comprising a gasket for tightening the cell as well as six screws for fixing the cell (see Figure S12). Powdered samples of $\text{Li}_{14}\text{SiP}_6$ (510 mg) were placed between two 8 mm dies, and the screws were fastened with a torque of 30 N m (corresponding to a theoretic pressure of 480 MPa), compressing the samples to 79% of the crystal density. For the determination of the compressed pellet thickness, six holes in a symmetric configuration were drilled into the current collectors, and the distance in between was measured using a precision caliper. Impedance spectra were recorded on a Bio-Logic potentiostat (SP-200) in a frequency range from 3 MHz to 50 mHz at a potentiostatic excitation of ± 50 mV. Data were treated using the software EC-Lab (V 11.26). The measurements were performed in an Ar-filled glovebox at 298 K. The electronic conductivity was determined with the same setup using a potentiostatic polarization applying voltages of 50, 100, and 150 mV for 16 h each. For the determination of the activation energy of the lithium ion conduction, the cell temperature was set to 273, 298, 313, 333, and 353 K using a climate chamber (ESPEC, LU-114). The exact temperature profile is described in the Supporting Information as well as in Figure S13. Prior to EIS measurements, the cell rested 120 min to allow for thermal equilibration. EIS measurements were performed at both heating and cooling cycles. Temperature-dependent measurements were conducted

outside the glovebox, and the pistons were additionally greased to ensure a tight sealing of the cell from the ambient environment.

DFT Simulations. Density functional theory (DFT) total energy computations and DFT-based molecular dynamics (MD) simulations were carried out to complement the experimentally derived structures. Comparable DFT-MD techniques were recently used to study the related Li_2SiP_2 system.³² Here, however, the presence of sites with fractional occupations make it necessary to construct a supercell model in which all atoms are located on discrete sites (Supporting Information). Such a supercell provides an approximant for the disordered structure but incurs substantial computational cost. Specifically, we used a $3 \times 3 \times 3$ expansion of the conventional unit cell, ensuring an approximately isotropic distribution of Si atoms on the 8c position (such as to avoid close Si...Si contacts) and assessed different discrete occupation models for the Li-containing sites. Total-energy computations using CASTEP³³ confirmed that a full occupation of the position 8c and a vacancy formation on 4b is preferred over the alternative scenario of vacancy formation on 8c ("vacancy formation" here being equivalent to a fractional occupation of that site), by up to $\sim 10 \text{ kJ mol}^{-1}$ in static computations (Figure S16), qualitatively corroborating the experimental refinement results. For the final 378-atom supercell model, high-temperature DFT-MD simulations were carried out using cp2k.³⁴ The system was gradually heated to 1300 K (30 ps), held at 1023 K (2.5 ps), followed by a production run at that temperature (5 ps), all with a time step of 0.5 fs. Details of the protocol are provided as Supporting Information.

3. RESULTS AND DISCUSSION

Syntheses and Structure of $\text{Li}_{14}\text{SiP}_6$. For the search of novel Li-rich compositions we investigated stoichiometric ratios along the line connecting Li_3P and Li_8SiP_4 in the composition triangle of the ternary system Li/Si/P (Figure 1). Extrapolation of this sequence to higher amounts of lithium by the formal addition of " Li_3P " units results in the nominal compositions " $\text{Li}_{11}\text{SiP}_5$ ", " $\text{Li}_{14}\text{SiP}_6$ ", " $\text{Li}_{17}\text{SiP}_7$ ", and " $\text{Li}_{20}\text{SiP}_8$ ". Materials of these compositions were prepared applying a recently described preparative route for phosphidotetrelates starting from mechanical alloying of the elements in stoichiometric amounts, followed by a high-temperature reaction of the mixtures in sealed, carbon-coated silica glass ampules.¹⁹ After the mechanical alloying process, powder X-ray diffraction (PXRD) data reveal the initial formation of a cubic anti-fluorite structure type. However, the extremely broadened reflections indicate small crystal sizes. Additionally, at that stage an intense and broad X-ray amorphous halo implies the presence of large amounts of glassy phases. The microcrystalline, single-phase $\text{Li}_{14}\text{SiP}_6$ is obtained by quenching the hot ampule with the ball-milled product in water after 6–18 h of annealing at 973 K. Variation of annealing time within that frame does not lead to detectable differences in the crystal structure or sample purity. Simultaneous refinement of powder Mo X-ray and neutron diffraction shows a high agreement of the two methods and confirms the structure model (Figure 2). Details of the Rietveld refinements are shown in Table 1.

Experiments with the nominal stoichiometry of " $\text{Li}_{11}\text{SiP}_5$ " in analogy to $\text{Li}_{14}\text{SiP}_6$ reveal a mixture of $\text{Li}_{14}\text{SiP}_6$ and Li_8SiP_4 ,¹⁸ whereas investigations of compositions with a higher amount of lithium and phosphorus (" $\text{Li}_{17}\text{SiP}_7$ " and " $\text{Li}_{20}\text{SiP}_8$ ") lead to a mixture of $\text{Li}_{14}\text{SiP}_6$ and Li_3P (Figure S3 in the Supporting Information). According to these results, $\text{Li}_{14}\text{SiP}_6$ is assumed to be the lithium-richest compound on the quasi-binary line between Li_3P and " Si_3P_4 ". Moreover, no significant phase width according to " $\text{Li}_{14-4x}\text{Si}_{1+x}\text{P}_6$ " is found at the Li_3P -rich side, while at the Li_3P -poor side a Si-enriched composition " $\text{Li}_{14-4x}\text{Si}_{1+x}\text{P}_6$ " seems to exist (Supporting Information).

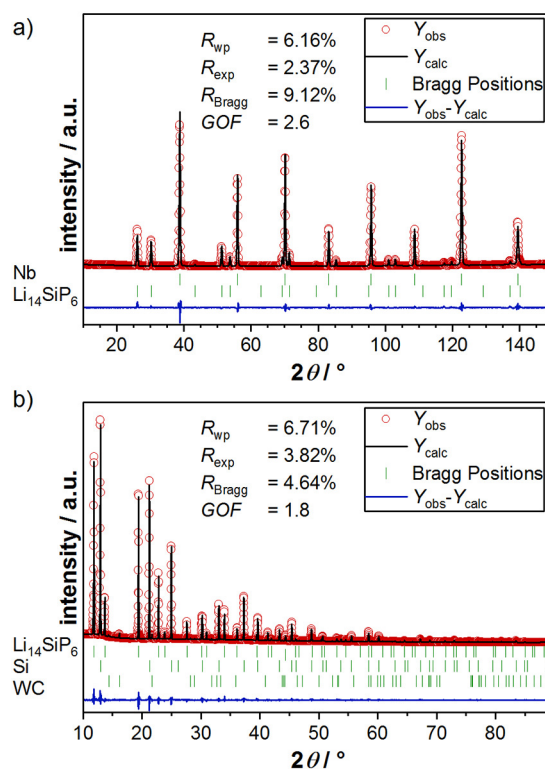


Figure 2. Results from the joint Rietveld refinement of $\text{Li}_{14}\text{SiP}_6$. (a) Rietveld analysis of the powder neutron diffraction pattern ($\lambda = 1.5482 \text{ \AA}$) of $\text{Li}_{14}\text{SiP}_6$ at 300 K. (b) Rietveld analysis of the powder X-ray diffraction pattern ($\lambda = \text{Mo K}\alpha_1$) of $\text{Li}_{14}\text{SiP}_6$ at 300 K. In both diffraction patterns red circles indicate observed intensities Y_{obs} , black lines show calculated intensities Y_{calc} , blue lines reveal the difference between observed and calculated intensities, and green marks indicate Bragg positions of $\text{Li}_{14}\text{SiP}_6$ and Nb (ampule) or $\text{Li}_{14}\text{SiP}_6$, Si (added as internal standard to the PXRD sample) and WC (abrasion), respectively.

Table 1. Details of the Joint Rietveld Structure Refinement of $\text{Li}_{14}\text{SiP}_6$ from Neutron and X-ray Diffraction Measurements at 300 K

empirical formula	$\text{Li}_{2.33}\text{Si}_{0.17}\text{P}$ (neutron diffr.)	$\text{Li}_{2.33}\text{Si}_{0.17}\text{P}$ (X-ray diffr.)
T/K	300	
fw/g mol ⁻¹	51.86	
space group (no.)	$Fm\bar{3}m$ (225)	
unit cell params/ \AA	$a = 5.93927(1)$	
Z	4	
$V/\text{\AA}^3$	209.507(1)	
$\rho_{\text{calc}}/\text{g cm}^{-3}$	1.644	
diffracted beam	neutrons	X-rays
$\lambda/\text{\AA}$	1.5482	0.70926
2θ range/deg	9.0000–151.9000	10.0000–89.7860
R_p	4.62%	4.79%
R_{wp}	6.16%	6.71%
R_{exp}	2.37%	3.82%
χ^2	6.73	3.07
GOF	2.6	1.8
R_{Bragg}	9.12%	4.64%
R_t	5.79%	14.8%
depository no.	CSD-1915806	CSD-1915824

The lithium-rich compound $\text{Li}_{14}\text{SiP}_6$ crystallizes in the Li_3Bi structure type³⁵ with the cubic space group $Fm\bar{3}m$ (no. 225) and

a lattice parameter of 5.915 66(6) Å at 4 K (Figure 3). The crystal structure was determined from the data of a single crystal

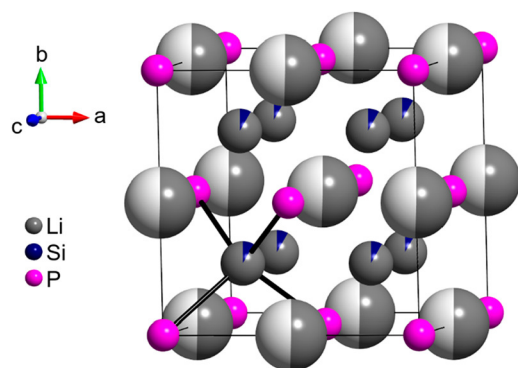


Figure 3. Structure of $\text{Li}_{14}\text{SiP}_6$ at 4 K. P atoms, mixed Li/Si sites, and partially occupied Li sites are depicted as pink, gray/indigo, and gray/white displacement ellipsoids, respectively, set at 90% probability. Black lines mark (Li/Si)–P bonds resulting in (Li/Si) $_4$ tetrahedra.

X-ray diffraction measurement at 123 K, from temperature-dependent powder neutron diffraction measurements between 4 and 1023 K, and from a simultaneous refinement of powder neutron and X-ray diffraction patterns obtained at 300 K. Atomic coordinates and anisotropic displacement parameters as well as the results from the powder neutron diffraction measurement at 4 K and from the single crystal X-ray diffraction at 123 K are given in the [Supporting Information](#).

The unit cell of $\text{Li}_{14}\text{SiP}_6$ contains three crystallographic atom positions (P1, Li1/Si1, and Li2). The structure is closely related to the anti-fluorite type of structure, as it is based on a cubic close packing (ccp) of P atoms on the $4a$ site, with all tetrahedral voids ($8c$ site) fully occupied by Li1 and Si1 atoms in a mixed occupancy ratio of 11:1. Additionally, all octahedral voids ($4b$ site) are occupied by Li atoms (Li2) with a probability of 50%. All interatomic Si–P (2.561 6(1) Å; due to symmetry identical: Li1–P, Li2–Si, Li1–Li2), Li2–P (2.969 64(1) Å), and P–P distances (4.199 70(1) Å) are within the range of those found for related ternary or binary compounds such as Li_8SiP_4 ,¹⁸ Li_2SiP_2 ,^{18,25} LiSi_2P_3 ,²⁵ $\text{Li}_{10}\text{Si}_2\text{P}_6$,²⁴ Li_3P ,³⁶ and $\text{Li}_{17}\text{Si}_4$.³⁷ As a consequence of the occupational disorder of Li1 and Si1, the structure contains $[\text{SiP}_4]^{8-}$ tetrahedra (ortho-phosphidosilicate) and P^{3-} ions in a ratio of 1:2; the negative charge is compensated by 14 lithium ions located in close vicinity.

Despite the structural similarity of $\text{Li}_{14}\text{SiP}_6$ to the Li_3Bi structure type, the compositionally related compound Li_3P crystallizes in a different structure type (space group: $P6_3/mmc$). Whereas $\text{Li}_{14}\text{SiP}_6$ derives from a ccp of P atoms, Li_3P can be derived from a hexagonal close packing of P atoms. In this structure the tetrahedral voids and the trigonal faces shared by octahedral voids are occupied with Li. In $\text{Li}_{14}\text{SiP}_6$, Li also fills tetrahedral voids, but is additionally centered in octahedral voids. The variances in the structure suggests a stabilization of the cubic phase by the introduction of Si atoms that covalently bind to four P atoms. Due to the conservation of charge balance, the incorporation of Si (or formal Si^{4+}) reduces the amount of Li^+ by a factor of 4, which in consequence leads to a partially filled Li position ($8c$ site).

In $\text{Li}_{14}\text{SiP}_6$, the presence of isolated tetrahedral SiP_4 anions is confirmed by the ^{29}Si MAS NMR spectrum showing one distinct resonance at 10.4 ppm (Figure S8 in the Supporting Information), which is rather close to the value of 11.5 ppm

observed for discrete $[\text{SiP}_4]^{8-}$ tetrahedra in Li_8SiP_4 , whereas the signals of covalently connected tetrahedra occur in the range from -3.3 to -14.8 ppm as observed for Li_2SiP_2 and $\text{Li}_3\text{Si}_3\text{P}_7$.^{18,24}

Although the crystal structure contains only one crystallographic P site, two broad, distinct signals are detected in the ^{31}P MAS NMR spectra at -226.9 and -316.8 ppm (12 kHz, Figure S9 in the Supporting Information). In spite of the disorder of Li and Si, the P atoms are situated in different chemical environments—surrounded by either eight Li atoms or by one Si atom and seven Li atoms in the neighboring tetrahedral voids—and by a different number of atoms in the six, partially filled octahedral voids. These considerably different chemical environments lead to a strong broadening of the signals.³⁸ As observed in the ^{31}P MAS NMR spectra of related compounds,^{18,24} a covalent Si–P bond has a significant effect on the chemical shift: the lower the number of neighboring Si atoms and thus the higher the negative partial charge of the P atom, the stronger the upfield shift of the signal. Consequently, the signal at -226.9 ppm can be assigned to the terminal phosphorus atoms in the covalently bound $[\text{SiP}_4]^{8-}$ units that matches well the characteristic range of terminal phosphorus atoms of $[\text{SiP}_4]^{8-}$ tetrahedra in Li_8SiP_4 ¹⁸ and $\text{Li}_{10}\text{Si}_2\text{P}_6$,²⁴ whereas the signal at -316.8 ppm is assigned to the isolated P^{3-} units without covalent bonds and surrounded by eight lithium ions in a cubic arrangement.

According to the ratio of one $[\text{SiP}_4]^{8-}$ tetrahedron containing four P atoms and two P^{3-} anions, the ratio of the total integrated intensity of the two ^{31}P NMR signals should be 2:1. The slightly higher experimental ratio of 2.3:1 (12 kHz) either results from an overlap of the signals with the spinning sidebands of the respective adjacent signals, as their accessible spinning frequencies are in the range of the chemical shift difference of the two signals, or indicates the additional presence of bridging P atoms between edge- or corner-sharing SiP_4 tetrahedra. Such bridging P atoms might cause a larger shift between -120 and -240 ppm,^{18,24,38} which could overlap with the signals of terminal P atoms. However, the probability of a subsequent occupation of neighboring tetrahedral voids by Si atoms leading to sharing corners or edges of SiP_4 tetrahedra should be rather small, owing to the electrostatic repulsion of the formally 4-fold positively charged Si atoms.

As known from all other lithium phosphidosilicates, the ^6Li MAS NMR spectrum of $\text{Li}_{14}\text{SiP}_6$ shows only one signal at 5.4 ppm (Figure S7 in the Supporting Information).^{18,24,25}

Thermal Properties of $\text{Li}_{14}\text{SiP}_6$. In order to apply the maximum entropy method at 1023 K, $\text{Li}_{14}\text{SiP}_6$ was studied by temperature-dependent powder neutron diffraction experiments. Within the investigated temperature range from 4 to 1023 K, the unit cell parameter increases from 5.9158(1) to 6.0785(3) Å in the lower temperature range. Between 623 and 673 K $\text{Li}_{14}\text{SiP}_6$ decomposes entirely, indicating a fast transition. The phase mixture is thermodynamically stable up to temperatures between 873 and 923 K. The lithium-rich phase $\text{Li}_{14}\text{SiP}_6$ reappears at 923 K with a proportion of about 80% and is completely converted at 973 K (Figure 4). During these transition processes all Bragg reflections of the involved compounds remain distinct with narrow line widths, suggesting the formation of large crystal domains. The transition temperatures are confirmed by DSC of $\text{Li}_{14}\text{SiP}_6$, and the corresponding evaluation is given as [Supporting Information](#).

The supplementary evaluation of the executed Rietveld refinements from temperature-dependent neutron diffraction

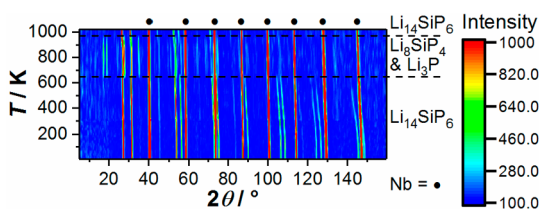


Figure 4. 2D plot of the data of temperature-dependent neutron diffraction measurements from 4 to 1023 K in a 2θ range from 5° to 160° (sample sealed under Ar). With increasing temperature $\text{Li}_{14}\text{SiP}_6$ decomposes into Li_8SiP_4 and Li_3P and is re-formed again. The ampule material Nb is indicated with solid circles.

experiments exhibited a nonlinear increase of the lattice parameters of $\text{Li}_{14}\text{SiP}_6$ upon heating (Figure 5). Furthermore,

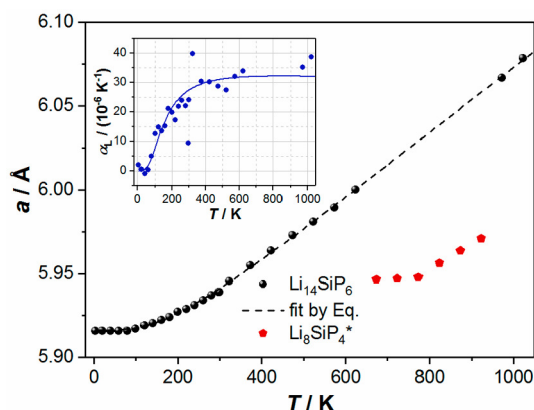


Figure 5. Thermal dependence of the lattice parameters a and of the thermal expansion coefficient (calculated as $a_1(T) = \partial \ln(a(T))/\partial T$) of the $\text{Li}_{14}\text{SiP}_6$ sample upon heating under Ar. The normalized $a/2$ lattice parameters for the intermediate phase Li_8SiP_4 are shown by red points.

the quasi-linear trend of increasing lattice parameters observed prior to the phase transition is continued at 973 and 1023 K, indicating a complete recovery of the initial structure obtained via quenching. The lattice dimension of Li_8SiP_4 , as normalized to formula units, has been found systematically smaller and is characterized by a lower thermal expansion rate than that of $\text{Li}_{14}\text{SiP}_6$.

Similar to other thermodynamic quantities, the temperature evolution of the lattice dimensions and, correspondingly, the thermal expansion can be modeled. As it has been shown in previous studies,^{39–41} the thermal dependency of the lattice parameter can be modeled by means of the first-order Grüneisen approximation:

$$V(T) = (a(T))^3 = V_0 + \frac{\gamma}{K_T} U(T)$$

$$= V_0 + \frac{\gamma}{K_T} \left[9Nk_B T \left(\frac{T}{\theta_D} \right)^3 \int_0^{\theta_D/T} \frac{x^3}{e^x - 1} dx \right] \quad (1)$$

where V_0 denotes the hypothetical cell volume at zero temperature, γ is the Grüneisen constant, K_T is the bulk modulus, and U is the internal energy of the system. Both γ and K_T are assumed to be temperature independent, and the use of the Debye approximation for the internal energy U in eq 1 with the characteristic temperature θ_D usually provides a reasonable description.

The least-squares minimization fit of the experimental temperature dependence of cell volumes by eq 1 yields $207.093 \pm 0.066 \text{ \AA}^3$, $2507 \times 10^{-14} \pm 37 \times 10^{-14} \text{ Pa}^{-1}$ and $659 \pm 31 \text{ K}$ for V_0 , the γ/K_T ratio, and θ_D , respectively. The fit was characterized by a high coefficient of determination, 0.999965, and the graphical results are shown in Figure 5 by dashed lines.

The linear thermal expansion coefficient was calculated from the thermal evolution of the lattice parameter via $a_1(T) = \partial \ln(a(T))/\partial T$, and the result is shown in the inset of Figure 5. The thermal expansion of $\text{Li}_{14}\text{SiP}_6$ grows upon heating from 0 K to ca. $27.5 \times 10^{-6} \text{ K}^{-1}$ and becomes almost temperature independent, $\alpha_1 = 32 \times 10^{-6} \text{ K}^{-1}$, above 500 K, which is corresponding to ca. $0.8 \theta_D$, indicating a quasi-classical behavior of $\text{Li}_{14}\text{SiP}_6$ at these temperatures.

Lithium Ion Mobility. The dynamic behavior of the lithium ions was investigated via the temperature-dependent evolution of the static ^7Li NMR line width in the relevant temperature range. Since the central transition of the $I = 3/2$ nucleus ^7Li is only broadened by the homo- ($^7\text{Li}-^7\text{Li}$) and heteronuclear (here: $^7\text{Li}-^{31}\text{P}$) dipolar couplings, and both types of interactions scale with the second Legendrian ($3 \cos^2 \beta - 1$), any dynamic process should produce a (partial) averaging of the orientational dependence and hence entail a narrowing of the NMR line.

The temperature-dependent evolution of the ^7Li NMR spectra is shown in Figure 6a. Only one Lorentzian-shaped

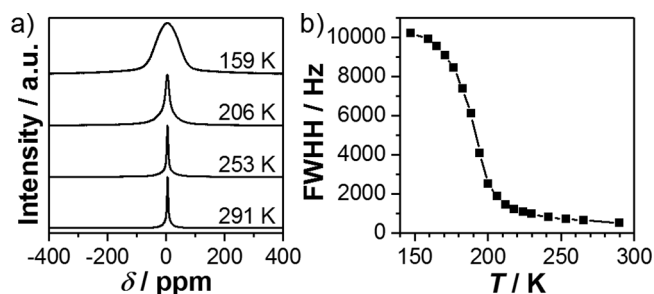


Figure 6. (a) ^7Li NMR spectra of $\text{Li}_{14}\text{SiP}_6$ recorded at different temperatures. (b) Evolution of the temperature-dependent ^7Li line widths of $\text{Li}_{14}\text{SiP}_6$. The solid line serves only as a guide to the eye.

signal at 4.8 ppm is visible at room temperature with a line width of 523 Hz. Upon cooling of the $\text{Li}_{14}\text{SiP}_6$ sample, this signal gradually broadens and develops a Gaussian line shape with a line width of 10.2 kHz at 147 K. Figure 6b shows the temperature-dependent evolution of the line width (fwhh) of the static ^7Li measurements. A rough estimation of the activation energy can be done by the empirical Waugh–Fedin relation, $E_A^{\text{NMR}} = 0.156 T_{\text{onset}}$. The onset temperature was determined to be 190 K, which leads to an activation energy of 30 kJ mol^{-1} ($\sim 0.31 \text{ eV}$).

In addition, the lithium ion conductivity of $\text{Li}_{14}\text{SiP}_6$ was determined from impedance measurements in a blocking electrode configuration. Impedance spectra at different temperatures (273, 298, 313, 333, and 353 K, according to the temperature profile shown in the inset) are displayed in Figure 7a, featuring a semicircle at high frequencies and a low-frequency tail. The semicircle can be described as parallel circuit element of a resistor and a constant phase element (R/Q), with R representing both intragrain and grain boundary contributions to the lithium ion transport, which could not be resolved, and thus only the total ionic resistance of the sample could be determined. The fitted α values (>0.98) of the constant phase

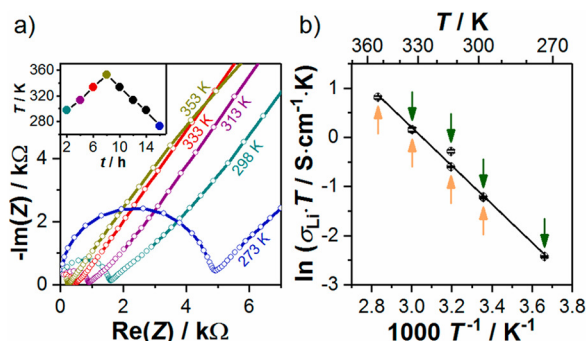


Figure 7. (a) Nyquist plot of $\text{Li}_{14}\text{SiP}_6$ measured under blocking conditions, with spectra recorded at temperatures between 273 and 353 K during a heating cycle, according to color coding of the inset, which shows the temperature profile of a cycle for these temperature-dependent measurements. Colored dots indicate the temperatures at which impedance was measured. (b) Arrhenius plot of the product of conductivity and temperature ($\sigma_{\text{Li}} T$) obtained in the heating as well as in the cooling branch, with error bars for each based on the standard deviation from independent measurements with three cells; the shown linear fit through both branches was used to obtain the activation energy $E_{\text{A}}^{\text{PEIS}}$. Since the differences of the average ($\sigma_{\text{Li}} T$) values obtained during heating vs cooling are very small, they are marked by the orange and green arrows, respectively.

elements are reasonable close to 1; hence, the constant phase exponent was neglected, in which case the Q parameter becomes essentially equivalent to a capacitance, with a value of $\sim 4.2 \times 10^{-10}$ F for 298 K. This value lies in between the typical range for intragrain ($\sim 10^{-12}$ F) and grain boundary ($\sim 10^{-9}$ F) capacitances.⁴² The ionic conductivity was determined to be $\sigma_{\text{Li}}(\text{Li}_{14}\text{SiP}_6) = (1.09 \pm 0.06) \times 10^{-3} \text{ S cm}^{-1}$ at 298 K (obtained from three independently measured cells). The activation energy for lithium ion transport (Figure 7b) is investigated by temperature-dependent impedance measurements in a range from 273 to 353 K, yielding an $E_{\text{A}}^{\text{PEIS}}$ of $32.2 \pm 0.6 \text{ kJ mol}^{-1}$ ($\sim 0.33 \text{ eV}$); this was determined from three independently measured cells, using the $\sigma_{\text{Li}} T$ values of only the first heating and cooling cycle of each sample. The temperature ramp of a heating and cooling cycle is displayed in the inset of Figure 7a. Colored dots indicate at which temperatures PEIS measurements were performed. In this context it shall be mentioned that conductivities (and thus the product of $\sigma_{\text{Li}} T$) for heating and cooling differ by less than 5% at 298 and 333 K, whereas at 313 K

the $\sigma_{\text{Li}} T$ values obtained in the cooling branch are clearly higher than those obtained in the heating branch (by $\sim 58\%$), although the cell was in thermal equilibrium. This hysteresis was reproducibly observed for all measured cells of this compound (three independently built and measured cells) and hence is no artifact, but rather must be a compound-related phenomenon. The exact reason for the observed hysteresis is still under investigation. Error bars are calculated separately for heating and cooling steps by taking the mean of three independent measurements. DC polarization measurements in the range from 50 to 150 mV reveal an electronic conductivity of $(1.64 \pm 0.04) \times 10^{-7} \text{ S cm}^{-1}$ at 298 K (based on the standard deviation of three cells).

Lithium Diffusion Pathways in $\text{Li}_{14}\text{SiP}_6$. In $\text{Li}_{14}\text{SiP}_6$ only lithium (in its natural isotope composition) possesses a negative scattering length ($b_{\text{Li}} = -1.9 \text{ fm}$). This is very beneficial, since the study of experimental lithium diffusion pathways may be limited to the analysis of the distribution of negative components in nuclear density maps. Accurate nuclear density maps were extracted from the experimental structure factors and phases measured at 1023 K by the maximum entropy method (MEM). This method in general is based on the estimation of 3D scattering densities from a limited amount of information by maximizing information entropy under restraints, consistent with experimental observations.⁴³ Compared to Fourier analysis the MEM often delivers more accurate electron/nuclear density maps from powder diffraction data sets having “limited” statistics; that is, termination effects and artifacts of various kinds often occur to be less pronounced in MEM evaluations.

Negative nuclear density maps for $\text{Li}_{14}\text{SiP}_6$ reconstructed from experimental structure factors using the program Dynomia⁴⁴ are plotted in Figure 8. The MEM analysis of the nuclear densities yields 3D lithium diffusion pathways in $\text{Li}_{14}\text{SiP}_6$ involving both of the lithium sites 4b and 8c. Large sphere-like volumes on negative nuclear density maps correspond to the lithium location and are connected by well-resolved necks, which define the energy barrier for lithium diffusion in $\text{Li}_{14}\text{SiP}_6$. As illustrated, it is obvious that there is a connection between face-sharing tetrahedral and octahedral voids. Thus, neither lithium diffusion via edge-sharing tetrahedral voids nor a lithium ion hopping mechanism between edge-sharing octahedral voids could be ascertained for $\text{Li}_{14}\text{SiP}_6$. The latter is also hindered by the large interatomic distances of the adjacent Li2 atoms centered in the octahedral voids (4b).

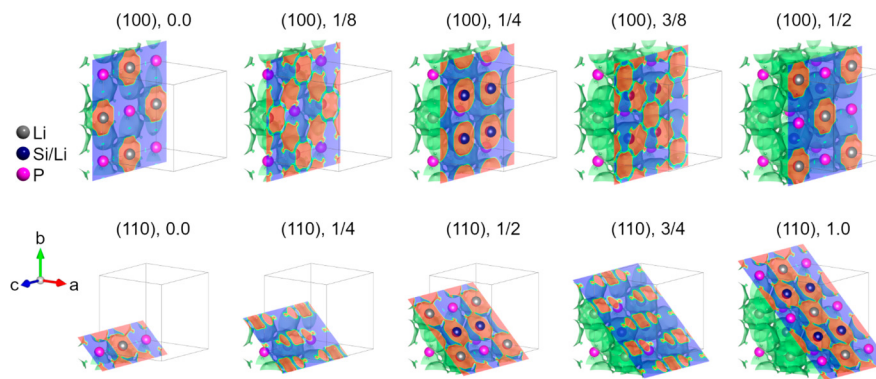


Figure 8. Negative nuclear density distribution in $\text{Li}_{14}\text{SiP}_6$ reconstructed from experimental structure factors at 1023 K using the maximum entropy method (surface threshold $-0.01 \text{ fm}/\text{\AA}^3$, cell grid $256 \times 256 \times 256$) for various lattice planes defined by Miller indices (h, k, l) and number of position. Li, P, and mixed Li/Si sites are shown as gray, pink, and dark blue spheres, respectively.

The lithium motion, which is visualized in Figure 9a, occurs from the 8c site (Li1) to a vacancy on the 4b site. Interestingly

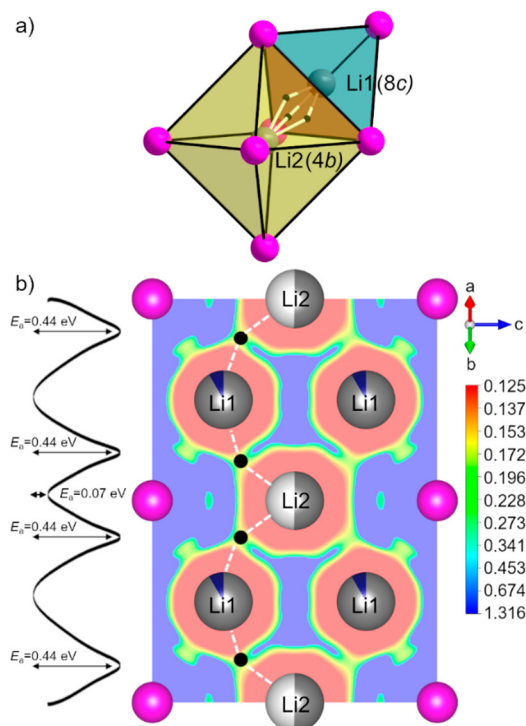


Figure 9. (a) Sketch of diffusion pathways in $\text{Li}_{14}\text{SiP}_6$ between face-sharing tetrahedral (8c) and octahedral voids (4b) indicated by white lines going straight through the neck ● at the general position (0.40276 | 0.59724 | 0.305). Li and P are shown as gray and pink spheres, respectively. (b) The 2D section cut (110, $d = 1.0$ plane) of the lithium one-particle-potential (OPP, red $\hat{=}$ low, blue $\hat{=}$ high) and its schematic 1D section along dashed lines connecting five Li atoms in a chain Li2-●-Li1-●-Li2-●-Li1-●-Li2, where ● corresponds to the neck connecting neighboring sites with partial Li occupations. Li, P, and mixed Li/Si sites are shown as gray, pink, and dark blue spheres, respectively.

the diffusion does not occur along the direct connection (shortest distance) between the two adjacent sites 8c and 4b, but proceeds via a well-defined neck (i.e., ●) with the lattice coordinates of 96k (0.40276 | 0.59724 | 0.305) and ..m site symmetry.

Assuming a quasi-classical behavior of $\text{Li}_{14}\text{SiP}_6$ at temperatures above 500 K, the experimental nuclear/probability densities can be analyzed in the form of an activation energy landscape. Since the lithium is the only negative scatterer in $\text{Li}_{14}\text{SiP}_6$, the one-particle potential (OPP) for lithium was recalculated from negative nuclear densities. Its 2D distribution in the (110, $d = 1.0$) plane is shown in Figure 9b. The direct Li1–Li2 pathway is characterized by an activation barrier larger than 1.4 eV ($\sim 135 \text{ kJ mol}^{-1}$) at 32f (0.36 | 0.64 | 0.36). A sufficiently lower activation barrier of 0.44 eV ($\sim 42 \text{ kJ mol}^{-1}$) occurs along the pathway involving the previously mentioned neck at 96k, i.e., Li1-●-Li2. The small activation barrier at the Li2 site is considered as an artifact of the data evaluation.

While it is not feasible for DFT simulations to map out all atomistic diffusion pathways in the system, due to the presence of disorder (which formally makes all pathways inequivalent and requires a supercell approximant; Methods section), we did perform DFT-based MD simulations at high temperature that

qualitatively corroborate the mechanism for lithium diffusion in the title compound. At a simulation temperature around that of the MEM analysis (1023 K), the Li atoms are seen to be highly mobile and frequently change positions (Figure 10a,b); several

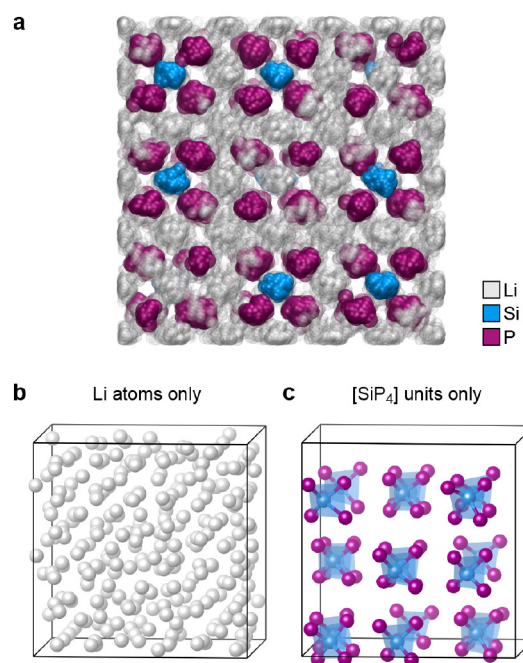


Figure 10. DFT-MD modeling of Li^+ dynamics in $\text{Li}_{14}\text{SiP}_6$. (a) Snapshots from a trajectory at around 1023 K, showing atoms as partially translucent spheres (Li/Si, smaller; P, larger) and overlaying 100 equidistant images to provide an impression of the atomic mobility. The cell has been shifted by $(a/4, a/4, 0)$ to ease visualization. (b) Final image of the simulation, showing the Li atoms only and indicating the boundaries of the simulation cell by a thin line. (c) Same but showing only the Si atoms and the P atoms in their direct vicinity; the tetrahedral $[\text{SiP}_4]^{8-}$ units remain intact during the simulation, as emphasized by shading. Structures were visualized using VMD⁴⁵ and VESTA.²⁹ Details of the supercell model construction are provided as Supporting Information.

instances of Li atom motion across the 8c and 4b sites were observed in the DFT-MD trajectory. On the other hand, the heavier Si and P atoms show thermal vibrations, but the *ccp*-like anion sublattice and the $[\text{SiP}_4]^{8-}$ units remained intact otherwise during our simulation, providing further evidence for the validity of the structural model (Figure 10c). At such high temperature, the structure could be viewed as a framework of isolated $[\text{SiP}_4]^{8-}$ and P^{3-} units between which the Li atoms are readily moving in all directions, consistent with the experimentally observed Li mobility even at much lower temperature.

4. CONCLUSION

The so far lithium-richest phosphidosilicate $\text{Li}_{14}\text{SiP}_6$ crystallizes in the highly symmetric space group $Fm\bar{3}m$ (no. 225). The compound combines structural simplicity with P atoms forming a simple *ccp* atom arrangement with an intriguing degree of complexity, specifically mixed occupations, and high mobility of Li atoms. The formation of a cubic structure starts already during the mechanical milling process, as the powder X-ray diffraction experiments reveal the corresponding admittedly broadened but evident reflection pattern, and is finished upon a heat treatment at 973 K. DSC analyses and temperature-

dependent neutron diffraction experiments revealed a remarkable thermal behavior of the novel compound. $\text{Li}_{14}\text{SiP}_6$ is a high-temperature phase and decomposes at temperatures below 973 K into Li_8SiP_4 and Li_3P . The decomposition and re-formation proceeds within a distinct temperature range, and, therefore, in order to obtain pure $\text{Li}_{14}\text{SiP}_6$, rapid cooling of the samples after the heat treatment is essential. Structural analysis combining both neutron and X-ray diffraction methods as well as static and MAS solid-state NMR spectroscopy reveals a disorder of Si and Li atoms within the tetrahedral voids of the *ccp* of P atoms. An investigation of the negative nuclear density distribution via MEM affords a clearer understanding of the lithium ion motion within the crystal structure. The data show that the 3D lithium ion diffusion involves both *4b* and *8c* lithium sites and that it occurs preferably between face-sharing tetrahedral and octahedral voids. The material shows an ionic conductivity of about $1.1 \times 10^{-3} \text{ S cm}^{-1}$ at 298 K, an electronic conductivity of $1.6 \times 10^{-7} \text{ S cm}^{-1}$ at 298 K, and an activation energy of 30–32 kJ mol^{-1} . Hence, compared to the related compound Li_8SiP_4 , the incorporation of supplementary lithium ions as well as the structural change and the occurring cation disorder within the structure result in considerably increased ionic conductivity, higher mobility, and lower activation energy.^{18,19}

Since the first report of Li ion conductivity in lithium phosphidotetrelates,¹⁸ the ionic conductivity in $\text{Li}_{14}\text{SiP}_6$ reported here marks an increase over 2 orders of magnitude in this system within three years. With only a moderate number of known examples in hand, the reported conductivities almost match those of well-established crystalline lithium ion conductors,¹⁶ and a further enhancement of the ionic transport via manipulation by chemical, electronic, and structural means is anticipated. Further investigations on the electrochemical stability and performance of $\text{Li}_{14}\text{SiP}_6$ and future, related materials are necessary to provide information if this material class is conceivable for application in all-solid-state batteries.

■ ASSOCIATED CONTENT

Supporting Information

The Supporting Information is available free of charge on the ACS Publications website at DOI: 10.1021/jacs.9b05301.

Details of the crystal structure determination, coordination polyhedra, phase width analysis, DSC, ⁶Li, ²⁹Si, and ³¹P MAS NMR spectroscopy, EIS, and DFT simulations (PDF)

X-ray crystallographic data (CIF)

X-ray crystallographic data (CIF)

X-ray crystallographic data (CIF)

X-ray crystallographic data (CIF)

■ AUTHOR INFORMATION

Corresponding Author

*Thomas.faessler@lrz.tu-muenchen.de

ORCID

Wilhelm Klein: 0000-0002-6351-9921

Volker L. Deringer: 0000-0001-6873-0278

Leo van Wüllen: 0000-0002-2493-7258

Hubert A. Gasteiger: 0000-0001-8199-8703

Thomas F. Fässler: 0000-0001-9460-8882

Author Contributions

#S.S. and H.E. contributed equally to this work.

Notes

The authors declare no competing financial interest.

Additional data supporting this publication is available at <https://doi.org/10.17863/CAM.42985>.

■ ACKNOWLEDGMENTS

The work was carried out as part of the research project ASSB coordinated by ZAE Bayern. The project is funded by the Bavarian Ministry of Economic Affairs, Regional Development and Energy. V.L.D. acknowledges a Leverhulme Early Career Fellowship and support from the Isaac Newton Trust. This work used the ARCHER UK National Supercomputing Service via EPSRC Grant EP/P022596/1. The authors greatly acknowledge Tassilo Restle for DSC measurements and Johannes Landesfeind and Tanja Zünd for the design of the conductivity measurement cell.

■ REFERENCES

- (1) Janek, J.; Zeier, W. G. A Solid Future for Battery Development. *Nat. Energy* **2016**, *1*, 16141.
- (2) Kireeva, N.; Pervov, V. S. Materials Space of Solid-State Electrolytes: Unraveling Chemical Composition-Structure-Ionic Conductivity Relationships in Garnet-Type Metal Oxides Using Cheminformatics Virtual Screening Approaches. *Phys. Chem. Chem. Phys.* **2017**, *19*, 20904–20918.
- (3) Richards, W. D.; Miara, L. J.; Wang, Y.; Kim, J. C.; Ceder, G. Interface Stability in Solid-State Batteries. *Chem. Mater.* **2016**, *28*, 266–273.
- (4) West, A. R. *Solid State Chemistry and its Applications*, 2nd ed.; student ed.; John Wiley & Sons, Ltd: West Sussex, UK, 2014.
- (5) Zeier, W. G.; Zhou, S.; Lopez-Bermudez, B.; Page, K.; Melot, B. C. Dependence of the Li-Ion Conductivity and Activation Energies on the Crystal Structure and Ionic Radii in $\text{Li}_6\text{MLa}_2\text{Ta}_2\text{O}_{12}$. *ACS Appl. Mater. Interfaces* **2014**, *6*, 10900–10907.
- (6) Kraft, M. A.; Culver, S. P.; Calderon, M.; Böcher, F.; Krauskopf, T.; Senyshyn, A.; Dietrich, C.; Zevalkink, A.; Janek, J.; Zeier, W. G. Influence of Lattice Polarizability on the Ionic Conductivity in the Lithium Superionic Argyrodites $\text{Li}_6\text{PS}_3\text{X}$ (X = Cl, Br, I). *J. Am. Chem. Soc.* **2017**, *139*, 10909–10918.
- (7) Kanno, R.; Hata, T.; Kawamoto, Y.; Irie, M. Synthesis of a New Lithium Ionic Conductor, thio-LISICON—Lithium Germanium Sulfide System. *Solid State Ionics* **2000**, *130*, 97–104.
- (8) Murayama, M.; Kanno, R.; Irie, M.; Ito, S.; Hata, T.; Sonoyama, N.; Kawamoto, Y. Synthesis of New Lithium Ionic Conductor thio-LISICON—Lithium Silicon Sulfides System. *J. Solid State Chem.* **2002**, *168*, 140–148.
- (9) Murayama, M.; Kanno, R.; Kawamoto, Y.; Kamiyama, T. Structure of the thio-LISICON, Li_4GeS_4 . *Solid State Ionics* **2002**, *154–155*, 789–794.
- (10) Deiseroth, H.-J.; Kong, S.-T.; Eckert, H.; Vannahme, J.; Reiner, C.; Zaiß, T.; Schlosser, M. $\text{Li}_6\text{PS}_3\text{X}$: A Class of Crystalline Li-Rich Solids with an Unusually High Li^+ Mobility. *Angew. Chem., Int. Ed.* **2008**, *47*, 755–758.
- (11) Kamaya, N.; Homma, K.; Yamakawa, Y.; Hirayama, M.; Kanno, R.; Yonemura, M.; Kamiyama, T.; Kato, Y.; Hama, S.; Kawamoto, K.; Mitsui, A. A Lithium Superionic Conductor. *Nat. Mater.* **2011**, *10*, 682–686.
- (12) Bron, P.; Johansson, S.; Zick, K.; Schmedt auf der Günne, J.; Dehnen, S.; Roling, B. $\text{Li}_{10}\text{SnP}_2\text{S}_{12}$: An Affordable Lithium Superionic Conductor. *J. Am. Chem. Soc.* **2013**, *135*, 15694–15697.
- (13) Kuhn, A.; Gerbig, O.; Zhu, C.; Falkenberg, F.; Maier, J.; Lotsch, B. V. A New Ultrafast Superionic Li-Conductor: Ion Dynamics in $\text{Li}_{11}\text{Si}_2\text{PS}_{12}$ and Comparison with other Tetragonal LGPS-Type Electrolytes. *Phys. Chem. Chem. Phys.* **2014**, *16*, 14669–14674.
- (14) Kato, Y.; Hori, S.; Saito, T.; Suzuki, K.; Hirayama, M.; Mitsui, A.; Yonemura, M.; Iba, H.; Kanno, R. High-Power All-Solid-State Batteries Using Sulfide Superionic Conductors. *Nat. Energy* **2016**, *1*, 16030.

- (15) Wang, B.; Chakoumakos, B. C.; Sales, B. C.; Kwak, B. S.; Bates, J. B. Synthesis, Crystal Structure, and Ionic Conductivity of a Polycrystalline Lithium Phosphorus Oxynitride with the γ - Li_3PO_4 Structure. *J. Solid State Chem.* **1995**, *115*, 313–323.
- (16) Bachman, J. C.; Muy, S.; Grimaud, A.; Chang, H.-H.; Pour, N.; Lux, S. F.; Paschos, O.; Maglia, F.; Lupart, S.; Lamp, P.; Giordano, L.; Shao-Horn, Y. Inorganic Solid-State Electrolytes for Lithium Batteries: Mechanisms and Properties Governing Ion Conduction. *Chem. Rev.* **2016**, *116*, 140–162.
- (17) Juza, R.; Schulz, W. Ternäre Phosphide und Arsenide des Lithiums mit Elementen der 3. und 4. Gruppe. *Z. Anorg. Allg. Chem.* **1954**, *275*, 65–78.
- (18) Toffoletti, L.; Kirchhain, H.; Landesfeind, J.; Klein, W.; van Wüllen, L.; Gasteiger, H. A.; Fässler, T. F. Lithium Ion Mobility in Lithium Phosphidosilicates: Crystal Structure, ^7Li , ^{29}Si , and ^{31}P MAS NMR Spectroscopy, and Impedance Spectroscopy of Li_8SiP_4 and Li_2SiP_2 . *Chem. - Eur. J.* **2016**, *22*, 17635–17645.
- (19) Eickhoff, H.; Strangmüller, S.; Klein, W.; Kirchhain, H.; Dietrich, C.; Zeier, W. G.; van Wüllen, L.; Fässler, T. F. Lithium Phosphidogermanates α - and β - Li_8GeP_4 —A Novel Compound Class with Mixed Li^+ Ionic and Electronic Conductivity. *Chem. Mater.* **2018**, *30*, 6440–6448.
- (20) Boyce, J. B.; Huberman, B. A. Superionic Conductors: Transitions, Structures, Dynamics. *Phys. Rep.* **1979**, *51*, 189–265.
- (21) Wang, Y.; Richards, W. D.; Ong, S. P.; Miara, L. J.; Kim, J. C.; Mo, Y.; Ceder, G. Design Principles for Solid-State Lithium Superionic Conductors. *Nat. Mater.* **2015**, *14*, 1026.
- (22) Carette, B.; Ribes, M.; Souquet, J. L. The Effects of Mixed Anions in Ionic Conductive Glasses. *Solid State Ionics* **1983**, *9–10*, 735–737.
- (23) Deng, Y.; Eames, C.; Fleutot, B.; David, R.; Chotard, J.-N.; Suard, E.; Masquelier, C.; Islam, M. S. Enhancing the Lithium Ion Conductivity in Lithium Superionic Conductor (LISICON) Solid Electrolytes through a Mixed Polyanion Effect. *ACS Appl. Mater. Interfaces* **2017**, *9*, 7050–7058.
- (24) Eickhoff, H.; Toffoletti, L.; Klein, W.; Raudaschl-Sieber, G.; Fässler, T. F. Synthesis and Characterization of the Lithium-Rich Phosphidosilicates $\text{Li}_{10}\text{Si}_2\text{P}_6$ and $\text{Li}_3\text{Si}_3\text{P}_7$. *Inorg. Chem.* **2017**, *56*, 6688–6694.
- (25) Haffner, A.; Bräuniger, T.; Johrendt, D. Supertetrahedral Networks and Lithium-Ion Mobility in Li_2SiP_2 and LiSi_2P_3 . *Angew. Chem., Int. Ed.* **2016**, *55*, 13585–13588.
- (26) WinXPow V3.0.2.1, 3.0.2.1; STOE & Cie GmbH: Darmstadt, Germany, 2011.
- (27) Hoelzel, M.; Senyshyn, A.; Juenke, N.; Boysen, H.; Schmahl, W.; Fuess, H. High-Resolution Neutron Powder Diffractometer SPODI at Research Reactor FRM II. *Nucl. Instrum. Methods Phys. Res., Sect. A* **2012**, *667*, 32–37.
- (28) Rodriguez-Carvajal, J.; Gonzales-Platas, J. *Full Prof Suite 2.05*; Institute Laue-Langevin Grenoble: France, 2011.
- (29) Momma, K.; Izumi, F. VESTA 3 for Three-Dimensional Visualization of Crystal, Volumetric and Morphology Data. *J. Appl. Crystallogr.* **2011**, *44*, 1272–1276.
- (30) Sheldrick, G. M. Crystal Structure Refinement with SHELXL. *Acta Crystallogr., Sect. C: Struct. Chem.* **2015**, *71*, 3–8.
- (31) *Proteus Thermal Analysis V4.8.2*; Netzsch-Gerätebau GmbH: Selb, 2006.
- (32) Yeandel, S. R.; Scanlon, D. O.; Goddard, P. Enhanced Li-Ion Dynamics in Trivalently Doped Lithium Phosphidosilicate Li_2SiP_2 : A Candidate Material as a Solid Li Electrolyte. *J. Mater. Chem. A* **2019**, *7*, 3953–3961.
- (33) Clark, S. J.; Segall, M. D.; Pickard, C. J.; Hasnip, P. J.; Probert, M. J.; Refson, K.; Payne, M. C. First Principles Methods Using CASTEP. *Z. Kristallogr. - Cryst. Mater.* **2005**, *220*, 567–570.
- (34) VandeVondele, J.; Krack, M.; Mohamed, F.; Parrinello, M.; Chassaing, T.; Hutter, J. Quickstep: Fast and Accurate Density Functional Calculations Using a Mixed Gaussian and Plane Waves Approach. *Comput. Phys. Commun.* **2005**, *167*, 103–128.
- (35) Zintl, E.; Brauer, G. Konstitution der Lithium Wismut Legierungen: 14. Mitteilung über Metalle u. Legierungen. *Z. Elektrochem.* **1935**, *41*, 297–303.
- (36) Dong, Y.; DiSalvo, F. J. Reinvestigation of Trilithium Phosphide, Li_3P . *Acta Crystallogr., Sect. E: Struct. Rep. Online* **2007**, *63*, No. i97–i98.
- (37) Zeilinger, M.; Benson, D.; Häussermann, U.; Fässler, T. F. Single Crystal Growth and Thermodynamic Stability of $\text{Li}_{17}\text{Si}_4$. *Chem. Mater.* **2013**, *25*, 1960–1967.
- (38) Franke, D.; Hudalla, C.; Maxwell, R.; Eckert, H. Phosphorus-31-Cadmium-113 and Phosphorus-31-Silicon-29 CP/MAS-NMR in Inorganic Semiconductors. *J. Phys. Chem.* **1992**, *96*, 7506–7509.
- (39) Vočadlo, L.; Knight, K. S.; Price, G. D.; Wood, I. G. Thermal Expansion and Crystal Structure of FeSi between 4 and 1173 K Determined by Time-of-Flight Neutron Powder Diffraction. *Phys. Chem. Miner.* **2002**, *29*, 132–139.
- (40) Senyshyn, A.; Boysen, H.; Niewa, R.; Banys, J.; Kinka, M.; Ya, B.; Adamiv, V.; Izumi, F.; Chumak, I.; Fuess, H. High-Temperature Properties of Lithium Tetraborate $\text{Li}_2\text{B}_4\text{O}_7$. *J. Phys. D: Appl. Phys.* **2012**, *45*, 175305.
- (41) Baran, V.; Dolotko, O.; Mühlbauer, M. J.; Senyshyn, A.; Ehrenberg, H. Thermal Structural Behavior of Electrodes in Li-Ion Battery Studied In Operando. *J. Electrochem. Soc.* **2018**, *165*, A1975–A1982.
- (42) Hodge, I. M.; Ingram, M. D.; West, A. R. Impedance and Modulus Spectroscopy of Polycrystalline Solid Electrolytes. *J. Electroanal. Chem. Interfacial Electrochem.* **1976**, *74*, 125–143.
- (43) Gilmore, C. Maximum Entropy and Bayesian Statistics in Crystallography: A Review of Practical Applications. *Acta Crystallogr., Sect. A: Found. Crystallogr.* **1996**, *52*, 561–589.
- (44) Momma, K.; Ikeda, T.; Belik, A. A.; Izumi, F. Dysnomia, a Computer Program for Maximum-Entropy Method (MEM) Analysis and its Performance in the MEM-Based Pattern Fitting. *Powder Diffr.* **2013**, *28*, 184–193.
- (45) Humphrey, W.; Dalke, A.; Schulten, K. VMD: Visual Molecular Dynamics. *J. Mol. Graphics* **1996**, *14*, 33–38.

Supporting Information

Fast Ionic Conductivity in the Most Lithium-Rich Phosphidosilicate $\text{Li}_{14}\text{SiP}_6$

Stefan Strangmüller,^[a, ‡] Henrik Eickhoff,^[a, ‡] David Müller,^[a] Wilhelm Klein,^[a] Gabriele Raudaschl-Sieber,^[a] Holger Kirchhain,^[b] Christian Sedlmeier,^[c] Volodymyr Baran,^[d] Anatoliy Senyshyn,^[d] Volker L. Deringer,^[e] Leo van Wüllen,^[b] Hubert A. Gasteiger,^[c] and Thomas F. Fässler*,^[a]

Content

Details of the crystal structure determination of $\text{Li}_{14}\text{SiP}_6$	S2
Coordination polyhedra of $\text{Li}_{14}\text{SiP}_6$	S8
Phase width analysis	S9
Differential scanning calorimetry (DSC)	S12
^6Li , ^{29}Si and ^{31}P MAS NMR spectroscopy	S14
Electrochemical impedance spectroscopy (EIS)	S17
DFT simulations (I): A supercell model for $\text{Li}_{14}\text{SiP}_6$	S21
DFT simulations (II): Molecular dynamics simulations	S24
References	S25

Details of the crystal structure determination of Li₁₄SiP₆

Table S1. Atomic coordinates for Li₁₄SiP₆ from co-refinement at 300 K.

atom	wyckoff positions	<i>x</i>	<i>y</i>	<i>z</i>	s.o.f.
P1	4 <i>a</i>	0	0	0	
Si1	8 <i>c</i>	1/4	1/4	1/4	0.08329(1)
Li1	8 <i>c</i>	1/4	1/4	1/4	0.91527(1)
Li2	4 <i>b</i>	1/2	0	0	0.50264(1)

Table S2. Anisotropic displacement parameters (Å²) for Li₁₄SiP₆ from co-refinement at 300 K.

atom	<i>U</i> ₁₁	<i>U</i> ₂₂	<i>U</i> ₃₃	<i>U</i> ₂₃	<i>U</i> ₁₃	<i>U</i> ₁₂
P1	0.04001(1)	0.04001(1)	0.04001(1)	0.0	0.0	0.0
Si1	0.04957(1)	0.04957(1)	0.04957(1)	0.0	0.0	0.0
Li1	0.04957(1)	0.04957(1)	0.04957(1)	0.0	0.0	0.0
Li2	0.12027(1)	0.12027(1)	0.12027(1)	0.0	0.0	0.0

Table S3. Selected interatomic distances in Li₁₄SiP₆ from co-refinement at 300 K.

atom pair		<i>d</i> / Å		atom pair		<i>d</i> / Å	
P1	Si1/Li1	8×	2.5718(1)	Si1/Li1	P1	4×	2.5718(1)
	Li2	6×	2.9696(1)		Li2	4×	2.5718(1)
Li2	Si1/Li1	8×	2.5718(1)	Si1/Li1	6×	2.9696(1)	
	P1	6×	2.9696(1)				

Results of the Rietveld structure refinement of $\text{Li}_{14}\text{SiP}_6$ via powder neutron diffraction at 4 K

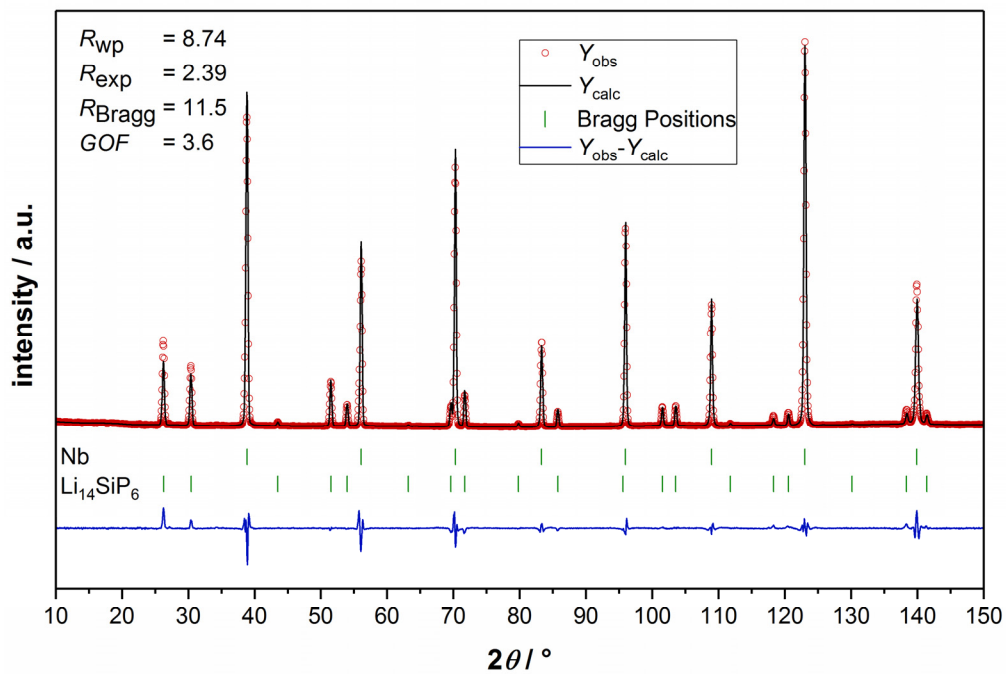


Figure S1. Rietveld analysis of the powder neutron diffraction pattern of $\text{Li}_{14}\text{SiP}_6$ at 4 K. Red circles indicate observed intensities Y_{obs} , black lines show calculated intensities Y_{calc} , blue lines reveal the difference between observed and calculated intensities, and green marks indicate Bragg positions of $\text{Li}_{14}\text{SiP}_6$ and Nb (ampoule).

Table S4. Details of the Rietveld structure refinement of $\text{Li}_{14}\text{SiP}_6$ from powder neutron diffraction measurements at 4 K.

empirical formula	$\text{Li}_{2.33}\text{Si}_{0.17}\text{P}$
T / K	4
formula weight / g mol^{-1}	51.86
space group (no.)	$Fm\bar{3}m$ (225)
unit cell parameters / \AA	$a = 5.91566(6)$
Z	4
$V / \text{\AA}^3$	207.019(3)
$\rho_{\text{calc.}} / \text{g cm}^{-3}$	1.664
2θ range / deg	9.0000-150.0000
R_p	0.0609
R_{wp}	0.0874
R_{exp}	0.0239
χ^2	13.4
GOF	3.6
R_{Bragg}	11.5
R_f	5.79
depository no.	CSD-1915817

Table S5. Atomic coordinates for Li₁₄SiP₆ at 4 K.

atom	wyckoff positions	<i>x</i>	<i>y</i>	<i>z</i>	s.o.f.
P1	4 <i>a</i>	0	0	0	
Si1	8 <i>c</i>	1/4	1/4	1/4	0.0834(2)
Li1	8 <i>c</i>	1/4	1/4	1/4	0.916(2)
Li2	4 <i>b</i>	1/2	0	0	0.505(7)

Table S6. Anisotropic displacement parameters (Å²) for Li₁₄SiP₆ at 4 K.

atom	<i>U</i> ₁₁	<i>U</i> ₂₂	<i>U</i> ₃₃	<i>U</i> ₂₃	<i>U</i> ₁₃	<i>U</i> ₁₂
P1	0.0256(6)	0.0256(6)	0.0256(6)	0.0	0.0	0.0
Si1	0.040(2)	0.040(2)	0.040(2)	0.0	0.0	0.0
Li1	0.040(2)	0.040(2)	0.040(2)	0.0	0.0	0.0
Li2	0.131(9)	0.131(9)	0.131(9)	0.0	0.0	0.0

Table S7. Selected interatomic distances in Li₁₄SiP₆ at 4 K.

atom pair		<i>d</i> / Å		atom pair		<i>d</i> / Å	
P1	Si1/Li1	8×	2.5616(1)	Si1/Li1	P1	4×	2.5616(1)
	Li2	6×	2.9578(1)		Li2	4×	2.5616(1)
Li2	Si1/Li1	8×	2.5616(1)	Si1/Li1	6×	2.9578(1)	
	P1	6×	2.9578(1)				

Results of the single crystal structure determination of Li₁₄SiP₆

Table S8. Crystallographic data and refinement parameters of Li₁₄SiP₆ from single crystal X-ray diffraction measurements at 123 K.

empirical formula	Li _{2.33} Si _{0.17} P
formula weight / g mol ⁻¹	51.86
crystal size / mm ³	0.05 × 0.045 × 0.03
crystal color	orange
<i>T</i> / K	123(2)
crystal system	cubic
space group (no.)	<i>Fm</i> $\bar{3}$ <i>m</i> (225)
unit cell parameters / Å	<i>a</i> = 5.9253(7)
<i>Z</i>	4
<i>V</i> / Å ³	208.03(7)
$\rho_{calc.}$ / g cm ⁻³	1.655
μ / mm ⁻¹	1.347
<i>F</i> (000) / e	146
ϑ range / deg	5.963 – 40.236
index range (<i>hkl</i>)	-10 ≤ <i>h</i> ≤ 10, -10 ≤ <i>k</i> ≤ 10, -10 ≤ <i>l</i> ≤ 10
reflections collected	554
independent reflections	54
<i>R</i> _{int}	0.0146
reflections with <i>I</i> > 2σ(<i>I</i>)	48
absorption correction	multi-scan
data / restraints / parameters	54 / 0 / 5
goodness-of-fit on <i>F</i> ²	1.191
<i>R</i> ₁ , <i>wR</i> ₂ (all data)	0.0513, 0.0900
<i>R</i> ₁ , <i>wR</i> ₂ [<i>I</i> > 2σ(<i>I</i>)]	0.0401, 0.0856
largest diff. peak and hole (e Å ⁻³)	0.442 / -0.528
depository no.	CSD-1915822

Table S9. Atomic coordinates for Li₁₄SiP₆.

atom	wyckoff positions	<i>x</i>	<i>y</i>	<i>z</i>	s.o.f.
P1	4 <i>a</i>	0	0	0	
Si1	8 <i>c</i>	1/4	1/4	1/4	0.0833
Li1	8 <i>c</i>	1/4	1/4	1/4	0.9167
Li2	4 <i>b</i>	1/2	0	0	0.5

Table S10. Anisotropic displacement parameters (Å²) for Li₁₄SiP₆.

atom	<i>U</i> ₁₁	<i>U</i> ₂₂	<i>U</i> ₃₃	<i>U</i> ₂₃	<i>U</i> ₁₃	<i>U</i> ₁₂
P1	0.0267(7)	0.0267(7)	0.0267(7)	0.0	0.0	0.0
Si1	0.019(1)	0.019(1)	0.019(1)	0.0	0.0	0.0
Li1	0.019(1)	0.019(1)	0.019(1)	0.0	0.0	0.0
Li2	0.09(2)	0.09(2)	0.09(2)	0.0	0.0	0.0

Table S11. Selected interatomic distances in Li₁₄SiP₆.

atom pair		<i>d</i> / Å		atom pair		<i>d</i> / Å	
P1	Si1/Li1	8×	2.5657(3)	Si1/Li1	P1	4×	2.5657(3)
	Li2	6×	2.9627(4)		Li2	4×	2.5657(3)
Li2	Si1/Li1	8×	2.5657(3)	Si1/Li1	P1	6×	2.9627(4)
	P1	6×	2.9627(4)				

Coordination polyhedra of $\text{Li}_{14}\text{SiP}_6$

In $\text{Li}_{14}\text{SiP}_6$ the disordered atoms (Li1/Si1) are tetrahedrally coordinated by four P1 and four Li2 atoms, each building up a cubic coordination sphere. The atoms Li2 are centered in a perfectly cubic arrangement of mixed atoms Li1/Si1. In the second coordination sphere Li2 is octahedrally coordinated by six atoms P1.

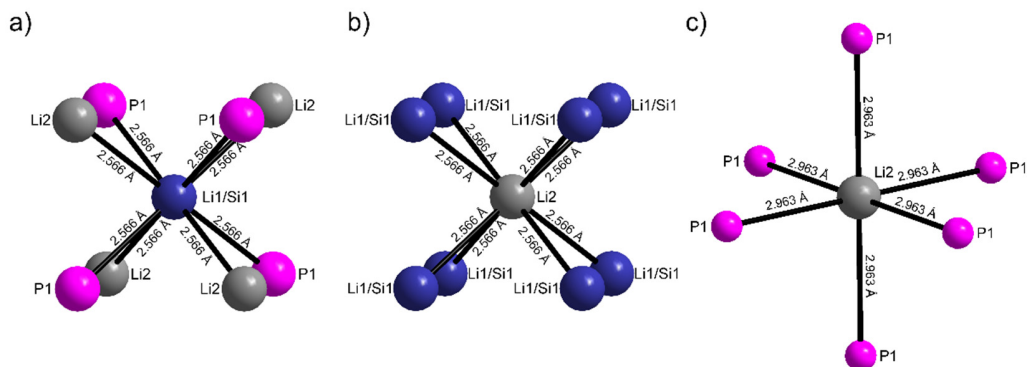


Figure S2. Coordination polyhedra of Si and Li atoms in the crystal structure of $\text{Li}_{14}\text{SiP}_6$ according to a single crystal structure determination at 123 K. The nearest neighbors of the atoms Si1/Li1 and Li2 are arranged in a highly symmetric cubic coordination. In the next nearest coordination sphere Li2 is surrounded by P atoms in an octahedral arrangement.

Phase width analysis

To investigate a possible phase width regarding the amount of lithium and silicon, respectively, a series of powder X-ray diffraction measurements (Figure S3) followed by Rietveld refinements of the recorded diffraction patterns were carried out. The stoichiometry of the compounds should correlate with the applied amounts of the used reagents, and thus, are expected to be 1:1 ($\text{Li}_{14}\text{SiP}_6$: Li_8SiP_4) for “ $\text{Li}_{11}\text{SiP}_5$ ”, 1:1 ($\text{Li}_{14}\text{SiP}_6$: Li_3P) for “ $\text{Li}_{17}\text{SiP}_7$ ” and 1:2 ($\text{Li}_{14}\text{SiP}_6$: Li_3P) for “ $\text{Li}_{20}\text{SiP}_8$ ”. The obtained values of the corresponding primary-phase-to-side-phase ratios are in good agreement with the expected results. The observed deviation could either be the result of various uncertainties during the measurement or the refinement, or a phase width or solid solution may be present (Table S12). Considering the latter cases, a high amount of Si within the structure causes a lower absolute number of atoms per formula unit and entails additional short, covalent Si-P bonds, both resulting in a smaller unit cell. The cubic cell parameter for $\text{Li}_{14}\text{SiP}_6$ refined for the aforementioned samples is the largest in pure $\text{Li}_{14}\text{SiP}_6$, but slightly smaller for the remaining three samples. Therefore a phase width at the Li_3P -rich side can be excluded, while at the Li_3P -poor side a Si-enriched composition “ $\text{Li}_{14-4x}\text{Si}_{1+x}\text{P}_6$ ” seems to be possible. However, the extent of Si enrichment without structural changes must be small, because even in “ $\text{Li}_{11}\text{SiP}_5$ ” the lattice parameter is close to that of $\text{Li}_{14}\text{SiP}_6$. It is also considerably larger than half of the Li_8SiP_4 cell parameter, which would correspond $x = 0.5$ in the composition stated above.

Analogous to the annealed samples the corresponding cell parameters of the reactive mixtures after ball milling have been indexed. The cell parameters of the reactive mixtures are in general distinctly larger than the corresponding parameters of the annealed samples. In combination with the crystalline, elemental Si in the sample this could be a hint for a metastable solid solution with an even higher amount of lithium. During the following annealing process the elemental Si is incorporated into the structure ending up in a smaller unit cell caused by the emerging covalent Si-P interactions (Figure S4 and Table S13).

Powder X-ray diffraction patterns and Rietveld refinement results

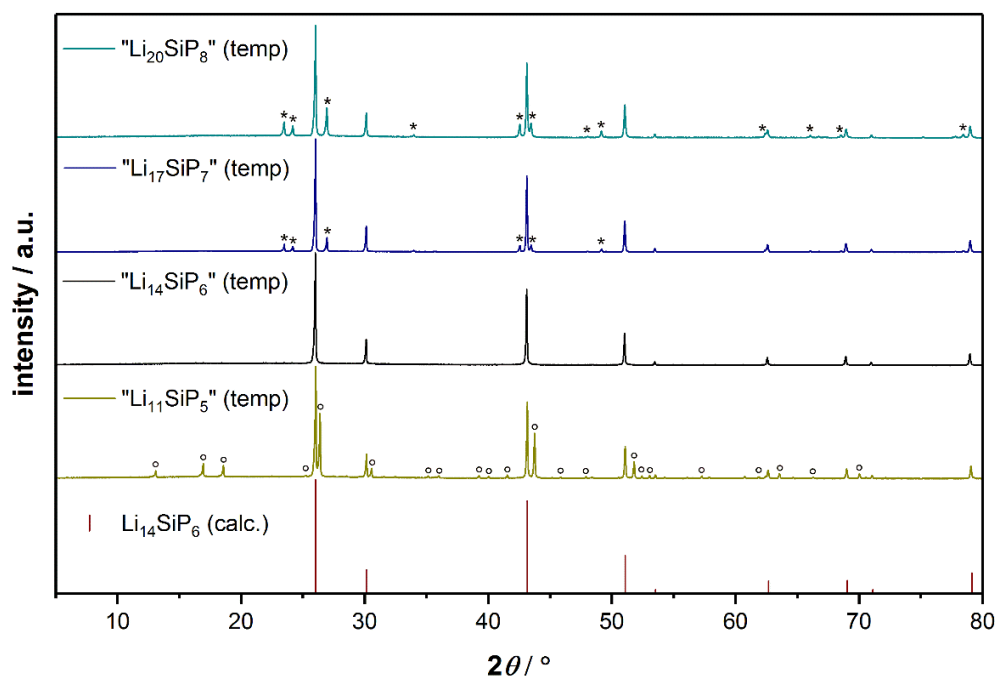


Figure S3. Powder X-ray diffraction patterns of the reactive mixtures “Li₂₀SiP₈” (cyan), “Li₁₇SiP₇” (navy), “Li₁₄SiP₆” (black) and “Li₁₁SiP₅” (dark yellow) after annealing at 973 K for 6 h and subsequent quenching. Li₃P (*) , Li₈SiP₄ (°) and WC (#) occur as side-phases. The calculated reflex positions and corresponding intensities of Li₁₄SiP₆ are shown in red.

Table S12. Rietveld refinement results of the reactive mixtures after annealing.

nominal compositions	product after annealing	relative portions of the obtained compounds
Li ₁₁ SiP ₅	Li ₁₄ SiP ₆ + Li ₈ SiP ₄	1.00(1) : 0.73(1); expected 1:1
Li ₁₄ SiP ₆	Li ₁₄ SiP ₆	1.00(2)
Li ₁₇ SiP ₇	Li ₁₄ SiP ₆ + Li ₃ P	1.00(1) : 1.10(3); expected 1:1
Li ₂₀ SiP ₈	Li ₁₄ SiP ₆ + Li ₃ P	1.00(1) : 2.33(2); expected 1:2

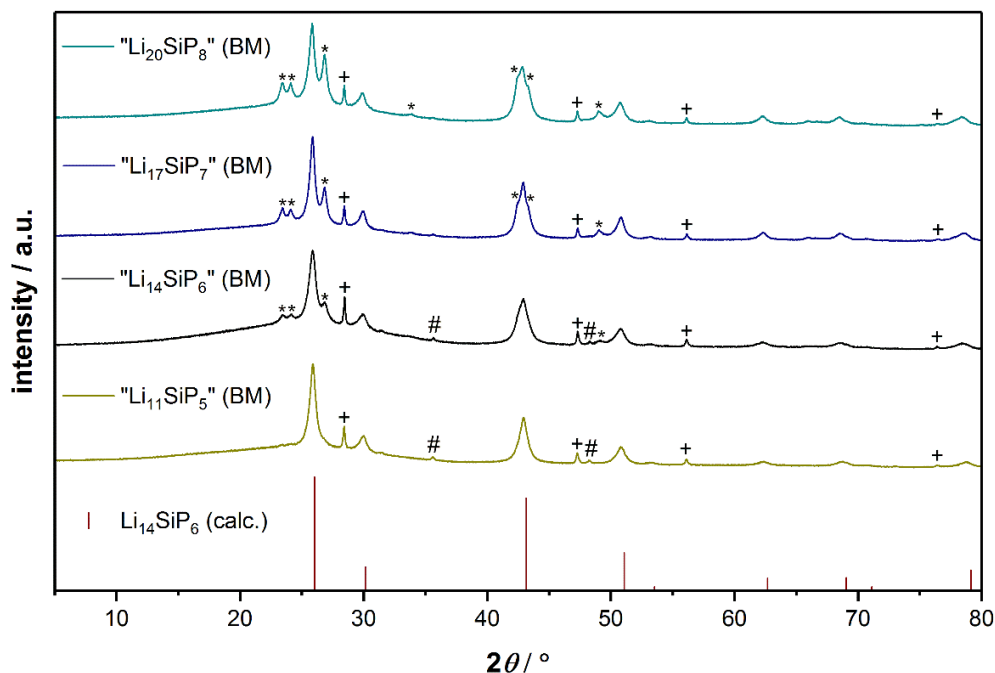


Figure S4. X-ray powder diffraction patterns of the reactive mixtures “Li₂₀SiP₈” (cyan), “Li₁₇SiP₇” (navy), “Li₁₄SiP₆” (black) and “Li₁₁SiP₅” (dark yellow) obtained via ball milling of the elements. Li₃P (*), Si (+) and WC (#) occur as side-phases. The calculated reflex positions and corresponding intensities of Li₁₄SiP₆ are shown in red.

Table S13. List of refined cell parameters of the reactive mixtures “Li₁₁SiP₅”, “Li₁₄SiP₆”, “Li₁₇SiP₇” and “Li₂₀SiP₈” before and after annealing.

nominal composition	cell parameter after BM	cell parameter after annealing
Li ₁₁ SiP ₅	5.947(2) Å	5.93291(8) Å
Li ₁₄ SiP ₆	5.957(3) Å	5.9380(2) Å
Li ₁₇ SiP ₇	5.956(2) Å	5.9361(1) Å
Li ₂₀ SiP ₈	5.961(2) Å	5.9356(1) Å

The cell parameters of the reactive mixtures have been evaluated via the “Index and Refine” WinXPOW software-tool, and the cell parameters of the annealed samples have been determined by Rietveld refinement executed with FullProf.

Differential scanning calorimetry (DSC)

DSC analysis was carried out from room temperature to 1023 K. Starting from the crystalline, disordered phase $\text{Li}_{14}\text{SiP}_6$ leads to a strong and exothermic signal with an onset temperature of 790.9 K (Figure S5), indicating the formation of Li_8SiP_4 as seen during powder neutron diffraction at elevated temperatures. However, the effect occurs at a much higher temperature compared to the above mentioned neutron diffraction data. Hence, also the second, endothermic thermal effect with an onset temperature of 936.6 K representing the reformation of $\text{Li}_{14}\text{SiP}_6$ appears deferred. As observed during supplementary experiments, slow cooling of the sample induces the decomposition of the high-temperature phase into Li_8SiP_4 and Li_3P . However, in the DSC measurement, due to the relatively high cooling rate of 10 K min^{-1} the decomposition of $\text{Li}_{14}\text{SiP}_6$ is eluded, which was also observed in the neutron diffraction experiments. This leads to a reappearance of the decomposition (onset temperature 746.2 K) as well as of the formation signal (onset temperature 935.8 K) during the second heating cycle. The diffraction pattern of $\text{Li}_{14}\text{SiP}_6$ after the DSC measurement shows the preservation of almost phase-pure $\text{Li}_{14}\text{SiP}_6$. Only extremely weak reflections of Li_3P and Li_8SiP_4 are observed (Figure S6).

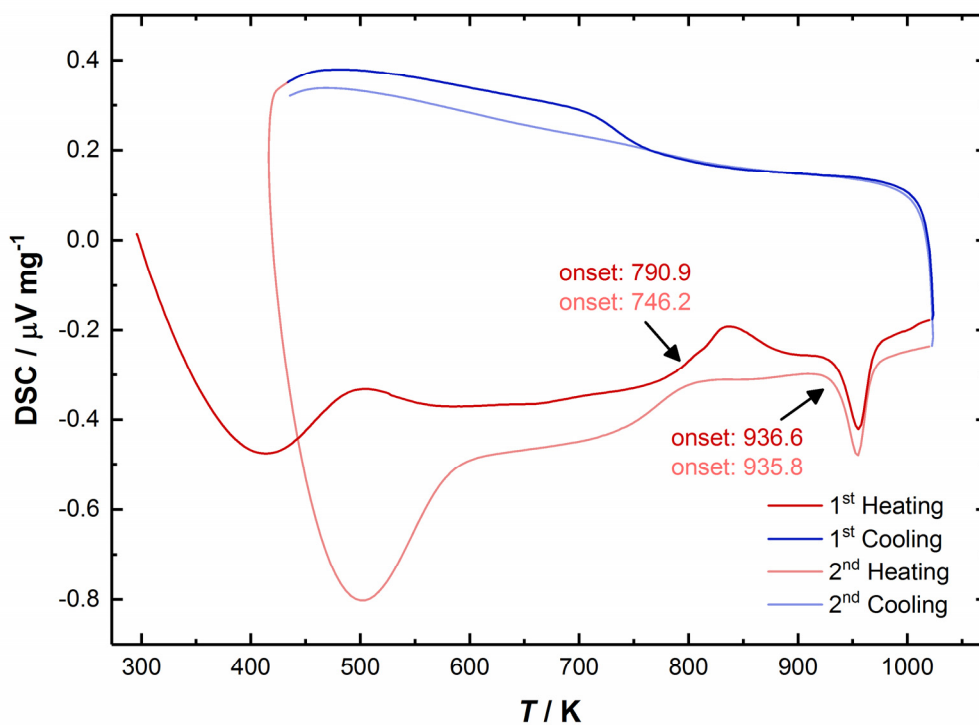


Figure S5. DSC thermogram of $\text{Li}_{14}\text{SiP}_6$. The arrows and numbers indicate the onset temperatures of the corresponding thermal effects.

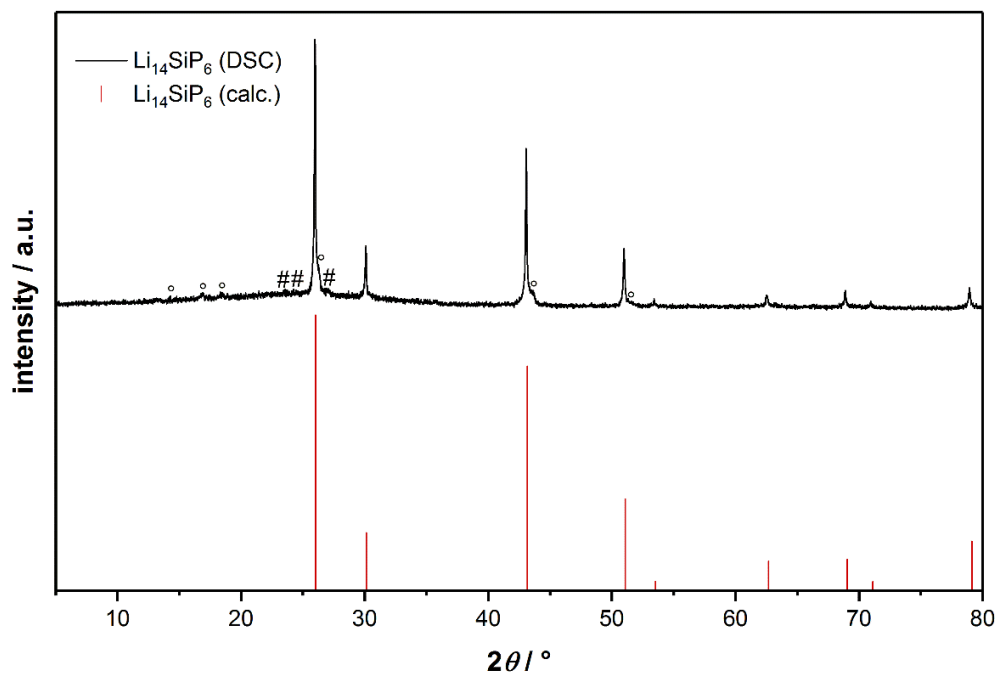


Figure S6. Powder X-ray diffractogram of crystalline $\text{Li}_{14}\text{SiP}_6$ (black) after DSC measurement. Li_3P (*) and Li_8SiP_4 (°) occur as side phases. The calculated reflex positions and corresponding intensities of $\text{Li}_{14}\text{SiP}_6$ are shown in red.

^6Li , ^{29}Si , and ^{31}P MAS NMR spectroscopy

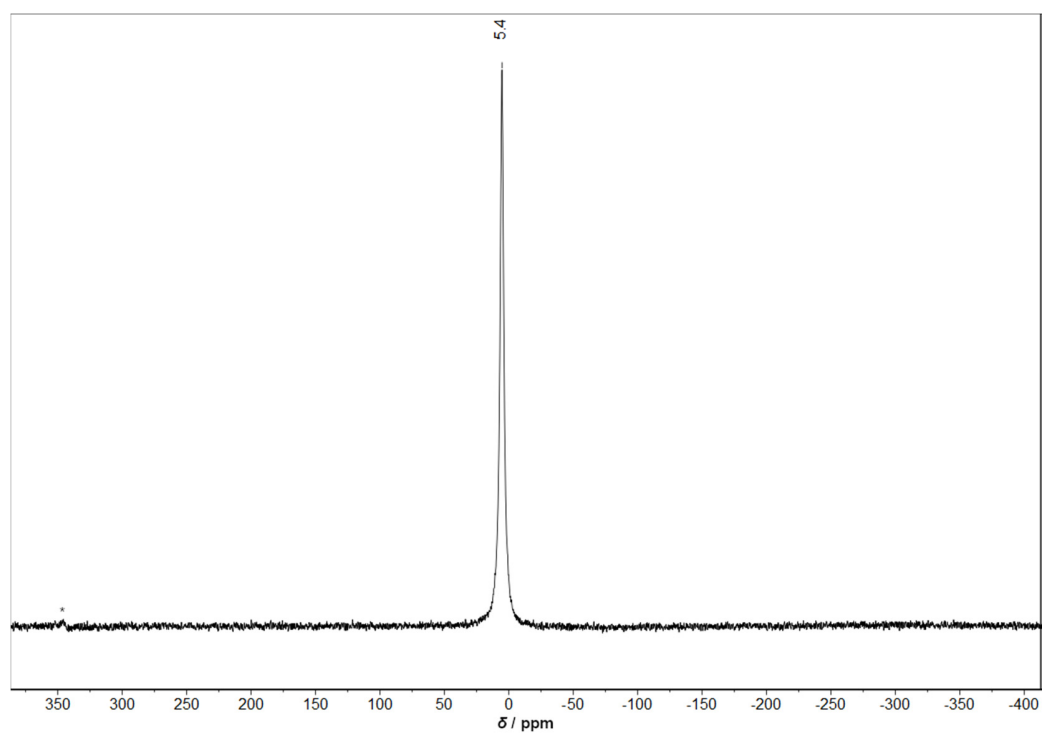


Figure S7. ^6Li MAS NMR spectrum of $\text{Li}_{14}\text{SiP}_6$. Spinning sideband marked by *.

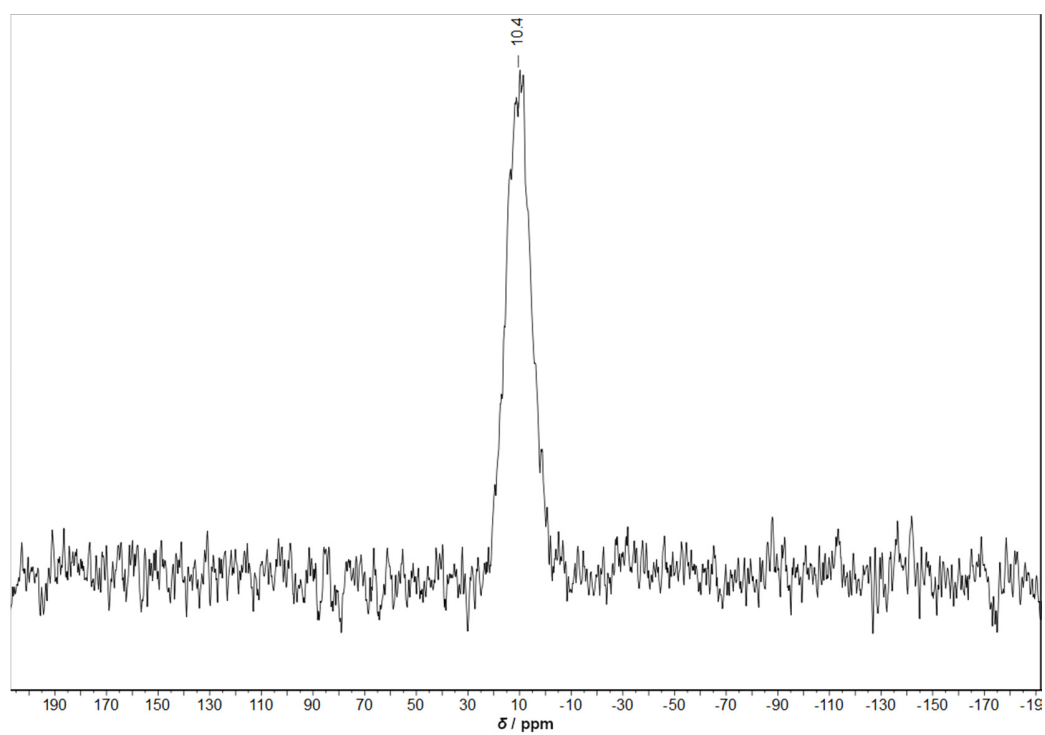


Figure S8. ^{29}Si MAS NMR spectrum of $\text{Li}_{14}\text{SiP}_6$.

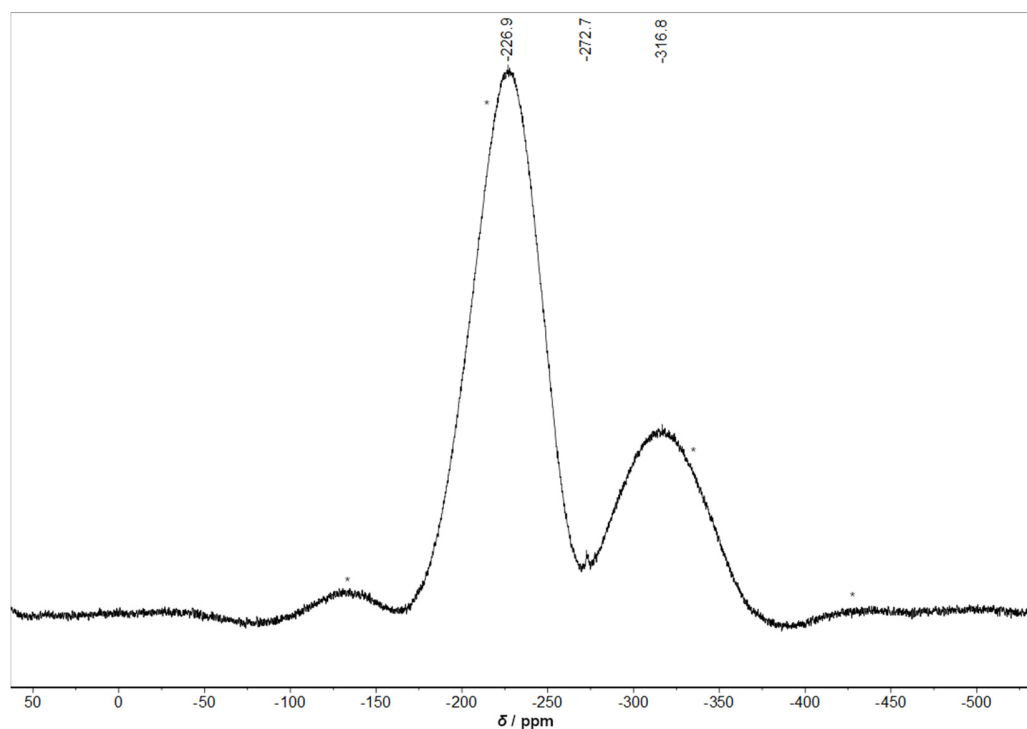


Figure S9. ^{31}P MAS NMR spectrum of $\text{Li}_{14}\text{SiP}_6$ (12 kHz). Spinning sidebands marked by *.

Regarding the ^{31}P MAS NMR spectrum recorded at 15 kHz the two broad, distinct signals are slightly shifted (-227.3 and -314.9 ppm), and the ratio of the total integrated intensity of the two signals is 2.5:1 (Figure S10). These deviations are assumed to be a consequence of the extreme broadening of the signals. The low intense signal at -272.7 ppm indicates the presence of small amounts of Li_3P (-278 ppm) in both spectra.[1, 2]

The ^{31}P MAS NMR spectrum of $\text{Li}_{14}\text{SiP}_6$ after impedance spectroscopy and DC conductivity measurements shows an additional signal at 9.9 ppm indicating the formation of phosphates during data collection.[3-5]

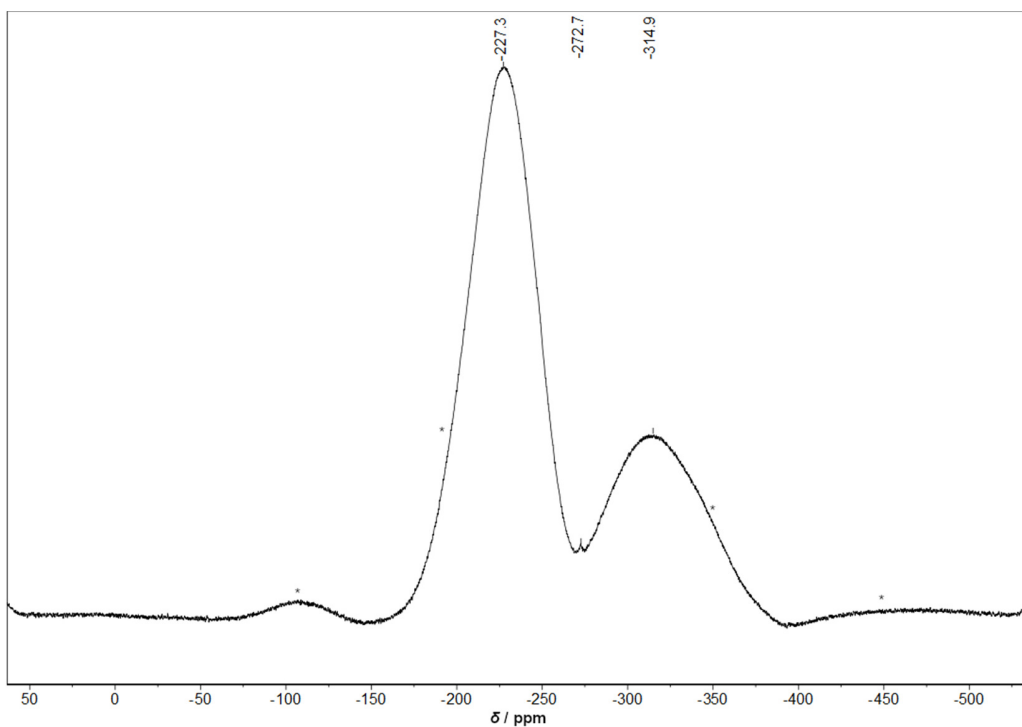


Figure S10. ^{31}P MAS NMR spectrum of $\text{Li}_{14}\text{SiP}_6$ (15 kHz). Spinning sidebands marked by *.

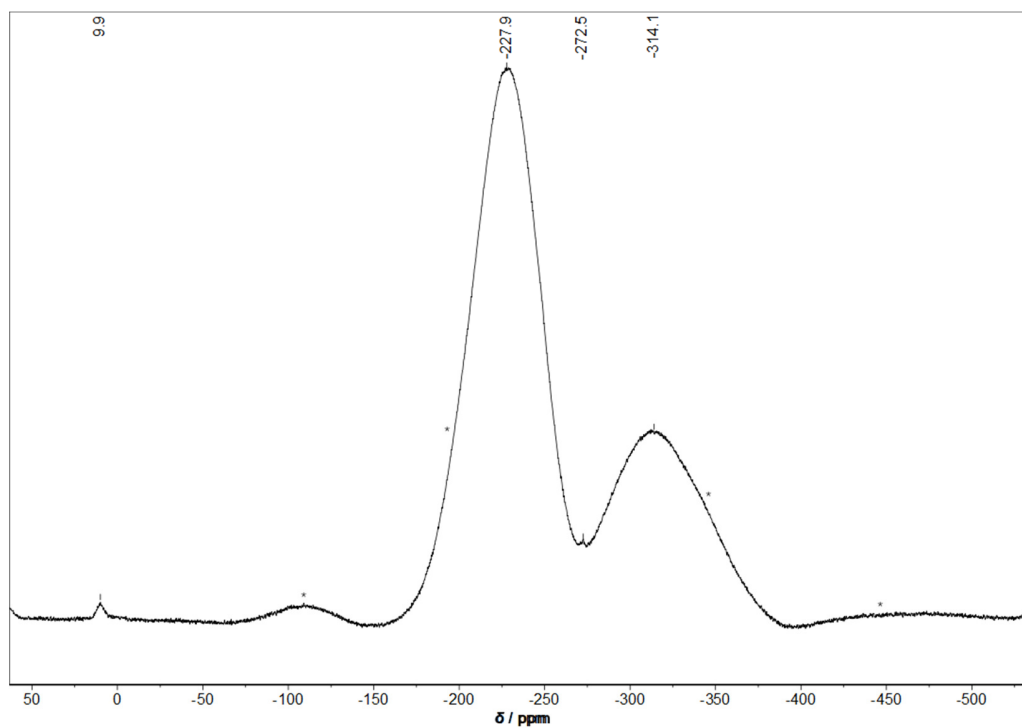


Figure S11. ^{31}P MAS NMR spectrum of $\text{Li}_{14}\text{SiP}_6$ (15 kHz) after impedance spectroscopy. Spinning sidebands marked by *.

Electrochemical impedance spectroscopy (EIS)

Cell setup

The impedance measurements were carried out using an in-house designed cell. The corresponding cell setup is shown in Figure S12.

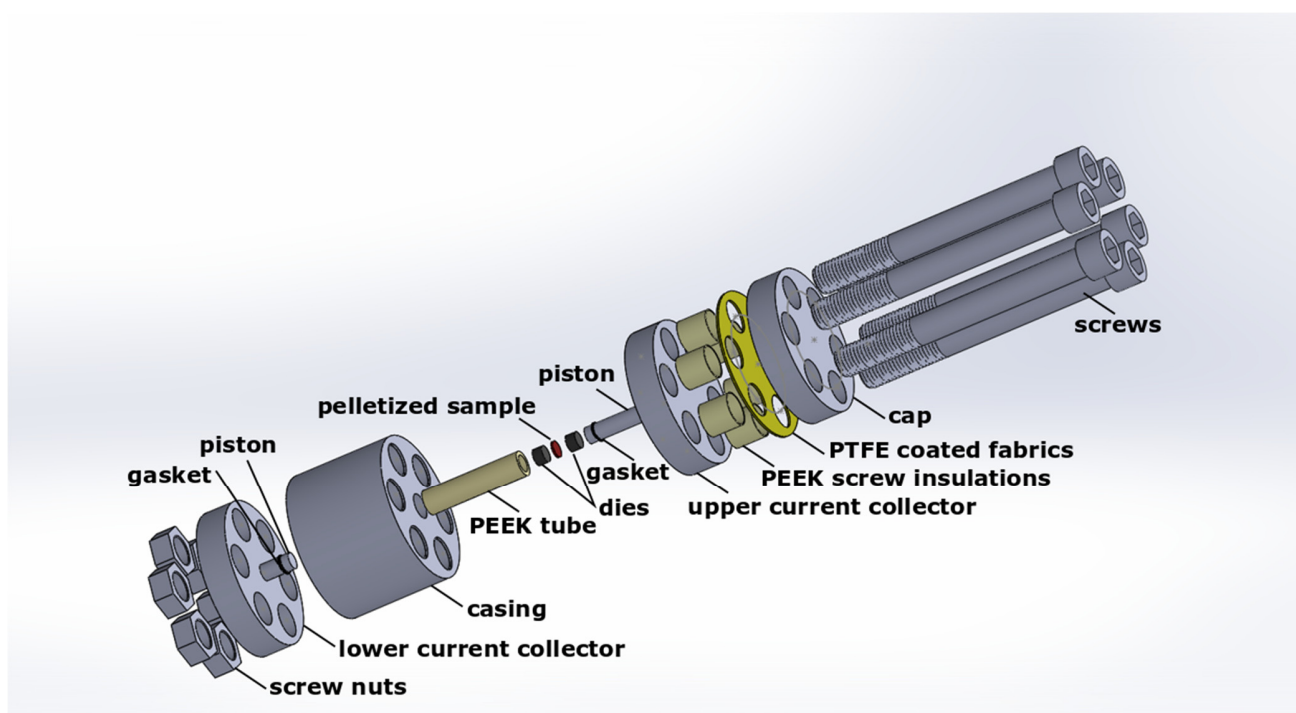


Figure S12. Explosion view of the cell assembly consisting of two stainless-steel current collectors, a stainless-steel casing, a PEEK-tube, hardened stainless-steel dies and pistons, each comprising a gasket for tightening the cell. The pressure is applied by fastening the six screws (including screw nuts) with a certain torque. The screws are electrically insulated from the upper current collector by PEEK-insulation tubes and PTFE coated fabrics (Fiberflon, Germany). The stainless-steel cap is for protecting the PTFE coated fabrics (Fiberflon, Germany) from abrasion by the screws.

Procedure and examination of cell tightness

The impedance analysis approach in this work comprises two different measurement types for each cell. First, lithium ion conductivity at room temperature was measured inside an Ar filled glovebox. Secondly, the cell was taken out of the glovebox and temperature dependent measurements were performed in a climate chamber in order to determine E_A^{PEIS} . Thereby, one cycle comprises heating the cell from 298 K to 353 K and a subsequent cool down to 273 K. During a cycle, the impedance was measured two times each at 298, 313 and 333 K (once during heating and once during cooling) and one time each at 353 and 273 K, as shown in Figure S13a. One complete measurement comprises four experimental steps: cycle 0, which is the measurement at 298 K inside the glovebox, followed by cycles 1, 2 and 3, which are temperature dependent measurements outside the glovebox according to the described temperature ramp. The quality of the sealing of the cell against ambient air was evaluated by comparing ionic conductivities of cycle 0 taken at 298 K inside the glovebox with the first 298 K measurement points of cycles 1–3 taken outside the glovebox, marked by the red diamonds in Figure S13a. Comparing the thus obtained conductivities, a slight decrease in conductivity is observed when operating the cell outside the glovebox ($\approx 8\%$ over the course of ≈ 34 h; see Figure 13b), presumably due imperfect cell sealing against ambient air which might lead to the decomposition reactions of the solid electrolyte with ambient air. Hence, for determining E_A^{PEIS} only cycle 1 of three independent measurements was used. In this case, the experimental error in the conductivity due to cell leakiness was estimated to be approximately 8%, compared to measuring under inert gas atmosphere.

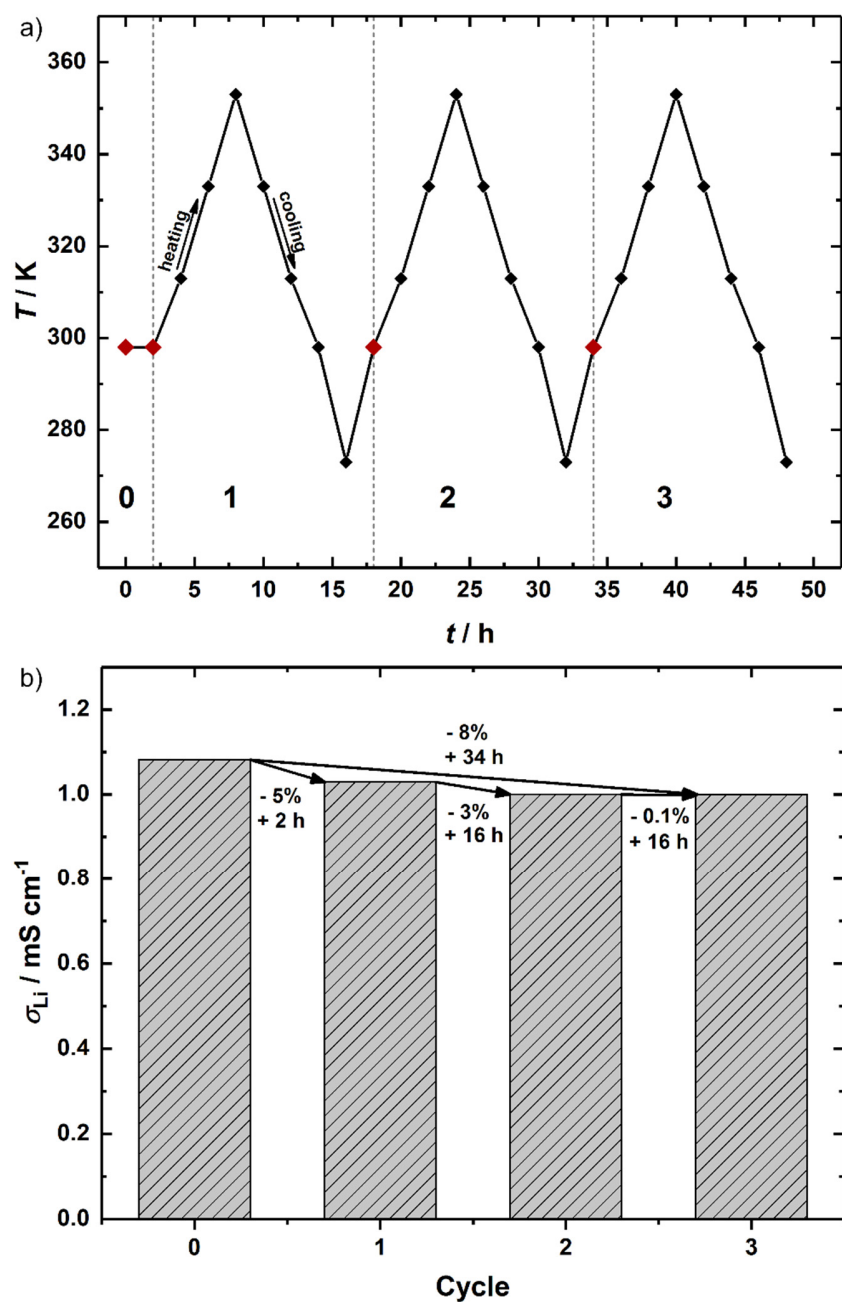


Figure S13. a) Temperature versus time profile of the lithium ion conductivity of $\text{Li}_{14}\text{SiP}_6$ in order to assess the sealing quality of the cell against ambient air. Black diamonds represent impedance measurements during heating and cooling cycles, red diamonds mark the points taken at 298 K, either still within the Ar-filled glovebox (cycle 0) or at the beginning of subsequent temperature cycles (cycles 1-3) during which the cell is exposed to ambient air. Individual cycles are indicated by numbers and separated by dashed lines. b) Lithium ion conductivity progression from cycle 0-1 (at 298 K), including the relative conductivity loss from cycle to cycle over the specified amount of time.

Scanning electron microscopy (SEM)

In order to get an impression of the morphology of the material a Scanning electron microscope (JEOL JSM-5900 LV) was employed. Both samples, a pellet fragment obtained by compressing of $\text{Li}_{14}\text{SiP}_6$ in the cell setup shown above (Figure S12) as well as a powdered sample, were fixed on a conductive carbon tape (Plano GmbH) mounted on an aluminum stub. Preparation and transport to the device were carried out under Ar. Only the transfer from the airtight container to the SEM vacuum chamber brought the samples in contact with air for a short time. However, to minimize damage to the samples this unavoidable step was performed as quickly as possible.

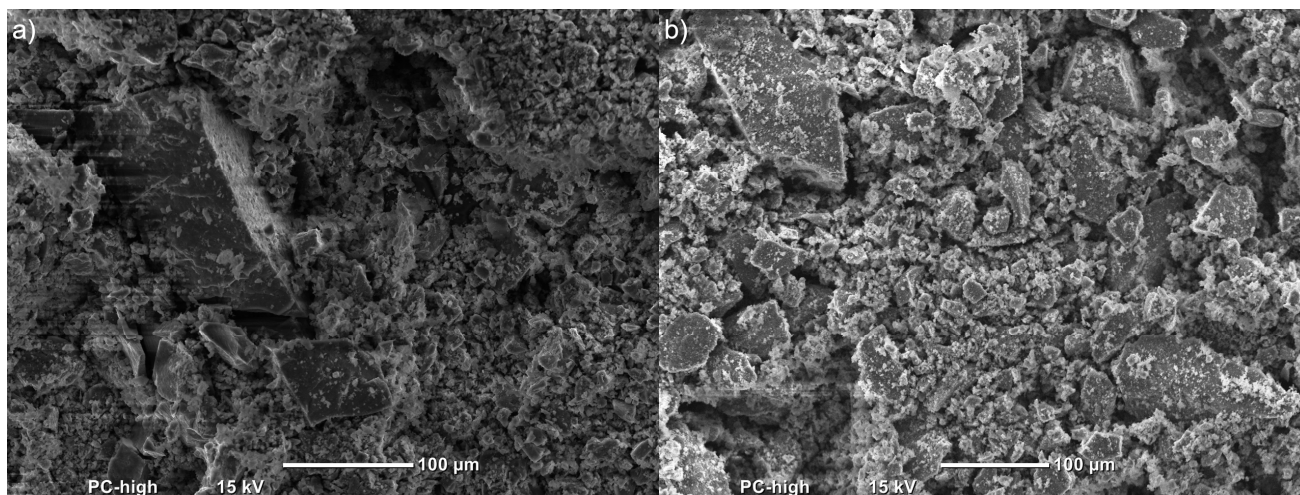


Figure S14. SEM images of $\text{Li}_{14}\text{SiP}_6$. a) Pellet compressed in the cell setup (Figure S12) and b) powdered sample.

DFT simulations (I): A supercell model for $\text{Li}_{14}\text{SiP}_6$

Despite its formally simple crystallographic description (three Wyckoff sites in the highly symmetric space group $Fm\bar{3}m$), the title compound has a rather intricate structure, because two of the sites show mixed and/or partial occupations. In the conventional unit cell (as given by the refinement of the diffraction data; Table 1), there are four formula units of $\text{Li}_{2.33}\text{Si}_{0.17}\text{P}$. However, to carry out first-principles computations one needs to construct a discrete structural model in which all atomic positions are fully occupied (thereby lowering the symmetry of the simulation cell to $P1$). We decided to construct a 378-atom cell based on a $3\times 3\times 3$ expansion (with a resulting lattice parameter of 17.74698 Å), which preserves the cubic cell shape and allows us to achieve an approximately even distribution of Si atoms. The process is illustrated in Figure S15.

The distribution of Li atoms on the $4b$ and $8c$ sites was evaluated based on single-point DFT computations (Figure S16), performed using CASTEP 8.0[6] and on-the-fly pseudopotentials. The Perdew-Burke-Ernzerhof (PBE) functional[7] was employed to treat exchange and correlation. Reciprocal space was sampled at the Γ point, and a Gaussian smearing scheme with width 0.2 eV was applied. The electronic convergence criterion was 10^{-7} eV per atom. The cut-off energy was 500 eV, and an extrapolation scheme was used to counteract finite-basis effects[8]. The most favorable occupation model (set as energy zero in Figure S16) was used as a starting point for subsequent DFT-MD simulations.

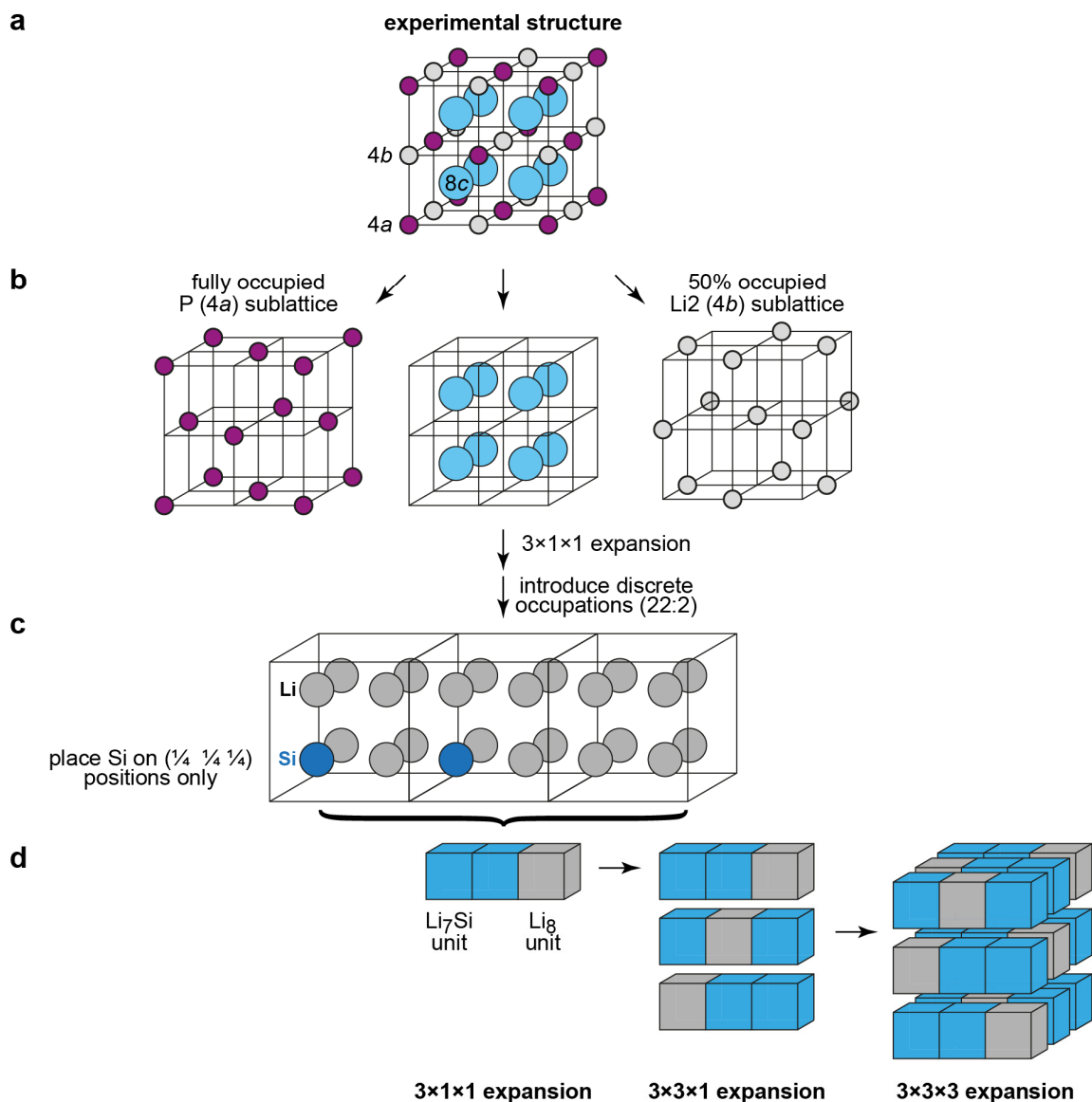


Figure S15. The construction of a discrete structural model to enable the computational modeling of $\text{Li}_{14}\text{SiP}_6$. a) The experimental structure, in which the 4a (occupied by P), 4b (half-occupied by Li) and 8c (mixed occupation of Li/Si) sites are relevant. b) Sketch of the three separate sublattices. The 4a site is taken to be fully occupied (*left*), and for the moment we assume a fully random occupation on 4b (*right*), using a random number generator. The 8c site is the most challenging one, as we need to distribute Li and Si atoms on it, in a way that preserves the stoichiometric composition. c) Using a $3 \times 1 \times 1$ expansion, the correct composition (22 Li sites and 2 Si sites) can be achieved. d) In order to arrive at a cubic and more isotropic structural model, we create a $3 \times 3 \times 3$ expansion of the conventional unit cell as shown.

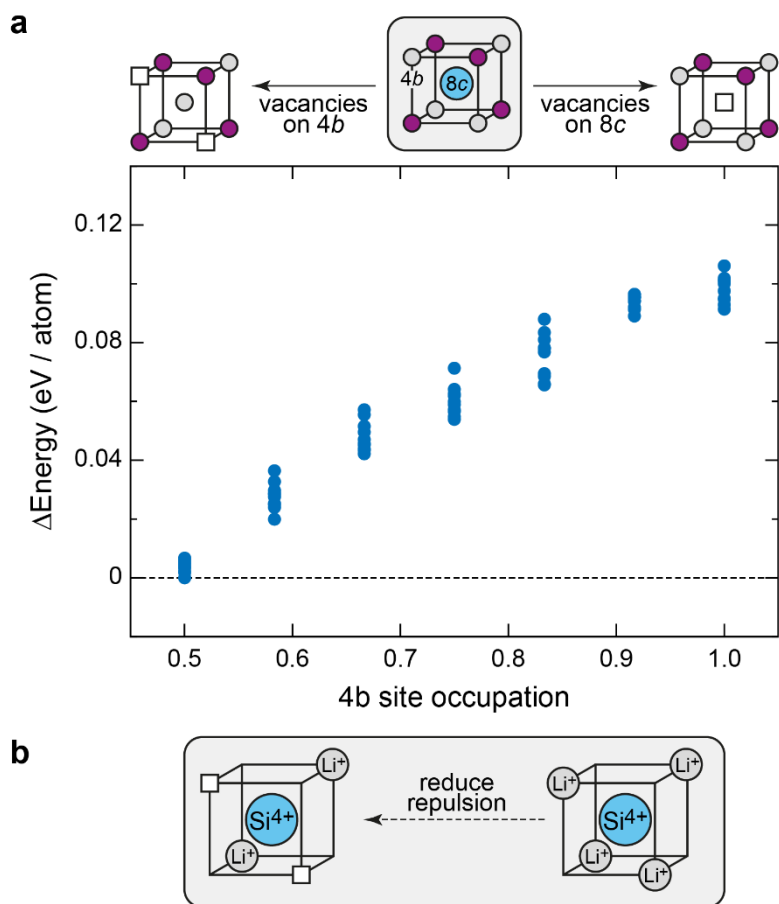


Figure S16. Probing possible $8c \rightarrow 4b$ intermixing of Li atoms, which is not observed in the refinement at $T = 4$ K, but which is needed for the proposed conduction mechanism. a) Energy per atom from DFT total-energy computations, given relative to the most stable structure, for an ensemble of 7×10 randomly occupied structural models that differ in how the Li atoms are distributed on the $8c$ and $4b$ sites. b) Simplified sketch rationalizing the preference for vacancies on $4b$ rather than $8c$ in the ground state.

DFT simulations (II): Molecular dynamics simulations

MD simulations in the NVT ensemble were carried out using the mixed Gaussian and plane-wave DFT approach as implemented in cp2k / Quickstep[9]. We used Goedecker-Teter-Hutter pseudopotentials[10] and the local density approximation. The time step was 0.5 fs throughout. The temperature was controlled using the canonical sampling through velocity rescaling thermostat[11].

Starting from the most favorable structural model determined by total-energy computations (see above), MD simulations were performed subsequently at 300, 500, 700, 900, 1100, and 1300 K. These initial simulations were run for 6×10000 steps (30 ps total), using single- ζ basis sets and a cutoff energy of 200 Ry, and serve only to provide a reasonable initial structure for the subsequent simulation at 1023 K. For the latter, we switched to optimized (“Molopt-SR”) double- ζ basis sets[12] and increased the cutoff energy to 300 Ry. The system was thermostatted with a small time constant ($\tau = 10$ fs) for 5000 steps (2.5 ps), and a final production run was then performed with $\tau = 100$ fs for 10000 steps (5 ps).

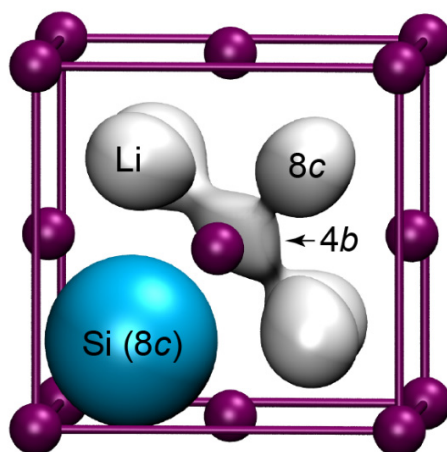


Figure S17. Isosurface plot for mass density maps of Si (blue) and Li (gray) atoms. To obtain this visualization, all atomic coordinates from the DFT-MD trajectory were translated back into the conventional unit cell and collected over 100 equidistant snapshots. Periodic boundary conditions have been switched off; therefore, only diffusion paths from and to the central $4b$ position are seen. The Si density isosurface is shown with arbitrary scaling and centered on $(\frac{1}{4} \frac{1}{4} \frac{1}{4})$, the position on which Si atoms are introduced in the computational structural model (Figure S15c). The positions of P atoms in the idealized model (4a) and the boundaries of the conventional unit cell are shown as a guide to the eye (purple).

References

- [1] S. Boyanov, J. Bernardi, E. Bekaert, M. Ménétrier, M. L. Doublet and L. Monconduit, *Chem. Mater.* **2009**, *21*, 298-308.
- [2] B. León, J. I. Corredor, J. L. Tirado and C. Pérez-Vicente, *J. Electrochem. Soc.* **2006**, *153*, A1829-A1834.
- [3] R. J. Kirkpatrick and R. K. Brow, *Solid State Nucl. Magn. Reson.* **1995**, *5*, 9-21.
- [4] R. K. Brow, D. R. Tallant, S. T. Myers and C. C. Phifer, *J. Non-Cryst. Solids* **1995**, *191*, 45-55.
- [5] Y. Deng, C. Eames, J.-N. Chotard, F. Lalère, V. Seznec, S. Emge, O. Pecher, C. P. Grey, C. Masquelier and M. S. Islam, *J. Am. Chem. Soc.* **2015**, *137*, 9136-9145.
- [6] S. J. Clark, M. D. Segall, C. J. Pickard, P. J. Hasnip, M. J. Probert, K. Refson and M. C. Payne, *Z. Kristallogr.* **2005**, *220*, 567-570.
- [7] J. P. Perdew, K. Burke and M. Ernzerhof, *Phys. Rev. Lett.* **1996**, *77*, 3865-3868.
- [8] G. P. Francis and M. C. Payne, *J. Phys.: Condens. Matter* **1990**, *2*, 4395-4404.
- [9] J. VandeVondele, M. Krack, F. Mohamed, M. Parrinello, T. Chassaing and J. Hutter, *Comput. Phys. Commun.* **2005**, *167*, 103-128.
- [10] S. Goedecker, M. Teter and J. Hutter, *Phys. Rev. B* **1996**, *54*, 1703-1710.
- [11] G. Bussi, D. Donadio and M. Parrinello, *J. Chem. Phys.* **2007**, *126*, 014101.
- [12] J. VandeVondele and J. Hutter, *J. Chem. Phys.* **2007**, *127*, 114105.

3.2.2 Reactivity of Lithium Phosphides with Ambient Atmosphere

In this subsection we evaluate the reactivity of lithium phosphides with ambient air using our *in situ* DRIFTS setup. For this, we use the lithium phosphidoaluminate Li_9AlP_4 as a representative for this class of phosphide-based solid lithium ion conductors.¹⁸⁵ Analogously to the above described lithium phosphidosilicates, the main building unit are AlP_4 -tetrahedra, with Al instead of Si as central atom. Since these tetrahedra resemble the PS_4 -units of lithium thiophosphates, we expect a similar susceptibility to hydrolysis of the main building blocks.^{49,65,159,186,187} This expectation has already been confirmed to some extent by the observation of an exothermic decomposition of Li_9AlP_4 in contact with water and the release of a gas with the smell of garlic, which is most likely PH_3 .

Nevertheless, our aim is to probe the reactivity of lithium phosphides selectively against the individual components of ambient air. Therefore, we exposed Li_9AlP_4 to O_2 , 1000 ppm CO_2/Ar , water vapor in Ar and the combination of 1000 ppm CO_2/Ar with water vapor using the *in situ* DRIFTS setup described in section 2.3. Additionally, we performed a measurement under Ar flow, as well as a baseline of the sample in “pristine” conditions, i.e. under glovebox atmosphere. Figure 3.1 displays the DRIFT spectra of the samples after a 2 h exposure to the indicated atmosphere followed by a 1 h Ar purge. Hence the shown spectra were taken under pure Ar atmosphere, except from spectrum a in Figure 3.1, which was taken under “glovebox atmosphere” with the cell connected to the gas feed system but the valves still closed.

The spectrum under pristine conditions (black line, **a**) shows several features, many of which we can explain by inevitable surface impurities. An overview of the observed bands and their assignment to the respective modes and compounds can be found in Table 3.1. The sharp peak at 3670 cm^{-1} can be attributed to LiOH .¹⁸⁸ The region from $1550 - 1420\text{ cm}^{-1}$ features two main peaks, which are attributed to Li_2CO_3 .¹⁸⁸ The bands at 810 cm^{-1} and 650 cm^{-1} can be assigned to the stretching vibrations of $[\text{AlO}_6]$ and $[\text{AlO}_4]$, respectively and the signal at 1070 cm^{-1} to the Al-O stretching mode.^{189–192} These vibrations can be assigned to Al-O-species such as $\text{AlO}(\text{OH})$ and/or Al_2O_3 , which most likely result from hydrolysis of the $[\text{AlP}_4]$ units and the release of PH_3 . Furthermore, we observe two signals at 2150 cm^{-1} and at 495 cm^{-1} . The first cannot exactly be attributed to a decomposition product but might be an overtone to the mode at 1070 cm^{-1} .¹⁹¹ The second band at lower wavenumbers could be explained by a bending mode of

[AlO₆], but since we observe both signals in reference measurements using attenuated total reflection (ATR) mode, which is less surface-sensitive, the signals could possibly also arise from the bulk sample itself and might be attributed to Al-P modes (ATR data not shown).

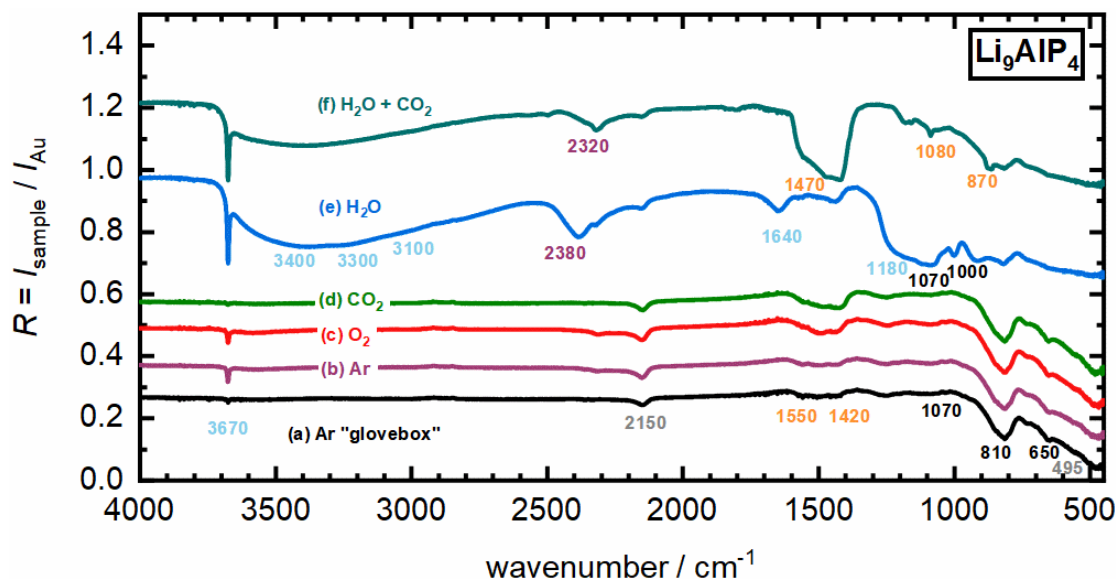


Figure 3.1: Selected spectra in reflectance units of the *in situ* DRIFTS experiments with pure Li₉AlP₄ according to the measurement procedure described in section 2.3. Arbitrary offset in the y-axis for better visibility. (a) Li₉AlP₄ under glovebox atmosphere with the cell connected to the setup but valves closed. Spectra (b) – (f) are taken under Ar atmosphere after exposing the sample for 2 h to the reactive gas (indicated in the plot) and a subsequent Ar purge for 1 h: (b) Ar, (c) O₂ (d) 1000 ppm CO₂ in Ar, (e) humidified Ar (estimated dew point of $T_{dp} \sim 13$ °C corresponding to ~ 14700 ppm H₂O in Ar), (f) 1000 ppm CO₂ in humidified Ar (estimated dew point of $T_{dp} \sim 13$ °C corresponding to ~ 14700 ppm H₂O in Ar). For each reactive gas a separate and independent measurement with a fresh sample was performed. The spectra under glovebox atmosphere (a) were collected prior to each experiment for all the samples; no difference in their spectra was observable, so that only one representative is shown. Modes are indicated by numbers and color coded regarding their origin: O-H (blue), -CO₃ (orange), Al-O (black), P-H (violet) and Al-P (gray, assumed). Please also refer to Table 3.1.

The spectrum under Ar flow (violet line, b) shows a slight increase of the LiOH signal, which suggests a minor intrusion of water vapor into the system by connecting gas feed system. However, the other signals stay unchanged, indicating a tight cell and stable operation conditions. An exposure to pure oxygen (red line, c) does not lead to any decomposition of Li₉AlP₄. Exposing the sample to 1000 ppm CO₂/Ar (green line, d) leads to no (significantly) increased carbonate signals while the LiOH-band can be barely seen. This indicates that the CO₂ converted the initially present LiOH to Li₂CO₃ but no further carbonates are formed, since the carbonate formation is thought to take place only via hydroxides.^{150,193,194}

Upon introducing water vapor into the system (blue line, e), several new features arise and signal intensities from decomposition products increase significantly, such as the LiOH band at 3670 cm^{-1} .¹⁸⁸ The region from $\sim 3600 - 2700\text{ cm}^{-1}$ is a superposition of various signals: the broad band at $\sim 3400\text{ cm}^{-1}$ can be attributed to adsorbed water on the sample surface (i.e., the removal of water vapor by the subsequent 1 hour purge with dry Ar appears to be incomplete) and to chemisorbed water in form of hydrates (e.g., $\text{AlO(OH)} \cdot x\text{H}_2\text{O}$).¹⁹⁵ Furthermore, the O-H stretching modes of AlO(OH) at ~ 3300 (asymmetric) and $\sim 3100\text{ cm}^{-1}$ (symmetric) are weakly indicated by small shoulders in the broad water signal.^{189,191,192} Typically, these two signals are very strong and prominent, however, in this case they are clearly overlaid by the broad water band. In the region from $1180 - 1000\text{ cm}^{-1}$, the observed signals strongly increase compared to the pristine sample, indicating an extensive decomposition of the sample. In this region one expects various modes of AlO(OH) at $\sim 1180\text{ cm}^{-1}$ (O-H asymmetric bending), and at $\sim 1070\text{ cm}^{-1}$ (O-H symmetric bending and Al=O stretching). Note that the Al=O stretching mode is known to shift depending on the crystal size of AlO(OH) (micro vs. nano particles) and morphology (crystalline vs. amorphous), which might explain minor deviations ($< 20\text{ cm}^{-1}$) of this mode compared to the literature.^{189,191,192} The O-H modes can also be attributed to the presence of LiOH. Furthermore, in the region below 700 cm^{-1} , in which several bending and deformation modes of Al-O are located, no distinct features can be identified anymore, but the low signal intensity in this region indicates an extensive absorption and hence confirms the presence of Al-O-species as decomposition products.¹⁹¹ The feature at 1640 cm^{-1} (H-O-H bending) could reveal adsorbed water on an oxide surface due to an insufficient removal of the water vapor by the argon purge.¹⁹⁵ Chemisorbed water in form of a more strongly bound hydrate is usually located at lower wavenumbers ($\sim 1600\text{ cm}^{-1}$), but since we do not observe the typical bands for water in the gas phase that appear between $3900 - 3600\text{ cm}^{-1}$ and also between $1800 - 1300\text{ cm}^{-1}$, we believe the observed signal indeed corresponds to a chemisorbed water species.¹⁹⁶⁻¹⁹⁸ In addition to the increased signals for AlO(OH) as a main decomposition product, one distinct, new bands at 2380 cm^{-1} was found. The signals can be assigned to a P-H stretching vibration of Al-P-H.¹⁹⁹⁻²⁰¹ Hence, we think this feature can be attributed to hydrolyzed $[\text{AlP}_4]$ units with Al-P-H bond, similar the reported hydrolysis mechanism of thiophosphates.⁶⁵

If CO₂ is present in combination with water vapor (turquoise line, **f**) an extensive formation of carbonates is observed, indicated by the duplet at ~1470 cm⁻¹ (asymmetric stretching modes C-O at 1550 and 1420 cm⁻¹), 1080 cm⁻¹ (asymmetric stretching mode C-O), and 870 cm⁻¹ (out-of-plane mode).²⁰² Surprisingly, the signals at O-H stretching vibrations around 1180 cm⁻¹ are clearly smaller compared to spectrum **e**. It is not absolutely clear, whether there are indeed less hydroxy species present on the surface due to extensive carbonate formation or if their intensity is decreased due to the formation of complex aluminum hydroxy carbonate species, such as the hydrated basic aluminum carbonate (Al₅(CO₃)(OH)₁₃ · 5H₂O). On the other hand, Johannes Sicklinger showed in his PhD thesis that the relative change in signal intensity for the use of undiluted samples might not necessarily reflect the real increase of the formed surface species compared to diluted samples.²⁰³

In summary, the *in situ* DIRFTS experiments suggest Al-O and Al-OH species as the main decomposition product of Li₉AlP₄ when brought into contact with water vapor. Note that the exact species could not be identified, therefore complementary analysis such as XRD and XPS are recommended. Nevertheless, the finding of Al-O species suggests a hydrolysis mechanism of the [AlP₄] units similar to what is known for [PS₄] units in thiophosphates. In the latter case, the P-S-tetrahedra are hydrolyzed to phosphates and thio-oxo-phosphates under the release of H₂S. We also performed the same experiments using LSPS and LPS and could find evidence for the presence of phosphates by dominant P-O stretching modes around 1000 cm⁻¹ (data not shown). Therefore, we believe this to be the hydrolysis mechanism of lithium phosphidoaluminates. Analogously, the lithium phosphidosilicates are thought to decompose to Si-O species in contact with water. However, based on the known structure motifs of the compounds, this was not an unexpected finding. Attempts to quantify the decomposition as a function of the exposure time were not successful, since the use of undiluted samples does not allow for a quantitative evaluation of the spectra and the since use of dilution media was not possible due to their interaction with water vapor.²⁰³

Results

Table 3.1: Overview of the observed bands in Figure 3.1 and their assignment to the various compounds and vibrations modes.

Observed signal [cm ⁻¹]	Color code	Vibration mode	Reference
(a) assigned to LiOH 3670	blue	O-H stretching	188
(b) assigned to H ₂ O ~3400 1640	blue	adsorbed / chemisorbed adsorbed/chemisorbed	195
(c) assigned to Li ₂ CO ₃ 1550/1420 1080 870	orange	C-O asymmetric stretching C-O asymmetric stretching C-O out-of-plane bending	188,202
(d) assigned to AlO(OH) / Al ₂ O ₃ 3300 / 3100 1180 1070/1000 810 650	blue blue black black black	O-H stretching O-H asymmetric bending Al=O stretching Al-O stretching Al-O stretching	189,191,192
(e) assigned to -Al-PH 2380/2320	violet	P-H stretching	199–201
(f) Li ₉ AlP ₄ (assumed) 2150 495	gray	Unknown Al-P stretching (assumed)	

As a quantification of the solid decomposition products was not possible, another approach was to assess the gaseous decomposition product PH₃, since also the gas phase over the sample is probed by the IR beam in DRIFTS. A quantitative analysis of PH₃ is possible, as the measured intensity in the gas phase is directly proportional to the concentration of the compound according to the *Lambert-Beer-law*

$$A = \log\left(\frac{I}{I^0}\right) = \varepsilon \cdot c \cdot l \quad (3.1)$$

with the absorbance A , absorptivity ϵ , concentration c , and the pathlength l of the IR beam.

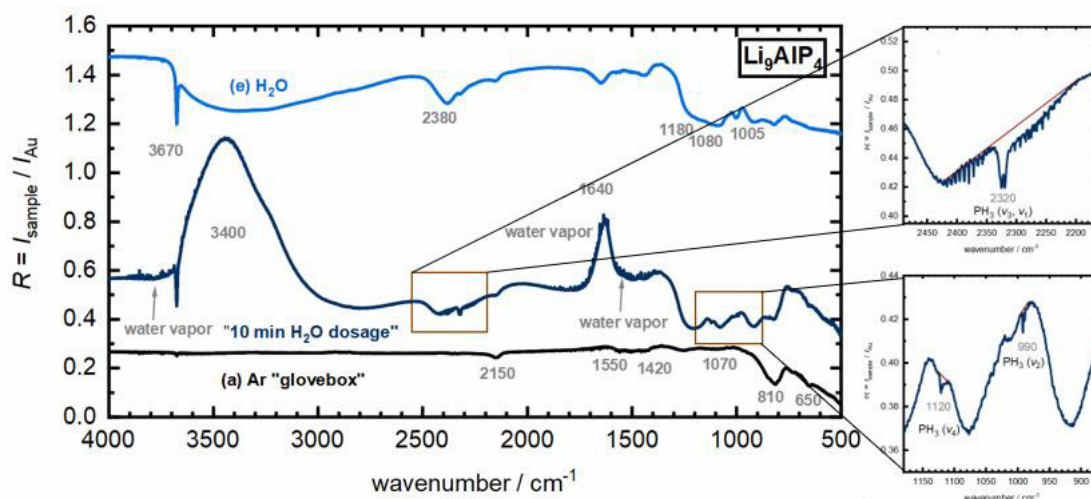


Figure 3.2: Spectra of the *in situ* DRIFT experiments with Li_9AlP_4 in reflectance units. Spectra (a) and (e) are the same as in Figure 3.1 and are recorded under glovebox atmosphere (a) and argon (1 h Ar purge after 2 h exposure to water vapor, e). The dark blue spectrum labelled with “10 min H_2O dosage” refers to the same sample as in (e) but taken after 10 min during the exposure to water vapor. Smaller spectra on the right are enlargements of regions where vibration modes of gaseous PH_3 are observed. Red lines are a guide-to-the-eye.

Figure 3.2 shows the spectrum of Li_9AlP_4 during the exposure to water vapor (dark blue line, taken after 10 min prior exposure to ~ 1.4 vol.% H_2O in Ar) as well as in the pristine state (black) and after a 2 hour exposure to ~ 1.4 vol.% H_2O in Ar and a subsequent 1 hour purge with dry Ar (light blue). The bands between $3900 - 3600 \text{ cm}^{-1}$ and $1800 - 1300 \text{ cm}^{-1}$ can be assigned to water in the gas phase.¹⁹⁶ Additionally, the bands at 3400 cm^{-1} and 1640 cm^{-1} , which typically indicate adsorbed water, are inverted.¹⁹⁵ We believe this is due to the fact that the water only absorbs on the gold sputtered sandpaper used to record the background spectra, while no water is absorbed on the sample since it instantaneously reacts with the SE. In this case, the intensity of the background is smaller compared to the sample intensity, leading to reflectance values > 1 and to a band inversion. During the Ar purge, the adsorbed water is removed from the Au surface and bands reinvert, as can be seen from spectrum (e). Therefore, the observed band inversion is solely a measurement artifact during water dosage. Conveniently, the bands for gaseous PH_3 are outside the regions affected by band inversion and can be investigated. In agreement with the literature, we observe the PH_3 modes at $\sim 2320 \text{ cm}^{-1}$

(two stretching vibrations at 2324 and 2318 cm^{-1}), 1120 cm^{-1} (bending vibration) and 990 cm^{-1} (bending vibration), as shown by the zoomed-in spectra plotted at the right-hand-side of Figure 3.2.^{201,204}

In future experiments, the PH_3 signals could be recorded over time to determine a reaction rate for the decomposition of Li_9AlP_4 with water vapor. Furthermore, the water concentration could be varied by adjusting the vapor pressure either via the temperature of the water through which the gas feed is bubbled or a variation of the water saturation pressure by the use of concentrated salt solutions.²⁰⁵ In doing so, one could investigate the threshold H_2O concentration that can be tolerated without a significant decomposition of the sample. Effectively, this simulates the required dew point of a dry-room. However, we did not perform these experiments for two reasons: (i) The evolution of PH_3 is a surface reaction and thus strongly dependent on the BET-surface area of the used material. Since the used Li_9AlP_4 was synthesized in small batches, it was not possible to precisely adjust the surface area to obtain meaningful results. (ii) For a quantitative gas phase analysis, experiments in transmission mode would be more suitable, since the signal intensity and thus the resolution is better compared to DRIFTS. Furthermore, the use of transmission mode allows to selectively investigate the gas phase without probing the solid sample, so that an overlap of gas and solid phase signals and the resulting inaccuracy can be avoided.

Overall, we conclude that the here conducted *in situ* DRIFTS measurements were a valuable diagnostic method to identify various surface species on Li_9AlP_4 , confirming the initially expected decomposition mechanism for the hydrolysis of the $[\text{AlP}_4]$ units. A quantitative analysis of the solid decomposition products was not possible due to experimental limitations of the technique. The quantitative evaluation of the gaseous decomposition product PH_3 is possible, however, other IR techniques might be more suitable for this purpose than DRIFTS.

4 Conclusions

Summarized in one sentence, the main objective of this PhD thesis was to lay the foundation for a new sub-group on ASSB research within the group at TUM. Initially, only little experience and no cell hardware for material or electrode testing existed in our group at the beginning of this PhD thesis. Thus, one dedicated aim was to develop appropriate cell hardware and to fully understand its usage in order to exclude experimental artifacts due to improperly designed ASSB cells. In addition, the preparation and characterization of slurry-processed cell components was investigated in order to facilitate the transition from pellet-type to sheet-type cell systems. The main findings are graphically summarized in Figure 4.1.

The development of the cell generations 1 – 3 is described in Section 2.1. In total, three different cell generations were developed and thoroughly validated. For this, we compared different sealing concepts such as O-ring (Gen 1 cell) and PTFE flat-seals (Gen 2 cell). We observed O-rings to not provide a sufficiently airtight sealing if they are not actively compressed. Using PTFE flat-seals instead, the cell could be sealed tightly, enabling long-term measurements with air-sensitive materials outside the glovebox. We provide essential calculations and considerations to properly design the dimensions of the cell components. Furthermore, different concepts for the pressure application are explored. Using screws, high pressures of several hundreds of MPa for small samples (8 mm diameter) can be achieved. We discuss the correlation between the applied torque and the expected pressure, but also show that while the pressure cannot be precisely determined by calculating it from the applied torque, it can be sufficiently good estimated. If the force is applied via a defined compression of springs, as it is the case for the Gen 2 and 3 cells, the pressure can be precisely adjusted, but the maximum applicable pressure (100 MPa) is significantly lower for the same sample dimension due to the commercially available springs. Lastly, we identify the stray capacitance for each cell design, which results from its components and is connected in parallel to the impedance response of the sample (i.e., it adds to the capacitance of the sample). Depending on its magnitude, the stray capacitance can have a significant influence on the performed impedance measurements. For the Gen 1 cell we found the stray

capacitance to be on the order of $\sim 10^{-10}$ F, which is the same order of magnitude as expected for polycrystalline SE materials and consequently has to be considered in the data analysis. Knowing the contribution of the individual cell components to the overall value, the stray capacitance could be decreased by one order of magnitude to $\sim 10^{-11}$ F for the Gen 2 cell. Consequently, the influence is negligible for sheet-type separators and electrodes, since their capacitance is a few orders of magnitude larger.

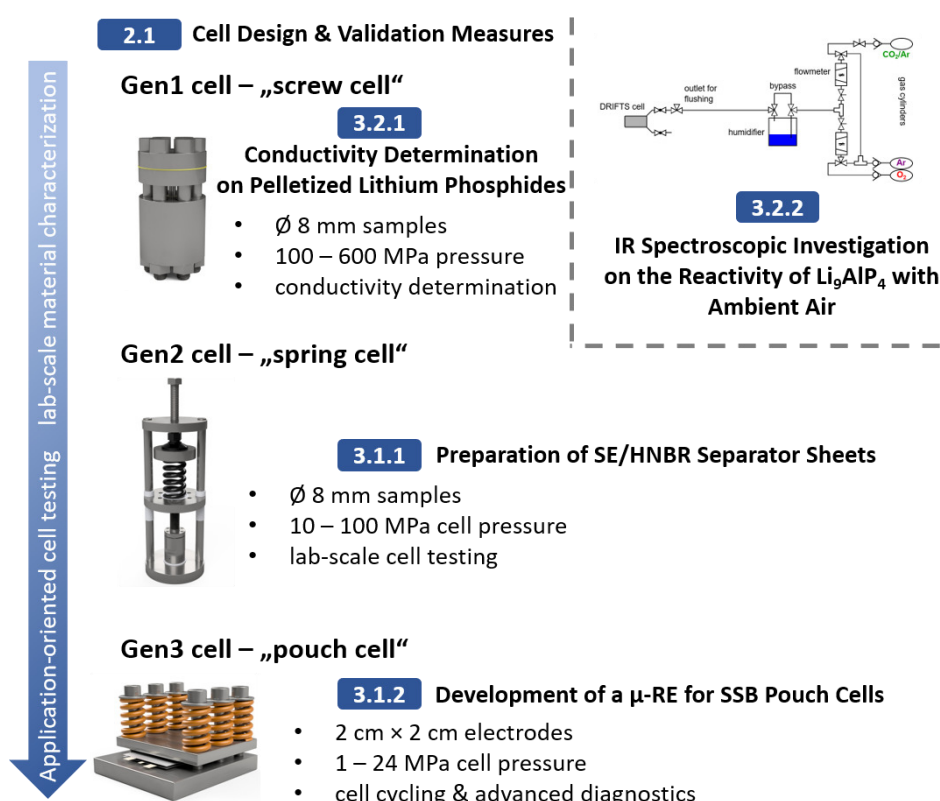


Figure 4.1: Graphical summary of the key ASSB cell developments and their use for ASSB material characterization and battery testing done in this PhD thesis. Section 2.1 described the design and validation measures for the sealing concept, pressure application, further geometric requirements and of the stray capacitance for the three different cell generations developed during this PhD thesis. Afterwards, we developed a slurry-based process in toluene to prepare SE/HNBR composite separator-sheets and characterized them in terms of porosity and conductivity using the spring cell setup (subsection 3.1.1). Using these sheets, we were able to prepare ASSB pouch cells, which allowed us to integrate a micro-reference electrode. By the use of half-cell potential and impedance measurements via the reference electrode, we were able to identify constraints for the use of indium-lithium electrodes (subsection 3.1.2). In parallel to the work on application-oriented sheet-type cell components based on sulfide SEs, we performed fundamental material characterization on the solid ion conductor class of the lithium phosphides. Using the screw cell, we determined the ionic conductivity of the most lithium-rich lithium phosphidosilicate $\text{Li}_{14}\text{SiP}_6$ (subsection 3.2.1). Furthermore, we performed IR spectroscopic investigations on the reactivity of the lithium phosphidoaluminate Li_9AlP_4 with components from ambient atmosphere to assess its atmospheric stability and its possible decomposition mechanism (subsection 3.2.2).

The study on the preparation of sheet-type composite separators is presented in Subsection 3.1.1. There, we report a slurry-based process in toluene to fabricate thin and flexible composites of an LPSCl and HNBR binder. The resulting sheets have a thickness of ~ 120 μm and a porosity of $\sim 50\%$ in their as-prepared state. We determined the sheet conductivity at a cell pressure of 70 MPa using Gen 2 cell and observed that the conductivity of a sheet with ~ 8 vol.-% HNBR is reduced by a factor of three compared to the pristine powder. Furthermore, we also prepared sheets from LPS-711 and LSPS and could show that the decrease in conductivity is independent from the used solid electrolyte but merely a function of the volumetric binder content. Lastly, we investigated the influence of fabrication and operating cell pressure on the determined sheet-conductivity.

With the ability to prepare LPSCl/HNBR sheets, we used these composite separators to make the transition from pellet-type cells to pouch cells (Gen 3 cell). In Subsection 3.1.2, we present a study on the integration of a micro-reference electrode (μ -RE) into an ASSB pouch cell. Thereby, we sandwiched a thin, electrically insulated, gold wire (64 μm diameter) between two separator-sheets. Upon compression, the gold wire is firmly embedded into the separator. Subsequently, the gold wire was electrochemically lithiated forming a lithium-gold alloy with a stable potential of ~ 0.31 V vs. Li^+/Li . We showed that artifact-free half-cell impedance spectra can be obtained in a Li|Li symmetric cell. Furthermore, we investigate the widely used In/InLi electrode. In doing so, we prepared electrodes by stacking and compressing of an In and a Li foil in the atomic ratio of $\sim 76:24$. The resulting electrode features two optically different faces, of which we believe one to consist of a solid solution of a small concentration of Li (~ 1 at.%) in In and the other of In-Li alloy. We prepared cells with a pure indium counter electrode and with the In/InLi electrode in both configurations (i.e., facing the SE separator with either the In or the In-Li-side) and could show by using the μ -RE that the two sides of the prepared In/InLi electrodes show electrochemically different behavior, which was not expected according to the literature.

In Section 3.2, we present the work from a cooperation project with the Chair for Inorganic Chemistry with Focus on Novel Materials, the group of Prof. Thomas Fässler at TUM. By this group, a new class of solid lithium ion conductors, namely lithium phosphides, was developed. In Subsection 3.2.1 a study on the synthesis of $\text{Li}_{14}\text{SiP}_6$ is shown. Using Gen 1 cells, we determined the ionic conductivity to $\sim 1.1 \times 10^{-3}$ S cm^{-1} at

room temperature and the activation energy for the lithium ion transport to $\sim 32 \text{ kJ mol}^{-1}$ ($\sim 0.33 \text{ eV}$) by means of impedance measurements. Complementary studies by static ^7Li NMR experiments revealed an activation energy of $\sim 30 \text{ kJ mol}^{-1}$ ($\sim 0.31 \text{ eV}$), which is in fairly good agreement with the values obtained by impedance experiments.

Lastly, we investigated the reactivity of the lithium phosphidoaluminate Li_9AlP_4 with ambient atmosphere components (O_2 , CO_2 , H_2O) via IR spectroscopy, as presented in Subsection 3.2.2. We modified the sampling cell of the IR spectrometer in a way that allows us to dose different gases. In doing so, we probed the reactivity of Li_9AlP_4 with O_2 , CO_2 , H_2O -vapor, and a combination of $\text{CO}_2 + \text{H}_2\text{O}$ -vapor. While no reactions with pure oxygen or carbon dioxide were observed, substantial Li_9AlP_4 decomposition was observed in the presence of water vapor. We could identify PH_3 as a gaseous decomposition product as well as the formation of $-\text{OH}$, $-\text{PH}$, $-\text{AlO}$ and $-\text{CO}_3$ (in the case of $\text{CO}_2 + \text{H}_2\text{O}$ vapor) species on the Li_9AlP_4 surface. Considering $[\text{AlP}_4]$ -units as the main structure motifs, we suggested a hydrolysis of the Al-P bond as the main decomposition pathway, similar to what is known from the $[\text{PS}_4]$ -units in thiophosphates.

References

- (1) Tarascon, J. M. The Li-Ion Battery: 25 Years of Exciting and Enriching Experiences. *Electrochem. Soc. Interface* **2016**, *25* (3), 79–83. <https://doi.org/10.1149/2.F08163if>.
- (2) Whittingham, M. S. Electrical Energy Storage and Intercalation Chemistry. *Science* **1976**, *192* (4244), 1126–1127. <https://doi.org/10.1126/SCIENCE.192.4244.1126>.
- (3) Whittingham, M. S. The Role of Ternary Phases in Cathode Reactions. *J. Electrochem. Soc.* **1976**, *123* (3), 315–320. <https://doi.org/10.1149/1.2132817>.
- (4) Mizushima, K.; Jones, P. C.; Wiseman, P. J.; Goodenough, J. B. Li_xCoO_2 ($0 < x < 1$): A New Cathode Material for Batteries of High Energy Density. *Solid State Ionics* **1981**, *3–4*, 171–174.
- (5) Nitta, N.; Wu, F.; Lee, J. T.; Yushin, G. Li-Ion Battery Materials: Present and Future. *Mater. Today* **2015**, *18* (5), 252–264. <https://doi.org/10.1016/j.mattod.2014.10.040>.
- (6) Yoshino, A.; Nakajima, T.; Sanechika, K. USP 4,688,595. 4,688,595, 1987.
- (7) Yoshino, A.; Nakajima, T.; Sanechika, K. EP 205856B2, 1987.
- (8) Yoshino, A.; Nakajima, T.; Sanechika, K. JP 1989293, 1987.
- (9) *The Royal Swedish Academy of Science. The Nobel Prize in Chemistry 2019 - Press Release.* The Royal Swedish Academy of Science. The Nobel Prize in Chemistry 2019 - Press Release. <https://www.nobelprize.org/prizes/chemistry/2019/press-release/>. <https://www.nobelprize.org/prizes/chemistry/2019/press-release/> (accessed 2022-12-30).
- (10) Blomgren, G. E. The Development and Future of Lithium Ion Batteries. *J. Electrochem. Soc.* **2017**, *164* (1), A5019–A5025. <https://doi.org/10.1149/2.0251701jes>.
- (11) Andre, D.; Kim, S. J.; Lamp, P.; Lux, S. F.; Maglia, F.; Paschos, O.; Stiaszny, B. Future Generations of Cathode Materials: An Automotive Industry Perspective. *J. Mater. Chem. A* **2015**, *3* (13), 6709–6732. <https://doi.org/10.1039/c5ta00361j>.
- (12) Tarascon, J. M.; Guyomard, D. The $\text{Li}_{1+x}\text{Mn}_2\text{O}_4/\text{C}$ Rocking-Chair System: A Review. *Electrochim. Acta* **1993**, *38* (9), 1221–1231. [https://doi.org/10.1016/0013-4686\(93\)80053-3](https://doi.org/10.1016/0013-4686(93)80053-3).
- (13) Hausbrand, R.; Cherkashinin, G.; Ehrenberg, H.; Gröting, M.; Albe, K.; Hess, C.; Jaegermann, W. Fundamental Degradation Mechanisms of Layered Oxide Li-Ion Battery Cathode Materials: Methodology, Insights and Novel Approaches. *Mater. Sci. Eng. B Solid-State Mater. Adv. Technol.* **2015**, *192* (B), 3–25. <https://doi.org/10.1016/j.mseb.2014.11.014>.
- (14) Korthauer, R. *Lithium-Ion Batteries: Basics and Applications, 1st Ed. p. 1-89*, 1st

- ed.; Korthauer, R., Ed.; Springer Berlin: Berlin, 2018.
- (15) Noh, H. J.; Youn, S.; Yoon, C. S.; Sun, Y. K. Comparison of the Structural and Electrochemical Properties of Layered $\text{Li}[\text{Ni}_x\text{Co}_y\text{Mn}_z]\text{O}_2$ ($x = 1/3, 0.5, 0.6, 0.7, 0.8$ and 0.85) Cathode Material for Lithium-Ion Batteries. *J. Power Sources* **2013**, *233*, 121–130. <https://doi.org/10.1016/j.jpowsour.2013.01.063>.
- (16) Jung, R.; Metzger, M.; Stinner, C.; Maglia, F.; Gasteiger, H. A. Oxygen Release and Its Effect on the Cycling Stability of $\text{LiNi}_x\text{Mn}_y\text{Co}_z\text{O}_2$ (NMC) Cathode Materials for Li-Ion Batteries. *J. Electrochem. Soc.* **2017**, *164* (7), A1361–A1377. <https://doi.org/10.1149/2.0021707jes>.
- (17) Padhi, A. K.; Nanjundaswamy, K. S.; Masquelier, C.; Okada, S.; Goodenough, J. B. Effect of Structure on the $\text{Fe}^{3+}/\text{Fe}^{2+}$ Redox Couple in Iron Phosphates. *J. Electrochem. Soc.* **1997**, *144* (5), 1609–1613. <https://doi.org/10.1149/1.1837649>.
- (18) Padhi, A. K.; Nanjundaswamy, K. S.; Goodenough, J. B. Phospho-Olivines as Positive-Electrode Materials for Rechargeable Lithium Batteries. *J. Electrochem. Soc.* **1997**, *144* (4), 1188–1194.
- (19) Dahn, J. R. Phase Diagram of Li_xC_6 . *Phys. Rev. B* **1991**, *44* (17), 9170–9177.
- (20) Ferg, E.; Gummow, R. J.; de Kock, A.; Thackeray, M. M. Spinel Anodes for Lithium-Ion Batteries. *J. Electrochem. Soc.* **1994**, *141* (11), L147–L150. <https://doi.org/10.1149/1.2059324>.
- (21) Obrovac, M. N.; Christensen, L.; Le, D. B.; Dahn, J. R. Alloy Design for Lithium-Ion Battery Anodes. *J. Electrochem. Soc.* **2007**, *154* (9), A849–A855. <https://doi.org/10.1149/1.2752985>.
- (22) Obrovac, M. N.; Krause, L. J. Reversible Cycling of Crystalline Silicon Powder. *J. Electrochem. Soc.* **2007**, *154* (2), A103–A108. <https://doi.org/10.1149/1.2402112>.
- (23) Peled, E.; Golodnitsky, D.; Ardel, G. Advanced Model for Solid Electrolyte Interphase Electrodes in Liquid and Polymer Electrolytes. *J. Electrochem. Soc.* **1997**, *144* (8), L208–L210. <https://doi.org/10.1149/1.1837858>.
- (24) Peled, E. The Electrochemical Behavior of Alkali and Alkaline Earth Metals in Nonaqueous Battery Systems—The Solid Electrolyte Interphase Model. *J. Electrochem. Soc.* **1979**, *126* (12), 2047–2051. <https://doi.org/10.1149/1.2128859>.
- (25) Ohzuku, T.; Ueda, A.; Yamamoto, N. Zero-Strain Insertion Material of $\text{Li}[\text{Li}_{1/3}\text{Ti}_{5/3}]\text{O}_4$ for Rechargeable Lithium Cells. *J. Electrochem. Soc.* **1995**, *142* (5), 1431–1435. <https://doi.org/10.1149/1.2048592>.
- (26) Sandhya, C. P.; John, B.; Gouri, C. Lithium Titanate as Anode Material for Lithium-Ion Cells: A Review. *Ionics*. 2014, pp 601–620. <https://doi.org/10.1007/s11581-014-1113-4>.
- (27) Obrovac, M. N.; Chevrier, V. L. Alloy Negative Electrodes for Li-Ion Batteries. *Chemical Reviews*. American Chemical Society December 10, 2014, pp 11444–11502. <https://doi.org/10.1021/cr500207g>.
- (28) Wetjen, M. Studies on the Differentiation and Quantification of Degradation Phenomena in Silicon-Graphite Anodes for Lithium-Ion Batteries Morten. *PhD thesis* **2018**, Technische Universität München.
- (29) Lin, D.; Liu, Y.; Cui, Y. Reviving the Lithium Metal Anode for High-Energy

- Batteries. *Nat. Nanotechnol.* **2017**, *12* (3), 194–206.
<https://doi.org/10.1038/nnano.2017.16>.
- (30) Bachman, J. C.; Muy, S.; Grimaud, A.; Chang, H. H.; Pour, N.; Lux, S. F.; Paschos, O.; Maglia, F.; Lupart, S.; Lamp, P.; Giordano, L.; Shao-Horn, Y. Inorganic Solid-State Electrolytes for Lithium Batteries: Mechanisms and Properties Governing Ion Conduction. *Chem. Rev.* **2016**, *116* (1), 140–162.
<https://doi.org/10.1021/acs.chemrev.5b00563>.
- (31) Helm, B.; Schlem, R.; Wankmiller, B.; Banik, A.; Gautam, A.; Ruhl, J.; Li, C.; Hansen, M. R.; Zeier, W. G. Exploring Aliovalent Substitutions in the Lithium Halide Superionic Conductor $\text{Li}_{3-x}\text{In}_{1-x}\text{Zr}_x\text{Cl}_6$ ($0 \leq x \leq 0.5$). *Chem. Mater.* **2021**, *33* (12), 4773–4782. <https://doi.org/10.1021/acs.chemmater.1c01348>.
- (32) Fenton, D. E.; Parker, J. M.; Wright, P. V. Complexes of Alkali Metal Ions with Poly(Ethylene Oxide). *Polymer.* **1973**, *14* (11), 589. [https://doi.org/10.1016/0032-3861\(73\)90146-8](https://doi.org/10.1016/0032-3861(73)90146-8).
- (33) Xu, S.; Sun, Z.; Sun, C.; Li, F.; Chen, K.; Zhang, Z.; Hou, G.; Cheng, H. M.; Li, F. Homogeneous and Fast Ion Conduction of PEO-Based Solid-State Electrolyte at Low Temperature. *Adv. Funct. Mater.* **2020**, *30* (51), 2007172.
<https://doi.org/10.1002/adfm.202007172>.
- (34) Walke, P.; Freitag, K. M.; Kirchhain, H.; Kaiser, M.; van Wüllen, L.; Nilges, T. Electrospun $\text{Li}(\text{TFSI})@$ Polyethylene Oxide Membranes as Solid Electrolytes. *Zeitschrift für Anorg. und Allg. Chemie* **2018**, *644* (24), 1863–1874.
<https://doi.org/10.1002/zaac.201800370>.
- (35) Rajendran, S.; Mahalingam, T.; Kannan, R. Experimental Investigations on PAN-PEO Hybrid Polymer Electrolytes. *Solid State Ionics* **2000**, *130* (1), 143–148.
[https://doi.org/10.1016/S0167-2738\(00\)00283-6](https://doi.org/10.1016/S0167-2738(00)00283-6).
- (36) Fergus, J. W. Ceramic and Polymeric Solid Electrolytes for Lithium-Ion Batteries. *J. Power Sources* **2010**, *195* (15), 4554–4569.
<https://doi.org/10.1016/j.jpowsour.2010.01.076>.
- (37) Thangadurai, V.; Narayanan, S.; Pinzaru, D. $\text{Li}_6\text{A}\text{La}_2\text{Ta}_2\text{O}_{12}$ (A=Sr, Ba): Novel Garnet-like Oxides for Fast Lithium Ion Conduction. *Chem. Soc. Rev.* **2014**, *43* (13), 4714–4727. <https://doi.org/10.1039/c4cs00020j>.
- (38) Thangadurai, V.; Weppner, W. $\text{Li}_6\text{A}\text{La}_2\text{Ta}_2\text{O}_{12}$ (A=Sr, Ba): Novel Garnet-like Oxides for Fast Lithium Ion Conduction. *Adv. Funct. Mater.* **2005**, *15* (1), 107–112. <https://doi.org/10.1002/adfm.200400044>.
- (39) Buschmann, H.; Dölle, J.; Berendts, S.; Kuhn, A.; Bottke, P.; Wilkening, M.; Heitjans, P.; Senyshyn, A.; Ehrenberg, H.; Lotnyk, A.; Duppel, V.; Kienle, L.; Janek, J. Structure and Dynamics of the Fast Lithium Ion Conductor “ $\text{Li}_7\text{La}_3\text{Zr}_2\text{O}_{12}$.” *Phys. Chem. Chem. Phys.* **2011**, *13* (43), 19378–19392.
<https://doi.org/10.1039/c1cp22108f>.
- (40) Bernuy-Lopez, C.; Manalastas, W.; Lopez Del Amo, J. M.; Aguadero, A.; Aguesse, F.; Kilner, J. A. Atmosphere Controlled Processing of Ga-Substituted Garnets for High LL-Ion Conductivity Ceramics. *Chem. Mater.* **2014**, *26* (12), 3610–3617. <https://doi.org/10.1021/cm5008069>.
- (41) Aono, H.; Sugimoto, E.; Sadaoka, Y.; Imanaka, N.; Adachi, G. The Electrical Properties of Ceramic Electrolytes for $\text{LiM}_x\text{Ti}_{2-x}(\text{PO}_4)_3 + \text{YLi}_2\text{O}$, M = Ge, Sn,

- Hf , and Zr Systems. *J. Electrochem. Soc.* **1993**, *140* (7), 1827–1833. <https://doi.org/10.1149/1.2220723>.
- (42) Aono, H.; Sugimoto, E.; Sadaoka, Y.; Imanaka, N.; Adachi, G. Ionic Conductivity of Solid Electrolytes Based on $\text{Li}_{1.3}\text{Al}_{0.3}\text{Ti}_{1.7}(\text{PO}_4)_3$. *J. Electrochem. Soc.* **1996**, *137* (4), 1023–1027.
- (43) Itoh, M.; Inaguma, Y.; Jung, W. H.; Chen, L.; Nakamura, T. High Lithium Ion Conductivity in the Perovskite-Type Compounds $\text{Ln}_{1/2}\text{Li}_{1/2}\text{TiO}_3$ (Ln=La,Pr,Nd,Sm). *Solid State Ionics* **1994**, *70–71* (PART 1), 203–207. [https://doi.org/10.1016/0167-2738\(94\)90310-7](https://doi.org/10.1016/0167-2738(94)90310-7).
- (44) Morata-Orrantia, A.; García-Martín, S.; Morán, E.; Alario-Franco, M. Á. A New $\text{La}_{2/3}\text{Li}_x\text{Ti}_{1-x}\text{Al}_x\text{O}_3$ Solid Solution: Structure, Microstructure, and Li^+ Conductivity. *Chem. Mater.* **2002**, *14* (7), 2871–2875. <https://doi.org/10.1021/cm011149s>.
- (45) Kobylianska, S. D.; V'yunov, O. I.; Belous, A. G.; Bohnke, O. New Lithium Ion Conductors Based on System $(\text{Li,Na,La})\{\text{Ti,Nb,Ta}\}\text{O}$ with Perovskite Structure. *Solid State Phenom.* **2013**, *200* (8), 279–285. <https://doi.org/10.4028/www.scientific.net/SSP.200.279>.
- (46) Kanno, R.; Murayama, M. Lithium Ionic Conductor Thio-LISICON: The $\text{Li}_2\text{S}-\text{GeS}_2-\text{P}_2\text{S}_5$ System. *J. Electrochem. Soc.* **2001**, *148* (7), A742–A746. <https://doi.org/10.1149/1.1379028>.
- (47) Kanno, R.; Hata, T.; Kawamoto, Y.; Irie, M. Synthesis of a New Lithium Ionic Conductor, Thio-LISICON-Lithium Germanium Sulfide System. *Solid State Ionics* **2000**, *130* (1), 97–104. [https://doi.org/10.1016/S0167-2738\(00\)00277-0](https://doi.org/10.1016/S0167-2738(00)00277-0).
- (48) Murayama, M.; Kanno, R.; Irie, M.; Ito, S.; Hata, T.; Sonoyama, N.; Kawamoto, Y. Synthesis of New Lithium Ionic Conductor Thio-LISICON - Lithium Silicon Sulfides System. *J. Solid State Chem.* **2002**, *168* (1), 140–148. <https://doi.org/10.1006/jssc.2002.9701>.
- (49) Yamakawa, Y.; Hama, S.; Mitsui, A.; Hirayama, M.; Kato, Y.; Kamaya, N.; Kanno, R.; Kamiyama, T.; Yonemura, M.; Kawamoto, K.; Homma, K. A Lithium Superionic Conductor. *Nat. Mater.* **2011**, *10* (9), 682–686. <https://doi.org/10.1038/nmat3066>.
- (50) Bron, P.; Johansson, S.; Zick, K.; Der Günne, J. S. A.; Dehnen, S.; Roling, B. $\text{Li}_{10}\text{SnP}_2\text{S}_{12}$: An Affordable Lithium Superionic Conductor. *J. Am. Chem. Soc.* **2013**, *135* (42), 15694–15697. <https://doi.org/10.1021/ja407393y>.
- (51) Bron, P.; Dehnen, S.; Roling, B. $\text{Li}_{10}\text{Si}_{0.3}\text{Sn}_{0.7}\text{P}_2\text{S}_{12}$ – A Low-Cost and Low-Grain-Boundary-Resistance Lithium Superionic Conductor. *J. Power Sources* **2016**, *329*, 530–535. <https://doi.org/10.1016/j.jpowsour.2016.08.115>.
- (52) Kato, Y.; Saito, R.; Sakano, M.; Mitsui, A.; Hirayama, M.; Kanno, R. Synthesis, Structure and Lithium Ionic Conductivity of Solid Solutions of $\text{Li}_{10}(\text{Ge}_{1-x}\text{M}_x)\text{P}_2\text{S}_{12}$ (M = Si, Sn). *J. Power Sources* **2014**, *271*, 60–64. <https://doi.org/10.1016/j.jpowsour.2014.07.159>.
- (53) Boulineau, S.; Courty, M.; Tarascon, J. M.; Viallet, V. Mechanochemical Synthesis of Li-Argyrodite $\text{Li}_6\text{PS}_5\text{X}$ (X = Cl, Br, I) as Sulfur-Based Solid Electrolytes for All Solid State Batteries Application. *Solid State Ionics* **2012**, *221*, 1–5. <https://doi.org/10.1016/j.ssi.2012.06.008>.

- (54) Pecher, O.; Kong, S. T.; Goebel, T.; Nickel, V.; Weichert, K.; Reiner, C.; Deiseroth, H. J.; Maier, J.; Haarmann, F.; Zahn, D. Atomistic Characterisation of Li^+ Mobility and Conductivity in $\text{Li}_{7-x}\text{PS}_{6-x}\text{I}_x$ Argyrodites from Molecular Dynamics Simulations, Solid-State NMR, and Impedance Spectroscopy. *Chem. - A Eur. J.* **2010**, *16* (28), 8347–8354. <https://doi.org/10.1002/chem.201000501>.
- (55) Deiseroth, H. J.; Kong, S. T.; Eckert, H.; Vannahme, J.; Reiner, C.; Zaiß, T.; Schlosser, M. $\text{Li}_6\text{PS}_5\text{X}$: A Class of Crystalline Li-Rich Solids with an Unusually High Li^+ Mobility. *Angew. Chemie - Int. Ed.* **2008**, *47* (4), 755–758. <https://doi.org/10.1002/anie.200703900>.
- (56) Deiseroth, H. J.; Maier, J.; Weichert, K.; Nickel, V.; Kong, S. T.; Reiner, C. Li_7PS_6 and $\text{Li}_6\text{PS}_5\text{X}$ (X: Cl, Br, I): Possible Three-Dimensional Diffusion Pathways for Lithium Ions and Temperature Dependence of the Ionic Conductivity by Impedance Measurements. *Zeitschrift für Anorg. und Allg. Chemie* **2011**, *637* (10), 1287–1294. <https://doi.org/10.1002/zaac.201100158>.
- (57) Rao, R. P.; Adams, S. Studies of Lithium Argyrodite Solid Electrolytes for All-Solid-State Batteries. *Phys. Status Solidi Appl. Mater. Sci.* **2011**, *208* (8), 1804–1807. <https://doi.org/10.1002/pssa.201001117>.
- (58) Kong, S. T.; Deiseroth, H. J.; Maier, J.; Nickel, V.; Weichert, K.; Reiner, C. $\text{Li}_6\text{PO}_5\text{Br}$ and $\text{Li}_6\text{PO}_5\text{Cl}$: The First Lithium-Oxide-Argyrodites. *Zeitschrift für Anorg. und Allg. Chemie* **2010**, *636* (11), 1920–1924. <https://doi.org/10.1002/zaac.201000121>.
- (59) Lotsch, B. V.; Maier, J. Relevance of Solid Electrolytes for Lithium-Based Batteries: A Realistic View. *J. Electroceramics* **2017**, *38* (2–4), 128–141. <https://doi.org/10.1007/s10832-017-0091-0>.
- (60) Tachez, M.; Malugani, J. P.; Mercier, R.; Robert, G. Ionic Conductivity of and Phase Transition in Lithium Thiophosphate Li_3PS_4 . *Solid State Ionics* **1984**, *14* (3), 181–185. [https://doi.org/10.1016/0167-2738\(84\)90097-3](https://doi.org/10.1016/0167-2738(84)90097-3).
- (61) Dewald, G. F.; Ohno, S.; Kraft, M. A.; Koerver, R.; Till, P.; Vargas-Barbosa, N. M.; Janek, J.; Zeier, W. G. Experimental Assessment of the Practical Oxidative Stability of Lithium Thiophosphate Solid Electrolytes. *Chem. Mater.* **2019**, *31* (20), 8328–8337. <https://doi.org/10.1021/acs.chemmater.9b01550>.
- (62) Wenzel, S.; Leichtweiß, T.; Weber, D. A.; Sann, J.; Zeier, W. G.; Janek, J.; Randau, S. Direct Observation of the Interfacial Instability of the Fast Ionic Conductor $\text{Li}_{10}\text{GeP}_2\text{S}_{12}$ at the Lithium Metal Anode. *Chem. Mater.* **2016**, *28* (7), 2400–2407. <https://doi.org/10.1021/acs.chemmater.6b00610>.
- (63) Nakano, T.; Kimura, T.; Sakuda, A.; Tatsumisago, M.; Hayashi, A. Characterizing the Structural Change of Na_3PS_4 Solid Electrolytes in a Humid N_2 Atmosphere. *J. Phys. Chem. C* **2022**, *126* (17), 7383–7389. <https://doi.org/10.1021/acs.jpcc.2c00421>.
- (64) Zhang, J.; Gu, X. Hydrolysis Mechanism of Li-Argyrodite $\text{Li}_6\text{PS}_5\text{Cl}$ in Air. *Rare Met.* **2022**. <https://doi.org/10.1007/s12598-022-02188-7>.
- (65) Muramatsu, H.; Hayashi, A.; Ohtomo, T.; Hama, S.; Tatsumisago, M. Structural Change of $\text{Li}_2\text{S} - \text{P}_2\text{S}_5$ Sulfide Solid Electrolytes in the Atmosphere. *Solid State Ionics* **2011**, *182*, 116–119. <https://doi.org/10.1016/j.ssi.2010.10.013>.
- (66) Chen, Y. T.; Marple, M. A. T.; Tan, D. H. S.; Ham, S. Y.; Sayahpour, B.; Li, W.

- K.; Yang, H.; Lee, J. B.; Hah, H. J.; Wu, E. A.; Doux, J. M.; Jang, J.; Ridley, P.; Cronk, A.; Deyscher, G.; Chen, Z.; Meng, Y. S. Investigating Dry Room Compatibility of Sulfide Solid-State Electrolytes for Scalable Manufacturing. *J. Mater. Chem. A* **2022**, *10* (13), 7155–7164. <https://doi.org/10.1039/d1ta09846b>.
- (67) Sano, H.; Morino, Y.; Yabuki, A.; Sato, S.; Itayama, N.; Matsumura, Y.; Iwasaki, M.; Takehara, M.; Abe, T.; Ishiguro, Y.; Takahashi, T.; Miyashita, N.; Sakuda, A.; Hayashi, A. AC Impedance Analysis of the Degeneration and Recovery of Argyrodite Sulfide-Based Solid Electrolytes under Dry-Room-Simulated Condition. *Electrochemistry* **2022**, *90* (3). <https://doi.org/10.5796/ELECTROCHEMISTRY.22-00013>.
- (68) Jung, W. D.; Jeon, M.; Shin, S. S.; Kim, J. S.; Jung, H. G.; Kim, B. K.; Lee, J. H.; Chung, Y. C.; Kim, H. Functionalized Sulfide Solid Electrolyte with Air-Stable and Chemical-Resistant Oxysulfide Nanolayer for All-Solid-State Batteries. *ACS Omega* **2020**, *5* (40), 26015–26022. <https://doi.org/10.1021/acsomega.0c03453>.
- (69) Xu, M.; Song, S.; Daikuhara, S.; Matsui, N.; Hori, S.; Suzuki, K.; Hirayama, M.; Shiotani, S.; Nakanishi, S.; Yonemura, M.; Saito, T.; Kamiyama, T.; Kanno, R. $\text{Li}_{10}\text{GeP}_2\text{S}_{12}$ -Type Structured Solid Solution Phases in the $\text{Li}_{9+\delta}\text{P}_{3+\delta}\text{S}_{12-k}\text{O}_k$ System: Controlling Crystallinity by Synthesis to Improve the Air Stability. *Inorg. Chem.* **2022**, *61* (1), 52–61. <https://doi.org/10.1021/acs.inorgchem.1c01748>.
- (70) Lu, X.; Camara, O.; Liu, Z.; Windmüller, A.; Tsai, C.-L.; Tempel, H.; Yu, S.; Kungl, H.; Eichel, R.-A. Tuning the Moisture Stability of Multiphase B- Li_3PS_4 Solid Electrolyte Materials. *Electrochem. Sci. Adv.* **2022**. <https://doi.org/10.1002/elsa.202100208>.
- (71) Riphaut, N.; Strobl, P.; Stiaszny, B.; Zinkevich, T.; Yavuz, M.; Schnell, J.; Indris, S.; Gasteiger, H. A.; Sedlmaier, S. J. Slurry-Based Processing of Solid Electrolytes: A Comparative Binder Study. *J. Electrochem. Soc.* **2018**, *165* (16), A3993–A3999. <https://doi.org/10.1149/2.0961816jes>.
- (72) Lee, K.; Kim, S.; Park, J.; Park, S. H.; Coskun, A.; Jung, D. S.; Cho, W.; Choi, J. W. Selection of Binder and Solvent for Solution-Processed All-Solid-State Battery. *J. Electrochem. Soc.* **2017**, *164* (9), A2075–A2081. <https://doi.org/10.1149/2.1341709jes>.
- (73) Ruhl, J.; Riegger, L. M.; Ghidui, M.; Zeier, W. G. Impact of Solvent Treatment of the Superionic Argyrodite $\text{Li}_6\text{PS}_5\text{Cl}$ on Solid-State Battery Performance. *Adv. Energy Sustain. Res.* **2021**, *2* (2), 2000077. <https://doi.org/10.1002/aesr.202000077>.
- (74) Sakuda, A.; Kuratani, K.; Yamamoto, M.; Takahashi, M.; Takeuchi, T.; Kobayashi, H. All-Solid-State Battery Electrode Sheets Prepared by a Slurry Coating Process. *J. Electrochem. Soc.* **2017**, *164* (12), A2474–A2478. <https://doi.org/10.1149/2.0951712jes>.
- (75) Wang, X.; Ye, L.; Nan, C. W.; Li, X. Effect of Solvents on a $\text{Li}_{10}\text{GeP}_2\text{S}_{12}$ -Based Composite Electrolyte via Solution Method for Solid-State Battery Applications. *ACS Appl. Mater. Interfaces* **2022**, *14* (41), 46627–46634. <https://doi.org/10.1021/acsmi.2c12920>.
- (76) Sakuda, A. Favorable Composite Electrodes for All-Solid-State Batteries. *J. Ceram. Soc. Japan* **2018**, *126* (9), 675–683. <https://doi.org/10.2109/jcersj2.18114>.

-
- (77) Tan, D. H. S.; Meng, Y. S.; Jang, J. Scaling up High-Energy-Density Sulfidic Solid-State Batteries: A Lab-to-Pilot Perspective. *Joule* **2022**, *6* (8), 1755–1769. <https://doi.org/10.1016/j.joule.2022.07.002>.
- (78) Batzer, M.; Heck, C. A.; Michalowski, P.; Kwade, A. Current Status of Formulations and Scalable Processes for Producing Sulfidic Solid-State Batteries. *Batter. Supercaps* **2022**. <https://doi.org/10.1002/batt.202200328>.
- (79) Koerver, R.; Walther, F.; Aygün, I.; Sann, J.; Dietrich, C.; Zeier, W. G.; Janek, J. Redox-Active Cathode Interphases in Solid-State Batteries. *J. Mater. Chem. A* **2017**, *5* (43), 22750–22760. <https://doi.org/10.1039/c7ta07641j>.
- (80) Koerver, R.; Janek, J.; Leichtweiß, T.; Zeier, W. G.; Hartmann, P.; Dietrich, C.; Zhang, W.; Binder, J. O.; Aygün, I. Capacity Fade in Solid-State Batteries: Interphase Formation and Chemomechanical Processes in Nickel-Rich Layered Oxide Cathodes and Lithium Thiophosphate Solid Electrolytes - Supporting Information. *Chem. Mater.* **2017**, *29* (13), 5574–5582. <https://doi.org/10.1021/acs.chemmater.7b00931>.
- (81) Oh, D. Y.; Kim, D. H.; Jung, S. H.; Han, J. G.; Choi, N. S.; Jung, Y. S. Single-Step Wet-Chemical Fabrication of Sheet-Type Electrodes from Solid-Electrolyte Precursors for All-Solid-State Lithium-Ion Batteries. *J. Mater. Chem. A* **2017**, *5* (39), 20771–20779. <https://doi.org/10.1039/c7ta06873e>.
- (82) Nam, Y. J.; Oh, D. Y.; Jung, S. H.; Jung, Y. S. Toward Practical All-Solid-State Lithium-Ion Batteries with High Energy Density and Safety: Comparative Study for Electrodes Fabricated by Dry- and Slurry-Mixing Processes. *J. Power Sources* **2018**, *375*, 93–101. <https://doi.org/10.1016/j.jpowsour.2017.11.031>.
- (83) Wang, C.; Yu, R.; Duan, H.; Lu, Q.; Li, Q.; Adair, K. R.; Bao, D.; Liu, Y.; Yang, R.; Wang, J.; Zhao, S.; Huang, H.; Sun, X. Solvent-Free Approach for Interweaving Freestanding and Ultrathin Inorganic Solid Electrolyte Membranes. *ACS Energy Lett.* **2022**, *7* (1), 410–416. <https://doi.org/10.1021/acsenerylett.1c02261>.
- (84) Kawaguchi, T.; Nakamura, H.; Watano, S. Parametric Study of Dry Coating Process of Electrode Particle with Model Material of Sulfide Solid Electrolytes for All-Solid-State Battery. *Powder Technol.* **2017**, *305*, 241–249. <https://doi.org/10.1016/j.powtec.2016.09.085>.
- (85) Kawaguchi, T.; Nakamura, H.; Watano, S. Dry Coating of Electrode Particle with Model Particle of Sulfide Solid Electrolytes for All-Solid-State Secondary Battery. *Powder Technol.* **2018**, *323*, 581–587. <https://doi.org/10.1016/j.powtec.2016.03.055>.
- (86) Nakamura, H.; Kawaguchi, T.; Masuyama, T.; Sakuda, A.; Saito, T.; Kuratani, K.; Ohsaki, S.; Watano, S. Dry Coating of Active Material Particles with Sulfide Solid Electrolytes for an All-Solid-State Lithium Battery. *J. Power Sources* **2020**, *448* (October 2019), 227579. <https://doi.org/10.1016/j.jpowsour.2019.227579>.
- (87) Froboese, L.; Groffmann, L.; Monsees, F.; Helmers, L.; Loellhoeffel, T.; Kwade, A. Enhancing the Lithium Ion Conductivity of an All Solid-State Electrolyte via Dry and Solvent-Free Scalable Series Production Processes. *J. Electrochem. Soc.* **2020**, *167* (2), 020558. <https://doi.org/10.1149/1945-7111/ab6f77>.
- (88) Zhang, W.; Leichtweiß, T.; Culver, S. P.; Koerver, R.; Das, D.; Weber, D. A.;

- Zeier, W. G.; Janek, J. The Detrimental Effects of Carbon Additives in $\text{Li}_{10}\text{GeP}_2\text{S}_{12}$ -Based Solid-State Batteries. *ACS Appl. Mater. Interfaces* **2017**, *9* (41), 35888–35896. <https://doi.org/10.1021/acsami.7b11530>.
- (89) Strauss, F.; Stepien, D.; Maibach, J.; Pfaffmann, L.; Indris, S.; Hartmann, P.; Brezesinski, T. Influence of Electronically Conductive Additives on the Cycling Performance of Argyrodite-Based All-Solid-State Batteries. *RSC Adv.* **2019**, *10* (2), 1114–1119. <https://doi.org/10.1039/c9ra10253a>.
- (90) Culver, S. P.; Koerver, R.; Zeier, W. G.; Janek, J. On the Functionality of Coatings for Cathode Active Materials in Thiophosphate-Based All-Solid-State Batteries. *Advanced Energy Materials*. Wiley-VCH Verlag June 1, 2019. <https://doi.org/10.1002/aenm.201900626>.
- (91) Sakuda, A.; Kitaura, H.; Hayashi, A.; Tadanaga, K.; Tatsumisago, M. Improvement of High-Rate Performance of All-Solid-State Lithium Secondary Batteries Using LiCoO_2 Coated with $\text{Li}_2\text{O-SiO}_2$ Glasses. *Electrochem. Solid-State Lett.* **2008**, *11* (1), 11–14. <https://doi.org/10.1149/1.2795837>.
- (92) Sakuda, A.; Kitaura, H.; Hayashi, A.; Tadanaga, K.; Tatsumisago, M. Modification of Interface Between LiCoO_2 Electrode and $\text{Li}_2\text{S} - \text{P}_2\text{S}_5$ Solid Electrolyte Using $\text{Li}_2\text{O-SiO}_2$ Glassy Layers. *J. Electrochem. Soc.* **2009**, *156* (1), A27. <https://doi.org/10.1149/1.3005972>.
- (93) Sakuda, A.; Kitaura, H.; Hayashi, A.; Tadanaga, K.; Tatsumisago, M. All-Solid-State Lithium Secondary Batteries with Oxide-Coated LiCoO_2 Electrode and $\text{Li}_2\text{S-P}_2\text{S}_5$ Electrolyte. *J. Power Sources* **2009**, *189* (1), 527–530. <https://doi.org/10.1016/j.jpowsour.2008.10.129>.
- (94) Ohta, N.; Takada, K.; Sakaguchi, I.; Zhang, L.; Ma, R.; Fukuda, K.; Osada, M.; Sasaki, T. LiNbO_3 -Coated LiCoO_2 as Cathode Material for All Solid-State Lithium Secondary Batteries. *Electrochem. commun.* **2007**, *9* (7), 1486–1490. <https://doi.org/10.1016/j.elecom.2007.02.008>.
- (95) Zhang, W.; Weber, D. A.; Weigand, H.; Arlt, T.; Manke, I.; Schröder, D.; Koerver, R.; Leichtweiss, T.; Hartmann, P.; Zeier, W. G.; Janek, J. Interfacial Processes and Influence of Composite Cathode Microstructure Controlling the Performance of All-Solid-State Lithium Batteries. *ACS Appl. Mater. Interfaces* **2017**, *9* (21), 17835–17845. <https://doi.org/10.1021/acsami.7b01137>.
- (96) Machida, N.; Kashiwagi, J.; Naito, M.; Shigematsu, T. Electrochemical Properties of All-Solid-State Batteries with ZrO_2 -Coated $\text{LiNi}_{1/3}\text{Mn}_{1/3}\text{Co}_{1/3}\text{O}_2$ as Cathode Materials. *Solid State Ionics* **2012**, *225*, 354–358. <https://doi.org/10.1016/j.ssi.2011.11.026>.
- (97) Strauss, F.; Bartsch, T.; De Biasi, L.; Kim, a. Y.; Janek, J.; Hartmann, P.; Brezesinski, T. Impact of Cathode Material Particle Size on the Capacity of Bulk-Type All-Solid-State Batteries. *ACS Energy Lett.* **2018**, *3* (4), 992–996. <https://doi.org/10.1021/acsenergylett.8b00275>.
- (98) Shi, T.; Tu, Q.; Tian, Y.; Xiao, Y.; Miara, L. J.; Kononova, O.; Ceder, G. High Active Material Loading in All-Solid-State Battery Electrode via Particle Size Optimization. *Adv. Energy Mater.* **2020**, *10* (1), 1902881. <https://doi.org/10.1002/aenm.201902881>.
- (99) Rajagopal, R.; Subramanian, Y.; Ryu, K. S. Improving the Electrochemical

- Performance of Cathode Composites Using Different Sized Solid Electrolytes for All Solid-State Lithium Batteries. *RSC Adv.* **2021**, *11* (52), 32981–32987. <https://doi.org/10.1039/d1ra05897e>.
- (100) Alexander, W. A.; Calvert, L. D.; Gamble, R. H.; Schinzel, K. The Lithium-Indium System I. *Can. J. Chem.* **1976**, *54* (7), 1052–1060.
- (101) Sangster, J.; Pelton, A. D. The In-Li (Indium-Lithium) System. *J. Phase Equilibria* **1991**, *12* (1), 37–41.
- (102) Jung, Y. S.; Lee, K. T.; Kim, J. H.; Kwon, J. Y.; Oh, S. M. Thermo-Electrochemical Activation of an In-Cu Intermetallic Electrode for the Anode in Lithium Secondary Batteries. *Adv. Funct. Mater.* **2008**, *18* (19), 3010–3017. <https://doi.org/10.1002/adfm.200701526>.
- (103) Nam, Y. J.; Park, K. H.; Oh, D. Y.; An, W. H.; Jung, Y. S. Diagnosis of Failure Modes for All-Solid-State Li-Ion Batteries Enabled by Three-Electrode Cells. *J. Mater. Chem. A* **2018**, *6* (30), 14867–14875. <https://doi.org/10.1039/c8ta03450h>.
- (104) Dugas, R.; Dupraz, Y.; Queminn, E.; Koç, T.; Tarascon, J.-M. Engineered Three-Electrode Cells for Improving Solid State Batteries. *J. Electrochem. Soc.* **2021**, *168* (9), 090508. <https://doi.org/10.1149/1945-7111/ac208d>.
- (105) Tan, D. H. S.; Chen, Y. T.; Yang, H.; Bao, W.; Sreenarayanan, B.; Doux, J. M.; Li, W.; Lu, B.; Ham, S. Y.; Sayahpour, B.; Scharf, J.; Wu, E. A.; Deysler, G.; Han, H. E.; Hah, H. J.; Jeong, H.; Chen, Z.; Meng, Y. S. Carbon Free High Loading Silicon Anodes Enabled by Sulfide Solid Electrolytes for Robust All Solid-State Batteries. *Science* **2021**, *373* (6562), 1494–1499.
- (106) Yamamoto, M.; Terauchi, Y.; Sakuda, A.; Takahashi, M. Slurry Mixing for Fabricating Silicon-Composite Electrodes in All-Solid-State Batteries with High Areal Capacity and Cycling Stability. *J. Power Sources* **2018**, *402*, 506–512. <https://doi.org/10.1016/j.jpowsour.2018.09.070>.
- (107) Yamamoto, M.; Terauchi, Y.; Sakuda, A.; Kato, A.; Takahashi, M. Effects of Volume Variations under Different Compressive Pressures on the Performance and Microstructure of All-Solid-State Batteries. *J. Power Sources* **2020**, *473*. <https://doi.org/10.1016/j.jpowsour.2020.228595>.
- (108) Bron, P.; Roling, B.; Dehnen, S. Impedance Characterization Reveals Mixed Conducting Interphases between Sulfidic Superionic Conductors and Lithium Metal Electrodes. *J. Power Sources* **2017**, *352*, 127–134. <https://doi.org/10.1016/j.jpowsour.2017.03.103>.
- (109) Wenzel, S.; Sedlmaier, S. J.; Dietrich, C.; Zeier, W. G.; Janek, J. Interfacial Reactivity and Interphase Growth of Argyrodite Solid Electrolytes at Lithium Metal Electrodes. *Solid State Ionics* **2018**, *318* (February), 102–112. <https://doi.org/10.1016/j.ssi.2017.07.005>.
- (110) Masias, A.; Felten, N.; Garcia-Mendez, R.; Wolfenstine, J.; Sakamoto, J. Elastic, Plastic, and Creep Mechanical Properties of Lithium Metal. *J. Mater. Sci.* **2019**, *54* (3), 2585–2600. <https://doi.org/10.1007/s10853-018-2971-3>.
- (111) Doux, J. M.; Nguyen, H.; Tan, D. H. S.; Banerjee, A.; Wang, X.; Wu, E. A.; Jo, C.; Yang, H.; Meng, Y. S. Stack Pressure Considerations for Room-Temperature All-Solid-State Lithium Metal Batteries. *Adv. Energy Mater.* **2020**, *10* (1), 1–6. <https://doi.org/10.1002/aenm.201903253>.

- (112) Krauskopf, T.; Richter, F. H.; Zeier, W. G.; Janek, J. Physicochemical Concepts of the Lithium Metal Anode in Solid-State Batteries. *Chemical Reviews*. American Chemical Society 2020, pp7745–7794. <https://doi.org/10.1021/acs.chemrev.0c00431>.
- (113) Schlenker, R.; Stępień, D.; Koch, P.; Hupfer, T.; Indris, S.; Roling, B.; Miß, V.; Fuchs, A.; Wilhelmi, M.; Ehrenberg, H. Understanding the Lifetime of Battery Cells Based on Solid-State Li₆PS₅Cl Electrolyte Paired with Lithium Metal Electrode. *ACS Appl. Mater. Interfaces* **2020**, *12* (17), 20012–20025. <https://doi.org/10.1021/acsami.9b22629>.
- (114) Janek, J.; Zeier, W. G. A Solid Future for Battery Development. *Nature Energy*. 2016. <https://doi.org/10.1038/nenergy.2016.141>.
- (115) Kato, Y.; Hori, S.; Saito, T.; Suzuki, K.; Hirayama, M.; Mitsui, A.; Yonemura, M.; Iba, H.; Kanno, R. High-Power All-Solid-State Batteries Using Sulfide Superionic Conductors. *Nat. Energy* **2016**, *1* (4), 1–7. <https://doi.org/10.1038/nenergy.2016.30>.
- (116) Richards, W. D.; Miara, L. J.; Wang, Y.; Kim, J. C.; Ceder, G. Interface Stability in Solid-State Batteries. *Chem. Mater.* **2016**, *28* (1), 266–273. <https://doi.org/10.1021/acs.chemmater.5b04082>.
- (117) Hartmann, P.; Leichtweiss, T.; Busche, M. R.; Schneider, M.; Reich, M.; Sann, J.; Adelhelm, P.; Janek, J. Degradation of NASICON-Type Materials in Contact with Lithium Metal: Formation of Mixed Conducting Interphases (MCI) on Solid Electrolytes. *J. Phys. Chem. C* **2013**, *117* (41), 21064–21074. <https://doi.org/10.1021/jp4051275>.
- (118) Connell, J. G.; Fuchs, T.; Hartmann, H.; Krauskopf, T.; Zhu, Y.; Sann, J.; Garcia-Mendez, R.; Sakamoto, J.; Tepavcevic, S.; Janek, J. Kinetic versus Thermodynamic Stability of LLZO in Contact with Lithium Metal. *Chem. Mater.* **2020**, *32* (23), 10207–10215. <https://doi.org/10.1021/acs.chemmater.0c03869>.
- (119) Zhu, Y.; Connell, J. G.; Tepavcevic, S.; Zapol, P.; Garcia-Mendez, R.; Taylor, N. J.; Sakamoto, J.; Ingram, B. J.; Curtiss, L. A.; Freeland, J. W.; Fong, D. D.; Markovic, N. M. Dopant-Dependent Stability of Garnet Solid Electrolyte Interfaces with Lithium Metal. *Adv. Energy Mater.* **2019**, *9* (12), 1–11. <https://doi.org/10.1002/aenm.201803440>.
- (120) Aguesse, F.; Manalastas, W.; Buannic, L.; Del Amo, J. M. L.; Singh, G.; Llordés, A.; Kilner, J. Investigating the Dendritic Growth during Full Cell Cycling of Garnet Electrolyte in Direct Contact with Li Metal. *ACS Appl. Mater. Interfaces* **2017**, *9* (4), 3808–3816. <https://doi.org/10.1021/acsami.6b13925>.
- (121) Wang, Y.; Liu, T.; Kumar, J. Effect of Pressure on Lithium Metal Deposition and Stripping against Sulfide-Based Solid Electrolytes. *ACS Appl. Mater. Interfaces* **2020**, *12* (31), 34771–34776. <https://doi.org/10.1021/acsami.0c06201>.
- (122) Zhou, W.; Wang, S.; Li, Y.; Xin, S.; Manthiram, A.; Goodenough, J. B. Plating a Dendrite-Free Lithium Anode with a Polymer/Ceramic/Polymer Sandwich Electrolyte. *J. Am. Chem. Soc.* **2016**, *138* (30), 9385–9388. <https://doi.org/10.1021/jacs.6b05341>.
- (123) Wang, C.; Yang, Y.; Liu, X.; Zhong, H.; Xu, H.; Xu, Z.; Shao, H.; Ding, F. Suppression of Lithium Dendrite Formation by Using LAGP-PEO (LiTFSI)

- Composite Solid Electrolyte and Lithium Metal Anode Modified by PEO (LiTFSI) in All-Solid-State Lithium Batteries. *ACS Appl. Mater. Interfaces* **2017**, *9* (15), 13694–13702. <https://doi.org/10.1021/acsami.7b00336>.
- (124) Xu, C.; Sun, B.; Gustafsson, T.; Edström, K.; Brandell, D.; Hahlin, M. Interface Layer Formation in Solid Polymer Electrolyte Lithium Batteries: An XPS Study. *J. Mater. Chem. A* **2014**, *2* (20), 7256–7264. <https://doi.org/10.1039/c4ta00214h>.
- (125) Kim, T.; Kim, K.; Lee, S.; Song, G.; Jung, M. S.; Lee, K. T. Thermal Runaway Behavior of $\text{Li}_6\text{PS}_5\text{Cl}$ Solid Electrolytes for $\text{LiNi}_{0.8}\text{Mn}_{0.1}\text{Co}_{0.1}\text{O}_2$ and LiFePO_4 in All-Solid-State Batteries. *Chem. Mater.* **2022**, *34* (20), 9159–9171. <https://doi.org/10.1021/acs.chemmater.2c02106>.
- (126) Strangmüller, S.; Eickhoff, H.; Müller, D.; Klein, W.; Raudaschl-Sieber, G.; Kirchhain, H.; Sedlmeier, C.; Baran, V.; Senyshyn, A.; Deringer, V. L.; Van Wüllen, L.; Gasteiger, H. A.; Fässler, T. F. Fast Ionic Conductivity in the Most Lithium-Rich Phosphidosilicate $\text{Li}_{14}\text{SiP}_6$. *J. Am. Chem. Soc.* **2019**, *141* (36), 14200–14209. <https://doi.org/10.1021/jacs.9b05301>.
- (127) Sedlmeier, C.; Kutsch, T.; Schuster, R.; Hartmann, L.; Bublitz, R.; Tominac, M.; Bohn, M.; Gasteiger, H. A. From Powder to Sheets: A Comparative Electrolyte Study for Slurry-Based Processed Solid Electrolyte/Binder-Sheets as Separators in All-Solid-State Batteries. *J. Electrochem. Soc.* **2022**, *169* (7), 070508. <https://doi.org/10.1149/1945-7111/ac7e76>.
- (128) rhd Instruments. *Compre Cell*. <https://www.rhd-instruments.de/en/products/cells/comprecell>. accesse December 2022.
- (129) Koerver, R.; Zhang, W.; De Biasi, L.; Schweidler, S.; Kondrakov, A. O.; Kolling, S.; Brezesinski, T.; Hartmann, P.; Zeier, W. G.; Janek, J. Chemo-Mechanical Expansion of Lithium Electrode Materials-on the Route to Mechanically Optimized All-Solid-State Batteries. *Energy Environ. Sci.* **2018**, *11* (8), 2142–2158. <https://doi.org/10.1039/c8ee00907d>.
- (130) Bron, P.; Dehnen, S.; Roling, B. $\text{Li}_{10}\text{Si}_{0.3}\text{Sn}_{0.7}\text{P}_2\text{S}_{12}$ – A Low-Cost and Low-Grain-Boundary-Resistance Lithium Superionic Conductor. *J. Power Sources* **2016**, *329*, 530–535. <https://doi.org/10.1016/j.jpowsour.2016.08.115>.
- (131) Kato, A.; Nose, M.; Yamamoto, M.; Sakuda, A.; Hayashi, A.; Tatsumisago, M. Mechanical Properties of Sulfide Glasses in All-Solid-State Batteries. *J. Ceram. Soc. Japan* **2018**, *126* (9), 719–727.
- (132) Böge, A.; Böge, W. *Handbuch Maschinenbau - Grundlagen Und Anwendungen Der Maschinenbau-Technik*, 22nd ed.; Böge, A., Ed.; Springer Vieweg, 2014.
- (133) Koerver, R.; Aygün, I.; Leichtweiß, T.; Dietrich, C.; Zhang, W.; Binder, J. O.; Hartmann, P.; Zeier, W. G.; Janek, J. Capacity Fade in Solid-State Batteries: Interphase Formation and Chemomechanical Processes in Nickel-Rich Layered Oxide Cathodes and Lithium Thiophosphate Solid Electrolytes. *Chem. Mater.* **2017**, *29* (13), 5574–5582. <https://doi.org/10.1021/acs.chemmater.7b00931>.
- (134) Doux, J. M.; Yang, Y.; Tan, D. H. S.; Nguyen, H.; Wu, E. A.; Wang, X.; Banerjee, A.; Meng, Y. S. Pressure Effects on Sulfide Electrolytes for All Solid-State Batteries. *J. Mater. Chem. A* **2020**, *8* (10), 5049–5055. <https://doi.org/10.1039/c9ta12889a>.

- (135) Restle, T. M. F.; Strangmüller, S.; Baran, V.; Senyshyn, A.; Kirchhain, H.; Klein, W.; Merk, S.; Müller, D.; Kutsch, T.; van Wüllen, L.; Fässler, T. F. Super-Ionic Conductivity in ω -Li₉TrP₄ (Tr = Al, Ga, In) and Lithium Diffusion Pathways in Li₉AlP₄ Polymorphs. *Adv. Funct. Mater.* **2022**, *22*, 2112377. <https://doi.org/10.1002/adfm.202112377>.
- (136) Fletcher, S. The Two-Terminal Equivalent Network of a Three-Terminal Electrochemical Cell. *Electrochem. commun.* **2001**, *3* (12), 692–696. [https://doi.org/10.1016/S1388-2481\(01\)00233-8](https://doi.org/10.1016/S1388-2481(01)00233-8).
- (137) Lasia, A. *Electrochemical Impedance Spectroscopy and Its Applications*, p. 7-64; Springer, 1999.
- (138) Lvovich, V. F. *Applications to Electrochemical and Dielectric Phenomena*, p. 1 - 96; Wiley: Hoboken, 2012.
- (139) Irvine, J. T. S.; Sinclair, D. C.; West, A. R. Electroceramics: Characterization by Impedance Spectroscopy. *Adv. Mater.* **1990**, *2* (3), 132–138. <https://doi.org/10.1002/ADMA.19900020304>.
- (140) Abelard, P.; Baumard, J. F. Study of the Dc and Ac Electrical Properties of an Yttria-Stabilized Zirconia Single Crystal [(ZrO₂)_{0.88x}-(Y₂O₃)_{0.12}]. *Phys. Rev. B* **1982**, *26* (2), 1005–1017.
- (141) Fleig, J.; Maier, J. The Impedance of Ceramics with Highly Resistive Grain Boundaries: Validity and Limits of the Brick Layer Model. *J. Eur. Ceram. Soc.* **1999**, *19* (6–7), 693–696. [https://doi.org/10.1016/s0955-2219\(98\)00298-2](https://doi.org/10.1016/s0955-2219(98)00298-2).
- (142) Armstrong, R. D.; Dickinson, T.; Willis, P. M. The A.C. Impedance of Powdered and Sintered Solid Ionic Conductors. *J. Electroanal. Chem.* **1974**, *53* (3), 389–405. [https://doi.org/10.1016/S0022-0728\(74\)80077-X](https://doi.org/10.1016/S0022-0728(74)80077-X).
- (143) Hodge I. M., Ingram M. D., W. A. R. Impedance and Modulus Spectroscopy of Polycrystalline. **1976**, *74*, 125–143.
- (144) Fleig, J.; Maier, J. Finite-Element Calculations on the Impedance of Electroceramics with Highly Resistive Grain Boundaries: I, Laterally Inhomogeneous Grain Boundaries. *J. Am. Ceram. Soc.* **1999**, *82* (12), 3485–3493. <https://doi.org/10.1111/j.1151-2916.1999.tb02270.x>.
- (145) Fleig, J.; Maier, J. A Finite Element Study on the Grain Boundary Impedance of Different Microstructures. *J. Electrochem. Soc.* **1998**, *145* (6), 2081–2089. <https://doi.org/10.1149/1.1838600>.
- (146) Braun, P.; Uhlmann, C.; Weber, A.; Störmer, H.; Gerthsen, D.; Ivers-Tiffée, E. Separation of the Bulk and Grain Boundary Contributions to the Total Conductivity of Solid Lithium-Ion Conducting Electrolytes. *J. Electroceramics* **2017**, *38* (2–4), 157–167. <https://doi.org/10.1007/s10832-016-0061-y>.
- (147) Ohno, S.; Bernges, T.; Buchheim, J.; Duchardt, M.; Hatz, A. K.; Kraft, M. A.; Kwak, H.; Santhosha, A. L.; Liu, Z.; Minafra, N.; Tsuji, F.; Sakuda, A.; Schlem, R.; Xiong, S.; Zhang, Z.; Adelhelm, P.; Chen, H.; Hayashi, A.; Jung, Y. S.; Lotsch, B. V.; Roling, B.; Vargas-Barbosa, N. M.; Zeier, W. G. How Certain Are the Reported Ionic Conductivities of Thiophosphate-Based Solid Electrolytes? An Interlaboratory Study. *ACS Energy Letters*. American Chemical Society March 13, 2020, pp 910–915. <https://doi.org/10.1021/acsenerylett.9b02764>.

-
- (148) Ashcroft, N. W.; Mermin, D. N. *Festkörperphysik, 3rd Ed.*, p. 762 - 768, 3rd ed.; Oldenbourg Wissenschaftsverlag: München, 2007.
- (149) Culler, S. R. *Diffuse Reflectance Infrared Spectroscopy: Sampling Techniques for Qualitative/Quantitative Analysis of Solids*, in: *Practical Sampling Techniques for Infrared Alaysis*, 1st ed.; Coleman, P. B., Ed.; CRC Press: Boca Raton, 1993.
- (150) Sicklinger, J.; Metzger, M.; Beyer, H.; Pritzl, D.; Gasteiger, H. A. Ambient Storage Derived Surface Contamination of NCM811 and NCM111: Performance Implications and Mitigation Strategies. *J. Electrochem. Soc.* **2019**, *166* (12), A2322–A2335. <https://doi.org/10.1149/2.0011912jes>.
- (151) Sicklinger, J.; Beyer, H.; Hartmann, L.; Riewald, F.; Sedlmeier, C.; Gasteiger, H. A. SO₃ Treatment of Lithium- and Manganese-Rich NCMs for Li-Ion Batteries: Enhanced Robustness towards Humid Ambient Air and Improved Full-Cell Performance. *J. Electrochem. Soc.* **2020**, *167* (13), 130507. <https://doi.org/10.1149/1945-7111/abb6cb>.
- (152) Sedlmeier, C. M. An In Situ DRIFTS Study of Surface Contaminants on Overlithiated Nickel-Cobalt-Manganese-Oxide. *Master's thesis* **2018**, No. September, Technische Universität München.
- (153) Massa, W.; Elschenbroich, C.; Hensel, F.; Hopf, H. *Kristallstrukturbestimmung, 7th Ed.*, p. 25 - 42, 7th ed.; Elschenbroich, C., Hensel, F., Hopf, H., Eds.; Vieweg+Teubner: Wiesbaden, 2011.
- (154) Zhang, W.; Weber, D. a.; Wenzel, S.; Sedlmaier, S. J.; Schneider, Y.; Walter, D.; Leichtweiss, T.; Nazar, L. F.; Houtarde, D.; Busche, M. R.; Dietrich, C.; Janek, J.; Schröder, D.; Weigand, H. In Situ Monitoring of Fast Li-Ion Conductor Li₇P₃S₁₁ Crystallization Inside a Hot-Press Setup. *Chem. Mater.* **2016**, *28* (17), 6152–6165. <https://doi.org/10.1021/acs.chemmater.6b02163>.
- (155) Moulder, J. F.; Stickle, W. F.; Sobol, P. E.; Bomben, K. D. *Handbook of XPS*; Chastain, J., King, R. C. J., Eds.; Physical Electronics, Inc.: Eden Prairie, 1995.
- (156) Heide, P. van der. *X-Ray Photoelectron Spectroscopy; An Introduction to Principles and Practices*, 1st ed.; WILEY: Hoboken, 2012.
- (157) Wenzel, S.; Randau, S.; Leichtweiß, T.; Weber, D. A.; Sann, J.; Zeier, W. G.; Janek, J. Direct Observation of the Interfacial Instability of the Fast Ionic Conductor Li₁₀GeP₂S₁₂ at the Lithium Metal Anode. *Chem. Mater.* **2016**, *28* (7), 2400–2407. <https://doi.org/10.1021/acs.chemmater.6b00610>.
- (158) Riphaut, N.; Stiaszny, B.; Beyer, H.; Indris, S.; Gasteiger, H. A.; Sedlmaier, S. J. Understanding Chemical Stability Issues between Different Solid Electrolytes in All-Solid-State Batteries. *J. Electrochem. Soc.* **2019**, *166* (6), A975–A983. <https://doi.org/10.1149/2.0351906jes>.
- (159) Chen, Y. T.; Marple, M. A. T.; Tan, D. H. S.; Ham, S. Y.; Sayahpour, B.; Li, W. K.; Yang, H.; Lee, J. B.; Hah, H. J.; Wu, E. A.; Doux, J. M.; Jang, J.; Ridley, P.; Cronk, A.; Deysher, G.; Chen, Z.; Meng, Y. S. Investigating Dry Room Compatibility of Sulfide Solid-State Electrolytes for Scalable Manufacturing. *J. Mater. Chem. A* **2022**, *10* (13), 7155–7164. <https://doi.org/10.1039/d1ta09846b>.
- (160) Reimer, L.; Hawkes, P. W. *Scanning Electron Microscopy - Physics of Image Formation and Microanalysis - 2nd Ed.*, p. 1-12, 2nd ed.; Hawkes, P. W., Ed.; Springer: Heidelberg, 1998.

- (161) Zhang, W.; Weber, D. A.; Weigand, H.; Arlt, T.; Manke, I.; Schröder, D.; Koerver, R.; Leichtweiss, T.; Hartmann, P.; Zeier, W. G.; Janek, J. Interfacial Processes and Influence of Composite Cathode Microstructure Controlling the Performance of All-Solid-State Lithium Batteries. *ACS Appl. Mater. Interfaces* **2017**, *9* (21), 17835–17845. <https://doi.org/10.1021/acsami.7b01137>.
- (162) Marks, T.; Trussler, S.; Smith, A. J.; Xiong, D.; Dahn, J. R. A Guide to Li-Ion Coin-Cell Electrode Making for Academic Researchers. *J. Electrochem. Soc.* **2011**, *158* (1), A51. <https://doi.org/10.1149/1.3515072>.
- (163) Ates, T.; Keller, M.; Kulisch, J.; Adermann, T.; Passerini, S. Development of an All-Solid-State Lithium Battery by Slurry-Coating Procedures Using a Sulfidic Electrolyte. *Energy Storage Mater.* **2019**, *17*, 204–210. <https://doi.org/10.1016/j.ensm.2018.11.011>.
- (164) Sedlmeier, C.; Schuster, R.; Schramm, C.; Gasteiger, H. A. A Micro-Reference Electrode for Electrode-Resolved Impedance and Potential Measurements in All-Solid-State Battery Pouch Cells and Its Application to the Study of Indium-Lithium Anodes. *J. Electrochem. Soc.* **2023**, *170*, 030536. <https://doi.org/10.1149/1945-7111/acc699>.
- (165) Dees, D. W.; Jansen, A. N.; Abraham, D. P. Theoretical Examination of Reference Electrodes for Lithium-Ion Cells. *J. Power Sources* **2007**, *174* (2), 1001–1006. <https://doi.org/10.1016/j.jpowsour.2007.06.128>.
- (166) Zhou, J.; Notten, P. H. L. Development of Reliable Lithium Microreference Electrodes for Long-Term In Situ Studies of Lithium-Based Battery Systems. *J. Electrochem. Soc.* **2004**, *151* (12), A2173. <https://doi.org/10.1149/1.1813652>.
- (167) Solchenbach, S.; Pritzl, D.; Kong, E. J. Y.; Landesfeind, J.; Gasteiger, H. A. A Gold Micro-Reference Electrode for Impedance and Potential Measurements in Lithium Ion Batteries. *J. Electrochem. Soc.* **2016**, *163* (10), A2265–A2272. <https://doi.org/10.1149/2.0581610jes>.
- (168) Bünzli, C.; Kaiser, H.; Novák, P. Important Aspects for Reliable Electrochemical Impedance Spectroscopy Measurements of Li-Ion Battery Electrodes. *J. Electrochem. Soc.* **2015**, *162* (1), A218–A222. <https://doi.org/10.1149/2.1061501jes>.
- (169) Klett, M.; Gilbert, J. A.; Trask, S. E.; Polzin, B. J.; Jansen, A. N.; Dees, D. W.; Abraham, D. P. Electrode Behavior RE-Visited: Monitoring Potential Windows, Capacity Loss, and Impedance Changes in $\text{Li}_{1.03}(\text{Ni}_{0.5}\text{Co}_{0.2}\text{Mn}_{0.3})_{0.97}\text{O}_2/\text{Silicon-Graphite}$ Full Cells. *J. Electrochem. Soc.* **2016**, *163* (6), A875–A887. <https://doi.org/10.1149/2.0271606jes>.
- (170) Koerver, R.; Aygün, I.; Leichtweiß, T.; Dietrich, C.; Zhang, W.; Binder, J. O.; Hartmann, P.; Zeier, W. G.; Janek, J. Capacity Fade in Solid-State Batteries: Interphase Formation and Chemomechanical Processes in Nickel-Rich Layered Oxide Cathodes and Lithium Thiophosphate Solid Electrolytes. *Chem. Mater.* **2017**, *29* (13), 5574–5582. <https://doi.org/10.1021/acs.chemmater.7b00931>.
- (171) Dietrich, C.; Zeier, W. G.; Walther, F.; Koerver, R.; Aygün, I.; Sann, J.; Janek, J. Redox-Active Cathode Interphases in Solid-State Batteries. *J. Mater. Chem. A* **2017**, *5* (43), 22750–22760. <https://doi.org/10.1039/c7ta07641j>.
- (172) Kato, Y.; Shiotani, S.; Morita, K.; Suzuki, K.; Hirayama, M.; Kanno, R. All-Solid-

- State Batteries with Thick Electrode Configurations. *J. Phys. Chem. Lett.* **2018**, *9* (3), 607–613. <https://doi.org/10.1021/acs.jpcllett.7b02880>.
- (173) Zhang, W.; Weber, D.; Weigand, H.; Arlt, T.; Manke, I.; Schröder, D.; Koerver, R.; Leichtweiss, T.; Hartmann, P.; Zeier, W. G.; Janek, J. Interfacial Processes and Influence of Composite Cathode Microstructure Controlling the Performance of All-Solid-State Lithium Batteries. *ACS Appl. Mater. Interfaces* **2017**, *9* (21), 17835–17845. <https://doi.org/10.1021/acsami.7b01137>.
- (174) Minnmann, P.; Quillman, L.; Burkhardt, S.; Richter, F. H.; Janek, J. Quantifying the Impact of Charge Transport Bottlenecks in Composite Cathodes of All-Solid-State Batteries. *J. Electrochem. Soc.* **2021**, *168* (4), 040537. <https://doi.org/10.1149/1945-7111/abf8d7>.
- (175) Schlenker, R.; Stępień, D.; Koch, P.; Hupfer, T.; Indris, S.; Roling, B.; Miß, V.; Fuchs, A.; Wilhelmi, M.; Ehrenberg, H. Understanding the Lifetime of Battery Cells Based on Solid-State $\text{Li}_6\text{PS}_5\text{Cl}$ Electrolyte Paired with Lithium Metal Electrode. *ACS Appl. Mater. Interfaces* **2020**, *12* (17), 20012–20025. <https://doi.org/10.1021/acsami.9b22629>.
- (176) Ikezawa, A.; Fukunishi, G.; Okajima, T.; Kitamura, F.; Suzuki, K.; Hirayama, M.; Kanno, R.; Arai, H. Performance of $\text{Li}_4\text{Ti}_5\text{O}_{12}$ -Based Reference Electrode for the Electrochemical Analysis of All-Solid-State Lithium-Ion Batteries. *Electrochem. commun.* **2020**, *116*, 106743. <https://doi.org/10.1016/j.elecom.2020.106743>.
- (177) Chang, G. H.; Choi, H. U.; Kang, S.; Park, J. Y.; Lim, H. T. Characterization of Limiting Factors of an All-Solid-State Li-Ion Battery Using an Embedded Indium Reference Electrode. *Ionics*. **2020**, *26* (3), 1555–1561. <https://doi.org/10.1007/s11581-019-03367-w>.
- (178) Costard, J.; Ender, M.; Weiss, M.; Ivers-Tiffée, E. Three-Electrode Setups for Lithium-Ion Batteries. *J. Electrochem. Soc.* **2016**, *164* (2), A80–A87. <https://doi.org/10.1149/2.0241702jes>.
- (179) Ender, M.; Weber, A.; Ivers-Tiffée, E. Analysis of Three-Electrode Setups for AC-Impedance Measurements on Lithium-Ion Cells by FEM Simulations. *J. Electrochem. Soc.* **2011**, *159* (2), A128–A136. <https://doi.org/10.1149/2.100202jes>.
- (180) Bach, P.; Stratmann, M.; Valencia-Jaime, I.; Romero, A. H.; Renner, F. U. Lithiation and Delithiation Mechanisms of Gold Thin Film Model Anodes for Lithium Ion Batteries: Electrochemical Characterization. *Electrochim. Acta* **2015**, *164*, 81–89. <https://doi.org/10.1016/j.electacta.2015.02.184>.
- (181) Haffner, A.; Bräuniger, T.; Johrendt, D. Supertetrahedral Networks and Lithium-Ion Mobility in Li_2SiP_2 And Li_2SiP_3 . *Angew. Chemie - Int. Ed.* **2016**, *55* (43), 13585–13588. <https://doi.org/10.1002/anie.201607074>.
- (182) Toffoletti, L.; Kirchhain, H.; Landesfeind, J.; Klein, W.; van Wüllen, L.; Gasteiger, H. A.; Fässler, T. F. Lithium Ion Mobility in Lithium Phosphidosilicates: Crystal Structure, ^7Li , ^{29}Si , and ^{31}P MAS NMR Spectroscopy, and Impedance Spectroscopy of Li_8SiP_4 and Li_2SiP_2 . *Chem. - A Eur. J.* **2016**, *22* (49), 17635–17645. <https://doi.org/10.1002/chem.201602903>.
- (183) Eickhoff, H.; Toffoletti, L.; Klein, W.; Raudaschl-Sieber, G.; Fässler, T. F. Synthesis and Characterization of the Lithium-Rich Phosphidosilicates $\text{Li}_{10}\text{Si}_2\text{P}_6$

- and $\text{Li}_3\text{Si}_3\text{P}_7$. *Inorg. Chem.* **2017**, *56* (11), 6688–6694. <https://doi.org/10.1021/acs.inorgchem.7b00755>.
- (184) Strangmüller, S. Investigation of Structure-Property Relationships in Solid State Electrolytes — Synthesis and Characterization of Lithium Phosphidotetrelates. *PhD thesis* **2021**, Technische Universität München.
- (185) Restle, T. M. F.; Sedlmeier, C.; Kirchhain, H.; Klein, W.; Raudaschl-Sieber, G.; Deringer, V. L.; van Wüllen, L.; Gasteiger, H. A.; Fässler, T. F. Fast Lithium Ion Conduction in Lithium Phosphidoaluminates. *Angew. Chemie - Int. Ed.* **2020**, *59* (14), 5665–5674. <https://doi.org/10.1002/anie.201914613>.
- (186) Schmedt auf der Günne, J.; Johansson, S.; Dehnen, S.; Bron, P.; Roling, B.; Zick, K. $\text{Li}_{10}\text{SnP}_2\text{S}_{12}$: An Affordable Lithium Superionic Conductor. *J. Am. Chem. Soc.* **2013**, *135* (42), 15694–15697. <https://doi.org/10.1021/ja407393y>.
- (187) Homma, K.; Yonemura, M.; Kobayashi, T.; Nagao, M.; Hirayama, M.; Kanno, R. Crystal Structure and Phase Transitions of the Lithium Ionic Conductor Li_3PS_4 . *Solid State Ionics* **2011**, *182* (1), 53–58. <https://doi.org/10.1016/j.ssi.2010.10.001>.
- (188) Meini, S.; Tsiouvaras, N.; Schwenke, K. U.; Piana, M.; Beyer, H.; Lange, L.; Gasteiger, H. A. Rechargeability of Li-Air Cathodes Pre-Filled with Discharge Products Using an Ether-Based Electrolyte Solution: Implications for Cycle-Life of Li-Air Cells. *Phys. Chem. Chem. Phys.* **2013**, *15* (27), 11478–11493. <https://doi.org/10.1039/c3cp51112j>.
- (189) Choi, E. G.; Song, K. H.; An, S. R.; Lee, K. Y.; Youn, M. H.; Park, K. T.; Jeong, S. K.; Kim, H. J. Cu/ZnO/AlOOH Catalyst for Methanol Synthesis through CO_2 Hydrogenation. *Korean J. Chem. Eng.* **2018**, *35* (1), 73–81. <https://doi.org/10.1007/s11814-017-0230-y>.
- (190) Park, J. H.; Min, D. J.; Song, H. S. Structural Investigation of $\text{CaO-Al}_2\text{O}_3$ and $\text{CaO-Al}_2\text{O}_3\text{-CaF}_2$ Slags via Fourier Transform Infrared Spectra. *ISIJ Int.* **2002**, *42* (1), 38–43. <https://doi.org/10.2355/isijinternational.42.38>.
- (191) Ram, S. Infrared Spectral Study of Molecular Vibrations in Amorphous, Nanocrystalline and $\text{AlO}(\text{OH}) \cdot \text{AH}_2\text{O}$ Bulk Crystals. *Infrared Phys. Technol.* **2001**, *42* (6), 547–560. [https://doi.org/10.1016/S1350-4495\(01\)00117-7](https://doi.org/10.1016/S1350-4495(01)00117-7).
- (192) Fripiat, J. J.; Bosnians, H.; Rouxhetlb, P. G. Proton Mobility in Solids Proton Mobility in Solids. I. Hydrogenic Vibration Modes and Proton Delocalization in Boehmite. *J. Phys. Chem.* **1967**, *71* (4), 1097–1111.
- (193) Kim, J.; Hong, Y.; Ryu, K. S.; Kim, M. G.; Cho, J. Washing Effect of a $\text{LiNi}_{0.83}\text{Co}_{0.15}\text{Al}_{0.02}\text{O}_2$ Cathode in Water. *Electrochem. Solid-State Lett.* **2006**, *9* (1). <https://doi.org/10.1149/1.2135427>.
- (194) Cho, D.-H.; Jo, C.-H.; Cho, W.; Kim, Y.-J.; Yashiro, H.; Sun, Y.-K.; Myung, S.-T. Effect of Residual Lithium Compounds on Layer Ni-Rich $\text{Li}[\text{Ni}_{0.7}\text{Mn}_{0.3}]\text{O}_2$. *J. Electrochem. Soc.* **2014**, *161* (6), A920–A926. <https://doi.org/10.1149/2.042406jes>.
- (195) Takeuchi, M.; Coluccia, S.; Martra, G.; Anpo, M. Evaluation of the Adsorption States of H_2O on Oxide Surfaces by Vibrational Absorption: Near- and Mid-Infrared Spectroscopy. *J. Near Infrared Spectrosc.* **2009**, *17* (6), 373–384.
- (196) Hakkarainen, T.; Mikkola, E.; Laperre, J.; Gensous, F.; Fardell, P.; Le Tallec, Y.;

- Baiocchi, C.; Paul, K.; Simonson, M.; Deleu, C.; Metcalfe, E. Smoke Gas Analysis by Fourier Transform Infrared Spectroscopy - Summary of the SAFIR Project Results. *Fire Mater.* **2000**, *24* (2), 101–112. [https://doi.org/10.1002/1099-1018\(200003/04\)24:2<101::AID-FAM729>3.0.CO;2-2](https://doi.org/10.1002/1099-1018(200003/04)24:2<101::AID-FAM729>3.0.CO;2-2).
- (197) Parker, S. F.; Refson, K.; Bewley, R. I.; Dent, G. Assignment of the Vibrational Spectra of Lithium Hydroxide Monohydrate, $\text{LiOH}\cdot\text{H}_2\text{O}$. *J. Chem. Phys.* **2011**, *134* (8), 84503. <https://doi.org/10.1063/1.3553812>.
- (198) Cizer, Ö.; Rodriguez-Navarro, C.; Ruiz-Agudo, E.; Elsen, J.; Van Gemert, D.; Van Balen, K. Phase and Morphology Evolution of Calcium Carbonate Precipitated by Carbonation of Hydrated Lime. *J. Mater. Sci.* **2012**, *47* (16), 6151–6165. <https://doi.org/10.1007/s10853-012-6535-7>.
- (199) Ceppatelli, M.; Scelta, D.; Serrano-Ruiz, M.; Dziubek, K.; Garbarino, G.; Jacobs, J.; Mezouar, M.; Bini, R.; Peruzzini, M. High Pressure Synthesis of Phosphine from the Elements and the Discovery of the Missing $(\text{PH}_3)_2\text{H}_2$ Tile. *Nat. Commun.* **2020**, *11* (1), 1–11. <https://doi.org/10.1038/s41467-020-19745-2>.
- (200) Lu, G.; Crowell, J. E. Evidence for a Precursor to Decomposition for Phosphine Adsorption on Rh / Al_2O_3 Surfaces. *J. Phys. Chem.* **1990**, *94* (15), 5644–5646.
- (201) Hardin, A. H.; Harvey, K. B. Infrared Absorption of Solid Phosphine. *Can. J. Chem.* **1964**, *42*, 84–89.
- (202) Pasierb, P.; Komornicki, S.; Rokita, M.; Rękas, M. Structural Properties of Li_2CO_3 - BaCO_3 System Derived from IR and Raman Spectroscopy. *J. Mol. Struct.* **2001**, *596* (1–3), 151–156. [https://doi.org/10.1016/S0022-2860\(01\)00703-7](https://doi.org/10.1016/S0022-2860(01)00703-7).
- (203) Sicklinger, J. Electrochemical and Spectroscopic Investigation of Lithium-Ion Battery Cathode Active Materials. *PhD thesis* **2022**, Technische Universität München.
- (204) McConaghie, V. M.; Nielsen, H. H. Some Preliminary Results on the Spectra of AsH_3 , AsD_3 and PH_3 . *Proc. Natl. Acad. Sci.* **1948**, *34*, 455–464. <https://doi.org/10.1073/pnas.34.9.455>.
- (205) Greenspan, L. Humidity Fixed Points of Binary Saturated Aqueous Solutions. *J. Res. Natl. Bur. Stand. - A. Phys. Chem.* **1977**, *81* (1), 89–96.

List of Figures

Figure 1.1: Schematic illustration of the main components and operation principle of a Li-ion battery (LIB). The cathode (positive electrode, right) consists in this case of LiCoO_2 (LCO) as cathode active material containing the Li-ions (red), which migrate through the electrolyte towards the anode (negative electrode, left), at which they intercalate into the graphite. The electrons travel via an external circuit, which a load is connected to, from cathode to anode and recombine with the lithium ions. Upon discharge, all processes are reversed. The figure is reprinted from Hausbrand *et al.*¹³ under a Creative Common BY-NC-ND 3.0 license. 4

Figure 1.2: Schematic illustration of a sheet-type, sulfide ASSB and its components: I. Metal anode on a copper current collector. II. Separator-sheet consisting of a sulfide solid electrolyte (dark yellow particles) and a polymeric binder (gray lines). III. Composite cathode coated on an aluminum current collector consisting of a CAM (gray particles), sulfidic catholyte (yellow particles), polymeric binder (gray lines) and conductive additive (black lines). Note that in this illustration a bimodal particle size distribution for the catholyte is used. Sulfidic electrolytes in separator and cathode are displayed in differently shaded colors since the used SEs in separator and composite cathode must not necessarily be the same. Dimensions of the electrodes are not drawn to scale. Compression effects such as particle rearrangement or deformation are neglected for simplicity. 11

Figure 2.1: Exploded-view drawing of the first cell generation, showing and labelling all components and describing the main characteristics of the cell. Adapted with permission from Strangmüller *et al.*¹²⁶. Copyright 2019 American Chemical Society. 18

Figure 2.2: Drawing and main characteristics of the second cell generation in side (a) and sectional view (b) with, showing and labelling all components. Reproduced from Sedlmeier *et al.*¹²⁷ with permission from J. Electrochem. Soc. under the terms of the Creative Commons Attribution 4.0 License. 19

Figure 2.3: Drawing and main characteristics of the third cell generation. (a) Assembled pouch cell in the home-made stainless-steel pouch cell holder. Pressure is applied by the defined compression of six springs. (b) Exploded-view drawing of the pouch cell assembly, in this case a symmetric $\text{In/InLi} \mid \text{In/InLi}$ cell with a μ -RE using two LPSCI/HNBR separator-sheets. Since it is a symmetric cell, all cell compounds are labelled only once. Note that the very thin ($64 \mu\text{m}$), wire-shaped micro-reference electrode (μ -RE) reaches to the middle of the separator-sheets but is difficult to see, as all cell parts are displayed in the correct dimensions. Also note that the pouch bag is not sealed in this illustration. Many thanks to Philip Rapp for the graphical processing of the technical drawings. Printed with permission from Philip Rapp. 20

Figure 2.4: Leak test of the generation 1 cell with water vapor sensitive Li_8SiP_4 , conducted by monitoring the impedance evolution over the course of 16 hours. One spectrum ($7 \text{ MHz} - 1 \text{ Hz}$, 10 mV perturbation voltage) is recorded every 2 hours. Cells

were assembled inside an argon filled glovebox at 25°C and measured under ambient atmosphere in a temperature chamber at 25°C. Screws were fastened with 30 Nm torque each. The cell, which is tightened by two O-rings applied to the ungreased pistons (a) leaks over time, indicated by the continuous increase in impedance, whereas additional greasing of both pistons (b) ensures a firm sealing over the course of 16 hours. The electrolyte resistance R_{SE} , obtained by an $R/Q+Q$ fit of the spectrum, is displayed versus time in (c) and (d) using non-greased and greased pistons, respectively. Note that the amount of sample is different for both cells and hence also the total resistance. The dashed line in (d) is a guide-to-the-eye. 22

Figure 2.5: Setup for the vacuum leak test of the PTFE flat-seal in the generation 2 cell. The steel bellows is attached to the empty cell body with a 340 μm thick PTFE flat-seal (compressed to 10% yield point). The bellows is attached to the steel line by a copper knife-edge gasket. All connections and valves in the experimental setup are connected via Swagelok® line fittings (a). Recording of the pressure in the experimental setup over the course of 70 hours after evacuation to ~ 0.5 mbar (b). For the blank measurement (blue line), the connection of the line with the steel bellows was closed with a blind plug. The measurement to evaluate the sealing properties of the PTFE flat-seal is displayed in ocher. Note that no data points were taken in the interval between 24-70 hours. 24

Figure 2.6: Lithium ion conductivity for an LSPS sample determined from EIS measurements conducted in a generation 1 cell inside a glovebox at 26°C. The conductivity is plotted against the torque T_a , which each of the six screws was fastened with. The corresponding calculated pressure (p_{calc}) for each torque is displayed on the upper x -axis and was calculated according to equation (2.1). Error bars correspond to the min/max values of two measurements with the same cell. 27

Figure 2.7: Illustration of the geometric effects that we faced during designing and validation the spring cell. Both phenomena have a negative impact on the contacting between the die (gray) and a rigid solid electrolyte (SE) sample (ocher). Important parameters to consider are the diameter of the die d , the deviation upon manufacture a , the angularity α , and the sample thickness t , as well as the surface roughness R_a . 32

Figure 2.8: Contributions to the calculated stray capacitance of the screw cell. Positions where the capacitors are located in the cell are marked by colored boxes and assigned to the respective cell parts. The capacitor indicated by the orange box is found for all six screws in the cell. For better visibility, cell components which are electrically connected are displayed in the same shade of gray. An exploded-view drawing of the cell is shown in Figure 2.1. 33

Figure 2.9: Illustration of an EIS spectrum for the conductivity determination of three stacked LSPS/HNBR (5.8 vol.-% HNBR) separator-sheets, measured in the spring cell at 70 MPa and 25°C in a frequency range from 7 MHz – 100 Hz. Data points (black circles) are displayed in a frequency range from 7 MHz – 10 kHz. The fit (blue line) was obtained by fitting the data with an R_1+R_2/Q_2+Q_3 equivalent circuit, as displayed. The ocher line results from a linear fit of the low-frequency tail between 30 – 4 kHz, which was extrapolated to the x -axis. The high-frequency resistance R_{HFR} (green) represents a superposition of the cell resistance and the grain bulk resistance R_{grain} . For the latter we expect an R/Q element, which however cannot be resolved at the used frequency and temperature. The blue semi-circle illustrates the grain boundary resistance R_{gb} . Note that

the green and blue features are manually added but their magnitude is in scale to the values obtained by the fit. The values for the solid electrolyte resistance R_{SE} determined via the equivalent circuit fit and the one obtained by the extrapolation of the linearly fitted low-frequency tail deviate by $\sim 1\%$. Sample thickness is 0.026 cm and sample area 0.50 cm². 40

Figure 2.10: Illustration of an exemplary *Arrhenius* plot of the product of conductivity and temperature ($\sigma \cdot T$) versus $1000/T$ and linear fit of the data points for Li₁₄SiP₆. Error bars are based on the standard deviation from three independent measurements. The activation energy E_A for lithium ion conduction in units of [kJ · mol⁻¹] is obtained from the slope m of the linear fit and the universal gas constant R . 42

Figure 2.11: Setup for *in situ* DRIFTS measurements exposing powdered solid electrolyte samples to various gas atmospheres containing different components of ambient atmosphere. The gas mixture can be adjusted by mixing gases from different sources using Ar as carrier gas: 1000 ppm CO₂ in Ar (green), Ar (violet) and O₂ (red); via the humidifier, it is possible to introduce water vapor into the system. The gas tight DRIFTS cell, which contains the sample, is placed in the IR spectrometer. Symbols of the components are explained on the right. Reprinted from *Christian Sedlmeier's* Master's thesis.¹⁵² 43

Figure 3.1: Selected spectra in reflectance units of the *in situ* DRIFTS experiments with pure Li₉AlP₄ according to the measurement procedure described in section 2.3. Arbitrary offset in the y -axis for better visibility. (a) Li₉AlP₄ under glovebox atmosphere with the cell connected to the setup but valves closed. Spectra (b) – (f) are taken under Ar atmosphere after exposing the sample for 2 h to the reactive gas (indicated in the plot) and a subsequent Ar purge for 1 h: (b) Ar, (c) O₂ (d) 1000 ppm CO₂ in Ar, (e) humidified Ar (estimated dew point of $T_{dp} \sim 13$ °C corresponding to ~ 14700 ppm H₂O in Ar), (f) 1000 ppm CO₂ in humidified Ar (estimated dew point of $T_{dp} \sim 13$ °C corresponding to ~ 14700 ppm H₂O in Ar). For each reactive gas a separate and independent measurement with a fresh sample was performed. The spectra under glovebox atmosphere (a) were collected prior to each experiment for all the samples; no difference in their spectra was observable, so that only one representative is shown. Modes are indicated by numbers and color coded regarding their origin: O-H (blue), -CO₃ (orange), Al-O (black), P-H (violet) and Al-P (gray, assumed). Please also refer to Table 3.1. 121

Figure 3.2: Spectra of the *in situ* DRIFT experiments with Li₉AlP₄ in reflectance units. Spectra (a) and (e) are the same as in Figure 3.1 and are recorded under glovebox atmosphere (a) and argon (1 h Ar purge after 2 h exposure to water vapor, e). The dark blue spectrum labelled with “10 min H₂O dosage” refers to the same sample as in (e) but taken after 10 min during the exposure to water vapor. Smaller spectra on the right are enlargements of regions where vibration modes of gaseous PH₃ are observed. Red lines are a guide-to-the-eye. 125

Figure 4.1: Graphical summary of the key ASSB cell developments and their use for ASSB material characterization and battery testing done in this PhD thesis. Section 2.1 described the design and validation measures for the sealing concept, pressure application, further geometric requirements and of the stray capacitance for the three different cell generations developed during this PhD thesis. Afterwards, we developed a slurry-based process in toluene to prepare SE/HNBR composite separator-sheets and

characterized them in terms of porosity and conductivity using the spring cell setup (subsection 3.1.1). Using these sheets, we were able to prepare ASSB pouch cells, which allowed us to integrate a micro-reference electrode. By the use of half-cell potential and impedance measurements via the reference electrode, we were able to identify constraints for the use of indium-lithium electrodes (subsection 3.1.2). In parallel to the work on application-oriented sheet-type cell components based on sulfide SEs, we performed fundamental material characterization on the solid ion conductor class of the lithium phosphides. Using the screw cell, we determined the ionic conductivity of the most lithium-rich lithium phosphidosilicate $\text{Li}_{14}\text{SiP}_6$ (subsection 3.2.1). Furthermore, we performed IR spectroscopic investigations on the reactivity of the lithium phosphidoaluminate Li_9AlP_4 with components from ambient atmosphere to assess its atmospheric stability and its possible decomposition mechanism (subsection 3.2.2). 128

Acknowledgements

The content of this PhD thesis was accomplished between November 2018 and November 2022 at the Chair for Technical Electrochemistry at the Technische Universität München (TUM).

First of all, I want to express my deep and sincere gratitude to my PhD supervisor, **Prof. Hubert A. Gasteiger**. Thank you, for working with you and learning from you. It is truly inspiring to see how much passion you put into the research and especially into your group. Thereby, the remarkable is not only what you do but more how you do it, down to the very last detail. You motivate the people around you to join that path even if it is sometimes outside of one's comfort zone. It was a pretty intense but exciting journey; I would certainly do it again!

Many thanks go to **Veronika Pichler** for keeping the chair running. You helped with all the organization and administrative tasks, allowing us to focus on the research. Thanks a lot for your support!

In the same way, I want so express my special gratitude to **Fabian Schatz**. You really put a lot of effort and commitment into the TUMint·Energy Research GmbH. Being the organizational talent you are, you enable young scientists to develop by providing everything necessary for proper research. On a personal level, you always have an open ear for any concern, which I truly appreciate.

A big thank you to the ASSB-Team at TEC: **Tobias Kutsch, Robin Schuster, Gioele Conforto** and **Moritz Bohn**. Since I started working basically alone on ASSB-topics at TEC for the first one and a half years, I was so grateful for you guys joining. I really appreciate how the continuous exchange and discussion positively influenced the working atmosphere and research quality. I am quite proud of what we achieved as a team and that after two years of diligent work, we now understand our cells and electrolyte systems in such a way that one can focus on interesting scientific questions. I am sure there will be a lot of exciting studies and findings in the next years to come. Now it is time to reap what we have been sowing for the last two years.

I want to thank all my former students **Raphaela Bublitz**, **Maria Lanzinger**, **Markus Pietsch**, **Maryke Kouyate**, **Carina Schramm** and **Mia Tominac**. Thanks for your motivation, curiosity and efforts in the projects we worked on together.

I also want to say thank you to **Prof. Thomas F. Fässler** as well as **Tassilo Restle**, **Stefan Löffler (geb. Strangmüller)**, **David Müller** and **Henrik Eickhoff** of the ACNM for the numerous collaboration studies we worked on together. It was really interesting for me to extend the view of an electrochemist to the fundamental, structural properties of solid ion conductors on a material level. We learnt quite a lot from each other and could exchange experiences from our fields of expertise, which all of us profited from. That is the beauty of scientific exchange!

A big thanks to all the current and former colleagues at TEC for the pleasant and inspiring atmosphere at the chair. Among them, special thanks to my friends **Maxi Graf**, **Lennart Reuter**, **Timon Lazaridis**, **Carla Harzer**, **Franziska Hnyk** and **Tanja Zünd** for high spirits, good office vibes and lots of sports and outdoor fun; no matter if it is squash, cycling, climbing or ski touring. Always a pleasure!

Last but not least, a heartfelt thanks to my **family** for the continuous support throughout the entire time: my mother **Lucia**, my father **Peter**, my brother **Alexander** his girlfriend **Petra** and my girlfriend **Anne-Marie**. It was some time consuming and intense four years, I know, but I could always rely on you and trust that you would be backing me up.

Scientific Contributions

Peer-reviewed publications

- **C. Sedlmeier**, R. Schuster, C. Schramm and H. A. Gasteiger: „*A Micro-Reference Electrode for Electrode-Resolved Impedance and Potential Measurements in All-Solid-State Battery Pouch Cells and Its Application to Indium-Lithium-Anodes*”, *J. Electrochem. Soc.*, 170, 030536 (2023).
<https://iopscience.iop.org/article/10.1149/1945-7111/acc699/pdf>
- **C. Sedlmeier**⁺, T. Kutsch⁺, R. Schuster, L. Hartmann, R. Bublitz, M. Tominac, M. Bohn and H. A. Gasteiger: „*From Powder to Sheets: A Comparative Electrolyte Study for Slurry-Based Processed Solid Electrolyte/Binder-Sheets as Separators in All-Solid-State Batteries*”, *J. Electrochem. Soc.*, 169, 070508 (2022).
<https://iopscience.iop.org/article/10.1149/1945-7111/ac7e76/pdf>
- T. M. F. Restle, **C. Sedlmeier**, H. Kirchhain, W. Klein, G. Raudaschl-Sieber, L. van Wüllen and T. F. Fässler: “*Fast Lithium Ion Conduction in Phosphide Li_9GaP_4* ”, *Chem. Mater.*, 33, 2957-2966 (2021).
<https://pubs.acs.org/doi/pdf/10.1021/acs.chemmater.1c00504>
- T. M. F. Restle, **C. Sedlmeier**, H. Kirchhain, W. Klein, G. Raudaschl-Sieber, V. L. Deringer, L. van Wüllen, H. A. Gasteiger and T. F. Fässler: “*Fast Lithium Ion Conduction in Lithium Phosphidoaluminates*”, *Angew. Chem. Int. Ed.*, 59, 5665-5674 (2020).
<https://onlinelibrary.wiley.com/doi/epdf/10.1002/anie.201914613>
- H. Eickhoff, **C. Sedlmeier**, W. Klein, G. Raudaschl-Sieber, H. A. Gasteiger and T. F. Fässler: “*Polyanionic Frameworks in the Lithium Phosphidogermanates Li_2GeP_2 and LiGe_3P_3 – Synthesis, Structure, and Lithium Ion Mobility*”, *Z. Anorg. Allg. Chem.*, 646, 95-102 (2020).
<https://onlinelibrary.wiley.com/doi/epdf/10.1002/zaac.201900228>
- J. Sicklinger, H. Beyer, L. Hartmann, F. Riewald, **C. Sedlmeier** and H. A. Gasteiger: “ *SO_3 Treatment of Lithium- and Manganese-Rich NCMs for Li-Ion Batteries: Enhanced Robustness towards Humid Ambient Air and Improved Full-Cell Performance*”, *J. Electrochem. Soc.*, 167, 130507 (2020).
<https://iopscience.iop.org/article/10.1149/1945-7111/abb6cb/pdf>

- S. Strangmüller, H. Eickhoff, G. Raudaschl-Sieber, H. Kirchhain, **C. Sedlmeier**, L. van Wüllen, H. A. Gasteiger and T. F. Fässler: “*Modifying the Properties of Fast Lithium-Ion Conductors – The Lithium Phosphidotetrelates $Li_{14}SiP_6$, $Li_{14}GeP_6$, and $Li_{14}SnP_6$* ”, *Chem. Mater.*, 32, 6925-6934 (2020).
<https://pubs.acs.org/doi/pdf/10.1021/acs.chemmater.0c02052>
- S. Strangmüller, H. Eickhoff, D. Müller, W. Klein, G. Raudaschl-Sieber, H. Kirchhain, **C. Sedlmeier**, V. Baran, A. Seyshyn, V. L. Deringer, L. van Wüllen, H. A. Gasteiger and T. F. Fässler: “*Fast Ionic Conductivity in the Most Lithium-Rich $Li_{14}SiP_6$* ”, *J. Am. Chem. Soc.*, 141, 14200-14209 (2019).
<https://pubs.acs.org/doi/pdf/10.1021/jacs.9b05301>

Oral presentations

- „*A Micro-Reference Electrode for Impedance and Potential Measurements in All-Solid-State Battery Pouch Cells*”, 241st Meeting of the Electrochemical Society (May 29 – June 2, 2022), **Vancouver** (Canada).
- „*From Powder to Sheets – Fabrication of Free-Standing Slurry-Based Processed Solid Electrolyte Separator-sheets*”, Batterieforum Deutschland 2021 (January 18 – January 21, 2021), **Berlin** (Germany); *Online presentation*.

Poster presentations

- **C. Sedlmeier**[≠], T. Kutsch[≠], R. Schuster, R. Bublitz and H.A. Gasteiger: „*From Powder to Sheets – Fabrication of Free-Standing Slurry-Based Processed Solid Electrolyte Separator-sheets*”, Batterieforum Deutschland 2021 (January 18 – January 21, 2021), **Berlin** (Germany); *Online poster presentation*.
- **C. Sedlmeier**, T. Zünd and H. A. Gasteiger: “*A Novel Cell Setup for High-Pressure Impedance Measurements on Solid Electrolytes for All-Solid-State Lithium-Ion Batteries*”, Batterieforum Deutschland 2019 (January 23 – January 25, 2019), **Berlin** (Germany)
- D. Müller[≠], **C. Sedlmeier**[≠], T. Zünd, H. A. Gasteiger and T. F. Fässler: “*Impedance Measurements of the Solid Solution $Li_8Ge_{1-x}Si_xP_4$ in a High-Pressure Impedance Cell Setup*”, Bunsenkolloquium 2018 (November 14 – November 16, 2018), **Frankfurt** (Germany)

[≠] These authors contribute equally.